

UNIVERSITÀ DEGLI STUDI MILANO - BICOCCA

Scuola di Dottorato in Scienze

Dottorato in Fisica e Astronomia, Ciclo XXII

Coordinatore: Prof. Claudio Destri

EVALUATIONS OF HIGH DENSITY PLASMA
HEATING THROUGH *O-X-B* DOUBLE MODE
CONVERSION OF *EC*-WAVES IN *FTU*
TOKAMAK

Tutore: Dr. Mario Zannoni

Correlatore: Dr. Alessandro Bruschi

Tesi di: William Bin

Matricola n. 708228

Anno Accademico 2009-2010

*Some scientists work so hard
there is no time left for serious thinking.*

Francis Crick

Introduction

The work presented in this PhD Thesis has been performed in the framework of the research on Thermonuclear Fusion in magnetically confined plasmas of tokamak-like devices. The effort is aimed at a feasibility study of Electron Cyclotron Resonance Heating (ECRH) in overdense plasmas. The main aim of this Thesis consists in the study of the applicability of the mode conversion scheme, known as 'O-X-B Double Mode Conversion', to the Italian tokamak FTU (Frascati Tokamak Upgrade), with the use of millimeter-waves at the 140 GHz frequency. This overdense plasma heating technique, not yet demonstrated at electron density of $2.4 \cdot 10^{20} \text{ m}^{-3}$ and consequently at such a high frequency, exploits the conversion of an ordinary polarized wave (O) launched from the plasma boundary with a very narrow angular range and reaching the cutoff region, into the extraordinary (X) one, followed by a subsequent conversion into Bernstein (B) waves, which are then absorbed by the plasma.

Simulations have been performed, by using a ray tracing code, to find the optimal launching conditions for the O-X coupling in FTU. The assessment of conversion efficiency was carried out first with the use of a one-dimensional model, that considers the density and the magnetic field gradients in the plasma. Moreover, the conversion predicted by recent bi-dimensional theoretical models available in literature has been evaluated. The inhomogeneities of a toroidal plasma are thus accounted with a more realistic description.

The experimental part of the work for the Thesis can be divided into two main activities. The first one has been carried out at the laboratories of the research center ENEA in Frascati (Roma), where the tokamak FTU is operating. In this phase, experiments have been performed, aimed at the detailed study of the density profiles and gradients, which characterize the overdense plasma regimes. Proper experimental procedures have been developed, to prepare with reliability the optimal plasma 'target'. The second experimental activity has been carried out at the Istituto di Fisica del Plasma '*Piero Caldirola*' (IFP/CNR Milano), and consists in the contribution given for the design and construction of a new EC millimeter-waves launcher for FTU, whose installation is scheduled for the first months of 2011. The system has been designed to reach the launching angles requested for O-X-B mode conversion, which have been defined in the present work and that are not achievable with the present launching system.

After an introduction in Chapter 1 on the Thermonuclear Fusion energy and on the International Thermonuclear Experimental Reactor (ITER) project, the basic principles of the theory of the Electron Cyclotron waves in tokamak plasmas and the hot plasma Electron Bernstein Waves, together with the possible mode conversion schemes aimed to excite them, are presented respectively in Chapters 2 and 3. The treatment of the wave propagation, in these two Chapters, aims to provide the reader with the theoretical basis of the predictive models developed in this Thesis and presented hereinafter, providing the necessary references.

The results of the study carried out in FTU during last experimental campaigns, aimed to prepare the optimal plasma 'target' for the future experiments on mode conversion, are presented in Chapter 4, together with a description of the high density plasma regimes reachable since recent years in FTU.

The simulations of O-X mode conversion computed using the FTU plasma parameters and the results of the predictive work are presented in Chapter 5.

In the beginning of Chapter 6, a general description of the EC launcher presently installed in FTU is given, in order to show to the reader the motivations that led to the construction of a new launching system to perform new experiments, among which the O-X-B mode conversion ones.

The second part of Chapter 6 is dedicated to a detailed description of the new launcher, from mechanical and scientific points of view, marking the importance of the features of the new system for the aims of this Thesis. The results of millimeter-waves low power measurements and dynamical tests performed at IFP/CNR laboratories with the new launcher are shown, together with some 3D simulations of wave injections from the launching point of this system, with optimal angles for O-X coupling in the FTU plasma.

Contents

1	The Thermonuclear Fusion and the ITER Project	1
1.1	Introduction	1
1.2	The International Thermonuclear Experimental Reactor Project (ITER) . .	8
2	Electron Cyclotron Resonance Heating	11
2.1	Introduction	11
2.2	Wave Dispersion and Propagation	12
2.2.1	The Cold-Plasma Dielectric Tensor	13
2.2.2	The Dispersion Relation in Cold Magnetized Plasma	14
2.3	Single Particle-Wave Resonance	21
2.4	Applications of Electron Cyclotron Waves in Plasmas	23
2.4.1	The Electron Cyclotron Current Drive	23
2.4.2	Control and Stabilization of MHD modes	25
2.4.3	Further Electron Cyclotron Waves Applications	26
2.5	The Electron Cyclotron Launching System	27
2.5.1	Launcher Set-up	27
2.5.2	Launching Schemes	28
3	Electron Bernstein Waves and O-X-B Coupling	29
3.1	Introduction	29
3.2	The Hot Plasma Waves	30
3.2.1	The Electron Bernstein Waves	31
3.3	The SX-B Mode Conversion	35
3.4	Coupling Schemes to EBWs with X-mode Injection	38
3.4.1	The Direct SX-B Coupling	38
3.4.2	The FX-SX-B Scheme	38
3.5	A Third Scheme for EBWs Excitation	41

3.5.1	The O-X-B Double Mode Conversion Scheme	41
3.5.2	The O-SX Coupling	42
3.5.3	The O-X-B Power Transmission Efficiency	48
3.6	2D Models of O-SX Mode Conversion	52
3.7	Experiments on O-X-B Mode Conversion	57
3.7.1	EBWH Experiments in TCV via O-X-B Mode Conversion	59
4	The Optimal Plasma Target for O-SX Coupling	61
4.1	Introduction	61
4.2	The High Density in FTU	61
4.2.1	The Liquid Lithium Limiter	61
4.2.2	New Plasma Regimes with LLL	63
4.2.3	Plasma Density Measurements in FTU	64
4.2.4	Overdense Plasmas in FTU	66
4.3	Research of the Optimal Plasma Target for EBWH	68
4.3.1	Experimental Activity Dedicated to the Density Limit in view of the O-X-B Heating	72
4.3.2	Analysis of 360kA, 5.2 T Discharges from the FTU Database	81
4.3.3	The Optimal Plasma Target for EBWH Experiments	84
5	Evaluations of O-SX Mode Conversion in FTU	87
5.1	Introduction	87
5.2	Geometrical Calculations	88
5.3	Simulations with Real FTU Parameters	90
5.3.1	Effects of Density Fluctuations	96
5.3.2	Effects of Wave Polarization	97
5.3.3	O-SX Mode Conversion in a Slab Geometry based on a Gaussian Beam-Mode Analysis	102
5.4	Prediction of O-SX Conversion in FTU with a 2D Model	106
6	The New Front-Steering EC H&CD Launcher	111
6.1	Introduction	111
6.2	The Present ECRH Launcher of FTU	112

6.2.1	Limitations of the Present Launcher for Experiments on O-X-B Mode Coupling	115
6.3	Motivations for a New ECRH Launcher	116
6.4	Design of the New EC H&CD Launching System	118
6.4.1	Real-Time Control of the Steering Mirrors	122
6.4.2	The Steering Mirror and the Driving Mechanism	124
6.4.3	Motors and their Control	126
6.4.4	The Influence of Different Beam Size on O-X-B Mode Coupling . . .	128
6.4.5	Low Power Tests with the Launcher at Angles Relevant for O-X-B Mode Conversion	130
6.4.6	Dynamical Tests on a Real Scale Mock-up of the New System	131
7	Conclusions	135
A	EBWs Absorption	III
B	Preliminary Tests with the Pellet Injection System	V

Chapter 1

The Thermonuclear Fusion and the ITER Project

1.1 Introduction

Since last decades one of the purposes of humankind is the search of possible sources for future energy production. During recent years, a large number of renewable energy sources could be discovered, in principle, but the crucial point consists in finding sources able to satisfy the always increasing demand while keeping compatible with a sustainable development. So far, Men could not find any alternative for energy able to respect this critical request. In addition to the environmental issues, the alarming aspect of the World energy supply consists in the risk that most of the technologies in use nowadays may reach their maximum level of production in the short term and a gap may open between human demand of energy and the available supplies. Estimated consumption times of several energy sources are shown in Table 1.1. By the end of the century the energy demand may become about three times higher than the present consumption, due to the increasing request of energy from part of the countries now in development. An estimation on the total amount of energy consumed currently from Men can be done: $2.23 \text{ kW} \times 6.5 \text{ billions people} \times 1 \text{ year} = 15 \text{ TW}\cdot\text{year}$ [1], and this number will be likely growing much in the next decades, up to about two times more than now. The energy supply in the World, nowadays, is for 90% provided by burning fossil fuels and the release of CO_2 in the atmosphere implied by this kind of sources may lead to serious problems in the future, from the point of view of the environmental impact and global warming. CO_2 is

a greenhouse gas, which, with the time going by, increases the absorption of the infrared radiation which is re-emitted by the Earth¹. Up to now, measurements show a very steep increase of the CO₂ content in the atmosphere during the last tens of years. This aspect, in addition to the fact that fossil fuels are not inexhaustible, make the research of new form of energy sources inevitable. Unfortunately, despite several renewable energy resources were discovered during last decades and started to be routinely exploited, they are characterized by a low energy density². In addition, many of them, still have a strong environmental impact, not related to the CO₂ emission, due to the deep modifications on the natural scenery implied by their use.

Years of Use of the Different Fuels Available Today		
Fuel	Recoverable Reserves	Years Remaining
Coal	0.9·10 ¹² tons	210
Crude Oil	1.3·10 ¹² barrels	30-40
Natural Gas	190·10 ¹² m ³	60-70
Uranium (as ore)	4.7·10 ⁶ tons	85-270* / 2600-8000**
Uranium (from sea water)	4.5·10 ⁹ tons	81000-260000

*Assuming Light Water Reactor.

**Assuming breeder technology employment.

Table 1.1: Years of use of the different fuels available nowadays, calculated using the current rate of consumption. Table taken from reference [1].

Nowadays, thermonuclear fusion represents one of the most promising long-term energy supply for the future. The safety and 'cleanliness' of this source represents one of the most important aspects. CO₂ emissions are completely absent in the products and the environmental impact of hypothetical fusion plants may be extremely limited. In addition, the huge abundance of chemical elements that can be used as fusion fuels adds to the fact that, differently from what happens for the other energy supplies, fusion is capable to deliver a huge amount of energy, much more than any other known physical process used now. In fact, in fusion reactions (for example between deuterium (D) and tritium (T)) the

¹Records from the past indicate that variations >7°C of the average Earth temperature have taken place in the course of a few tens of years [2].

²Defined as the parameter which expresses how much energy can be extracted from 1 g of fuel.

energy density is largely the highest than for all the other processes that can be exploited today for energy. For instance, a fusion plant of 1 GW_e would need about 100 kg/year of D and 3 ton/year of Li, to produce 7 billions kWh of energy. A plant operating with coal would need about $1.5 \cdot 10^6$ tons of coal to produce the same amount of energy. In Table 1.2 the present contributions of coal and the other most important primary energy sources to the overall energy production are shown.

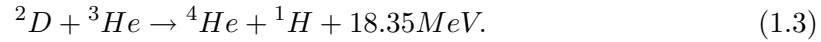
Contributions of Different Sources	
Primary Energy Source	Contribution to Energy Production
Oil	36.1%
Coal	27.6%
Gas	23.0%
Fission	6.0%
Hydro-electricity	6.3%
Solar, wind, wood, waste	$\approx 1.0\%$

Table 1.2: Contributions of the different most important primary energy sources to the overall energy production in the World, updated to 2006. Table taken from [1].

Control thermonuclear fusion is a challenging mission and the difficulty encountered in the reproduction of the processes in laboratory represents the bigger obstacle, from both technical and scientific points of view. Since Fifties, Men were studying the Physics of hot thermonuclear plasmas for civil purposes, in order to find the way to reproduce fusion reactions in the research laboratories, with the aim to make fusion become a reliable source of energy for the future on Earth. To be able to fuse light nuclei together, very high kinetic energies or very high pressures are required to overcome the repulsion force between them. Fusion reactions keep in life the stars by converting hydrogen into helium (as main reaction). In these process about 0.5% of the hydrogen mass is directly converted into energy, in accordance with the Einsteins equation $E = \Delta mc^2$:

$$\Delta E_{binding} = (N_{neutrons}m_{neutron} + N_{protons}m_{proton} - m_{nucleus}) \cdot c^2.$$

In principle, fusion is possible with several light elements, involving hydrogen isotopes and light nuclei, like for instance:



The advantage of these reactions is the natural abundance of elements, especially of deuterium³, but the drawback consists in stringent conditions for operations and higher energy threshold to start the reactions, due to the lower cross-section and energy release, with respect to the D-T reaction, which is the reference for controlled thermonuclear fusion (see Figure 1.1). This reaction, which has a cross section peaking at temperatures $T \approx 25$

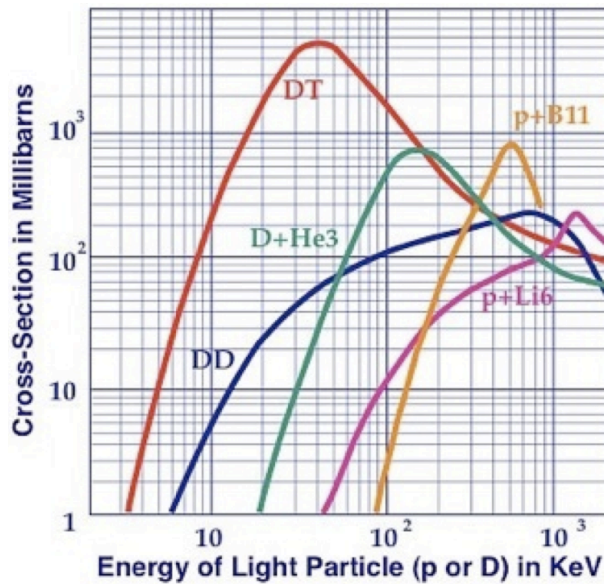
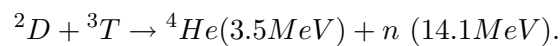


Figure 1.1: Cross-section of several fusion reactions between light elements vs the energy of D or p. It can be noticed that the D-T reaction has the maximum cross-section.

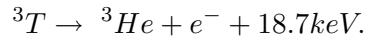
keV, converts the two hydrogen isotopes into an helium nucleus (an α particle) with a total amount of energy of 17.6 MeV per reaction, while a neutron, carrying about 80% of this energy, is released:



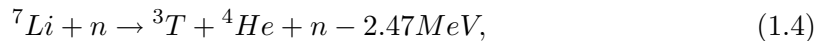
³An hypothetical fusion plant producing 1000 MW_e/year, would need just about 250 kg/year of D and T.

This means that 1 g of D-T fuel yields 90 MW_th of thermal energy which, converted into electricity with a typical efficiency of 0.33, yields 30 MW_eh.

The fuels can be found quite easily. Deuterium is widely available on Earth and can be extracted from the water⁴, where it is present in a concentration of about 35 g / m³, while tritium, which does not exist in nature since it is radioactive with a half-life of 12.3 years:



can be obtained from lithium, widely available from the following reactions on the Earth:



in its crust and in the sea water for example. Estimations on the availability and consumption of Li indicate that this element will be available on Earth for at least one billion of years [3]. Therefore fusion could be a sustainable energy source.

In order to fuse, the mutual electrostatic repulsion between positively charged atomic nuclei must be overcome during their collisions. This means they must be provided of the sufficient kinetic energy to do that. Since the overall energy of the gas is strictly in relation with the thermal velocity of the particles, the temperature of the fusion fuel has to be risen to very high values. In the case of D-T fusion, the required temperature is in the range of 100/150 · 10⁶ degrees centigrade, corresponding to 10 keV, making the gas become partially or completely ionized, forming a plasma.

Such a hot gas must be confined using (strong) magnetic fields. The torus is demonstrated to be the unique geometrical shape for the closed magnetic field lines, capable to keep the plasma confined in fusion devices. Some kind of machines are the tokamaks, stellarators, reversed field pinches and spherical tokamaks [4] [5]. Among them, the most diffuse configuration is the first one, the toroidal shaped tokamak [6], developed in Russia in the 1950s and 60s, which name is a russian acronym standing for toroidal camera with magnetic coils (***T**Oroidalnaya **K**Amera v **M**Agnitnykh **K**atushkakh*). In a tokamak the magnetic field confining the plasma is generated by a certain number of external coils, and by a toroidal current. The final configuration is formed by twisted toroidal field lines.

Additional heating systems are used, as well, to inject high power microwaves or particle

⁴A significant percentage of the common water H₂O is actually D₂O and HDO, and is called heavy water.

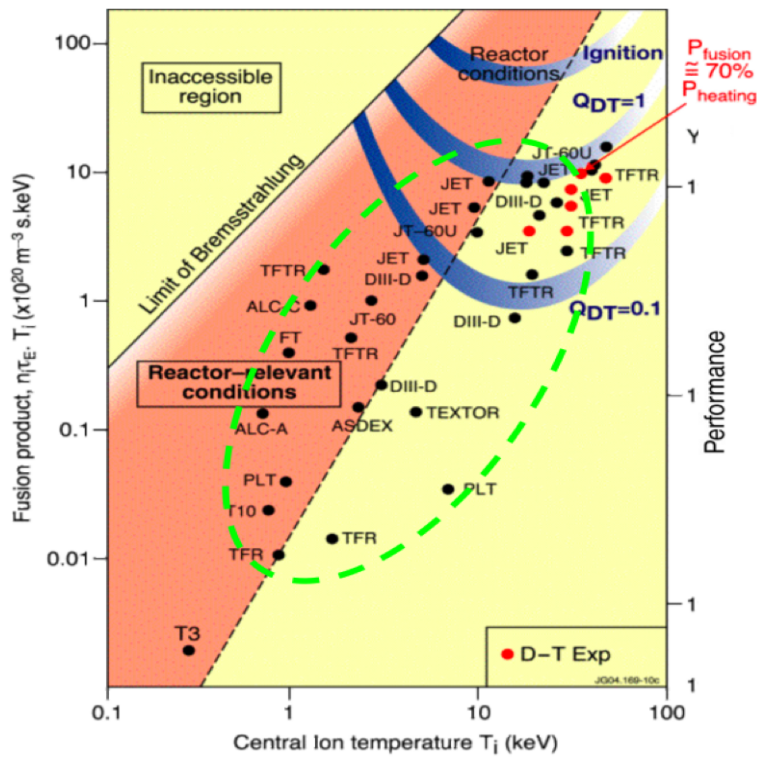


Figure 1.2: Results of several fusion devices. The red dots correspond to experiments performed in JET (in Europe) and TFTR (in the US) devices with D-T.

beams into the plasma⁵, up to the *Lawson criterion* for the ignition condition, defined in 1957 by John D. Lawson, at Harwell (UK), that written as function of the number of electrons per unit volume n , the ion plasma temperature T_i (in keV) and the energy

⁵The transfer of energy and momentum to the plasma can be obtained by acting directly on electrons or ions, depending from the frequency of the launched waves. The four methods used nowadays for heating and driving non-inductive currents in fusion plasma are the Electron Cyclotron Resonance Heating (ECRH), the Lower Hybrid (LH) waves, the Ion Cyclotron Resonance Heating (ICRH) and the Neutral Beam Injection (NBI). All the first three techniques consist in the launch of RF waves, respectively in the range of 50-200 GHz, 5-10 GHz and tens of MHz. ECRH and LH acts directly on electrons, while ICRH interacts on ions. The NBI, instead, consists in the injection of neutral beams into the plasma, not influenced by the presence of magnetic fields. All the arguments of the present Thesis will be dealing only with applications of ECRH and EC-waves in fusion plasmas. For a detailed treatment of the different approaches to heat and drive current in plasmas, see for instance reference [7].

confinement time⁶ τ_E , takes the following form:

$$nT_i\tau_E > 6 \cdot 10^{21} \frac{\text{keV s}}{\text{m}^3}, \quad (1.6)$$

for the D-T plasmas. An important parameter of a fusion plant is the factor Q, defined

Reactor Parameters	
Unit size (GW _e)	1 - 1.5
Fusion power (GW)	3 - 5
Q	30 - 40
Temperature (°·10 ⁶)	150 - 200
Plasma density (10 ²⁰ particles/m ³)	1 - 1.5

Table 1.3: Typical parameters of a fusion reactor. Table taken from [8].

as:

$$Q = \frac{P_{fusion}}{P_{heating}},$$

called power multiplication factor (in Figure 1.3 the typical parameters of a fusion reactor are reported). It defines the ratio between the energy produced by thermonuclear fusion reactions (gain) P_{Fusion} and the power provided from outside through additional heating systems (expense) $P_{Heating}$. It is clear that fusion will have to reach a Q factor well beyond 1, before establishing as a reliable energy source for the future. In principle, if the ignition phase may be obtained in the reactor, $Q \rightarrow \infty$; nevertheless, also in the case the conditions for ignition are not reached, a satisfactory value of Q may be obtained.

A second important parameter, which defines the efficiency of the confinement, is the ratio β between the kinetic plasma pressure p and the magnetic pressure $B^2/2\mu_0$:

$$\beta = \frac{p}{B^2/2\mu_0},$$

usually measured relative to the total, local magnetic field. It may be shown that the power arising from thermonuclear reactions roughly scales with p^2 [6].

The first demonstration of D-T fusion reliability was obtained in 1997 [9] in the Joint European Torus (JET) [10], which is presently the largest fusion device in the World. A fusion power generation of 16 MW was demonstrated and the fusion reactions were

⁶Related to the thermal insulation of the plasma from the outside.

maintained for 5 s. In Figure 1.2, the results of JET and several other fusion devices are reported, for D-T and D-D operations.

1.2 The International Thermonuclear Experimental Reactor Project (ITER)

The crucial demonstration of a $Q > 1$ regime has not been demonstrated so far, since also the experiments performed during the past in JET tokamak reached a maximum $Q \approx 0.65$ of power multiplication factor.

ITER Parameters	
Major Radius	6.2 m
Minor Radius	2.0 m
Plasma Elongation	1.85
Toroidal Magnetic Field	5.3 T
Nominal Plasma Current	15 MA
Additional Heating Power	73 MW
Plasma Pulse Length	400 s
Average Electron Density	$1.1 \cdot 10^{20} \text{ m}^{-3}$
Average Ion Temperature	8.9 keV
Peak Fusion Power	500 MW
Fusion Power Gain (Q)	>10

Table 1.4: Main ITER parameters. Table taken from [11].

To demonstrate the advantage of fusion, the scientific community has decided to proceed to the next step of thermonuclear fusion with the construction of the International Thermonuclear Experimental Reactor (ITER) [12], based on the collaboration of European Union, Japan, Republic of China, India, Republic of Korea, Russian Federation and the USA. In Figure 1.3 a section of the ITER device is represented. ITER is expected to demonstrate a never met Q factor >10 in the power gain of the fusion energy processes. In the Table 1.4 the main parameters of the ITER design are reported. Additional plasma heating systems, are foreseen in ITER; among these, an Electron Cyclotron Heating and Current Drive (EC H&CD) system (see Table 1.5). Another crucial goal of ITER will

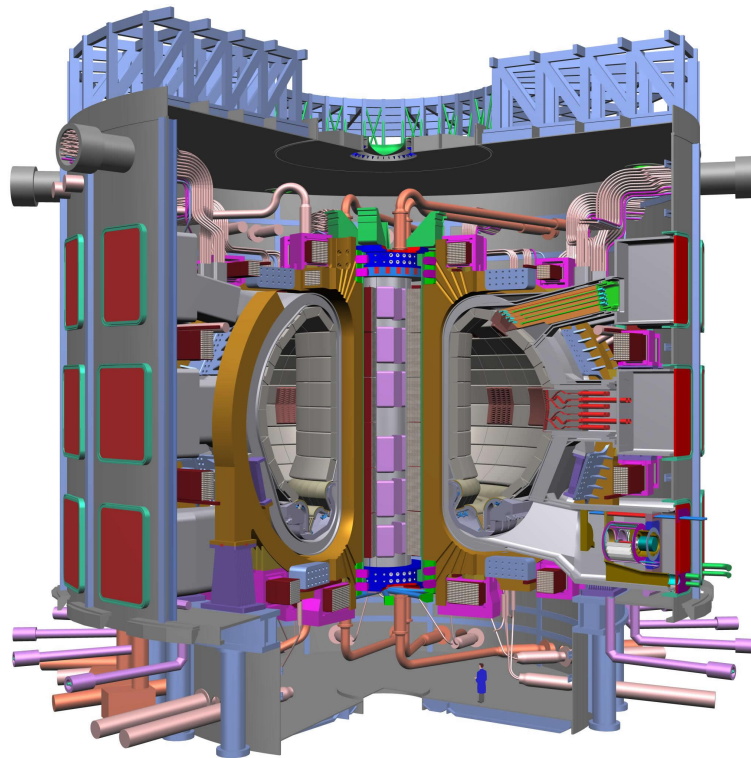


Figure 1.3: Section of the International Thermonuclear Experimental Reactor (ITER). The dimensional scale of the machine can be deduced by comparing the device with the representation of a man, put in the bottom right of the picture.

be the implementation and test of the key technologies and processes needed for future fusion plants; for instance, the superconducting components, like magnet and coils, all the components that should be able to withstand higher heat loads, never tested before, and remote handling systems, which are essential in presence of the activated components that will be present inside the machine vessel. Concerning the physical processes, the goal of ITER will be the test of tritium breeding, starting from the lithium contained in the materials inside the camera or deposited inside the high temperature blankets, which will cover the machine wall and will surround the plasma [13].

A significant effort is spent from the European Fusion Technology Program, in the frame of the development of the best candidate materials for ITER. In particular, a International Fusion Material Irradiation Facility (IFMIF) which consists in a facility able to provide high fluxes of 14 MeV neutrons to irradiate different candidate materials under test for future reactors, is being designed in these years, with an international collaboration be-

Power Delivered in ITER		
Heating System	Baseline (MW)	Possible Upgrades (MW)
NBI	33	16.5
EC H&CD (170 GHz)	20	20
IC H&CD (40-55 MHz)	20	/
LH H&CD (5 GHz)	/	20
Total Power	73	130
EC H Start-up	>2	/
Diagnostic NB	>2	/

Table 1.5: Heating and current drive actuators of ITER, with the power respectively delivered to the plasma by each system.

tween the different countries taking part to the ITER project.

Concluding, ITER is the next necessary step in the fusion field. It should confirm nuclear fusion as a all-day-life compatible energy source for the humankind, since for the first time the physics and technologies requirement for realizing controlled fusion at a $Q > 1$ regime, are all integrated in a single device.

Chapter 2

Electron Cyclotron Resonance Heating

2.1 Introduction

A fusion device needs auxiliary external heating systems to reach the requested particle energies or to keep the plasma confined, as pointed out in Chapter 1. Among them, the Electron Cyclotron Resonance Heating (ECRH) and the Electron Cyclotron Current Drive (ECCD) [14] [15] [16] [17] play an important role. Nowadays, the use of ECRH has a relevant importance for thermonuclear experimental devices, due to several reasons. Firstly, electromagnetic waves with frequency in the range of the electron cyclotron one enable very precise spatial power deposition into the plasma, of the order of a few centimeters. When an oblique injection is performed, a current is driven locally, and the fine shaping of the current profile is possible. Thus, ECCD represent an ideal tool for manipulating local plasma instabilities, like Magneto Hydro Dynamic (MHD) modes. In fact, electron cyclotron waves are absorbed exclusively by electrons, with typically more than 90% of wave power being deposited in less than 10% of plasma volume [15]. Such a high level of localization can not be obtained neither using other radio-frequency heating systems, working at lower frequencies, like Ion Cyclotron Resonance Heating (ICRH) and Lower Hybrid (LH), nor using Neutral Beam Injection (NBI) systems. In the case of ECRH the absorption is limited to regions where the gyromotion of electrons is in resonance with the wave frequency. Furthermore, EC waves are excited in the transition from vacuum propagation to plasma, without crossing an evanescent region. Radiation can be coupled

to the plasma in the form of well defined narrow beams, with low diffraction associated with the short wavelength, using rather simple systems. Overmoded waveguides, typically corrugated, are able to transmit the low-loss $HE_{1,1}$ mode, from the sources to the tokamak. Quasi-optical components, like metallic mirrors, are used to propagate Gaussian beams with low losses¹, in free space. In order to avoid arcing, evacuated waveguides have been employed in the recent years. EC wave launching systems can be put relatively far from the plasma, unlike in the case of lower frequencies systems, whose coupling requires antennas installed in the plasma boundary proximity, with consequent risk of interaction with plasma and impurities introduction. Launching waves from remote antennas is clearly preferred, for reducing the interactions and for giving flexibility in source placement. Another recent motivation which stimulated the use of EC systems is given by the development of high power (up to 2MW) gyrotrons [18], able to deliver high frequency radiation (up to 170GHz). This happens in parallel to the advances in the development of the technologies requested in the plants, like for instance new kinds of gyrotron internal structures, new windows, made of synthetic diamond, able to withstand higher thermal loads than the older ones (made of ceramics, typically boron nitride and beryllium oxide) and recent advanced matched systems [19] able to absorb and measure the powers produced by the modern sources. After the first experiments, performed in the Sixties [20] [21] [22], ECRH has been carried out also in tokamaks, demonstrating its versatility, not only as a very efficient method to heat magnetically confined plasmas in large devices and to perform ECCD, but also for further purposes, like plasma start-up and MHD modes stabilization.

2.2 Wave Dispersion and Propagation

EC waves heat electrons, in plasma regions where the local cyclotron frequency or higher harmonics approximately equal the frequency of the propagating wave. Ions heating is just a consequence of the collisions with electrons. This means that, when an EC additional heating is present, the ion temperature is generally lower than electron temperature, and approaches the electron one in the case of high density, i.e. of high collisionality. The theory of ECW propagation and absorption is mostly verified with experiments and reliable predictive models are available to describe most of the effects of EC waves which take place in the plasma.

¹Typical losses on copper mirrors are of the order of 0.2%

2.2.1 The Cold-Plasma Dielectric Tensor

In general, propagation of EC waves in a uniform magnetized plasma can be adequately described by the so called 'cold-plasma' model. In this model, electrons and ions are considered to be two frictionless charged fluids at temperature $T_{e,i} = 0$ (thermal particles motion is neglected), confined by a constant background magnetic field, which is assumed to be a zero-order quantity, static in time and uniform in space, together with the density of the plasma itself. The dispersion relation of the possible waves, representing the plasma response to an external electromagnetic perturbation, can be written using the dielectric tensor, once it has been obtained by the susceptibilities of the single plasma species. In order to develop the theory of the waves, solutions of the linearized equations, in which all the perturbative terms are considered to be proportional to $\exp[i(\mathbf{k} \cdot \mathbf{r} - \omega t)]$, are considered. Applying the Fourier analysis on the electric displacement vector \mathbf{D} , which, according to the Ampère equation:

$$\nabla \times \mathbf{B} = \frac{4\pi\mathbf{j}}{c} + \frac{1}{c} \frac{\partial \mathbf{E}}{\partial t} = \frac{1}{c} \frac{\partial \mathbf{D}}{\partial t}, \quad (2.1)$$

includes both the vacuum displacement vector and plasma current, the following expression can be written:

$$\mathbf{D}(\omega, \mathbf{k}) = \epsilon(\omega, \mathbf{k}) \cdot \mathbf{E}(\omega, \mathbf{k}) = \mathbf{E}(\omega, \mathbf{k}) + \frac{4\pi i}{\omega} \mathbf{j}(\omega, \mathbf{k}), \quad (2.2)$$

where $\epsilon(\omega, \mathbf{k})$ is the dielectric tensor. Taking advantage of the additive property of the dielectric tensor, it is possible to write it in terms of the sum over all the susceptibilities χ_s of the different plasma components s :

$$\epsilon(\omega, \mathbf{k}) = \mathbf{1} + \sum_s \chi_s(\omega, \mathbf{k}), \quad (2.3)$$

where $\mathbf{1}$ is the unit dyadic.

Furthermore, the susceptibility of every singular specie can be determined in the frame of the cold-plasma theory by writing the motion equation of the singular plasma specie s [23], in terms of the cyclotron gyrofrequency:

$$\omega_{cs} = \frac{q_s B_0}{m_s c}, \quad (2.4)$$

and of the plasma frequency of the s species:

$$\omega_{ps}^2 = \frac{4\pi n_s q_s^2}{m_s}, \quad (2.5)$$

here both written in Gaussian units. Using the relation 2.3 it is possible to obtain the expression for the cold-plasma dielectric tensor:

$$\boldsymbol{\epsilon} \cdot \mathbf{E} = \begin{pmatrix} S & -iD & 0 \\ iD & S & 0 \\ 0 & 0 & P \end{pmatrix} \begin{pmatrix} E_x \\ E_y \\ E_z \end{pmatrix} \quad (2.6)$$

where the clear structure of the matrix is obtained, thanks to the use of elements S , D and P (which initials letters stay respectively for *sum*, *difference* and *plasma*), and that group in a compact way different expressions of ω , ω_{ps} and ω_{cs} :

$$S = \frac{1}{2}(R + L), \quad D = \frac{1}{2}(R - L),$$

and:

$$R = 1 - \sum_s \frac{\omega_{ps}^2}{\omega(\omega + \omega_{cs})}, \quad (2.7)$$

$$L = 1 - \sum_s \frac{\omega_{ps}^2}{\omega(\omega - \omega_{cs})}, \quad (2.8)$$

$$P = 1 - \sum_s \frac{\omega_{ps}^2}{\omega^2}. \quad (2.9)$$

The cold-plasma model is useful to describe the physics of most of the phenomena of interest with good approximation, in particular when finite Larmor radius and pressure or temperature effects can be neglected in the treatment. Note that the mathematical formulations of R , L and P just derived above, exclude the particular cases when $\omega = \pm\omega_{cs}$ and $\omega = 0$.

2.2.2 The Dispersion Relation in Cold Magnetized Plasma

The propagation of a monochromatic electromagnetic field in a cold magnetized plasma is governed by the wave equation:

$$\nabla \times (\nabla \times \mathbf{E}) = \frac{\omega^2}{c^2} \mathbf{E} + \frac{4\pi i \omega}{c^2} \mathbf{j} \quad (2.10)$$

After Fourier analysis, equation 2.10 transforms in:

$$\mathbf{k} \times (\mathbf{k} \times \mathbf{E}) + \frac{\omega^2}{c^2} \boldsymbol{\epsilon} \cdot \mathbf{E} = 0 \quad (2.11)$$

or, by using the dimensionless refractive index vector $\mathbf{N} = \mathbf{k}c/\omega$, in the following way:

$$\mathbf{N} \times (\mathbf{N} \times \mathbf{E}) + \boldsymbol{\epsilon} \cdot \mathbf{E} = 0. \quad (2.12)$$

Thanks to cylindrical symmetry, $N_y = 0$ can be set without losing generality, i.e. $N = \sqrt{N_x^2 + N_z^2} = \sqrt{N^2 \sin^2 \vartheta + N^2 \cos^2 \vartheta}$, where ϑ defines the angle between the magnetic field $\mathbf{B}_0 = B_0 \hat{\mathbf{z}}$ and the vector \mathbf{N} . Making use of equation 2.6, the expression 2.12 can be written in tensor notation:

$$\begin{pmatrix} S - N^2 \cos^2 \vartheta & -iD & N^2 \cos \vartheta \sin \vartheta \\ iD & S - N^2 & 0 \\ N^2 \cos \vartheta \sin \vartheta & 0 & P - N^2 \sin^2 \vartheta \end{pmatrix} \begin{pmatrix} E_x \\ E_y \\ E_z \end{pmatrix} = 0. \quad (2.13)$$

To find a nontrivial solution of the homogeneous equation 2.12 for \mathbf{E} , the determinant of the 3x3 matrix Λ_{ij} in 2.13 must satisfy:

$$\det [\epsilon_{ij} - N^2 \delta_{ij} + N_i N_j] = 0 \quad (2.14)$$

This enables to find the so called *dispersion relation* between ω and \mathbf{k} of a wave propagating in a medium characterized by a certain local density (ω_p) and magnetic field (ω_c):

$$AN^4 + BN^2 + PRL = 0 \quad (2.15)$$

where R, L, P are the cold plasma expressions defined in 2.7 - 2.9 and:

$$A = S \sin^2 \vartheta + P \cos^2 \vartheta \quad (2.16)$$

$$B = -[RL \sin^2 \vartheta + PS(1 + \cos^2 \vartheta)]. \quad (2.17)$$

Let us call the dispersion relation 2.15 as \mathcal{D} , it can be equivalently written in the form:

$$\mathcal{D}(N, \omega_p^2, \omega_c, \vartheta) = \tan^2 \vartheta + \frac{P(N^2 - R)(N^2 - L)}{(SN^2 - RL)(N^2 - P)} = 0 \quad (2.18)$$

which turns out to be much more convenient to highlight the solutions, at least in the two limiting cases $\vartheta = \pi/2$ (perpendicular propagation) and $\vartheta = 0$ (parallel propagation):

$$\vartheta = \frac{\pi}{2} \quad (N_z = 0) \quad \Rightarrow \quad N^2 = P, \quad N^2 = \frac{RL}{S} \quad (2.19)$$

$$\vartheta = 0 \quad (N_x = 0) \quad \Rightarrow \quad N^2 = L, \quad N^2 = R, \quad P = 0. \quad (2.20)$$

The transit from one case to the other, i.e. when the \mathbf{k} vector is oblique and points the $\vartheta = 90^\circ$ direction, takes place through a smooth transformation between the dispersion relations of a given propagation mode. The mode associated with $N^2 = P$ and $N^2 = L$, respectively for \perp and \parallel propagation, is called the ordinary mode (O-mode); the one

described by $N^2 = RL/S$ and $N^2 = R$, respectively for \perp and \parallel propagation, is the extraordinary mode (X-mode). The $P = 0$ case, for propagation along the magnetic field, represents the electrostatic solution, unlike the other two solutions $N^2 = L$ and $N^2 = R$, which are transverse circularly polarized waves (see section 2.2.2), i.e. $\mathbf{k} \cdot \mathbf{E} = 0$. In any case, when a magnetic field \mathbf{B} is superimposed, the cold plasma becomes a birefringent medium, with different dispersion relations for the two possible modes.

Wave Accessibility

The propagation of the waves in a medium can take place only for values of the refractive index in the range $0 < N^2 < \infty$. This means that accessible regions for a certain mode are the ones delimited by the points corresponding to $N^2 = 0$ (cutoffs) and $N^2 \rightarrow \infty$ (resonances). Other resonant phenomena take place between the single particles and the wave at (respectively) the $\omega = \ell\omega_{ce}$ and $\omega = \ell\omega_{ci}$ layers, where ℓ is the number of harmonic. Substituting $N^2 = 0$ in the equation 2.15, cutoff takes place when the product $PRL = 0$, i.e. when one of the three quantities P , R or L equals zero. They represent the limiting layers between regions, in which the refractive index is purely real (neglecting absorption processes) or imaginary, when no propagation can take place. In this last case the wave is said to be evanescent. That is, its amplitude experiences an electromagnetic strong spatial decay in the direction of propagation and, in practice, the wave is reflected back.

The case $P = 0$ represents the cutoff for the ordinary wave and is the only cutoff for this mode. It is often indicated as the 'density' cutoff, being the condition $P \equiv 1 - \omega_{ps}^2/\omega^2 = 0$ verified when $\omega_{ps}^2 = \omega^2$, where $\omega_{ps}^2 \sim n_s$ (see 2.5). Considering the ions staying at rest as a uniform background ($m_i \rightarrow \infty$), and taking into account a two-species plasma, formed only by electrons and ions, the O-mode cutoff is at the region where $\omega_{pe}^2 = \omega^2$. In tokamak configuration, where density profile is typically monotonic and peaked at the center of the plasma, the accessibility of EC waves to the inner regions is possible from both the Low Field Side (*LFS*), with O-mode, and the High Field Side (*HFS*), with both modes, provided the condition $\omega_{pe}^2 < \omega^2$ holds true. This means that, when plasma density is such that the condition $\omega_{pe}^2 \geq \omega^2$ is reached, at a certain layer of the density profile, a central region is inaccessible for the ordinary polarized waves. The cutoff layer limits the inaccessible region and the regime is sometimes called *overdense*². The possibility to come

²Typically, the term *overdense* refers to the situation when heating at the center is prevented by the density, i.e. in the case when the electron cyclotron layer $\omega_{ce} = \omega$ is (partially) "hidden" by the O-mode

across such plasma scenarios during operations in fusion machines is the key starting point for the work performed in this Thesis.

The other two cases, $R = 0$ and $L = 0$, represent the X-mode cutoffs, respectively named right-hand (RH) and left-hand (LH) cutoff. Furthermore, from equation 2.18, it can be seen that in the limit of very large N^2 , a resonance occurs as well, at propagation angle such that:

$$\tan^2 \vartheta = -\frac{P}{S}. \quad (2.21)$$

This resonance is called the upper hybrid (UH) resonance and belongs to the X-mode dispersion relation. It is evident a dependence of the upper hybrid resonance location in the plasma from the angle ϑ of propagation of the X-wave, but it can be verified that this dependence is not so strong, at least for propagation angles which are not too far from $\pi/2$ with respect to B_0 .

Bearing in mind the definition of the refractive index vector $\mathbf{N} = c\mathbf{k}/\omega$, an alternative

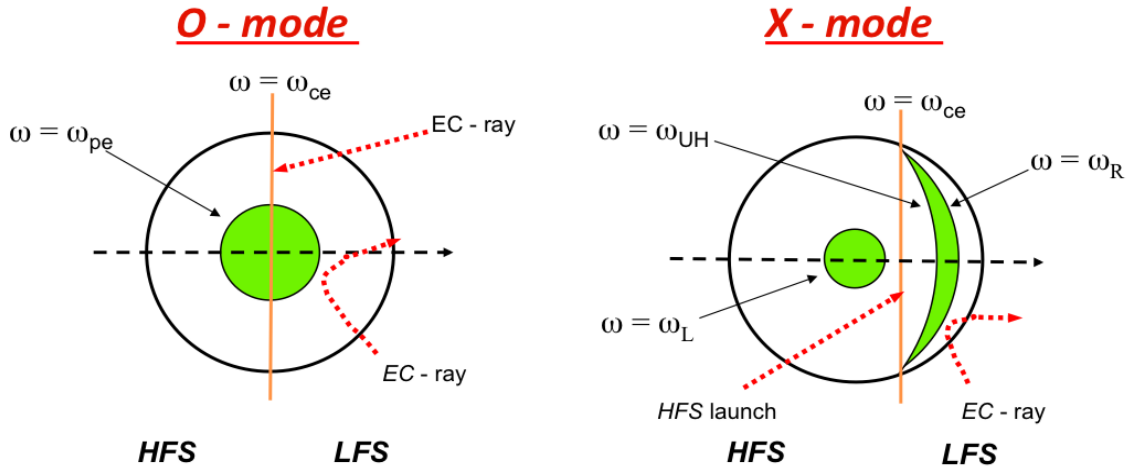


Figure 2.1: The fundamental O-mode (on the right) and X-mode (on the left) accessibility, represented in a poloidal section of a tokamak-like device, which axes are on the left of the two sections. The green regions are prevented to the respective EC-waves.

useful way to write the X-mode cutoffs and upper hybrid resonance for perpendicular propagation ($N_z = 0$), starting from the following form of 2.19, is:

$$c^2 k_{\perp}^2 = \frac{(\omega^2 - \omega_R^2)(\omega^2 - \omega_L^2)}{(\omega^2 - \omega_{UH}^2)}. \quad (2.22)$$

cutoff $\omega_{pe}^2 = \omega^2$.

For $k_{\perp} \rightarrow 0$, the left and right cutoff can be explicitied:

$$\omega_{R,L} = \sqrt{\left(\frac{\omega_{ce}}{2}\right)^2 + \omega_{pe}^2} \pm \frac{\omega_{ce}}{2}, \quad (2.23)$$

and the upper hybrid, when $k_{\perp} \rightarrow \infty$:

$$\omega_{UH} = \sqrt{\omega_{pe}^2 + \omega_{ce}^2}. \quad (2.24)$$

For oblique propagation, the cut-offs 2.23 change position in the plasma and the expressions are generally given for a constant N_{\parallel} :

$$\omega_{R,L} = \sqrt{\left(\frac{\omega_{ce}}{2}\right)^2 + \frac{\omega_{pe}^2}{1 - N_{\parallel}^2}} \pm \frac{\omega_{ce}}{2}. \quad (2.25)$$

In a tokamak-like configuration a non-null region between the RH cutoff and the upper hybrid layer (UHL) is always present. This region is evidently inaccessible to the fundamental extraordinary mode (X1-mode). This is the reason why extraordinary waves at first harmonic can not be used to heat plasmas when launched from LFS, because they can not reach the electron cyclotron layer $\omega_{ce} = \omega$ (where the EC power is delivered to plasma by resonant mechanisms) without crossing this region³. In Figure 2.1 and 2.2 the accessibility of O- and X-mode is represented, respectively in a poloidal section of a tokamak-like plasma and in the Clemmow-Mullaly-Allis CMA diagram.

In addition, it may be shown that, considering also ions dynamic (two dynamic species plasma) in the calculations⁴, a second term $(\omega^2 - \omega_{LH}^2)$ appears with the $(\omega^2 - \omega_{UH}^2)$ in the denominator of equation 2.22. The quantity ω_{LH}^2 is such that:

$$\frac{1}{\omega_{LH}^2} = \frac{1}{\omega_{ci}^2 + \omega_{pi}^2} + \frac{1}{|\omega_{ci}\omega_{ce}|} \quad (2.26)$$

and is the so called lower hybrid resonant frequency, the second resonance of the dispersion relation of extraordinary mode; it is always verified that $\omega_{LH} < \omega_{UH}$. Such LHR is often used to deliver power to the plasma in the fusion devices, like in FTU (Frascati Tokamak Upgrade) tokamak [24] [25]. Then, the behavior of the extraordinary mode turns out to be more complicated than ordinary mode, and, unlike the O-mode, the magnetic field intensity, as well as density, influences the positions of cutoffs (and UH/LH resonant frequencies). Hence, in presence of EC resonance, the propagation of X1-mode

³Actually, just the fact that the RH cutoff always "hides" the resonant layer $\omega_{ce} = \omega$ in tokamak configuration, is enough to prevent the use of X1-mode from LFS to heat plasmas.

⁴Then ions frequencies are summed together with electron ones, in relations 2.7 - 2.8.

is divided into two regions in tokamak configuration, limited by RH, LH cutoffs and UH layer, and this fact gives rise to two different branches of the dispersion relation, which, depending on the phase velocity ω/k , are marked as SX-mode (slow) and FX-mode (fast) branch. Transfer of energy to the particles can be obtained injecting waves at frequencies

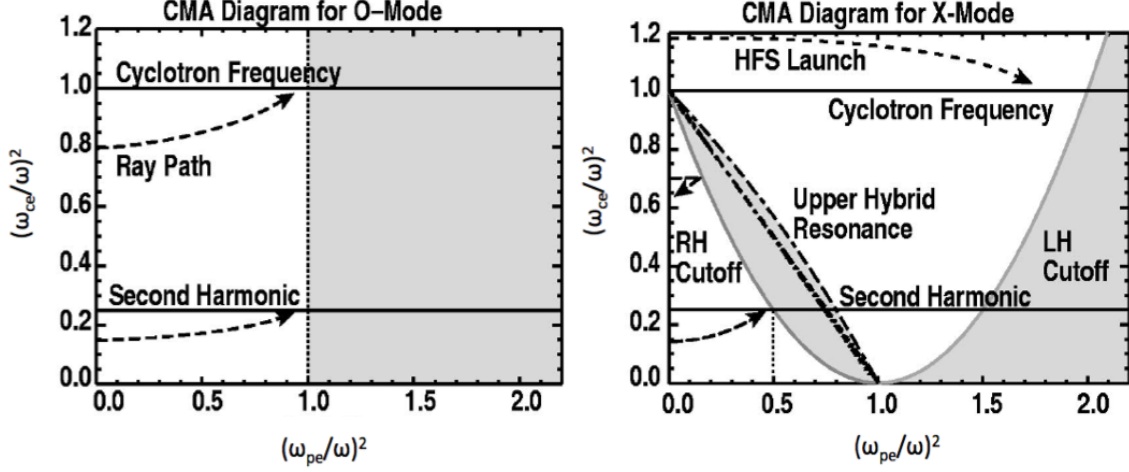


Figure 2.2: A representation of the O- and X-mode accessibility in a cold plasma, called Clemmow-Mullaly-Allis CMA diagram. Resonances and cutoffs form regions which are inaccessible by the waves launched from LFS, represented with the arrows. Picture taken from [17].

corresponding to different harmonics of the EC resonances. These may have a better accessibility and may reach higher density cutoffs [17]. For instance, the X2-mode is often used to by-pass the problem of RH cutoff and deposit EC power at the resonant layer. Nevertheless, these are not of interest for this work since they require higher wave frequencies than those achievable at the power level of interest for high magnetic field fusion devices.

Wave Polarization

From the second and third rows of equation 2.13 it is possible to derive the polarization of the \mathbf{E} field, from the ratio between the transverse components:

$$\frac{iE_x}{E_y} = \frac{N^2 - S}{D}, \quad (2.27)$$

$$\frac{E_x}{E_z} = \frac{N^2 \sin^2 \vartheta - P}{N^2 \cos \vartheta \sin \vartheta}, \quad (2.28)$$

where N denotes the refractive index of O- or X-mode. It can be noted that the right hand side of equation 2.27 is real, therefore E_x and E_y must be 90° out of phase; this implies the polarization to be typically elliptical. From the relations above, the following results are obtained for propagation along the magnetic field ($\vartheta = 0$):

$$N^2 = R \quad \Rightarrow \quad \frac{iE_x}{E_y} = 1 \quad (2.29)$$

$$N^2 = L \quad \Rightarrow \quad \frac{iE_x}{E_y} = -1. \quad (2.30)$$

These equations show that for parallel propagation the polarization of the two possible transverse modes is circular, the rotation being right-hand or left-hand ($iE_x/E_y = 1 \Rightarrow \odot$, or $iE_x/E_y = -1 \Rightarrow \ominus$, for $\mathbf{B} = \otimes$), i.e. respectively on the same gyration direction of electrons or ions around the magnetic field. Then, electron cyclotron and ion cyclotron frequencies are resonant, respectively for R-wave and L-wave, and this fact can be also verified analytically in equations 2.7 - 2.8, where the quantities R and L diverge when the denominators tend to 0, hence $N^2 \rightarrow \infty$ in the dispersion relations, for the respective electron or ion resonant frequencies.

For X-mode propagation across the magnetic field ($\perp \mathbf{B}$), the dispersion relation 2.19 $N^2 = RL/S$ can be substituted in the equation 2.27, obtaining:

$$\frac{E_x}{E_y} = -\frac{R-L}{i(R+L)}. \quad (2.31)$$

Firstly, this demonstrates that \mathbf{E} is in the (x, y) -plane, therefore in general the X-wave is partially longitudinal and partially transverse. Furthermore, since the dispersion relation 2.19 shows that the X-mode resonances ω_{UH} and ω_{LH} occur when the denominator $(R+L) \rightarrow 0$, to have $N^2 \rightarrow \infty$, also $|E_x/E_y| \rightarrow \infty$ in equation 2.31, being the denominator the same. Then $E_y \rightarrow 0$ as ω approaches ω_{UH} and ω_{LH} , and the wave becomes purely longitudinal. This behavior of the X-mode at the upper hybrid layer can be seen as a cold plasma explanation of a phenomenon better described in the next chapter using a hot plasma approach, which is one of the key points of the Physics considered for this thesis. The polarization of a wave is maintained along the propagation, at least in the limit of a cold plasma model⁵. The polarization fixed by the launcher at the plasma edge is conserved in the plasma. Then, the polarization at the vacuum-plasma threshold represents the boundary condition for coupling a certain mode in the medium. So, in order to inject

⁵It may be demonstrated that, if hot plasma effects are included in the description of wave propagation, the polarization is not perfectly conserved [26], despite the modifications expected are small.

a wave from vacuum, able to couple a precise mode in the plasma, the proper elliptical polarization has to be generated "before" or "at" the last mirror of the launcher. In practice, this is done using optical birefringent elements, for instance rotatable grooved mirrors, which are typically put in the mitre bends of the transmission line, connected to the launching system. The regulation of the mirrors must be such that the polarization of the launched wave equals the low density limit of equations 2.27 and 2.28. Using the typical reference system to describe the polarization of a wave, i.e. rotating the coordinates in such a way that the z -axis defines the direction of propagation of the incident wave ($\mathbf{k} = k\hat{\mathbf{z}}$), the polarization requested at the boundary to excite pure O-wave (upper sign) or X-wave (lower sign) in the plasma is given by:

$$\frac{iE_p}{E_y} = Y \frac{\mp \sqrt{\sin^4 \vartheta + \frac{4 \cos^2 \vartheta}{Y^2} - \sin^2 \vartheta}}{2 \cos \vartheta}, \quad (2.32)$$

where $Y = \omega_{ce}/\omega$ and E_p is the electric field component in the plane containing \mathbf{k} and \mathbf{B} . The polarizations given by equation 2.32 are elliptical at any injection angle, for both O-mode and X-mode, except for $\pi/2$, in which case the coupling of the pure modes in the plasma takes place for purely transverse and linearly polarized field at the edge, respectively parallel and perpendicular to \mathbf{B}_0 for O-mode and X-mode. Once in the plasma, this polarization is conserved only in the case of the ordinary wave, since, as already said, the electric field of the extraordinary wave develops a component parallel to the wave vector \mathbf{k} , which gives rise to a longitudinal elliptical polarization [27] [28]. On the other side, in the case of propagation along the magnetic field ($\vartheta = 0$), the coupling takes place between transverse circularly polarized modes, which conserve identically either in vacuum or in the plasma, and no further components are developed in the medium.

2.3 Single Particle-Wave Resonance

EC waves are generally absorbed by cyclotron damping in the proximity of the electron cyclotron frequency layer or its harmonics, where $\omega = \ell\omega_{ce}$. From the analytic expressions for absorption and emission of a wave traveling in the plasma [29], non-null values can be obtained only for electrons which parallel component p_{\parallel} of the momentum satisfies the following relation:

$$\gamma - \ell Y - N_{\parallel} \frac{p_{\parallel}}{m_e c} = 0, \quad (2.33)$$

where $Y = \omega_{ce}/\omega$, ℓ is the number of harmonic and $\gamma = [1 - (v_{\perp}^2 + v_{\parallel}^2)/c^2]^{-1/2}$ is the relativistic factor. The resonant condition above can be rearranged in the form [30]:

$$\omega = \frac{\ell\omega_{ce}}{\gamma} + k_{\parallel}v_{\parallel}, \quad (2.34)$$

from which the Doppler-shifted nature of the resonant condition is clear. A proper rear-

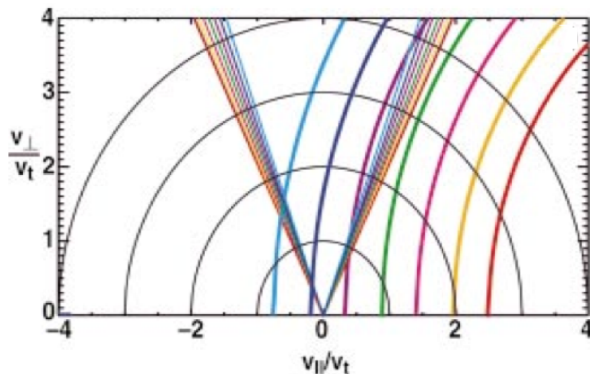


Figure 2.3: In this figure, taken by [17], the resonance curves in the velocity space are represented by the colored curved lines, the boundary of the particle trapped in the field (see further on for a description of the trapping process) by colored straight lines and black curves are the contours of constant velocity.

range of the terms in equation 2.33 allows to demonstrate that in the case of $|N_{\parallel}| < 1$, the resonant condition represents analytically an ellipse⁶ (see Figure 2.3) in the velocity space $(u_{\perp}, u_{\parallel})$.

The increase in electrons energy distribution, hence the electron heating, is demonstrated to be a diffusion process in velocity [17], and the resonance is demonstrated to act essentially on the perpendicular direction with respect to the magnetic field \mathbf{B} . For both 1st harmonic O-mode (O1-mode) and 2nd harmonic X-mode (X2-mode) the wave absorption is an increasing function of density.

Plasma heating profiles obtainable using EC power often are different from the expected absorption that one may calculate using equations able to describe local wave-particle interactions. Energy and particle confinement is modified during the EC heating and this

⁶When propagation of EC waves is described by a cold plasma model, $|N_{\parallel}| < 1$ always holds true. This not always happens in the case of Electron Bernstein Waves (EBW), that will be derived in the next chapter using a hot plasma model. They represent the third propagation mode of EC waves and sometimes they can achieve parallel refractive index N_{\parallel} larger than 1, thanks to their electrostatic character.

gives rise to a complex plasma response to the wave perturbation.

For this reason, also in view of the experiments whose predictions are the aim of the present Thesis, the measurements of plasma heating profile represent the main way to demonstrate the power delivered to the plasma, to be compared to the expected efficiency of the O-X-B heating process that will be described in the next Chapter.

2.4 Applications of Electron Cyclotron Waves in Plasmas

2.4.1 The Electron Cyclotron Current Drive

EC waves can be used also for driving non-inductive current in magnetically confined toroidal plasmas [31] [32]. Two effects are responsible for Electron Cyclotron Current Drive (ECCD), both based on the damping of waves with $k_{\parallel} \neq 0$, which are absorbed solely by electrons with a well determined velocity component v_{\parallel} . Being the damping of EC waves highly localized around the resonant layers (see section 2.3), also the current profile, as well as the power release in heating processes, can be modeled with high precision. Oblique injection of electron cyclotron waves at an angle with respect to the magnetic field, allows to control the plasma confinement⁷. Typically, an optical depth⁸ at least > 3 is requested to allow convenient CD operations [33]. Differently from what happens for the other non-inductive current drive systems, EC waves transfer little parallel momentum to electrons. In fact, the wave damping makes the perpendicular particle energy increase mostly and the electrons that have a parallel velocity in the required direction turn out to be heated preferentially. For obtaining an efficient ECCD, power should be deposited as much as

⁷The possibility to perform a very precise local re-shaping of the current density profile using EC waves, means to have the capability to control precisely also the magnetic shear \mathcal{S} , defined as:

$$\mathcal{S} = \frac{r}{q} \frac{dq}{dr},$$

where r is the minor radius of the toroidal plasma and q is called the *safety factor*. This factor is defined as the ratio between the number of toroidal orbits per poloidal one, or equivalently the number of toroidal orbits needed to let a magnetic twisted field line become a close path. It represents a very important parameter in magnetically confined plasmas, from the point of view of the plasma stability. The *safety factor* $q(r)$ turns out to be inversely proportional to both the pitch angle of the total magnetic field \mathbf{B} with respect to the equatorial plane and to the local current density $\mathbf{j}(r)$. Hence, higher values of q mean less steeply twisted field lines.

⁸The optical depth between s_1 and s_2 is defined as $\tau = \int_{s_1}^{s_2} \alpha ds$ along the wave path, where α is the absorption coefficient. The transmitted power is therefore $P_0 e^{-\tau}$.

possible on the fastest electrons. Therefore, the situation in which a population of electrons with high parallel momentum is previously created by means of other additional heating systems (e.g. by LHCD), is ideal to increase ECCD efficiency [34] [35] [36].

The two processes responsible for the current driven by EC waves with $k_{\parallel} \neq 0$, are known as *Fisch-Boozer* [37] and *Ohkawa* [38] mechanisms (see Figure 2.4): the first is based on the absorption of radiation by electrons shifted to a less collisional regime in velocity space, though the transfer of perpendicular energy from the wave to the particles. The

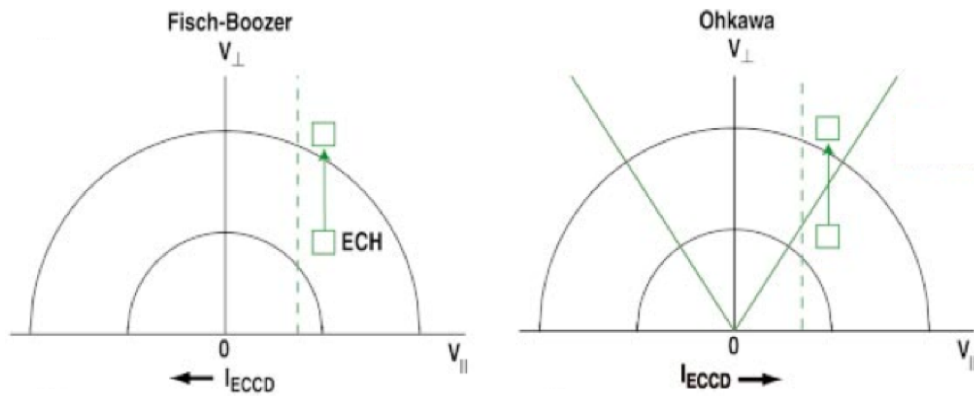


Figure 2.4: The *Fisch-Boozer* (on the left) and the *Ohkawa* (on the right) processes responsible for ECCD in plasmas, are illustrated schematically in velocity space, where the trapped particles boundary are indicated on the right with straight oblique lines.

second is related to the unbalance of the population of passing electrons on the two toroidal directions and creates a current with opposite sign than the trapped electrons. In steady state, actually, a tendency to de-trapp particles, and hence to re-balance the two opposite flows in v_{\parallel} , is given by collisional processes. Nevertheless, being the trapping process an asymmetrical mechanism in v_{\parallel} ⁹, while de-trapping being symmetrical, from the balance of the phenomena, a net current is driven with opposite sign respect to the electrons trapped by the wave. *Fisch-Boozer* and *Ohkawa* mechanisms give rise to ECCD in opposite directions, so the balance between the two phenomena must be carefully taken into account in the analysis of experimental data.

In FTU tokamak, injection of EC waves, aimed to drive non-inductive current, is generally performed in plasma regions where the dominant mechanism is the *Fisch-Boozer* one, whose current drive efficiency, obtained by changing the collisional regime of particles

⁹EC wave injected with a given sign of k_{\parallel} acts only on particles with the same sign than v_{\parallel} .

with EC waves, can be properly described [31] [37] [39].

2.4.2 Control and Stabilization of MHD modes

The equilibrium of the configurations used to confine plasmas in tokamak-like devices, which use magnetic confining fields with curvatures and gradients, are described by force balance equations obtainable from the Magneto Hydro Dynamic (MHD) theory. Even in a simpler ideal MHD model, in which the resistivity of the plasma is neglected, some different kinds of instability are predicted [40] [41] [42]. Among the main ones, the *kink* instabilities play an important role. Such modes take place in correspondence of rational values of the *safety factor* $q = m/n$ and are responsible for plasma column bending (hence for losing the confinement). Despite the ideal MHD theory is able to describe some plasma phenomena with a simplified description, in the real cases other kinds of MHD instabilities play an important role in the equilibrium of the plasma confinement and can be described uniquely with a resistive regime of MHD theory. Instabilities given by tearing of magnetic surfaces and reconnection of the magnetic field lines are predicted by the theory and are usually responsible for disruptions of the plasma during the operations. Such instabilities are associated with local distortions of the current density profile, typically leading to the degradation of the overall energy confinement¹⁰. When $q = 1$ an instability, called *Sawteeth oscillation* (ST), appears in the plasma [44]. ST instability is a macroscopic phenomenon, studied also in FTU tokamak [45], which affects a significant volume of the plasma core. For $q > 1$, finite-resistive processes give rise to the birth of magnetic islands, rapidly rotating, called *tearing modes* (TM), in correspondence of rational values of q . Plasma disruptions can be avoided controlling MHD instabilities, by delivering, for example with an external additional heating system, heat and current into the island or in the proximity of the rational surface on which it develops. The precise power injection needed to restore locally the perturbed current profile can be ensured only by ECRH systems. Thanks to plenty of experiments performed during last tens of years in important fusion devices, the fine EC power deposition has been demonstrated to be useful to control either the ST phenomenon [45], [46], by increasing or decreasing its period in a controlled way, or the TM instabilities [47] [48] [49], by injecting EC power in the islands region, sometimes

¹⁰For instance, in ITER, a neoclassical tearing (m, n)-mode activity in the plasma may lower the fusion gain factor $Q = P_{fusion}/P_{aux.heating}$ considerably, up to 25% for a (3, 2)-mode and even 50% in the case of (2, 1)-mode [43].

also in phase with their rotational motion. The importance of MHD mode stabilization is one of the main goals of the ECRH system in ITER.

2.4.3 Further Electron Cyclotron Waves Applications

In addition to the applications already described above, many other uses of ECRH systems are possible. For assisted plasma start-up, EC power deposition is used to perform pre-ionization, obtaining ohmic discharges with a lower loop voltage than the nominal one. Already demonstrated previously in other fusion devices¹¹, this topic is under study in FTU tokamak since recent years [50]. The importance of this application derives from the attempt to obtain breakdown in gases, using a lower flux consumption of the ohmic systems, in view of long pulse plasma devices, like FAST [51] [52], and in particular in view of ITER.

Plasma disruptions caused by MHD activity, with loop voltage used as a premonitory signal of the disruption [53] [54] [55], are prevented by a direct heating on the position of the tearing modes¹². This has been demonstrated to be an efficient way to delay or completely avoid disruptions in FTU and ASDEX-U.

Furthermore, the very localized heating offered by the ECRH gave the possibility to study the confinement properties of plasmas in many devices. For instance, in FTU, a modulated and out-of-phase injection of ECRH radiation on two nearby radial locations was used [56], to modulate the temperature gradients, in order to perform studies on critical temperature gradients of interest.

Again, in FTU, EC heating was showed to be useful, combined with LHCD, to create durable transport barriers [57] [58], capable to ensure highest plasma confinement levels and central electron temperatures and densities.

¹¹Experiments on ECRH assisted plasma start-up have been performed in the past in many tokamak, like JT-60U, DIII-D, T-10, Tore Supra, ASDEX-U

¹²Before disruption a coupling between the MHD modes occurs. During the experiments performed in FTU a fixed position was set for the power injection, shot by shot, generally the calculated one for $q = 2$ mode, which usually is the most dangerous for plasma stability.

2.5 The Electron Cyclotron Launching System

The EC waves can be injected into the plasma from remote locations. The launcher represents the matching element between plasma and the transmission components. The conditions imposed by the launcher, that can be fixed or sometimes changed dynamically by control systems acting on the launcher, select the injection angles of the beams for aiming the desired plasma regions, and the beam size and front-phase curvature, which determines their convergence/divergence in the plasma. Generally, mirrors are used for beam shaping and focusing. Usually, the needed polarization is selected with polarizers located along the transmission line, such that the best coupling with a definite propagation mode can occur at the plasma-vacuum interface¹³. When the coupling efficiency with the selected mode is less than 100%, both O-mode and X-mode are excited and then propagate independently in the plasma. The need of fast movability of the injection angles is of increasing importance for recent experiments of plasma physics, especially for real-time control applications. The mounting and driving mechanism become crucial, to ensure a fast dynamic of the system.

2.5.1 Launcher Set-up

In general, two possible configurations can be considered for the design of a launcher. The mirror (or a set of mirrors) can be placed in the plasma proximity, in a 'front steering' configuration, as the one foreseen for the EC launcher of ITER, or in the so called 'remote steering' configuration [59] [60], with the moving mirrors placed outside the vacuum and far away from the plasma.

In the present EC launcher installed in the FTU tokamak, the launching mirrors are put far from the plasma, while the injection angles are obtained through repeated reflections at the port walls connected to the vessel (for a detailed description of this launcher see Chapter 6). A new front steering launcher, designed for complementing the present ECRH system for FTU, will be described in details in Chapter 6.

¹³From section 2.2.2, it can be understood that the polarization must be parallel or perpendicular to the central magnetic field of the machine, for coupling respectively O-mode and X-mode in normal injection with < 100% efficiency, and elliptical for all other launching angles.

2.5.2 Launching Schemes

The main condition an ECRH launcher has to satisfy, dependently on the magnetic configuration and on the frequency ω of the launched radiation, is to let the launched wave access the $\omega = \ell\omega_{ce}$ layer. This means that, in general, the $P = 0$ layer for O-mode, and the $L = 0$ and $R = 0$ layers for X-mode, should not be present in the regions of plasma between $\omega = \ell\omega_{ce}$ and the launching point. Four main launching schemes can be thought in a tokamak-like configuration. Two of them consist in the launch of X-mode. In both cases the $L = 0$ and $R = 0$ layers are not crossed by the propagating wave. The first consists in launching X1-mode from the HFS, while the second one represents the use of $X\ell$ -mode from LFS, aiming $\omega = \ell\omega_{ce}$, under the restriction on the plasma density given by $\omega_{pe}^2 \leq \ell(\ell - 1)\omega_{ce}^2$. In the third scheme, the O1-mode is launched from LFS and can reach the resonant layer $\omega = \omega_{ce}$, provided the density is not high enough to make the O-mode cutoff layer $\omega = \omega_{pe}$ appear in the plasma region between the resonance and the launching point (see section 2.2.2), in which case the plasma is said to be in an overdense regime. This kind of coupling is the preferred one for high magnetic field and high temperature plasmas. When the heating concerns an overdense plasma, a fourth scheme is needed, typically used in low field and high density machines, known as O-X-B scheme. This scheme still consist in launching the O-mode from the LFS, but with a definite launching angle. It consists in two successive mode conversions, object of the predictive calculations performed in this Thesis, whose aim is the demonstration, for the first time, of the O-X-B scheme in the plasma of FTU, using the available frequency of the ECRH system, as will be detailed in the next Chapters. A fifth scheme is known as the direct X-B scheme, and consists in launching a fast X-wave (FX) from the LFS. It will be introduced in the next Chapter, as well, despite it does not have relevant importance for EC applications in the present fusion machines, and in particular in FTU.

Chapter 3

Electron Bernstein Waves and O-X-B Coupling

3.1 Introduction

In Chapter 2 it was shown that, when the plasma density is high enough to reach the condition $\omega_{pe}^2 \geq \omega^2$ in the density profile, the internal region is inaccessible for the O-waves. When the injection is performed from the LFS, such a region is prevented to both O- and X1-mode (since the central regions are always inaccessible for X1-mode), and the regime is said to be overdense. The possibility to come across such scenarios and heat the overdense regions of the plasma can be found only with the use of a hot plasma dielectric tensor, able to take into account also finite Larmor radius effects. A hot description of the plasma, that is being introduced in the next Section, enables to demonstrate the existence of a third EC mode (Section 3.2.1), that allows EC heating in the regions where the condition $\omega_{pe} > \omega_{ce}$ holds true, which are prevented to O- and X-modes. Since these hot waves can not be launched from outside, but can only be excited in the plasma through mode conversions, the mode coupling at the basis of their excitation will be described in Section 3.3 and the possible launching schemes to be used in real devices will be presented in the subsequent sections. A recent 2D model of mode conversion will be detailed in Section 3.6, being applied to the FTU plasma in Chapter 5, and a brief presentation of the main results of the main experiments performed so far on mode conversion, will be made at the end of the Chapter, in Sections 3.7.

3.2 The Hot Plasma Waves

When an SX-wave is excited into the plasma, it can propagate unperturbed in most of the region limited by the upper hybrid resonance (UHR) and its high density ω_L cutoff 2.25, according to the dispersion relation 2.18 (see Figure 2.1). When it propagates towards the higher densities regions, a cold plasma description is sufficient to explain a back-reflection of the wave, toward the UHL¹, once the ω_L cutoff is reached. The reason for this lies in the natural behavior of rays to deflect always towards higher refractive index regions. The physics of the wave propagation can be described using a simple cold plasma model, since neglecting temperature effects does not imply any substantial change in the description of the phenomena under study. This fact is not true any more when the SX-wave approaches the UHR layer. In fact, while approaching $X + Y^2 = 1$, the wave becomes purely longitudinal and N_x goes to infinity, according to cold plasma theory (see section 2.2.2). The wavelength decreases abruptly (or equivalently, the wave number k increases), and consequently the phase velocity of the wave goes to zero. Sooner or later, the scale length of λ reaches the size of the electron gyroradius and hence finite Larmor radius effects begin to play an important role, while approaching the UHR². From this point, kinetic effects have to be taken into account for the description of the phenomena. In a hot plasma description, when the phase velocity approaches the electron thermal velocity, the SX-wave is not absorbed at the UHL, as one may expect, but it is smoothly converted in a new electron cyclotron mode. To demonstrate that, it becomes necessary to switch to a hot plasma description and finite Larmor radius effects must be taken into account. Since the wavelength reaches the same order of magnitude of the Larmor radius $\rho = mv_{th}c/(ZeB)$ (in Gauss units), where $Z = 1$ for electrons and $v_{th} \equiv v_{\perp \mathbf{B}} = 2\sqrt{K_B T_e/m_e}$ is the electron thermal velocity, in proximity of the resonance the approximation of null gyroradius decays. Assuming a Maxwellian velocity distribution function, a magnetic field directed on the z axis ($\mathbf{B} = B\hat{\mathbf{z}}$) and neglecting relativistic effects, we can introduce the finite Larmor parameter:

$$\mu = \frac{1}{2} \frac{k_{\perp}^2 v_{th}^2}{\omega_c^2} = \frac{1}{2} k_{\perp}^2 \rho^2,$$

¹Which written with the quantities X and Y is $X + Y^2 = 1$

²In general, when the plasma temperatures becomes high enough, the electron gyroradius $\rho = mcv_{th}/(eB)$ approaches the scale length of λ and finite Larmor radius effects have to be considered.

where k_\perp represents the components of the \mathbf{k} vector perpendicular to \mathbf{B} . Expressing the Doppler effects as the frequency distance from the n^{th} cyclotron harmonic resonance:

$$\zeta_n = \frac{\omega + n\omega_c}{|k_z|v_{th}}, \quad (3.1)$$

we can write the hot plasma dielectric tensor [61]:

$$\epsilon = \mathbb{1} + \frac{\omega_p^2}{\omega^2} \zeta_0 \sum_{n=-\infty}^{+\infty} \begin{bmatrix} \frac{n^2}{\mu} \tilde{I}_n Z_n & in \tilde{I}'_n Z_n & -n \sqrt{\frac{2}{\mu}} \tilde{I}_n [1 + \zeta_n Z_n] \\ -in \tilde{I}'_n Z_n & \left[\frac{n^2}{\mu} \tilde{I}_n - 2\mu \tilde{I}'_n \right] Z_n & i \sqrt{2\mu} \tilde{I}'_n [1 + \zeta_n Z_n] \\ -n \sqrt{\frac{2}{\mu}} \tilde{I}_n [1 + \zeta_n Z_n] & -i \sqrt{2\mu} \tilde{I}'_n [1 + \zeta_n Z_n] & 2\zeta_n \tilde{I}_n [1 + \zeta_n Z_n] \end{bmatrix} \quad (3.2)$$

where $\mathbb{1}$ denotes the identity tensor and the abbreviations $\tilde{I}_n = e^{-\mu} I_n(\mu)$ and $Z_n = Z(\zeta_n)$ have been used, in which I_n is the n^{th} order modified Bessel function and Z is the plasma dispersion function:

$$Z(\zeta_j) = \frac{1}{\sqrt{\pi}} \int_{-\infty}^{+\infty} \frac{e^{-\xi^2}}{\xi - \zeta_j} d\xi. \quad (3.3)$$

In the limit of null Larmor gyroradius, i.e. when respectively $\mu \rightarrow 0$ and $\zeta_n \rightarrow +\infty$, the hot plasma dielectric tensor 3.2 reduces to the cold one 2.6, by expanding the quantities \tilde{I}_n and Z_n .

3.2.1 The Electron Bernstein Waves

A new wave is then possible in hot magneto-plasmas, a third solution of the dispersion relation. This mode is electrostatic and its nature can be better described by restricting to propagation across the field, when $N_z = 0$, thus neglecting the Doppler effects. Under this condition $\zeta_n \rightarrow \infty$ and $1 + \zeta_n Z_n \approx -1/2\zeta_n^2$. Hence, the dispersion relation can be found as solution the following [62]:

$$\det \begin{bmatrix} \Lambda_{xx} & \Lambda_{xy} & 0 \\ -\Lambda_{xy} & \Lambda_{yy} & 0 \\ 0 & 0 & \Lambda_{zz} \end{bmatrix} = 0, \quad (3.4)$$

where Λ_{ij} are the same components of the matrix in equation 2.13, this time obtained using the approximated ($N_z = 0$) hot dielectric tensor 3.2 for the ϵ_{ij} components. The eigenvectors of the dielectric tensor are the allowed propagation modes. The first mode is the generalization of the 'cold' O-mode and is given by $\Lambda_{zz} = 0$. It is characterized by having \mathbf{E} parallel to the \mathbf{B}_0 field and its dispersion relation is $N^2 = \epsilon_{zz}$.

The remaining eigenvectors of 3.4 can be found by solving the determinant of the matrix:

$$\det \begin{bmatrix} \Lambda_{xx} & \Lambda_{xy} \\ -\Lambda_{xy} & \Lambda_{yy} \end{bmatrix} = 0, \quad (3.5)$$

Without losing generality, we can consider that propagation takes place only in the $x-z$ -plane. In this case, the dispersion relation can be simplified as following:

$$N^2 = \frac{\epsilon_{xx}\epsilon_{yy} + \epsilon_{xy}^2}{\epsilon_{xx}}. \quad (3.6)$$

This equation can be considered the generalization of the dispersion relation 2.19 for X-mode, already studied in Chapter 2 with the cold plasma treatment, that we write again here in a re-arranged way:

$$N^2 = \frac{RL}{S} = \frac{S^2 - D^2}{S}. \quad (3.7)$$

Unlikely what happens for O-mode, in this case there are two propagation modes solutions of the dispersion relation, both extraordinary, i.e. $\mathbf{E} \perp \mathbf{B}_0$. The first is actually the X-mode already encountered, while the other one is a 'new' mode. Differently from what happens in the 'cold' counterpart 3.7, in equation 3.6 ϵ_{xx} , ϵ_{yy} and ϵ_{xy} are function of the unknown N^2 . Now, the equation 3.6 turns out to be transcendental and not simply algebraic, as was in the cold plasma description, since here the quantity μ appears in the exponents, as well as $\epsilon_{xx} \neq \epsilon_{yy}$. In particular, the sum over the Bessel functions gives rise to a large number of possible roots ω for any given \mathbf{N} , and hence a large number of pairs (ω, \mathbf{k}) , which define different waves. They are named Electron Bernstein Waves (EBWs), in honour of the famous physicist Ira B. Bernstein [63], and are the harmonics of the third EC-mode existing in magneto-plasmas, named the electrostatic B-mode. The same equation 3.6 describes both X- and B-mode and this fact is of crucial importance for the X-B mode conversion (being described in Section 3.3), which is the second conversion occurring in the O-X-B scheme that will be introduced in Section 3.5. In order to obtain the description of the mere B-mode, it is interesting to analyze the limit of large $\mu = 1/2k_{\perp}^2 v_{th}^2 / \omega_c^2$, as done in reference [62]. On the other side, in the hypothesis of perpendicular propagation, which means $\zeta_n \rightarrow \infty$ in 3.1, the opposite limit of small μ is equivalent to come back to a cold plasma treatment, and hence it is not interesting for the description of B-waves. Under the condition of large μ (which means short wavelength or large Larmor radius) an analytical formula for the dispersion relation of the Electron Bernstein Waves can be

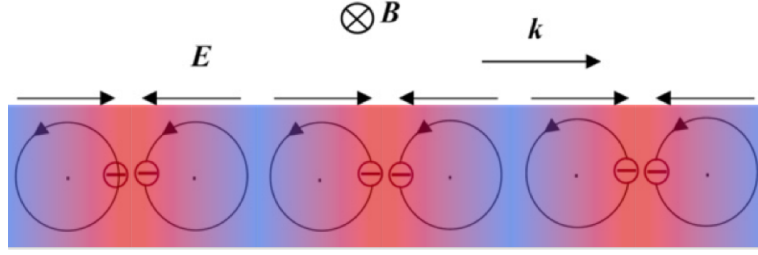


Figure 3.1: In this figure, modified from [62], the Electron Bernstein Waves are schematically represented. The collective rotation in phase of the electrons around their guiding centers sustain the longitudinal EBW. The red and blue regions have been added to visualize the periodic charge accumulation and lack.

written, since the function \tilde{I}_n is characterized by having an asymptotic behaviour [61]:

$$\tilde{I}_n = e^{-\mu} I_n(\mu) = \frac{1}{\sqrt{2\pi\mu}} \left[1 - \frac{4n^2 - 1^2}{1!8\mu} + \frac{(4n^2 - 1^2)(4n^2 - 3^2)}{2!(8\mu)^2} - \dots \right]. \quad (3.8)$$

In this limit, the term $2\mu\tilde{I}'_n$ in the hot dielectric tensor 3.2 becomes dominant, giving the following solutions for equation 3.5:

$$\Lambda_{yy} = 0 \Rightarrow \text{transverse wave, } \mathbf{E} \equiv E_y, \quad \perp \mathbf{k} : \quad \mathbf{X}\text{-mode} \quad (3.9)$$

$$\Lambda_{xx} = 0 \Rightarrow \text{longitudinal wave, } \mathbf{E} \equiv E_x, \quad \parallel \mathbf{k} : \quad \mathbf{B}\text{-mode.} \quad (3.10)$$

The dispersion relation of the Bernstein mode (Figure 3.2) is obtained from the equation $\Lambda_{xx} \equiv \epsilon_{xx} = 0$ [63] [61]. It can be written in the following simplified form [62], by using the approximation $Z_n \simeq -1/\zeta_n$:

$$\mu = X \sum_{-\infty}^{+\infty} \frac{n^2 \tilde{I}_n(\mu)}{1 + nY}. \quad (3.11)$$

The Electron Bernstein Waves are longitudinal waves. They propagate and are sustained by the coherent motion of the electrons around their guiding centre in the magnetic field, with frequency and phase in accordance with the wave (see Figure 3.1). The phase velocity ω/k of the wave must be equal to the electron velocity. It is important to underline that the velocity of the particles must be equal just to the ratio of ω and k , with no specific relation to the singular values of the two quantities. For instance, electrons rotating around the magnetic field lines with the frequency ω_c , are able to sustain the propagation not only of the $(\omega = \omega_c, \lambda \simeq 4\rho)$ -waves, but also of the $(\omega = \ell\omega_c, \lambda \simeq 4\rho/\ell)$ -harmonics. The

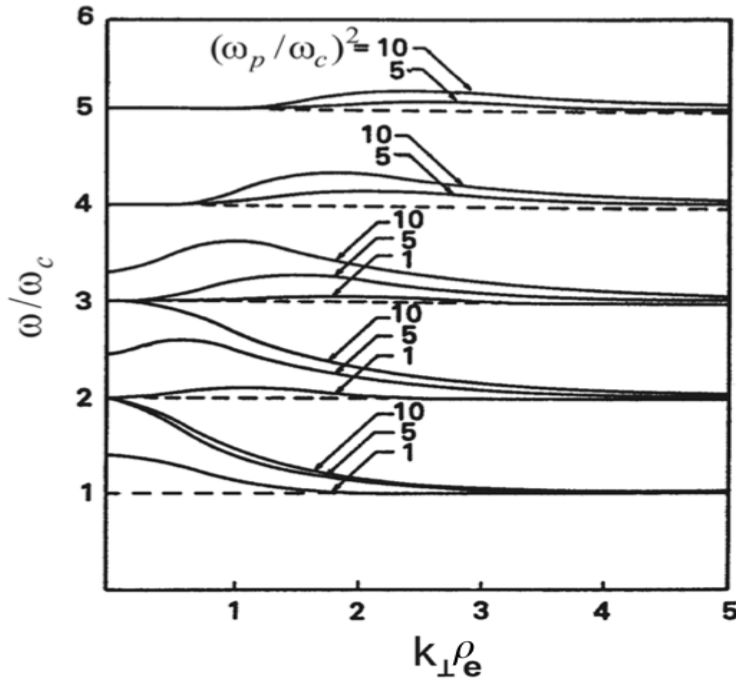


Figure 3.2: EBW dispersion relation, where the frequency is normalized with the cyclotron frequency and the wave vector with the thermal electron gyroradius, taken from [62].

lower is the phase velocity of the perturbation ω/k , the more efficient is the support by the electrons population, since the number of possible resonant particles increases in this case, being also the particles belonging to the bulk of an hypothetical Maxwellian distribution able to participate. To enable this constructive process, for example at the first harmonic, the wave must have a frequency of the same order (but higher) of the cyclotron frequency ω_c of interest. This coherence give rise to a periodic charge accumulations³, propagating in the same direction of the wave vector as longitudinal waves ($\mathbf{E} \parallel \mathbf{k}$). Electrons contribute to the propagation of the wave and since the motion of the electrons around the field lines must be considered, finite Larmor radius effects become of basic importance. The wavelength is of the order of four times the electron gyroradius ($\lambda \simeq 4\rho$). Still under the assumption of wave propagation perpendicular to the magnetic field, the refractive index becomes infinite only in the proximity of the cyclotron harmonics $\ell\omega_c = \omega$, where the waves are strongly damped (or excited) and can release power to the particles⁴. In all the

³Rarefaction and compression of electrons perpendicular to the magnetic field

⁴The power exchange, occurs only for a half of electron gyration, namely the one during which the particle moves in the same direction of \mathbf{k} . In the other half revolution, in fact, the particle travels in

other plasma regions, instead, the free propagation is ensured by the vanishing imaginary part of the dispersion relation. Therefore, orthogonal EBWs exist only between cyclotron harmonics, but it is not true any more in the case of oblique propagation, in which case the harmonics can couple⁵.

The mechanisms responsible for EBWs absorption at the harmonic resonance are basically the relativistic EC interaction or the non-relativistic Doppler-broadened absorption, depending on the ratio between the electron thermal velocity and the N_{\parallel} of the wave. More details on EBWs damping and a comparison between the dependences of B-mode and X2-mode power absorptions on non-local parameters is reported in Appendix A.

3.3 The SX-B Mode Conversion

We can now go back to analyze the propagation of an SX-wave from the higher density plasma regions toward the UH layer $\omega = \omega_{UH}$. As already said, the cold plasma treatment is no more sufficient to describe the behaviour of the wave, once it is upcoming the resonant region. Only the hot dielectric tensor can describe properly the response of the plasma. The B-branch turns out to be the natural extension of the SX-branch, in correspondence of the region of density just slightly higher than the UH layer (see Figure 3.3). Actually, as seen in Section 3.2.1, the SX-wave and the B-wave do belong to the same branch of the hot dispersion relation⁶. As a consequence, in the proximity of the resonant upper hybrid layer (UHL), the SX-mode is not absorbed, but a spontaneous conversion into a backward propagating Bernstein wave occurs [65], taking into account that the longitudinal components of the X-wave, strongly increases while approaching the UHL, becoming dominant. This conversion occurs with very high efficiency, i.e. with a very low coupling efficiency between SX-mode and FX-mode, which depends on the frequency of the wave. The SX-FX coupling, in fact, can occur through the tunneling of the evanescent layer existing between these two branches of the X-mode (see the FX-SX conversion in Section 3.4.2). In most cases, like the one of FTU, this back-tunneling efficiency of SX-mode is

counter-direction respect to the wave, tracing, in practice, an entire wave cycle in half gyrocircle, with a sort of 'double velocity' towards the wave.

⁵Since in the case of oblique propagation $Z_n \neq -1/\zeta_n$, the approximation done above is not valid any more and the value of Z_n must be inserted precisely in the dispersion relation of the B-mode 3.11. This remove the divergences in correspondence of multiple values of ω_c . For a detailed treatment see reference [61].

⁶The roots of the two dispersion relations merge, then the SX- and B-mode coincide.

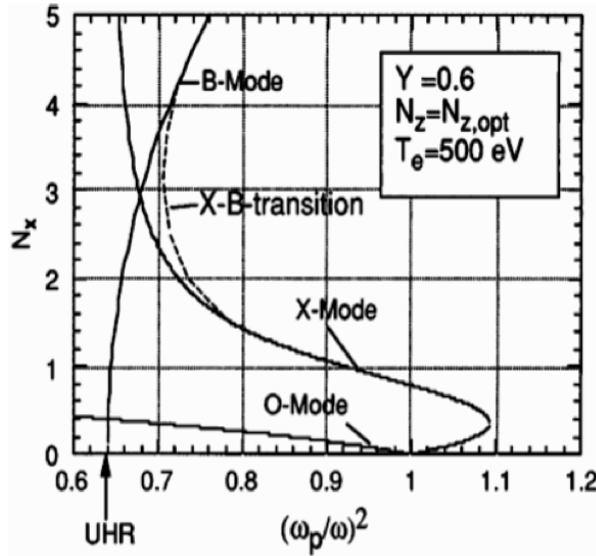


Figure 3.3: Behavior of the radial component of the refractive index, perpendicular to the magnetic field, versus the normalized plasma frequency, calculated with the parameters of the stellarator device W7-AS, for an O-X-B mode conversion (see further on in this Chapter for the description of this scheme). It can be noticed how the X-branch in the dispersion relation is the natural extension of the B-branch, in a hot plasma description. Picture taken from reference [64].

near 0% at the UHL, and hence the coupling efficiency between SX- and B-mode is near 100%. Therefore, no special actions are needed in order to start the B-waves at the UH, but exciting a SX-wave in the higher density regions with respect to the UH layer, to initialize this natural smooth transition between the electromagnetic and the electrostatic branches of the hot dispersion function.

While the orthogonal component of the \mathbf{k} vector increases in the proximity of the UH, the wave slows down⁷, and the electron-ion collisions gradually tend to damp the wave. The collisional damping is highly efficient in this case because of the electrostatic nature of the SX-wave near the UH layer. With a hot plasma description, the thermal frequency $v_{th}k_{\perp}$, on which kinetic effects are based, increases quickly while the wave is approaching the UH layer, and the condition $v_{th}k_{\perp} > \nu_{collisions}$ soon becomes true, before an effective collisional damping has enough time to take place. Hence, the SX-wave is not absorbed at the UH layer, but the (predominant) kinetic effects are such that its trajectory bends and continues toward higher density regions, while conversion to the n^{th} harmonic of B-mode

⁷In the sense of the phase velocity ω/k_{\perp} .

occurs, where n is such that:

$$n\omega_c < \omega_{UH} < (n+1)\omega_c.$$

The B-waves generated at the UH, then, propagate towards higher densities and are strongly absorbed around the cyclotron harmonics. The propagation of EBWs is not limited by a density limit, since the wave vector remains always real for increasing densities. This does not happen for O-, FX- and SX-mode, which upper density limits in magneto-plasmas are the well known $\omega = \omega_p$, $\omega = \omega_R$ (or RH), $\omega = \omega_L$ (or LH) layers respectively. Such a feature of EBWs is of strong interest in view of high density plasma operations, in particular in over-dense scenarios, for heating (or receiving from) the central plasma regions, prevented to both O- and X-mode. This was the initial motivation for studying, and then using, EBWs. The already known plasma heating techniques and temperature diagnostics used in the EC-waves field, have no accessibility in over-dense plasmas, while this limit does not exist for Bernstein Waves. Subsequently, other useful features of these waves were discovered, like for instance a high cyclotron absorption capability, which offers the possibility of plasma heating at harmonics frequencies higher than the 2nd. For the other heating schemes, the most efficient absorption for heating magnetically confined plasmas is usually found for the 2nd in extraordinary mode.

On the other side, EBWs suffer of the presence of a lower density limit, which is the UH layer. In the plasma regions internal to $\omega = \omega_{UH}$, the relevant frequency becomes ω_c , instead of the usual ω_p , and the condition to be satisfied for the propagation to take place is $\omega \geq \omega_c$ instead of $\omega \geq \omega_p$. The physical explanation of the capability of EBWs to propagate in plasma regions where $\omega_c < \omega_p$ ⁸, lies in the fact that the Larmor radius is:

$$\rho > \lambda_D = \sqrt{\frac{K_B T_e}{4\pi n_e e^2}} \quad (3.12)$$

in these regions. In the expression above, λ_D is the Debye length. This means that the electron gyrorotation performed under the condition $\omega_c < \omega_p$, is able to transmit a perturbation experienced by a particle to the other particles, beyond the shielding sphere, defined with a λ_D radius length.

⁸Provided the condition $\omega_c \leq \omega$ being satisfied everywhere.

3.4 Coupling Schemes to EBWs with X-mode Injection

Being EBWs space charge waves, they need the presence of populations of particles moving in phase to be sustained. For this reason, they do not exist in vacuum but they can only be excited in the plasma. First experiments on the use of EBWs were performed exciting them directly in the plasma using electrostatic antennas inserted into the medium [66] [67] [68]. This method is clearly not useful in the case of the modern devices, in which millimeter waves are injected to heat high temperature fusion plasmas. In fact, to perform a direct excitation of EBWs, antennas dimensions of the order of the electron gyroradius (<0.1 mm) would be needed and furthermore the high temperatures prevent any contact between external objects with the internal regions of the plasma. Hence, EBWs can be excited in the plasma exclusively through mode conversions from externally launched electromagnetic waves. The exciting process is possible through the already described coupling between SX-waves and EBWs at the inner side of the UH layer where the wavelength reduces down to the order of the electron gyroradius.

3.4.1 The Direct SX-B Coupling

To reach the UHL from the higher density plasma regions, a possible scheme consists in a HFS launch of an SX-wave in the direction of the UHL, like in Figure 3.4, in such a way that the coupling to the EBWs can occur spontaneously, while the wave is approaching the resonant layer. A high field side launch is possible with the use of the first harmonic X-wave. Nevertheless this scheme can be useful only for not too high densities, namely for a density value such that the ω_L cutoff layer does not appear along the path of the wave to the UHR. When the density is high enough, instead, the ω_L cut off prevents also the use of X-mode in the internal regions. For this reason the use of the direct SX-B coupling scheme is not of interest in view of overdense plasmas heating experiments, despite some results on direct SX-B coupling, in which the Doppler-shifted power deposition [69], and the Electron Bernstein Wave Current Drive (EBWCD) [70], are well described in literature (see also [71] [72]).

3.4.2 The FX-SX-B Scheme

In some cases it is possible to excite the SX-mode by launching a FX-wave from the LFS [73], where the launching system is usually located in most of the fusion machines.

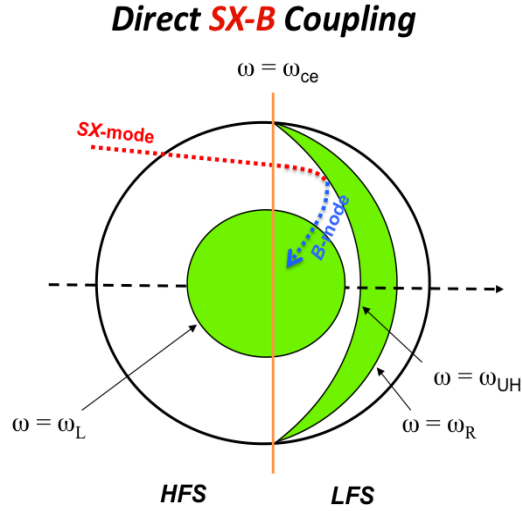


Figure 3.4: Schematic poloidal view of the (direct) coupling between a SX-wave launched from the HFS and the B-mode, at the UHL. The green regions are the ones prevented to X-mode.

To let this coupling occur, the launched wave (FX) must be able to propagate beyond the low density cutoff $\omega = \omega_R$, by tunneling the evanescent region between the RH layer and the UHL. Over this region, the coupling to SX-mode occurs (see Figure 3.5), and the excited mode subsequently converts to Electron Bernstein Waves at the UHL, in the way described above.

When the RH cutoff is close to the UHR, the situation is known as the classical Budden-type of mode conversion scenarios [74], in which the launched FX-wave power is partially transmitted to the SX-mode and partially is absorbed. The absorbed component of the power is the fraction that is mode converted to the EBWs, while the transmitted to SX-mode will encounter its own LH cutoff. Hence, the process playing the role in the FX-SX-B conversion scheme can be thought similarly to an interferometric phenomenon between two reflection points (the RH and LH cutoffs), which can let the wave phases become optimal for SX-B mode coupling, in correspondence of a central point (the UHR layer) [75]. In this representation, the power percentage converted to EBWs is the effective dissipation of the R-UHL-L mode conversion resonator.

The excitation of EBWs by FX launch from vacuum needs a steep plasma density gradient such that the density scale length of the medium must be of the order of the vacuum wavelength of the wave. Since the cold plasma dispersion relation is not valid to describe

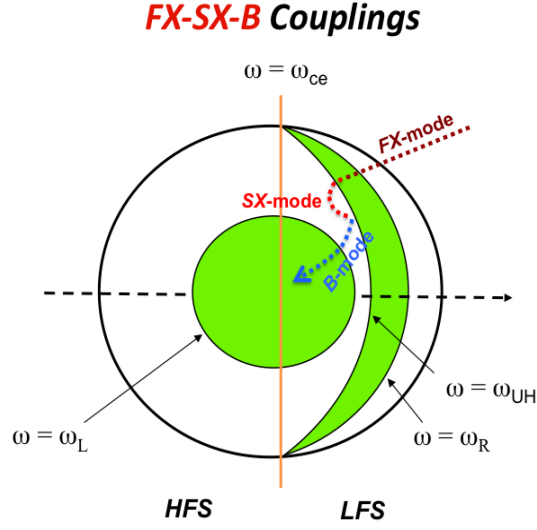


Figure 3.5: Schematic poloidal view of the FX-SX-B scheme. The FX-wave couples the SX-wave by tunneling the evanescent region (green) between the low density cutoff of the X-mode and the UHL. The SX-mode, then, converts to B-mode.

wave propagation where a resonant layer is present in between two cutoffs limiting points, to perform calculations (here not reported) it becomes necessary to revert back to the wave equation 2.10 and introduce a "scattering" potential [75] [76] [77], defined on the quantities S and D introduced in section 2.2.1. The power conversion coefficient from FX-to B-mode turns out to be:

$$\mathbb{T}_{FX-B} = 4e^{-\pi\eta}(1 - e^{-\pi\eta}) \cos^2 \left(\frac{\phi}{2} + \vartheta \right), \quad (3.13)$$

where ϑ is the phase of the gamma function $\Gamma(-i\eta/2)$, ϕ is the phase difference between the SX-mode which propagates toward the LH cutoff and the reflected component propagating toward the UHL. The η parameter (Budden [74]) is obtained by expanding the "scattering" potential cited above around the UHR, to find the location of the RH cutoff, as in reference [77]:

$$\eta = \frac{\omega_{ce} L_n}{c} \frac{\alpha}{\sqrt{\alpha^2 + 2(L_n/L_B)}} \sqrt{\left[\frac{\sqrt{1 + \alpha^2} - 1}{\alpha^2 + (L_n/L_B)\sqrt{1 + \alpha^2}} \right]}, \quad (3.14)$$

where:

$$\alpha = \left[\frac{\omega_{pe}}{\omega_{ce}} \right]_{UHR}, \quad (3.15)$$

and $L_n = n_e/(\partial n_e/\partial x)$ and $L_B = B/(\partial B/\partial x)$ are the density and magnetic field scale lengths, respectively, evaluated at the UHR, as well. It is easy to notice that in the limit

$L_B \gg L_n$, quite usual especially in high density scenarios, the expression 3.14 reduces to:

$$\eta \approx \frac{\omega_{ce} L_n}{c\alpha} \sqrt{[\sqrt{1 + \alpha^2} - 1]}, \quad (3.16)$$

wich for $\alpha \sim 1$ becomes:

$$\eta \approx \frac{1}{2} \frac{\omega_{ce} L_n}{c} \approx 293.5 |BL_n|_{UHR}, \quad (3.17)$$

where B and L_n are expressed in Tesla and meters, respectively. The maximum conversion efficiency ($\mathbb{T}_{FX-B} = 1$) expressed by equation 3.13 can be obtained by simultaneously equalize the quantity $\phi/2 + \vartheta$ to any integer multiple of π and $e^{-\pi\eta} = 0.5$, that means $\eta \approx 0.22$, and hence:

$$|BL_n|_{UHR} \approx 5.8 \times 10^{-4} Tm. \quad (3.18)$$

This expression shows how the FX-SX-B mode conversion is applicable only to fusion devices operating at low magnetic fields, or equivalently with a low frequency⁹ heating system, in presence of a steep density gradient. This happens for instance in machines like spherical tokamaks, reversed field pinches and high β stellarators experiments, when operations are at low magnetic field only. Nevertheless, finally it must be also noticed that the frequency can not be too low, since when the UHR "shifts" outside the plasma volume, the FX-SX-B scheme becomes clearly not applicable to excite EBWs and heat the plasma. At the frequencies used in the FTU ECRH system, the FX-SX coupling computed with 3.13 is found negligible, excluding the use of this scheme to excite EBWs.

3.5 A Third Scheme for EBWs Excitation

3.5.1 The O-X-B Double Mode Conversion Scheme

It is clear that the crucial point for the excitation of the Electron Bernstein Waves in the plasma is the production of an SX-wave propagating towards the UHR. The narrow range of parameters allowed for the FX-SX-B mode conversion and the technical difficulties in the accessibility required by the direct SX-B coupling, are such that these techniques can not be widely used to excite EBWs in the large fusion devices. Additionally, in the latter scheme, sometimes the UHR can be completely enclosed into the RH cutoff layer of the X-mode, when the frequency is high. In this case the direct SX-B coupling cannot be

⁹Typically lower than 20 GHz.

performed at all, despite a wave launch from the HFS.

To overcome these problems, a third way to excite EBWs was suggested in 1973 by J. Preinhaelter [78]. This scheme consists in two consecutive mode conversions, like represented in Figure 3.6. The first one involves an O-wave launched from the LFS, which converts into a SX-wave. This coupling is used to excite the SX-mode beyond the UHL and is described in the next section. Also in this case, a second conversion to B-mode occurs at the UHR, once the SX-mode has been excited, similarly to what happens in the other schemes.

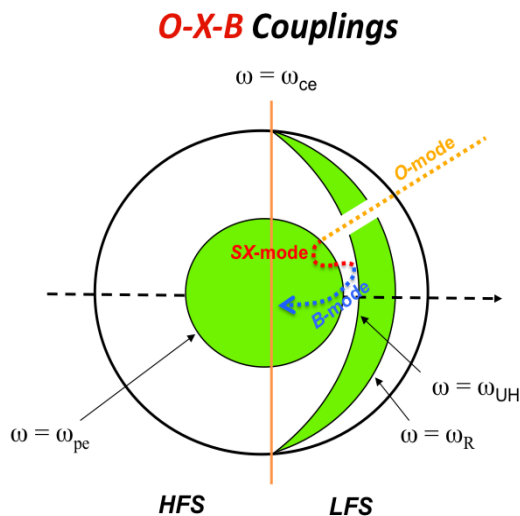


Figure 3.6: Schematic poloidal view of the O-(S)X-B mode conversion scheme. The O-wave is launched from the LFS and excites the SX-wave at the O-mode density cutoff layer. The X-wave, then, mode converts to EBWs, which can reach the central overdense plasma regions. The O-mode encounters no evanescent regions while approaching its cutoff layer. This is the reason why a white area has been drawn at its passage through the green region on the right of the picture, which is evanescent only for the X-mode.

3.5.2 The O-SX Coupling

Introduction

In geometrical optics, it is known that when a ray of light is propagating in a medium, whose refractive index is N_1 and reaches an interface with a second medium, with refractive index N_2 , refraction and reflection coefficients depend on the angle of incidence at the point

of refraction and on N_1 and N_2 , according to the Snell's law. In particular, in the case of a p -polarized wave, i.e. a wave with an oscillating electric field in the plane of incidence, the wave is completely refracted in the second medium when the incidence angle is:

$$\vartheta_B = \arctan\left(\frac{N_2}{N_1}\right). \quad (3.19)$$

This incidence angle is called *Brewster angle*, and gives rise to zero back-reflection into the first medium. The relation between the amplitudes of the incident and reflected waves can be demonstrated to be [79]:

$$A_{ref} = -\frac{\tan(\vartheta_1 - \vartheta_2)}{\tan(\vartheta_1 + \vartheta_2)} A_{inc}, \quad (3.20)$$

where ϑ_1 and ϑ_2 are respectively the incidence and the refraction angles. Being the power of a wave proportional to the square of its own amplitude, the transmitted (refracted) power T of a normalized incident wave can be written, from 3.20, as:

$$T = 1 - \frac{\tan^2(\vartheta_1 - \vartheta_2)}{\tan^2(\vartheta_1 + \vartheta_2)}. \quad (3.21)$$

Any incidence angle which is close enough to the *Brewster angle* ϑ_B allows a high value for the transmitted power. Similar physical phenomena take place, as well, in the case of radio waves propagating in the ionosphere (for a detailed treatment see [80]), and in the plasmas of fusion machines, like tokamaks and stellarators.

Propagation of O-Mode from LFS

In order to find the best condition for O-SX coupling, we start from the description of the propagation of an O-wave from LFS with a geometrical plasma model in slab geometry, where density and magnetic field gradients are considered to be parallel. This is a simplified description of a tokamak-like plasma, since in the real case the local magnetic field scales approximately as $1/R$, where R is the major tokamak radius, while the density profile of the plasma is, at a first approximation, poloidally symmetric and approximately centered on the vessel axis. When the propagation of an EC wave is considered, the ion dynamic can be ignored and the medium can be described with the cold plasma treatment, as already seen in the preceding Chapter. Let us consider, then, a homogeneous magnetic field $\mathbf{B} = B\hat{\mathbf{z}}$ and a density gradient $\nabla\mathbf{n}$, directed along the x -axis. The plasma is considered to be homogeneous along the y -axis and the z -axis. Only the x -component

of the refractive index vector \mathbf{N} is variable, with a dependence from the density (and hence from x), while N_y and $N_z \equiv N_{\parallel}$ are constants, according to the Snell's law¹⁰. We re-write the dispersion relation 2.15 and 2.18 in a third form, largely used in plasma physics, known as the *Appleton-Hartree* form:

$$N_x^2 + N_y^2 + N_z^2 = 1 - \frac{2X(1-X)}{2(1-X) - Y^2 \sin^2 \vartheta \pm \Gamma} \quad (3.22)$$

where

$$\Gamma = \sqrt{Y^4 \sin^4 \vartheta + 4(1-X)^2 Y^2 \cos^2 \vartheta}, \quad (3.23)$$

ϑ is the arbitrary angle between N and the magnetic field, $X = \omega_{pe}^2/\omega^2$ and $Y = \omega_{ce}/\omega$. The sign (+) in the expression 3.23 corresponds to the ordinary mode while (-) refers to the extraordinary mode. The dispersion relation analytically describes different branches, belonging to O-, SX- and FX-mode. The O- and SX-branches coalesce in the particular case of $\Gamma = 0$, i.e. when the conditions $X = 1$ and $\vartheta = 0$ are satisfied simultaneously. Actually, under the condition $X = 0$, also the O- and FX-branches coalesce, but this condition is mere degeneracy at low density, when both O- and FX-mode tend to vacuum propagation. The O- and SX-branches, instead, always connect analytically for $X = 1$, but they partly develops in the evanescence region where $N_{\perp}^2 < 0$. The only way to avoid these evanescence values consists in satisfying also $\vartheta = 0$, together with $X = 1$ ¹¹. In practice, these two conditions occur together when the phase velocity \mathbf{v}_{ph} of the wave is completely parallel to the magnetic field ($\vartheta = 0 \Rightarrow N_x = N_y = 0$) at the O-mode density cutoff layer $P = 0$ ($X = 1 \Rightarrow \omega_{pe} = \omega$), obtained in 2.20 for propagation across the field ($\vartheta = 0$). It is important to underline now that, unlike the X-mode cutoff layers, which position in the plasma depends from the values of the parallel refractive index N_{\parallel} with respect to the magnetic field, and hence from the value of ϑ that appears in the dispersion relation (according to equations 2.25), the O-mode cutoff is the same ($\omega_{pe} = \omega$), also in the case of oblique propagation. This is true for N_{\parallel} not too high, until the critical value:

$$N_{\parallel, c}^2 = \frac{Y}{Y+1} \quad (3.24)$$

¹⁰In a real tokamak-like configuration N_y and N_z are not constant, since the plasma geometry encountered by the wave while propagating is toroidal. In particular, it can be showed with geometrical calculations that, in an axisymmetric configuration, the quantity $k_{\parallel}(R_0 + r \cos \gamma)$ is conserved, if the plasma equilibrium is independent of ϕ [81], where ϕ and γ are the toroidal and poloidal angles, respectively, and R_0 the major radius of the machine.

¹¹In fact, these two conditions, together, imply a null value for Γ in 3.23, which is the only quantity in the dispersion relation 3.22 that enables to distinguish O- and X-mode propagation.

is reached [27]. When N_{\parallel} becomes higher than the value 3.24, the O-mode cutoff 'shifts' toward lower plasma density layers, and its position depends on the value of N_{\parallel} . Thus, the accessibility conditions and cutoff densities for the propagation of an ordinary polarized wave in terms of the corresponding plasma frequencies can be presented schematically as follows:

$$\text{O-mode cutoff} \Rightarrow \begin{cases} \omega_{pe}^2 = \omega^2, & \text{for } N_{\parallel}^2 \leq \frac{Y}{Y+1} \\ \omega_{pe}^2 = (1 - N_{\parallel}^2)(Y + 1)\omega^2, & \text{for } \frac{Y}{Y+1} < N_{\parallel}^2 < 1. \end{cases}$$

In other words, $|N_{\parallel}| = \sqrt{Y/(Y+1)}$ is the maximum value reachable by the parallel component of the refractive index at the $\omega_{pe} = \omega$ layer, which represents the deeper O-mode cutoff layer in the plasma.

The O-mode Coupling to SX-mode at $X = 1$ in Slab Geometry

Turning back to the coalescence of the O- and SX-branches in the non-evanescent plasma region (where $N_{\perp}^2 \geq 0$), it is interesting to investigate the wave properties when the condition $\vartheta = 0$ holds true, first. Under this condition, the *Appleton-Hartree* dispersion relation 3.22 gives rise to four expressions, depending on the sign of X and if the considered polarization is O-mode (upper sign) or X-mode (lower sign) [82]:

$$N_z^2 = \begin{cases} \frac{1-X \pm Y}{1 \pm Y}, & \text{for } X < 1 \\ \frac{1-X \mp Y}{1 \mp Y}, & \text{for } X > 1. \end{cases}$$

To take into account real propagation, we must restrict only to the range $0 < N_z^2 < 1$, to allow real propagation of the wave ($N_z^2 > 0$), together with a wave injection from vacuum ($N_z^2 < 1$). Thus, only the X-wave is allowed in the $X > 1$ region. Performing the limits for $X \rightarrow 1^+$ for X-mode in the $X > 1$ region, and for $X \rightarrow 1^-$ for O-mode in the $X < 1$ region, they both give:

$$N_{\parallel, opt}^2 \equiv N_{\parallel, c}^2 = \frac{Y|_{X=1}}{Y|_{X=1} + 1}, \quad (3.25)$$

where the symbol $Y|_{X=1}$ means that $Y = \omega_{ce}/\omega$ is evaluated at the O-mode cutoff layer $X = 1$. Expression 3.25 corresponds to the O-SX mode conversion optimal value for N_{\parallel} at cutoff, which is the same critical value defined in 3.24. In correspondence of this limiting value, the condition $\omega_L = \omega_{pe}$ holds true. Hence, it is possible in principle to obtain perfect conversion of an O-wave into a SX-wave, if the O-wave reaches the cutoff layer

with $N_z^2 = N_{\parallel, opt}^2 = Y/(Y + 1)$, while $N_x = N_y = 0$. In a magnetically confined plasma, this can be obtained with a launch such that the wave can reach the layer $\omega_{pe}^2 = \omega^2$, but with null components of the perpendicular phase velocity. In this case, the O-wave naturally excite a new wave at cutoff, which has the same polarization¹², wave number, phase and group velocity, but belonging to the SX-branch. If the O-wave reaches the cutoff with a non-optimum value of N_{\parallel} , or equivalently, with $N_{\perp} \gtrsim 0$, the transmission to SX-mode occurs with lower efficiency. The allowed values of N_{\parallel} and N_{\perp} around $N_{\parallel, c}$ and 0, respectively, can vary in ranges that strongly depends on the plasma parameters and the frequency of the incident wave¹³. In the case of non-optimal approach to the cutoff layer, the incident O-wave splits into a transmitted SX-wave, beyond $X = 1$, and a back-reflected O-wave. In our ideal slab model, where, without losing in generality, N_{\parallel} is constant along the propagation path and $N_y = 0$, the optimal O-wave is characterized by $\mathbf{N} = (\sqrt{1 - N_{\parallel, opt}^2}, 0, N_{\parallel, opt}^2)$ at the plasma edge, and reaches the cutoff layer with $\mathbf{N} = (0, 0, N_{\parallel, opt}^2)$. Therefore, in a slab geometry, the optimal launching angle is given by $\vartheta_{l, opt} = \arcsin(\sqrt{Y/(Y + 1)})$ ¹⁴. The O-X power transmission coefficient has been theoretically estimated several times since the beginning of the Seventies, with different approaches [83] [84] [85]. The results obtained are just slightly different and can be merged into the following expression for the transmission to SX-mode [86], known as the *Mjølhus formula*:

$$\mathbb{T}_{O-SX}(N_y, N_z) = \exp \left\{ - \pi k_0 L_n \sqrt{\frac{Y}{2}} [2(1 + Y)(N_{z, opt} - N_z)^2 + N_y^2] \right\}, \quad (3.26)$$

where $L_n = n/\partial n/\partial x$ is the local density scale length. Among all the expressions available in literature, equation 3.26 is the most reliable to describe the O-SX mode conversion in slab geometry, also for high values of $k_0 L_n$. This could be demonstrated after a comparison among them, performed with full wave calculations [82]. The analytic expression of $\mathbb{T}_{O-SX}(N_y, N_z)$ is a Gaussian function of the variables N_z and N_y , centered on the optimal

¹²According to equations 2.29 and 2.30, we remember that the polarization of the modes for longitudinal propagation is circular. In particular, the circular left-handed is the polarization of both the O-mode launched from LFS with ϑ angle into the plasma, once it has approached the parallel propagation. The polarization of FX-mode, instead, becomes circular right-handed, once the propagation is parallel.

¹³This fact will be shown to be the most critical aspect in view to obtain O-X conversion in the case of FTU, since the ECRH system operates at a high frequency, equal to 140 GHz.

¹⁴Attention must be paid not to confuse the launching angle with the angle that appears in the dispersion relation 3.22, which represents the angle between the \mathbf{B}_0 field and the wave number \mathbf{k} of the wave. In slab geometry, the relation $\vartheta = 90^\circ - \vartheta_l$ holds true between them.

values $N_{z, opt} = \sqrt{Y/Y + 1}$ and $N_{y, opt} = 0$. The width of the Gaussian bell decreases with Y , with the vacuum wave number $k_0 = 2\pi/\lambda_0$ of the wave and with $L_n = n/\partial n/\partial x$. Clearly, in the ideal case of a plane wave with $N_{\parallel, opt}$ and $N_{\perp} = 0$ at $X = 1$, the parameters in 3.26 are non influential on the perfect conversion. Nevertheless, calculations performed on a single plane wave are just ideal. In the real case, Gaussian beams are launched and the finite geometrical dimension together with the angular k -spectrum of the incident beam should be taken into consideration, in order to perform a realistic evaluation. Thus, the parameters Y , k_0 and L_n are always influential on the transmission and the tolerance on the injection precision, which ensures a reasonable amount of converted power, strongly depends on them. Since in the real case, Y and k_0 are fixed by the system, the quantity $L_n|_{X=1}$, given by the density profile of the plasma, is the crucial parameter. The steeper is the density gradient of the profile, the larger is the angular window allowed in the injection.

Polarization Mismatches

An important technical aspect in view to obtain the maximum conversion is the wave polarization control. We have shown in the preceding Chapter 2 that the polarization of the EC waves is always elliptical, for oblique propagation. This is the reason why a linearly polarized wave injected from outside with an oblique launch, excites both O-mode and X-mode, which propagates independently in the plasma. In experiments aimed to test O-X conversion, all the power coupled as X-mode in the LFS is lost, from the point of view of transmission. In fact, this component is completely reflected at the lower density cutoff $\omega_R = \omega$ (2.25) and increases the amount of stray radiation in the vessel. The ellipticity of the launched polarization is often unimportant in many plasma operations that foresee ECRH injections with launching angles not too far from 0, i.e. for quasi-perpendicular injections. Nevertheless in experiments aimed to test O-X coupling higher values are requested in the launch and the effective conversion must be normalized to the actual power propagating as O-mode in the plasma. An ideal EC launcher should provide a real time control on the polarization, with step-by-step optimal matching to O- and X-mode, at a given launching angle, by providing the proper ellipticity to the polarization of the wave. In order to evaluate polarization mismatches, we can re-write, for convenience,

the equations 2.27 and 2.28 in terms of the quantities X and Y :

$$\frac{iE_x}{E_y} = \frac{1}{Y} \left[\frac{1 - N^2}{X} (1 - Y^2) - 1 \right], \quad (3.27)$$

$$\frac{E_x}{E_z} = -\frac{1 - X - N^2 \sin^2 \vartheta}{N^2 \cos \vartheta \sin \vartheta}, \quad (3.28)$$

and obtain an expression for $(1 - N^2)/X$ from the *Appleton-Hartree* dispersion relation 3.22, to be substituted in 3.27:

$$\frac{iE_x}{E_y} = \frac{1}{Y} \left[\frac{2(1 - X)}{2(1 - X) - Y^2 \sin^2 \vartheta \pm \Gamma} (1 - Y^2) - 1 \right]. \quad (3.29)$$

We let $X \rightarrow 0$ in equations 3.28 and 3.29, finding the equations:

$$\frac{iE_x}{E_y} = -\frac{Y^2 \sin^2 \vartheta \pm \sqrt{Y^2 \sin^4 \vartheta + 4 \cos^2 \vartheta}}{2} \quad (3.30)$$

$$\frac{E_x}{E_z} = -\cot \vartheta, \quad (3.31)$$

for the polarization of the O- and X-waves at the plasma boundary. The polarization is elliptical for both modes and the electric field vector lies on the $x'y'$ -plane, rotated with respect to the xy -plane, on which the ratio R of the axes in the ellipse are:

$$R_{+,-} = \left| \frac{E_{x'}}{E_{y'}} \right| = \frac{\mp Y \sin^2 \vartheta + \sqrt{Y^2 \sin^4 \vartheta + 4 \cos^2 \vartheta}}{2 \cos \vartheta}, \quad (3.32)$$

where the upper and lower signs denote O- and X-mode. It is possible to demonstrate [82] that, since the power content in each mode is proportional to $\langle E_{x'}^2 \rangle + \langle E_{y'}^2 \rangle$, the fraction of power η_0 coupled in O-mode, when a linearly polarized wave is launched into a magnetized plasma with the electric field vector lying in the \mathbf{NB} -plane at the plasma boundary, can be written in the following way:

$$\eta_0 = \frac{1 + R_-^2 \cot^2 \phi}{(1 + R_-^2)(1 + \cot^2 \phi)}, \quad (3.33)$$

where ϕ is defined as the angle between the direction of oscillation of the wave electric field and the x' -axis.

3.5.3 The O-X-B Power Transmission Efficiency

In the power conversion efficiency coefficient 3.13 presented in paragraph 3.4.2, which refers to the expected mode conversion from FX-mode (launched from the LFS) to B-mode, a back-conversion of SX-mode, propagating from the LH cutoff toward the UHR,

into FX-mode, that leaves the plasma, is also considered. Also this coupling can occur by tunneling the evanescent layer between the UHR and the RH cutoff, in the same way (but in opposite direction) considered above for the FX-SX coupling. The efficiency of the tunneling process is related to the Budden parameter 3.14. Here we report such parameter in the exponential under the approximations $L_B \gg L_n$, like done for the expression 3.16, which holds true in the case of FTU:

$$\mathbb{T}_{SX-FX} = e^{-\pi\eta} = \exp \left\{ -\pi(\omega_{ce}L_n)/(c\alpha)\sqrt{\left[\sqrt{1+\alpha^2}-1\right]} \right\} \quad (3.34)$$

This component represents a power loss from the point of view of the overall O-X-B mode conversion process, since all the waves which tunnel and propagate away from the plasma as FX-mode, do not excite EBWs. The overall power mode conversion coefficient of the O-X-B scheme \mathbb{T}_{O-X-B} can be estimated using equations 3.26 and 3.34:

$$\mathbb{T}_{O-X-B} = \mathbb{T}_{O-SX} \cdot (1 - \mathbb{T}_{SX-FX}). \quad (3.35)$$

The expression 3.35 above shows how a high FX-SX-B efficiency automatically excludes high O-X-B efficiency, and vice-versa. This happens since the tunneling which is at the base of either the direct FX-SX conversion (which enable EBWs excitation) or the inverse SX-FX conversion (which causes power loss in the O-X-B scheme) is the same. To minimize the power losses, the coefficient η defined in 3.14 should be greater than 1. Therefore, the condition that must be satisfied to increase the efficiency of the FX-SX-B and O-X-B schemes are opposite, namely $\eta < 1$ and $\eta > 1$ respectively. Additionally a small k_{\parallel} is preferred in the first case while an optimal k_{\parallel} is needed in the second case. Equation 3.17 shows how, for a fixed magnetic field, the conversion from FX-mode launched from vacuum into B-mode occurs closer to peripheral plasma regions, where L_n is shorter, while the O-X-B mode conversion occurs deeper in the plasma and privileges a longer density scale length.

A big advantage of the O-X-B scheme consists in the fact that the optimal condition for O-X coupling is mainly geometrical, adjustable from outside just acting on the launching system, hence, in principle, quite easy to obtain. This is not the case when an optimization is performed for FX-SX coupling. In this case, in fact, the efficiency of the process is fixed by the plasma parameters and the optimization can be performed only by acting on them, with more challenging techniques¹⁵. Additionally, the FX-SX conversion is strongly

¹⁵Typically, limiters are used to change the local plasma density.

dependent on the local value of the magnetic field. This can be noticed by re-writing the transmission coefficients of the two conversions, highlighting in equations 3.26 and 3.34¹⁶ the different evanescent layers D_1 and D_2 to be tunneled by the wave in the two processes:

$$\mathbb{T}_{O-X} = e^{-D_1/\lambda} \quad \Rightarrow \quad D_1 = 2\pi^2 L_n \sqrt{\frac{Y}{2}} [2(1+Y)(N_{\parallel, opt} - N_{\parallel})^2 + N_y^2] \quad (3.36)$$

$$\mathbb{T}_{FX-SX} = e^{-D_2/\lambda} \quad \Rightarrow \quad D_2 = 2\pi^2 L_n Y^2 \sqrt{\frac{\sqrt{X+Y^2}}{XY} - 1} \quad (3.37)$$

where both the expressions are written making use of the quantities X and Y , evaluated at $\omega = \omega_{pe}$ and $\omega = \omega_{UHR}$ respectively. It can be noticed that the dependence on Y , and hence on the local magnetic field, is stronger in equation 3.37, than in equation 3.36. This dependence makes the FX-SX conversion efficiency decrease more rapidly with the increasing magnetic field, with respect to the O-SX conversion. The O-X-B scheme, then, is advantageous for higher magnetic field devices like, for instance, FTU tokamak.

The Effect of the Plasma Density Fluctuations

Another issue to be taken into account is the effect of the plasma density fluctuations. These imply negative consequences on the conversions, since fluctuations change the local density value in an unpredictable way. In general, density fluctuations are stronger at the plasma edge, where the FX-SX conversion takes place, but nevertheless the O-SX conversion, in the O-X-B scheme, is more sensitive to this phenomenon. Therefore, despite the O-SX coupling occurs deeper in the plasma, where the level of fluctuations is lower, the stronger dependence of the conversion on the local density makes the efficiency drop in presence of even a low level of fluctuations¹⁷. In a pictorial view, density fluctuations make the plasma surface at cutoff become rough and wavy, preventing a description of such a process but using a statistical approach. The pejorative consequences of the turbulence on the O-X conversion efficiency, is given by the modification of the real parallel and perpendicular components of the refractive index N at the cutoff layer with respect to the ones of the incident ray. Since the fluctuations have mainly poloidally directed (i.e. y axis) wavevectors [87], the effects of the roughness turn out to be mainly on the perpendicular components of N and introduce an effective poloidal beam divergence much higher than

¹⁶Assuming $\mathbb{T}_{FX-SX} \equiv \mathbb{T}_{SX-FX}$.

¹⁷The efficiency degradation implied by fluctuations is expected to be approximately the same for O-X-B and FX-SX-B, but no theory able to quantitatively compare them has been developed so far.

the intrinsic one. The effects on O-SX mode conversion can be described following the statistical treatment presented in [64], in which only fluctuations with a wave vector in the poloidal direction are considered. A probability density function of the poloidal component N_y can be written as:

$$p(N_y) = \frac{\lambda_y}{\sqrt{2\pi}\sigma_x} \exp\left(-\frac{N_y^2\lambda_y^2}{2(1-N_y^2)\sigma_x^2}\right) (1-N_y^2)^{-3/2}, \quad (3.38)$$

where $\sigma_x = L_n\Delta n_e/n_e$ is the fluctuation amplitude standard deviation, $\Delta n_e/n_e$ the relative fluctuation amplitude and λ_y the poloidal correlation length [78]. The O-SX power transmission function 3.26, weighted on density fluctuations, is then:

$$\mathbb{T}_{O-SX, mod}(N_z) = \int_{-1}^{+1} \mathbb{T}_{O-SX}(N_y, N_z)p(N_y)dN_y \quad (3.39)$$

For any theoretical conversion efficiency calculated on the plane wave approximation, the relation $\mathbb{T}_{O-SX, mod} \leq \mathbb{T}_{O-SX}$ always holds true, since the wavy nature of the plasma surface affects the O-SX coupling. However, deviations on the refractive index induced by the turbulences can also become of minor importance when the modifications on N_{\parallel} keep in the range of values given by the launching angular window¹⁸. Therefore, a wide angular window is always preferable, not only to have more flexibility in the beam injection, but also to lower the negative effects of phenomena that can be controlled only partially, like the refraction of the ray, or that can hardly be predicted, like local density fluctuations. The wideness of the angular window cannot be chosen a priori, but is fixed by the plasma parameters (the density scale length L_n) and the frequency of the wave (k_0), which dominate the *Mjølhus formula* 3.26 when $N_{\parallel} \neq N_{\parallel, opt}$ and $N_y \neq 0$. The statistical model given by 3.38 has been proofed to be valid with good reliability on the stellarator W7-AS [88]. It could be demonstrated that high conversion efficiencies were reachable¹⁹ in the two regimes, of low k_0L_n (≤ 10) and relatively high (>25 %) density fluctuation amplitude, or with $k_0L_n = 60$ and a relative fluctuation amplitude of less than 2 % [64]. These experiments could be performed by changing the edge rotational transform [89], which has a direct influence on the density profile shape and on the fluctuation activity.

¹⁸Angular tolerance in the launch which ensures 50% of transmitted power.

¹⁹Using a fixed injection angle.

Electron Bernstein Wave Emission

If the plasma description is done using a slab geometry, the O-X-B mode conversion is a reversible process [90]. Therefore, under this approximation, measuring B-X-O conversion is always equivalent to the measure O-X-B conversion. Both of them, must be performed at the proper (optimal) detection/injection angle, such that equation 3.24 turns out to be satisfied at $\omega = \omega_{pe}$ layer. While O-X-B scheme can be used to heat over-dense plasmas with EBWs, the B-X-O conversion is a natural emission of radiation which spontaneously emerges from the internal plasma regions, above the O-mode cutoff, as EBWs. This happens because in fusion plasmas the optical thickness of the EBWs is much larger than unity (see section A), even for the higher harmonic, and the medium behaves like a blackbody emitter for EBWs. This radiation, then, converts to ordinary polarization and leaves the plasma. In analogy to Electron Cyclotron Emission (ECE) radiation, the signal originated by B-X-O conversion is called Electron Bernstein Emission (EBE), and is widely used as a temperature diagnostic [91] [92] [93] [94], when the configuration is such that ECE signals are 'hidden' (i.e. when the accessibility regime is over-dense). According to Kirchhoff's law, the radiation which leaves the plasma by back conversion, is a measure of the central plasma temperature [95], being the EBE radiation a strongly localized signal²⁰. This localization, together with the natural non-influencing character of the EBE signal detection, based on B-X-O scheme, makes this kind of measurement more certain than measuring plasma heating through O-X-B mode conversion, since in this last case the proof of the conversion is less direct and the scaling of the energy confinement time with heating power [96]:

$$\tau_E \sim P^{-0.69}$$

has to be considered, leading to a rather uncertain measurement.

3.6 2D Models of O-SX Mode Conversion

Most of the analytical results in the theory for O-X-B mode conversion are obtained in a one-dimensional model (slab geometry), in which density and magnetic field gradients are considered to be parallel. The only spatial inhomogeneity is related to the constant density gradient. All the predictive models on mode conversions, including the ones introduced in

²⁰Considering a 100% efficiency of B-SX back conversion, the EBE signal intensity is then proportional to the central electron temperature, normalized to the SX-O conversion efficiency.

the previous sections, have been derived in such a slab description, despite some of them where analyzed for a realistic sheared magnetic field, like in [97]. During recent years, it has been demonstrated that a slab approximation may be insufficient to describe the O-SX mode conversion in the vicinity of the cutoff plasma density, in real devices. This analysis was initiated at first by H. Weitzner in 2004 [98]. It was demonstrated that in a 2D treatment, able to consider the real variation of the magnetic field on flux surfaces in tokamaks and stellarators, O-SX conversion occurs in a wider range of incident beam parameters, if compared with a 1D case, in which effective transformation takes place only in a precise range (typically narrow) of the parallel refractive indexes. After reference [98] other work was carried out on developing 2D models of O-X conversion, initially based on stronger simplified assumptions on the incident beam structure and magnetic field configuration [99] [100], and later developed with a more realistic approach [101] [102] [103]. Using the Stix representation [104] for the electric field:

$$E_{\pm} = \frac{E_x \pm iE_y}{\sqrt{2}}, \quad E_{\parallel} = E_z$$

already introduced²¹ in Chapter 2, the cold-plasma dielectric tensor in 2.6 can be re-written in the following useful form:

$$\boldsymbol{\varepsilon} \cdot \mathbf{E} = \begin{pmatrix} \varepsilon_+ & 0 & 0 \\ 0 & \varepsilon_- & 0 \\ 0 & 0 & \varepsilon_{\parallel} \end{pmatrix} \begin{pmatrix} E_+ \\ E_- \\ E_{\parallel} \end{pmatrix} \quad (3.40)$$

where:

$$\varepsilon_{\pm} = 1 - \frac{\omega_{pe}^2}{\omega(\omega \pm \omega_{ce})}, \quad \varepsilon_{\parallel} = 1 - \frac{\omega_{pe}^2}{\omega^2}$$

Given the dispersion relation of a cold magnetized plasma in 1D case, re-written in the following form:

$$N_{\perp}^2 [(\varepsilon_+ - \varepsilon_{\parallel})(\varepsilon_- - N^2) + (\varepsilon_- - \varepsilon_{\parallel})(\varepsilon_+ - N^2)] = 2\varepsilon_{\parallel}(\varepsilon_+ - N^2)(\varepsilon_- - N^2),$$

the propagation regions for the O- and SX-waves are separated by a slab evanescent region defined by the condition:

$$\varepsilon_{\parallel}(\varepsilon_+ - N_{\parallel}^2) < 0.$$

The O-SX (SX-O) conversion is explained in the 1D model with a tunneling of the O-mode (SX-mode) through this evanescent layer when the parallel refractive index N_{\parallel} satisfies

²¹With a slightly different normalization.

the conditions described in 3.5.2²², and the tunneling efficiency is given by expressions like the *Mjølhus formula* 3.26.

If the more realistic 2D geometry is considered, the topology is such that the two cutoff surfaces $\varepsilon_{\parallel} = 0$ and $\varepsilon_{+} = N_{\parallel}^2$ are not parallel and intersect in space along a certain line in the plasma, like shown in Figure 3.7. Consequently, no evanescent layer is expected by a beam passing from this intersection. Since the non-parallel nature of the O-mode and X-mode cutoff surfaces is related to the bi-dimensional topology, such an intersection always exists for a certain continuous range of values of the beam N_{\parallel} . It depends from the local parameters in the plasma and a change of N_{\parallel} implies just a spatial shift of the transformation region, which follows the intersection line between the two surfaces, differently from what happens in the 1D description, for which the two parallel cutoff surfaces can coincide just for a single value of the parallel refractive index.

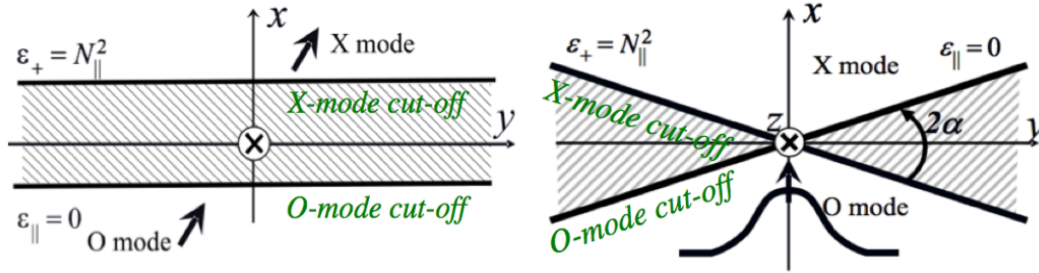


Figure 3.7: O-X transformation region in a 1D slab geometry (on the left), where the plasma density and magnetic field strength both vary along the radial direction of the machine (x -axis). A more realistic 2D geometry (on the right), where the plasma density and magnetic field strength vary in the xy -plane and cross in a certain point. The evanescent regions $\varepsilon_{\parallel}(\varepsilon_{+} - N_{\parallel}^2) < 0$ are dashed. The figure has been taken and modified from [102].

The model developed in references [99] - [103] is based on two flat cutoff surfaces²³ whose intersection forms an homogeneous region. Thus, the 3D tokamak-like geometry is reduced to a bi-dimensionally inhomogeneous problem. A proper coordinate system is introduced in [99], in which the z -axis is parallel to the homogeneous line (intersection between the cutoff surfaces), the y -axis is in the evanescent region delimited by the cutoffs and the

²²Therefore, in the new notations, when the cutoff surfaces $\varepsilon_{\parallel} = 0$ and $\varepsilon_{+} = N_{\parallel}^2$ coincide and the evanescent layer is then absent, giving rise to a complete conversion.

²³Therefore, this model describe adequately the conversion region only in the cases in which the curvature of the flux surfaces can be neglected.

x -axis is located in the propagation region of the left hand polarized waves, directed toward the higher plasma densities along the bisector of the angle 2α between the cutoff surfaces, as showed in Figure 3.7. Formally, the direction of the x -axis is directed along the vector $\nabla\varepsilon_{\parallel}/|\nabla\varepsilon_{\parallel}| + \nabla\varepsilon_{+}/|\nabla\varepsilon_{+}|$, such that the O-SX (SX-O) mode conversion can occur for a beam propagating in the positive (negative) direction along the x -axis. The (x, y) -coordinate origin is fixed on the line of the intersection between the cutoff surfaces for a given N_{\parallel} of the incident beam; in this way, the $x \equiv y = 0$ point coincide with the conditions $\varepsilon_{\parallel} = 0$ and $\varepsilon_{+} = N_{\parallel}^2$.

Two parameters can be introduced, which are:

$$L_{\nabla} = \frac{\sqrt{N_z}}{\sqrt[4]{(2k_0^2|\nabla\varepsilon_{\parallel}||\nabla\varepsilon_{+})}} \xrightarrow{\text{for } L_n \ll L_B} L_{\nabla} \approx \frac{L_n}{\sqrt{k_0 L_n}} \sqrt[4]{\frac{\omega_{ce}}{2\omega}}, \quad (3.41)$$

and the angle α , corresponding to half the angle between the two cutoff surfaces and defined by:

$$\tan(2\alpha) \approx \frac{L_n}{L_B} \frac{\sin\chi}{1 + \frac{\omega_{ce}}{\omega}}, \quad (3.42)$$

where L_n and L_B are respectively the scales of plasma density and magnetic field inhomogeneities in the proximity of the conversion point²⁴, already encountered in equation 3.14, while χ is the angle between plasma density and magnetic field intensity gradients. With a 2D treatment of O-X coupling, it is demonstrated that optimal conversion is foreseen uniquely for Gaussian beams [105] which phase fronts are properly modulated, in both cases in which a poloidal component of the magnetic field is taken into account (in a shearless limit) or neglected. This condition clearly is not easily achievable in practical use, since a plane phase front of the Gaussian beam at the minimum of the waist w (in the present Section the waist $w_{x, y}$ will be written as $\sqrt{2}a_{x, y}$, to preserve the original notation used in the considered model) is generally preferable, or most of the time even inevitable. For this reason it is important to predict the conversion efficiency of an optimal distribution that, outside the region of linear interaction, is a (two-dimensional on (y, z) -plane) Gaussian beam, propagating along the x -axis and with a plane phase front at the minimum waist:

$$A = \exp \left[-\frac{(y - y_0)^2}{2a_y^2} - \frac{z^2}{2a_z^2} + ik_0 N_y y + ik_0 N_z z \right]. \quad (3.43)$$

where $a_y^2 = w_y^2/2$ and $a_z^2 = w_z^2/2$, being w_y and w_z the waist sizes of the beam [105] in y - and z -directions. A detailed treatment of the solutions of passing and reflected

²⁴In a tokamak-like configuration the condition $L_n \ll L_B$ is typically satisfied.

beams at the coupling region, corresponding to an incident distribution given by equation 3.43 and in presence of a small poloidal component of the magnetic field, can be found in reference [102], where an explicit expression for the transformation efficiency $\mathbb{T}_{O-SX, 2D}$ ²⁵ is derived for the case of weak poloidal field limit:

$$\mathbb{T}_{O-SX, 2D}(a_y, a_z) = \frac{a_z \bar{a}_y a_y (1 + \tanh(\pi \tan \alpha))}{\bar{a}_z a_y^2 + a_0^2 \tanh(\pi \tan |\alpha|)} \exp(-\phi), \quad (3.44)$$

where $a_0 = L_\nabla / \sqrt{|\sin \alpha|}$ is the beam width of the optimal distribution, $\exp(-\phi)$ is a factor useful to take into account the degradation of the conversion due to non-optimal aiming of the beam to the transformation region²⁶, and:

$$\bar{a}_y^2 = a_0^2 \frac{a_y^2 + a_0^2 \tanh(\pi \tan |\alpha|)}{a_0^2 + a_y^2 \tanh(\pi \tan |\alpha|)}, \quad \bar{a}_z^2 = a_z^2 + \frac{\sigma^2 a_0^4}{a_y^2 + a_0^2 \coth(\pi \tan |\alpha|)}$$

are the effective width in y - and z -directions of the beam, after passing the transformation region.

The transformation coefficient 3.44 increases monotonically with the increasing of a_z , and becomes unitary only for divergent values of a_z , thus: $\mathbb{T}_{O-SX, 2D}(a_y, a_z) \xrightarrow{a_z \rightarrow \infty} 1$. The function:

$$a_y = \sqrt[4]{a_0^4 + \frac{\sigma^2 a_0^6}{a_z^2} \tanh(\pi \tan |\alpha|)}$$

defines the maxima:

$$\mathbb{T}_{O-SX, 2D}^{max}(a_y) = \frac{a_0^2 \exp(\pi \tan \alpha)}{a_y^2 \cosh(\pi \tan |\alpha|) + a_0^2 \sinh(\pi \tan |\alpha|)}$$

of a_y , for fixed a_z .

In conclusion, a 2D geometry turns out to be more adequate for describing the configurations of real toroidal plasmas and for this reason the results obtained are expected to be more reliable with respect to the one derived in a simpler mono-dimensional slab description. The main results of the model can be summed up as following:

²⁵The transformation efficiency here presented, which represent the ratio of the power fluxes in the converted and incident beams, is the correspondent in 2D model of the *Mjølhus formula* 3.26 for the transmission $\mathbb{T}_{O-SX}(N_y, N_z)$ from O-mode to SX-mode, calculated in a slab description.

²⁶The case $\exp(-\phi) = 1$ denotes the optimal aiming, i.e. when $y_0 = 0$ and $N_y = N_z \tan \vartheta \cos \alpha$, where ϑ is the angle between the magnetic field direction and the z -axis, defined when a poloidal component of the magnetic field is considered.

- O-SX and SX-O Mode Conversions are demonstrated to be locally non-reversible processes. Unlike the 1D case, the power transmission coefficient in opposite directions (i.e. opposite conversions) are shown to be different, also in the simpler case, when the poloidal magnetic field is not considered; the relations:

$$\frac{\mathbb{T}_{O-X}}{\mathbb{T}_{X-O}} = \exp(2\pi \tan \alpha) \quad (3.45)$$

holds true between the different cases above [99]. Since changing the beam propagation in the direction of plasma density increase and decrease; changing the toroidal field sign; inverting the poloidal injection/detection point symmetrically with respect to the equatorial plane; all imply a change of sign of the α angle, these reversal are equivalent from the point of view of power conversion efficiency in two dimensions. The expression 3.45 can be generalized with the following relations:

$$\underbrace{\mathbb{T}_{O-X}(\alpha, k_{\parallel}) \equiv \mathbb{T}_{O-X}(-\alpha, -k_{\parallel}) \equiv \mathbb{T}_{X-O}(\alpha, -k_{\parallel}) \equiv \mathbb{T}_{X-O}(-\alpha, k_{\parallel})}_{\Rightarrow \mathbb{T}_{O-X}(-\alpha, k_{\parallel}) \exp(-2\pi \tan \alpha)}$$

- An incident beam with strictly zero reflection at the conversion region can exist only for $\alpha > 0$ or $\alpha < 0$, for O-X conversion or for X-O conversion respectively. This means that perfect conversion can occur only for a given configuration of beam propagation, magnetic field direction and poloidal launching/receiving point, or (equivalently) for an even reversals of all these three parameters. Odd reversals of them imply a non-optimal conversion, which efficiency is given by 3.45.
- Variations of N_z do not preclude the achievement of the optimal beam structure, despite its variation is accompanied also by a displacement of coordinate. Such variations imply that the optimal distribution becomes $A(x - \Delta x, y - \Delta y, z, N_z + \Delta N_z)$, rather than $A(x, y, z, N_z)$.

3.7 Experiments on O-X-B Mode Conversion

The accessibility limitations due to the O-mode cutoff is as much strong as much the frequency used (and hence the magnetic field), is low. This is particularly true for the most general case of LFS launch, since in this case the RH cutoff prevents the alternative use of X-wave. Therefore, in low field ($B \sim 0.5$ T) spherical tokamaks and medium field ($B \sim 1.5$ T) fusion devices, operational plasma scenarios are often overdense. An empirical

density value can be defined for tokamak-like machines, known as the *Greenwald* density limit [106] [107], which fixes $\langle n_{e,G} = 0.27 \cdot I_p/a^2 \rangle$ as the upper density limit generally reachable in a configuration with plasma radius a and plasma current I_p . These values are taken by using the shaping parameters elongation, triangularity and safety factor q from the standard ITER operation model, i.e. $\kappa = 1.85$, $\delta = 0.5$ and $q_{95} = 3$. The *Greenwald* limit can be hardly ever overcome in common situations. Comparing the accessibility limitations of EC waves for different devices with $n_{e,G}$, it turns out that in spherical tokamaks the low EC harmonics can only access density up to a few percents of the *Greenwald* density limit. Also in medium field machines, like for instance TCV tokamak, at least a 2nd harmonic X2-mode injection is needed to penetrate 10% of $n_{e,G}$ [108], extended to 25% by using the 3rd extraordinary harmonic X3 [109]. EBWH, performed through the O-X-B double mode conversion scheme, was demonstrated for the first time in the W7-AS stellarator [64], by injecting O-waves into a high density high-confinement mode (H-mode) [110] scenario. In particular, in these first experiments, EBWH was demonstrated either in presence of EC resonance in the plasma or in the non-resonant case, i.e. in absence of the EC resonant layer²⁷, at lower central magnetic field. Later, it was applied in other fusion devices. In particular, for the reasons above, in low and medium magnetic field machines, EBW heating can be considered as an alternative way to heat the plasma under certain conditions, and in some cases it can be even the only possible way for using ECRH waves. This is the case of the RFX-mod reversed field pinch device [111]. The theoretical analysis performed to study the feasibility of ECRH applications in this device showed that in this case the O-X-B mode conversion scheme turns out to be the only possible way to heat RFX-mod plasma using EC-waves. In addition, finally, the use of EBWs can be very attractive, since EBWCD is demonstrated to be potentially more efficient than ECCD [70] [112] [113].

²⁷EBWs are generally absorbed in correspondence of the EC harmonics resonances. The non-resonant absorption is possible since they experience a cutoff layer at the UHR surface, which, in the non-resonant case, totally encloses the inner plasma. Therefore, radiation turns out to be trapped inside the plasma. The EBWs are either reflected at the UHR or back-converted to SX-waves. Such a SX-mode is then converted again to the EBWs at its next contact with the UHR. Only the X-polarized radiation reaching the small angular window for X-O conversion can escape the plasma. In the absence of EC resonance in the plasma the EBWs may be absorbed due to finite plasma conductivity after some reflections at the UHR layer.

3.7.1 EBWH Experiments in TCV via O-X-B Mode Conversion

The sole application of Electron Bernstein Waves Heating that was performed by O-X-B double mode conversion in an over-dense plasma of a standard aspect-ratio tokamak, was demonstrated in 2005 in the TCV tokamak [114] (aspect ratio =3.6), making use of the naturally generated steep density gradient that can be reproduced in this device. The proper density scale length L_n , needed for the O-X coupling to take place, was obtained in the H-mode plasma. The 2nd harmonic O-mode EC system featured by TCV was used to obtain O-X conversion at the O2-mode cutoff layer ($n_{e, cutoff} = 8.7 \cdot 10^{19} \text{ m}^{-3}$). The power absorption was measured using three diagnostics. EC power, scattered inside the torus,

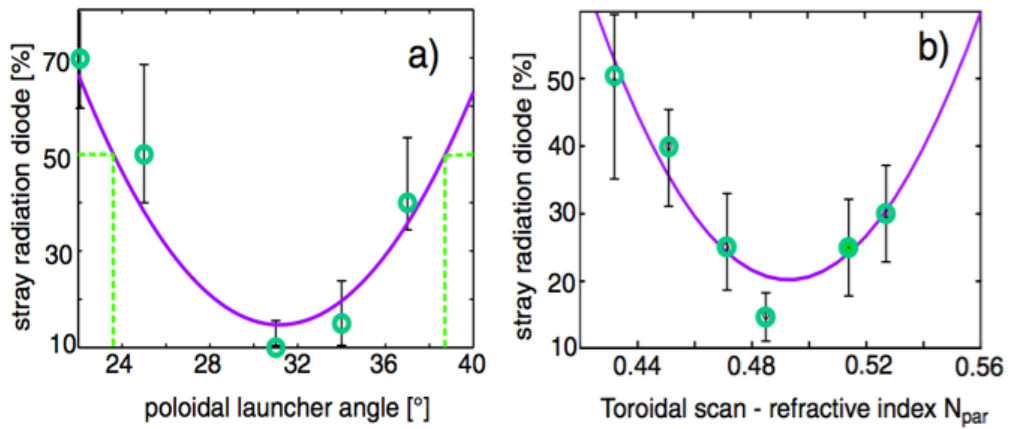


Figure 3.8: Normalized stray radiation power measured in TCV in a poloidal scan with the gyrotron (left), at fixed toroidal angle, and in a toroidal scan (right), at fixed poloidal angle. The dashed lines indicates the 50% of the maximum stray level. A minimum in the stray radiation level is found in both cases.

was measured by a few semiconductor diodes, installed in different sectors of the machine. The total absorbed power was measured by a diamagnetic loop, using power modulation techniques. Finally, the local deposition was measured with a high spatial resolution, 64 channels, soft x-ray wire chamber, vertically interfaced to the plasma and sensitive in the 2-25 keV range [108]. The stray power, measured during the short EC pulses (see Figure 3.8), was strongly influenced by Edge Localized Mode (ELM) dominated phases, ranging from 30%, during the ELM-free phases, to 80%, during the ELM phases. The reduced density scale length L_n at the plasma cutoff, which implies steep density gradient, was reached in the edge pedestal of H-mode plasmas with low $q_{95} = 2.2-2.4$, high triangularity $\delta = 0.5-0.6$

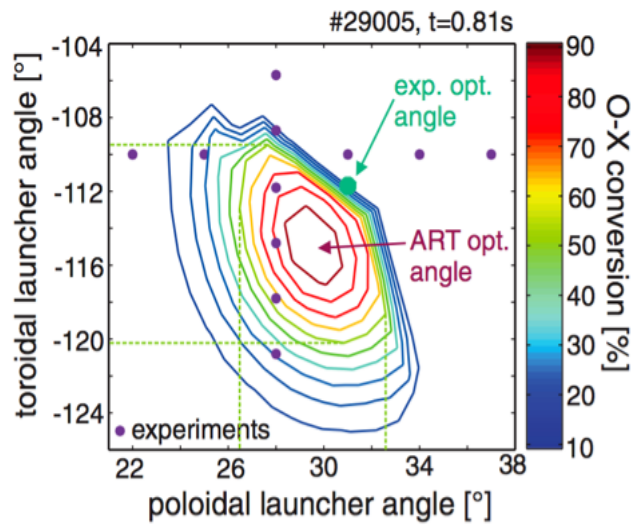


Figure 3.9: In this figure, the dots, representing the experimental measure of the stray radiation in the TCV camera during the EC scans are compared with the results on the conversion efficiency obtained using simulations.

and medium elongation $\kappa = 1.8$ [108]. The experimental determination of the optimum injection angle was performed by scans performed on the two poloidal and toroidal injection angles around the optimal window, previously estimated using a single ray simulation of the non-relativistic *ART* ray tracing code [115] [116], which includes O-X-B double mode conversion for wave propagation and absorption (see Figure 3.9). The angular scan, performed shot by shot, has been aimed to find a minimum level of stray radiation²⁸, which corresponds to the maximum of power absorption and thus defines the optimal launching angles. A good agreement between the theoretical and experimental radial deposition at overdense plasma regions was reached. These results constitutes the first proof of EBWH by O-X-B mechanism, acting in a standard aspect-ratio tokamak. For a detailed description of such experiments in TCV tokamak see references [117] [118] [119] [108].

²⁸In general, the experimental 50% absorption widths is larger than the one predicted using a single ray simulation (of a factor two, in the case of TCV). The reason of this lies in the fact that any injected beam is always characterized by having a finite dimension and a k -spectrum dispersion. Both these things are not taken into account by a single-ray tracing. These factors imply a broadening of the conversion efficiency function, while reducing its absolute value. Therefore, the condition $\mathbb{T}_{O-X} = 1$ can never be reached in the real case, while the 50% of power conversion (i.e. $\mathbb{T}_{O-X} = 0.5$) is expected to be reached in a larger window than the one calculated with the single-ray tracing.

Chapter 4

The Optimal Plasma Target for O-SX Coupling

4.1 Introduction

The feasibility study of EBW heating in FTU plasma at 140 GHz, the preparation of future experiments on this issue and the research of the proper plasma target to be used, are the core subjects of the present PhD Thesis.

After a brief description of the Liquid Lithium Limiter (LLL) recently installed in FTU, the high density plasma regimes reachable with the use of LLL and the interferometer used for the plasma density measurements in FTU (respectively in Sections 4.2.1, 4.2.2 and 4.2.3), together with the work aimed to the search of an optimal target for future experiments on O-X-B mode conversion are being presented here below in this Chapter. The predictive study of this phenomenon in FTU and the technical preparation of the future experiments will be presented in the next two Chapters 5 and 6.

4.2 The High Density in FTU

4.2.1 The Liquid Lithium Limiter

Since 2005, lithium has been routinely introduced in the FTU tokamak, as a new plasma facing component by means of a Liquid Lithium Limiter (LLL) [120] (Figure 4.1), in addition to the original two limiters (toroidal and poloidal) both made with TZM, an alloy of Titanium, Zirconium and 98% of Molybdenum. The main motivation for the use

of a liquid material is the interest in testing new plasma facing components, in view of future fusion reactors. Most of these new materials are alternative to the Carbon Fiber Composite and Tungsten and are promising, despite they also have technical problems still to be understood. The lithium limiter of FTU is based on the innovative concept of a

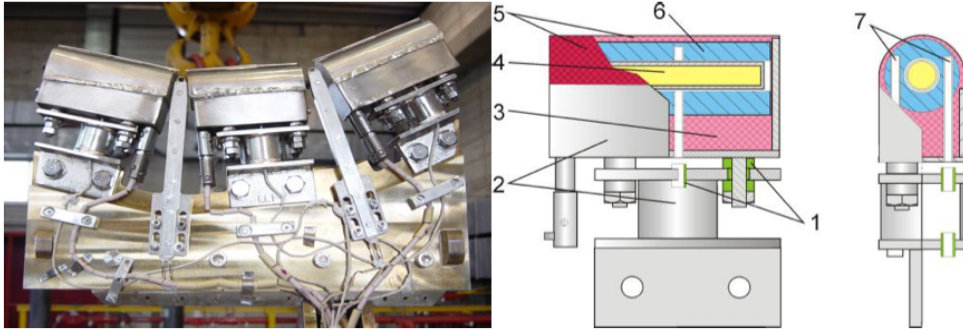


Figure 4.1: On the left, picture of the three units of the lithium limiter installed on their supporting structure. On the right, the following components of the LLL are showed: 1) ceramic break, 2) stainless steel case, 3)lithium filled-capillary structure, 4) heater, 5) Li evaporating surface 6) Mo heat accumulator, 7) thermocouples (figure taken from [121]).

Capillary Porous System (CPS) [122]. It is composed by three similar modules, separated one from each other, and electrically insulated. Two of the modules are based on the capillary surface tension that counteracts the electromagnetic $J \times B$ tearing-off forces and are made as a mat from wire meshes of *AISI 304* stainless steel with $15 \mu\text{m}$ pore radius and $30 \mu\text{m}$ wire diameter. In the third one the stainless steel wires has been replaced by tungsten ones. After the change to tungsten, the overall structure of the LLL is able to withstand heat load up to $5 \text{ MW} / \text{m}^2$ without significant damages¹. To extend the operations with LLL over $5 \text{ MW} / \text{m}^2$, a second step project is already under study, with the use of LH and ECRH as additional plasma heatings [122]. The overall system will also include an actively cooled system and a liquid lithium circuit for the renewal of the lithium surface, since increasing heat load over a certain limit means to overcome the critical temperature $T = 550^\circ$ of evaporation of lithium. The surface facing the plasma is re-filled through capillary forces by a liquid lithium reservoir, placed on the bottom of the structure [123].

¹Thermal gradients do not give rise to stresses in the lithium filled CPS and consequently no thermal induced cracking occurs, unlike the conventional solid materials.

4.2.2 New Plasma Regimes with LLL

Lithization of the machine inner wall, obtained with the insertion of the CPS LLL into the machine, leads to a strong reduction of heavy impurities and oxygen concentration in the plasma as well as a strong modification of particle recycling from the walls, due to a demonstrated pumping effect of lithium [124]. This implies better plasma performance than with the usual boron coating on the vessel walls [125] [121] [124], with direct consequences on plasma parameters, like Z_{eff} , which in ohmic discharges maintains a level well below 2 for high normalized² line electron density ranging between $0.15 \cdot 10^{20} \text{ m}^{-3} < n_e < 3 \cdot 10^{20} \text{ m}^{-3}$ (only in some cases at low densities $n_e < 4.0 \cdot 10^{19} \text{ m}^{-3}$, Z_{eff} seems to increase up to a factor 2). The radiation losses are then lower than 30 % of the input power and electron temperature in the SOL a factor > 1.5 higher than for discharges in boronized or fully metallic regimes. For these reasons, very interesting and unusual plasma regimes have

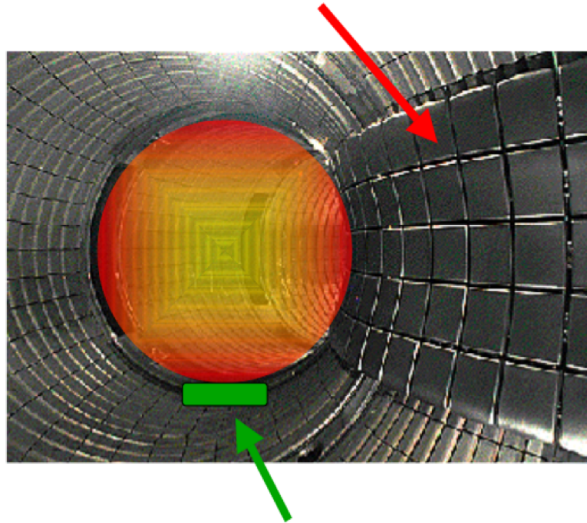


Figure 4.2: Picture of the internal side of the FTU vessel, taken from [126]. The red arrow indicates the position of the toroidal limiter, the green one show where the Liquid Lithium Limiter is inserted in the camera (only when used).

been obtained in FTU with the use of lithium during the last experimental campaigns. In particular, a strong peaking of the electron density profiles has been routinely reached.

²Usually, the integrated line density data acquired by the FTU interferometers [25] are used in a normalized form, where the normalization factor is the maximum plasma diameter, equivalent to 0.6 m. This means that integrated measures that should be measured in $[\text{m}^{-2}]$ are presented in $[\text{m}^{-3}]$.

This is true, in principle, with the use of both boron and lithium. Nevertheless, with lithium this happens at very high densities (line density $n_e > 1.0 \cdot 10^{20} \text{ m}^{-3}$). A strong steepening at normalized minor radius $r/a = 0.8$ is found, with a marked increase of the central density, while the peripheral density for $r/a > 0.8$ tends to remain nearly constant. Peaking factors $n_{e,0}/n_e$ up to 2.5 are obtained, typically when the line density n_e is greater than $1.0 \cdot 10^{20} \text{ m}^{-3}$. A strong activity of MARFE³ radiative instability [127], [128] inside the last closed surface⁴ is very often present. This regime is characterized by almost total absence of MHD activity at the plasma edge, thanks to the strong pumping capability of lithium, which suppresses the recycling of cold particles from the walls.

4.2.3 Plasma Density Measurements in FTU

The measurement of the plasma density is very important for this work. In FTU it is performed with the use of laser interferometers, starting from the measured change of the refraction index along the path of a laser beam, which crosses the plasma along a chord. The variation of the refractive index depends on the density of the plasma encountered by the beam; the phase change of the beam crossing the plasma with respect to a reference beam provides a measure of the line integrated density.

A scanning system (called *SIRIO*, represented in Figure 4.3), is used in FTU [129] [25] for this kind of measures. The system is an assemblage of five interferometers, among which two are scanning and three operate at fixed chords. *SIRIO* is located in a vertical port of the machine, which is 40 cm wide in the radial direction. From such an aperture, the FTU plasma can be scanned with the laser from the very edge, in the low field side, to 1/3 of the plasma radius, in the high field side. The port is mechanically divided into two sectors, each housing the beams of a 10W, CO₂ and a 1W, CO interferometers. The scanning ranges reached from these two sectors of the port are 0.86 - 1.04 m and 1.07 - 1.25 m of the major radius of the tokamak. The CO₂ interferometer is used to perform the line integrated density measurement, while the CO laser beam is used in order to compensate the mechanical vibrations of the overall system. The two colors used by the

³The term 'MARFE' is an acronym for '*Multifaceted Asymmetric Radiation From the Edge*'. This kind of instability defines a toroidally symmetric and poloidally asymmetric belt of high density, strongly radiating, cold plasma, localized at the high field side of a limiter tokamak, sometimes even extending all around the poloidal cross-section, thus detaching plasma from the first wall. It is caused by a reduction of the parallel thermal conductivity at the plasma edge, caused by a drop of the edge temperature.

⁴In FTU, MARFE instability develops especially in presence of low Z impurities, like lithium or boron.

CO₂ and CO lasers correspond respectively to wavelength of 10.6 μm and 5.4 μm . In order

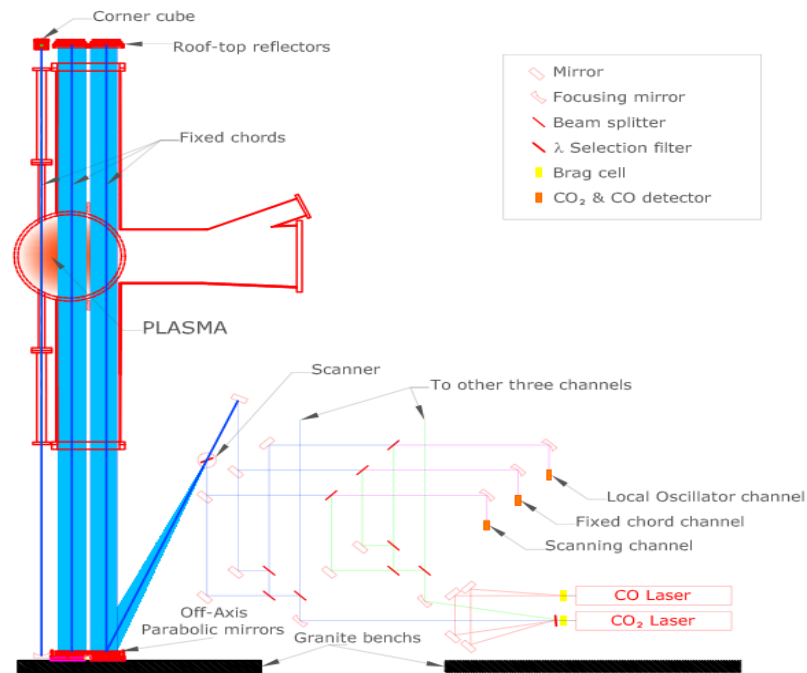


Figure 4.3: Sketch of the scanning interferometer of FTU. It can be seen that the two scanning interferometers are capable to cover 2/3 of the plasma diameter.

to use a single-photoconductive detector for the heterodyne detection of both the signals, two *Bragg cells* were included in the system. Two colors are combined by a dichroic mirror and modulated by means of the two *Bragg cells*, with different frequency shifts, corresponding to 40 MHz for the CO₂ and 30 MHz for the CO beam. At the end, the signals are electronically split. A fast tilting mirror, whose dimensions are 6 mm \times 4 mm and oscillating with a 8 kHz frequency in the focus of a second parabolic mirror, provide the production of the two vertical scanning beams and a measure of a density profile every 62.5 μs (16 kHz), which is a time short enough for most of the plasma phenomena. The spatial resolution of the interferometer is fixed by the beam width (which is approximately 1 cm in the plasma), since the number of independent line-average density data depends on the ratio between the scan amplitude and the beam diameter. Thus, the number of equivalent chords in FTU typically varies from 28 to 34, depending on the scan amplitude in use.

After the injection, each beam is then back-reflected to the launching point. A second

passage through the same optics allows the use of a single fixed detection line, with a typical detection noise of about $2 \times 10^{18} \text{ m}^{-2}$.

In addition to the scanning interferometers, three fixed chords of *SIRIO* are fixed at 0.755 m, 0.935 m (corresponding to the vessel center) and 1.17 m from the axis of the tokamak. Two additional measurements on fixed chords are provided by a CO_2 - HeNe lasers beam interferometer, with wavelengths respectively of $10.6 \mu\text{m}$ and $0.63 \mu\text{m}$. The radial positions of these two chords are again 0.935 m (camera center) and 1.135 m from the device axis. In FTU, the measurements performed at fixed positions, that can be acquired at frequencies up to 200 kHz, are typically used for the automatic plasma density control in feedback and for the density monitor.

Inversion methods are used to obtain the local density profile assuming the density as a function of the poloidal magnetic flux coordinate [130]. Most of the inverted density profiles are obtained using an expansion in polynomials, with known transform functions, while the data coordinates are transformed from radial to flux, and the inversion is reduced to a fitting operation. In other cases, a more accurate *Abel* inversion algorithm is also used to produce density profiles, in a real geometry, by using the line integrated density data without any fit. A particular approach was developed for the proper inversion of the density profiles, when the MARFE activity is so strong that oscillations turn out to be super-imposed on the detected interferometric line density signal to be inverted. This had to be done since such a disturbance in the line density channels can strongly compromise the correctness of the inversion computation. More details on the techniques used in such plasma regimes can be found in reference [126].

4.2.4 Overdense Plasmas in FTU

The availability of these particular regimes in FTU, became a stimulus for a deeper analysis of the high density plasma discharges. FTU is not only one of the tokamaks featuring the highest plasma densities reachable today, but also it can reach the highest values of the toroidal magnetic fields, up to 8 T. Thus, studies on plasma confinement and stability of magnetic configurations can be carried out, in wide ranges of B , n_e and plasma currents. In particular, since the first uses of lithium, the inverted electron density profiles showed maxima well beyond the value $n_e = 2.43 \cdot 10^{20} \text{ m}^{-3}$ (see an example in Figure 4.4), corresponding to the O1-mode cutoff density of the 140 GHz ECRH system of FTU, and with such a density level routinely reached, called 'overdense' regimes, from the point of

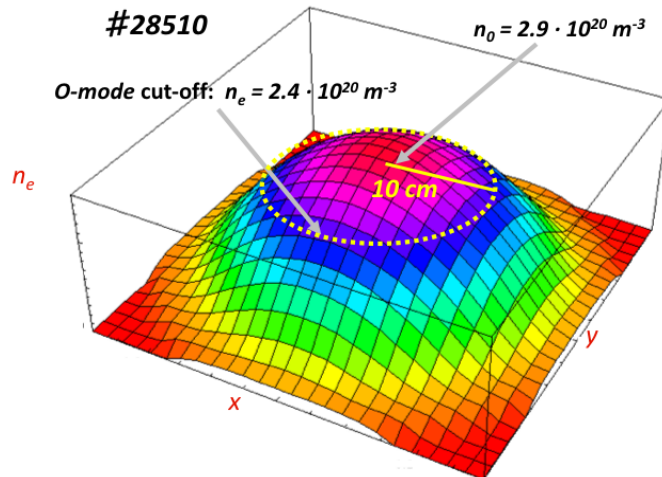


Figure 4.4: 3D reconstruction of a typical inverted high density profile of FTU (shot #28510). The radius where the O-mode cutoff density is overcome is shown. When the plasma density is high, such radius is typically in the range 10-15 cm from plasma center.

view of the EC heating. Plasma regions interdicted to both O- and X-mode launched from LFS, can be obtained by a strong gas puffing and lithization of the internal vessel walls. These new regimes, which characterize strongly FTU in the panorama of the present fusion machines, open the possibility to future experiments on overdense plasmas heating with Electron Bernstein Waves.

At the frequency used by the ECRH system of FTU, the FX-SX coupling obtained with the tunneling of a FX-wave launched from LFS through the evanescent region between the LFS cutoff of the X-mode and the UH layer could not be performed, since the tunneling efficiency, described by the formulae 3.13 and 3.14 presented in Chapter 3, turns out to be null with the FTU parameters. Such a result could be expected, since the tunneling of the evanescent region by part of a FX-wave from LFS (or vice-versa of a SX-wave towards the LFS), is finite only when the magnetic field, the density and the wave frequency are such that the wavelength is of the same order of magnitude, or larger, than the evanescent layer depth. This condition is more likely to be satisfied in low magnetic field devices, where a low frequency of the EC system is used. In the case of FTU, instead, the frequency is very high, with an associated wavelength in vacuum of approximately 2 mm, while the order of magnitude of the evanescent layer are centimeters.

The direct SX-B coupling, with a launch of the X-mode from HFS can not be taken into

consideration for obvious reasons, since the launching system of FTU is installed on the LFS of the vessel and no space is available on the HFS for optical components able to change the polarization and the direction of the beam, due to the presence of the toroidal limiter.

Thus, the interest in demonstrating overdense plasma heating in FTU with the use of EBWs led to develop a predictive model of the O-X-B mode conversion scheme, presented in Section 3.5, to excite Electron Bernstein Waves in the overdense plasma. In particular, since the losses caused by SX-FX coupling are expected to be approximately null with FTU parameters, the efficiency of the overall O-X-B scheme is almost completely given by the efficiency of the first O-(S)X conversion. Thus, the presence of the O1-mode cutoff of the 140 GHz ECR heating system, is a necessary condition in view to test the O-SX coupling, described in details in Section 3.5.2.

4.3 Research of the Optimal Plasma Target for EBWH

The very high density regimes obtained initially with the use of LLL (see for instance the density profile in Figure 4.5 and 4.6) were reached at 500 kA plasma current and 5.9 T magnetic field, which represents a standard operational configuration for FTU. The 1st harmonic resonance of the 140 GHz frequency of the ECRH system corresponds to plasma regions where the magnetic field is 5 T (this is true, at least, to a first approximation, when relativistic corrections are neglected and for perpendicular propagation with respect to the magnetic field). This means that a configuration with 5 T central toroidal magnetic field is such that the 1st harmonic of the EC resonance occurs in correspondence of the vessel center. For a different toroidal magnetic field, such 1st harmonic 'shifts' back or forward, accordingly to the approximate $1/R$ scaling of the magnetic field in a toroidal magnetic configuration, where R is the major radius of the torus. The simple relation $B_0 R_0 = B(R)R$ holds true between the central magnetic field B_0 at the major radius of the torus R_0 and the value of the field $B(R)$ at the generic radius R . In the case of FTU, when the central magnetic field B_0 is 5.9 T, the EC resonant layer corresponds to peripheral regions of the plasma. Applying the formula above, the resonance turns out to be approximately at 17 cm from the center of the camera. Such a high field is not relevant (generally) for the use of ECRH, since power deposition is usually needed in more central regions of the plasma. Nevertheless, the preliminary results obtained with 5.9 T central

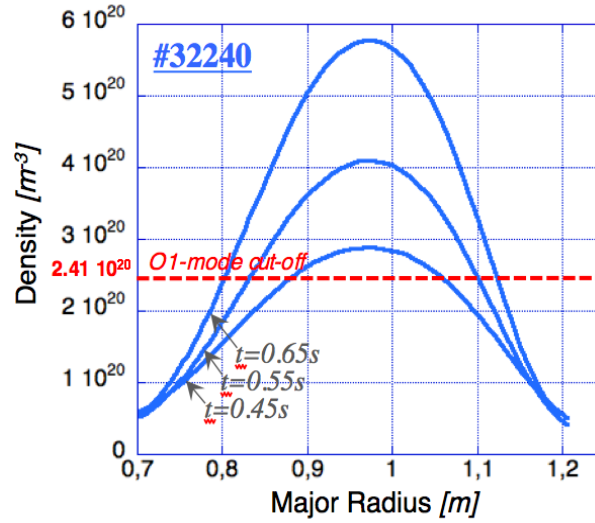


Figure 4.5: Inverted density profile of shot #32240 at three different times. The inversion of the profile (plasma axis and magnetic surfaces) is calculated on the magnetic equilibrium of the discharge. The density value corresponding to the O1-mode cutoff is indicated with the red line.

magnetic field were precious for a preliminary analysis of the FTU high density plasma discharges, in view of the use of EC waves.

The primary evidence, that was immediately found with the use of the Lithium Limiter, was that the operational *Greenwald* density limit [106] [107], here reported in an approximate form:

$$n_{e,G}[10^{20}m^{-3}] = \frac{I_p[MA]}{\pi a^2[m^2]}, \quad (4.1)$$

already cited in Chapter 3, could be routinely exceeded at 5.9 T, 500 kA, in strongly lithized discharges. The quantity a in the expression 4.1 is the minor radius of the torus. The *Greenwald* density limit is an operational limit generally found in magnetic confinement devices, especially in tokamak and Reverse Field Pinches. The physical mechanism acting under this operational threshold has not been understood deeply, so far, but it is demonstrated with experiments that generally exceeding the *Greenwald* limit leads to a disruption and loss of the plasma, in tokamak-like devices⁵.

Given the typical FTU parameters, the *Greenwald* threshold, which represents a limit on the integrated line density profile, corresponds, when the density profile is inverted, to a

⁵Typically, only stellarator devices, not provided of inductive plasma current, can cross the *Greenwald* limit.

density which in general is even higher than the $2.4 \cdot 10^{20} \text{ m}^{-3}$, needed to form an overdense central plasma region on which to test EBWH. Nevertheless, the overcoming of this limit opens the possibility to obtain more suitable plasma parameters for the conversion of the launched O-wave into the SX-wave. The plasma density in FTU is pre-defined program-

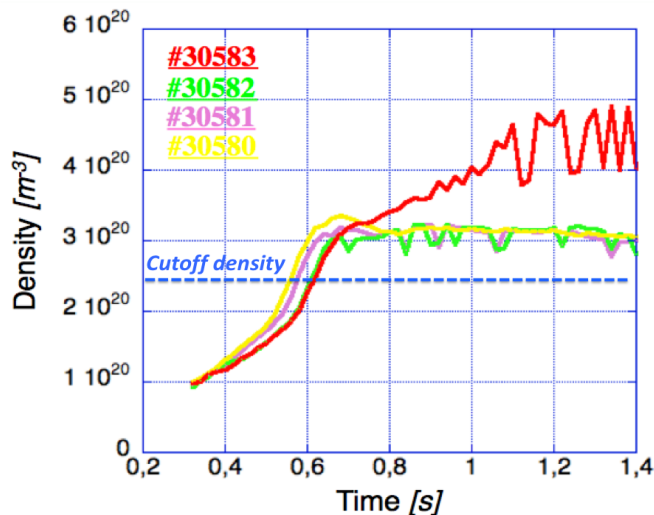


Figure 4.6: Central density values of some discharges performed using the LLL, with $B_0 = 5.9 \text{ T}$ and $I_p = 500 \text{ kA}$, versus time. The density value typically corresponding to the appearing of the O-mode cutoff in the inverted density profiles (considering the typical plasma radius of FTU) is marked. It is evident that this value is overcome by the peak density of the considered discharges.

ming the opening of apposite gas injection valves. This operation can be performed either manually or using a feedback control, which automatically refer to a pre-programmed density profile; sometimes these two regulations are used together, for a more precise control. However, the resulting plasma density is strongly affected also by other independent factors, in addition to the gas puffing, like the wall conditioning and the level of recycling or sputtering at the plasma boundary. Thus, the fine regulation of the density is generally a difficult operation. In particular, this is true when high density plasma operations are being carried out with the use of LLL, since the influence of lithium (and in general of 'light' impurities, like boron) on the regime is very strong.

The *Greenwald* limit calculated for typical values of the FTU plasma minor radius⁶, with a standard 500 kA plasma current, is typically in the range $1.8 \cdot 10^{20} \text{ m}^{-3} \leq n_{e,G} \leq 2.0 \cdot 10^{20}$

⁶The mean plasma radius in FTU is 28/29 cm, if no particular shrink or elongations are forced with external magnetic fields.

m^{-3} . The critical O-mode cutoff density in the inverted profiles, instead, appears in the central region when the normalized line density is around $\approx 1.6 \cdot 10^{20} \text{ m}^{-3}$, hence at density not too lower than $n_{e,G}$. The possibility to rise the density at very high limits offers a larger operating region in the research of a stable overdense regime, since the fine regulation of the density between the cutoff density (lower limit) and the *Greenwald* threshold (upper limit) would be more difficult.

Another reason for pushing the density at the highest levels is the increase of the local

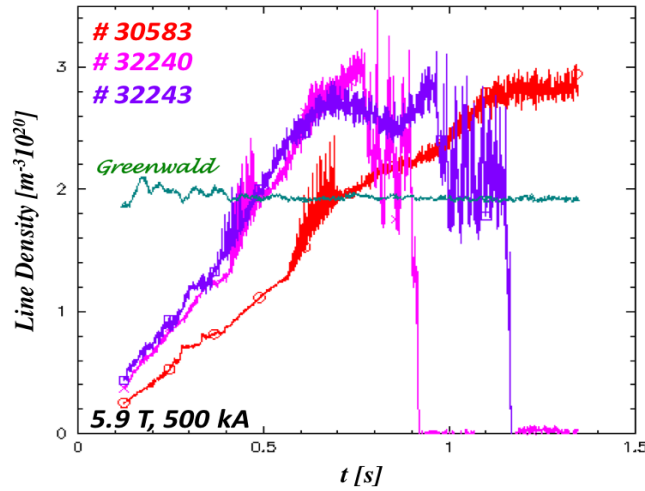


Figure 4.7: Normalized integrated line density profiles of three discharges performed at 5.9 T, 500 kA, measured by the central chord of the *SIRIO* interferometer [25], installed in FTU. Since in the three discharges the plasma currents and the magnetic equilibria are approximately the same, the *Greenwald* limit of one discharge (#30583), in green, is representative also for the others. It is evident that the *Greenwald* limit is extensively overcome at 5.9 T of the magnetic field.

density scale length parameter $L_n = n/\partial n/\partial x$, introduced in the expression 3.26, which defines the power transmission efficiency from O-mode to SX-mode, in a slab description. Equation 3.26 clearly suggests that a small density scale length (namely, a steep profile slope of the density at cutoff) is beneficial for power transmission. In general, the normalized density scale length $k_0 L_n$ is more significant, since O-X conversion is strongly influenced by the frequency. For typical parameters of FTU this quantity is particularly high, in the range $200 \leq k_0 L_n \leq 500$. The analytical form of the 3.26 shows the exponential decay of the transmission power, when $N_z \neq N_{z,opt}$ and $N_y \neq 0$, with $k_0 L_n$. In this contest of narrow operational range of launching angles, big effort was spent on

the research of stable FTU discharges characterized by steep profiles and high density gradients.

4.3.1 Experimental Activity Dedicated to the Density Limit in view of the O-X-B Heating

During last campaigns, part of the experimental work for this Thesis has been the study of the high density regimes, at magnetic fields different from the 5.9 T initially used to perform the first operations with LLL, and at different plasma currents. The aim of the experiments was to test high densities at magnetic field lower than the 5.9 T, to obtain a more centered ECR scenario. The validation of the correct procedures useful to obtain the stable plasma target with different parameters is important, either from the operational point of view or to perform reliable predictions and hence to plan O-X-B experiments in the correct way. The natural choice of the parameters for such experiments was a standard current of 500 kA and a central magnetic field of 5.2 T. This field is such that the EC resonance at 5 T corresponds with the plasma center, which in FTU is generally between 3 cm and 4.5 cm (96.5/98 cm of the major radius) from the center of the camera (at 93.5 cm). Nevertheless, lower magnetic fields enable the reach of a perfect O-SX mode conversion at the cutoff with a lower value of the beam N_{\parallel} with respect to the field⁷. This point is important, as well, since the highest is the request for N_{\parallel} in order to obtain conversion the more oblique must be the injection of the beam from the launcher into the plasma. Very oblique injections can generate difficulties, like a stronger deformation of the beam, caused by diffraction, and stronger interactions with the port side walls. In addition, injection obliqueness can imply less mode purity of the launched wave, when the polarization is not properly controlled. Therefore, also lower magnetic fields were tested in high density plasma discharges during the last campaigns in FTU. When the magnetic field is lower the resonant layer is displaced from the plasma center, this time in the HFS peripheral regions. A lower limit of 4.8 T for the central magnetic field was chosen, to test configurations with the internal absorption of EBWs, while 5.5 T was selected as the maximum field of interest. The choice of the magnetic fields had to be carried out by considering, case to case, the mutual positions of the resonant layer and the radial position of the cutoff layer in the density profiles, where the O-X mode conversion can occur. While

⁷The quantity $Y/Y + 1$, in fact, decrease (increase) with the reduction (rise) of the central magnetic field.

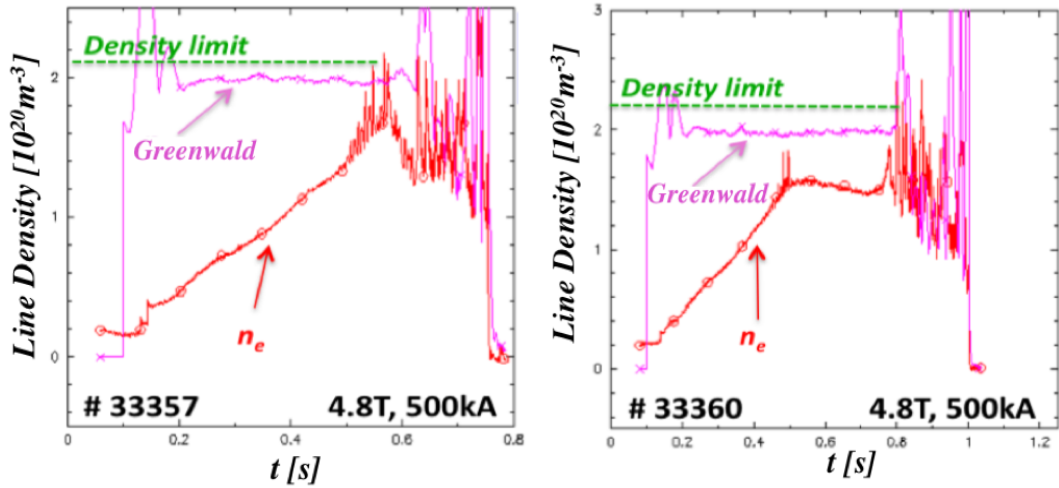


Figure 4.8: Density limit (green dashed line) found with a programmed density ramp-up (in red), until the disruption of the plasma occurs. In both the discharges taken as example, performed at 4.8 T, 500 kA, the density limit is found around $2.2 \cdot 10^{20} \text{ m}^{-3}$ line integrated density, normalized to the mean minor plasma radius (0.3 m). The oscillations in the density measurement that start around 0.5 s in both shots, indicate the presence of the MARFE instability. The light purple lines indicate the *Greenwald* limit versus time, calculated with the real-time measurements of plasma current and (major and minor) plasma radius.

the first information can be calculated a priori, the second one could be found only with the experiments, with an accurate analysis of the density profiles found at different fields. At first, some discharges has been performed with the use of LLL, aimed to find the density limit at 4.8 T, 500 kA. In these shots, a controlled density ramp-up was performed to find the density limit as the one at which the plasma disrupts (Figure 4.8, on the left). Such a limit was found near $2.2 \cdot 10^{20} \text{ m}^{-3}$ of the normalized line density signal. Subsequently, a stable density plateau was found (Figure 4.8, on the right), at 4.8 T, 500 kA, at a 'safe' value of the density, below the density limit found before. The calculation of the inverted density profiles, corresponding to the density plateau in Figure 4.9, shows that the peak central density is near the critical density $2.4 \cdot 10^{20} \text{ m}^{-3}$ of cutoff, but no stable overdense plasma region forms at the center, not allowing to obtain the proper plasma target for O-X-B experiments. From Figure 4.8, it can be noticed that the density limit found at 4.8 T is in the proximity of the threshold off the *Greenwald* limit, differently from what happens for 5.9 T, in which case the *Greenwald* limit is abundantly overcome, in lithized discharges, like shown in Figure 4.7. Similar experiments were performed at

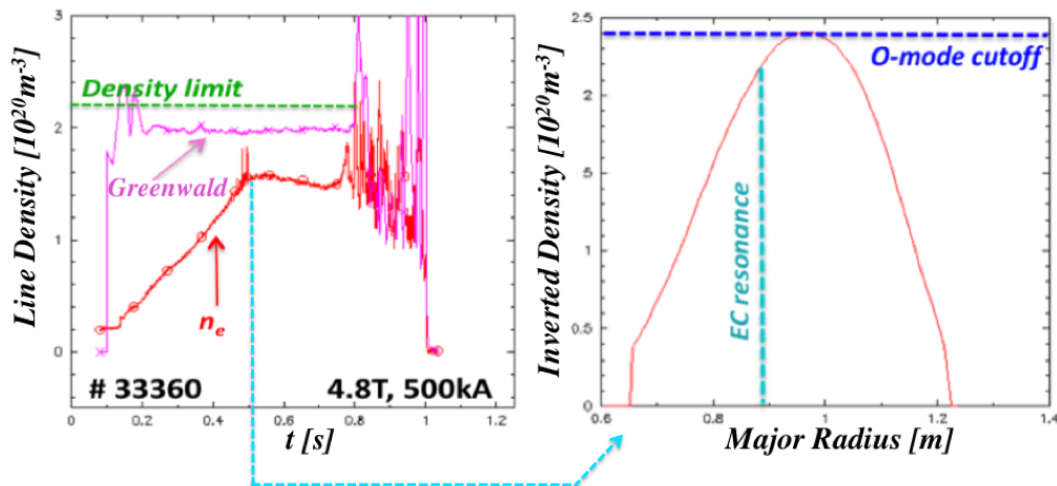


Figure 4.9: The inversion of the density profile performed on the magnetic equilibrium when the discharge is stable (at 0.5 s, in the example), put on the right, shows that the O-mode cutoff is reached just by the central peak density, but no overdense regions creates, in particular around the layer of the 1st harmonic EC resonance. Thus, staying at the results that could be obtained so far, the configurations with 4.8 T of the magnetic field can not be considered for the experiments on overdense plasma heating.

5.2 T magnetic field, with two different plasma currents of 500 kA and 700 kA.

With analogy with what has been done in the case of 4.8 T, also for 5.2 T the density limit was experimentally searched, first. Also in this case, a density ramp-up was programmed, with the two plasma currents and using the setup of gas puffing already tested with the other fields, to allow a direct comparison between the shots. Different density plateaus in the line density, at increasing density values step by step, have been performed in the plasma at 500 kA of the current, with the same ramp slope, until the disruption caused by density limit of shot #33719. The same limit has been then found with repetition, in other discharges with 500 kA of the current. The limit found with this approach almost coincide⁸ with the one found in 2009 in a single dedicated shot #32400 (see Figure 4.10), where a similar density ramp-up was performed and only a different conditioning of the FTU camera could affect the result. In both cases, with 5.2 T field, the limit turns out to be higher than in the case of 4.8 T. It occurs near $3.0 \cdot 10^{19} \text{ m}^{-3}$ over the *Greenwald* limit, giving rise to an operational range for the regulation of the density that enables

⁸For less than $\approx 1.0 \cdot 10^{19} \text{ m}^{-3}$ in the line density, probably given by the different conditioning of the machine.

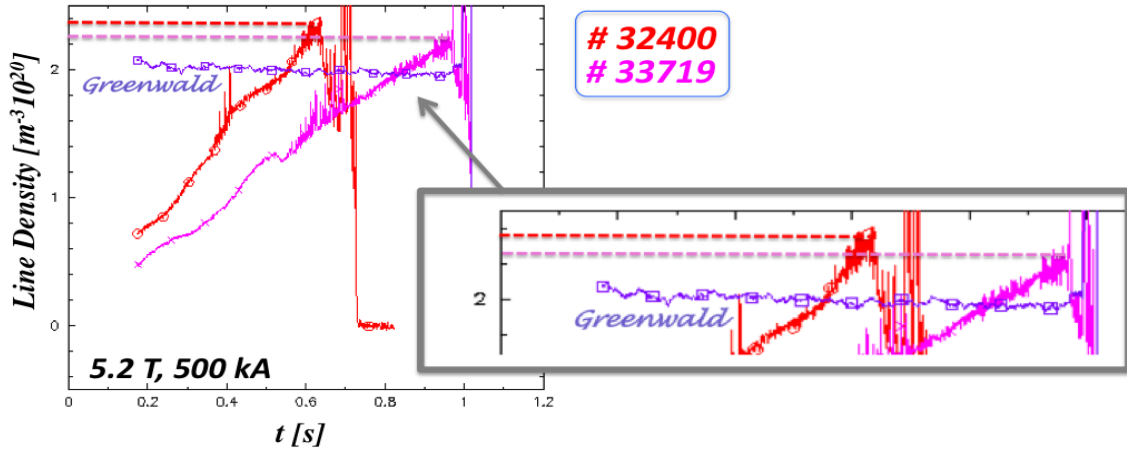


Figure 4.10: Density limits found in shot #33719 (light purple), performed in 2010 campaign, and in shot #32400 (red), performed in 2009, both at 5.2 T, 500 kA. The two limits seem to be slightly different. The reason for that probably lies in the different conditioning of the machine, which implies non-identical plasma conditions. As better shown in the zoomed area of the picture (on the right), the difference between the two limits is $\approx 1.0 \cdot 10^{19} \text{ m}^{-3}$ in the line density signal. The *Greenwald* limit for the two 500 kA currents, calculated in real-time, is also shown (dark purple line).

the formation of an overdense central plasma region, surrounding the EC resonance, while keeping a safe margin with respect to the density limit allowed at 5.2 T. The research of the density limit was carried out then for higher values of B_0 , selected in the range of the relevant fields for the use of EC, and led to the choice of 5.5 T as the highest field to be tested. In principle, the reason why a higher field is interesting, despite this implies also stronger requests in the injection of the wave, lies in the fact that a higher magnetic field is expected, in general, to allow a higher peak density. This would likely implies also a steeper density profile at cutoff, that is beneficial for the O-X power transmission. Such a result should be expected, in general, in toroidal confined plasmas [131]. Experimental evidences from the last campaigns of FTU, in fact, typically show a link between the value of central field and the maximum density limit that can be reached. Nevertheless, in practice, this was not the case for the density limit found at 5.5 T, 500 kA, that is shown in Figure 4.11. The limit that could be reached turns out to be around $2.3 \cdot 10^{20} \text{ m}^{-3}$ of the normalized line density, which is the same found in the case of $B_0 = 5.2 \text{ T}$. Deeper analysis is being dedicated to the density limit at this field in the next campaigns. Different

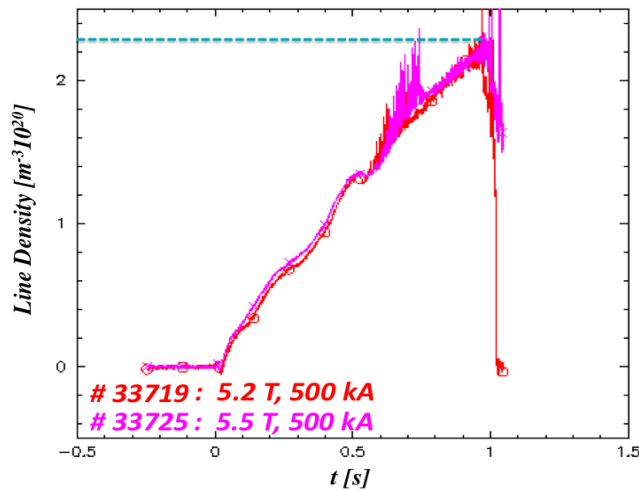


Figure 4.11: The line density of shot #33725, reaching the density limit at 5.5 T, 500 kA, superimposed to the one of shot #33719, used to find the limit at 5.2 T, 500 kA. The two limits turn out to be similar, both around $2.3 \cdot 10^{20} \text{ m}^{-3}$ despite the higher field of shot #33725 would lead to expect a higher threshold. The accurate procedure carried out during recent experiments, in the regulation of the reference density using the gas puffing, is evident in this picture. Identical increase of the two density ramps, despite the different magnetic equilibria of the two shots, could be performed. Also the MARFE instability, that can be recognized from the strong oscillations on the interferometer signal and which typically 'start' at a certain time during the discharge, has the same starting point in the two traces, showing a behavior independent on the magnetic field.

plasma currents were also tested, in order to verify the real influence of the current on the density regime. Currents of 500 kA and 700 kA were used in different discharges and then compared, all performed at the same field of 5.2 T. The results on the density limit value, shown in Figure 4.12, lead to conclude an independence of the density limit on the plasma current, despite the values of the *Greenwald* operational limits at 700 kA and 500 kA are different. Many attempts to overcome the *Greenwald* limit with the use of lithium have been made at current higher than 500 kA, like 700 kA, during last years, but all of them were without success, when the magnetic fields was lower than 6 T. This limit could be passed at 700 kA only by increasing the magnetic field to values higher than 6 T.

Density Peaking in Presence of MARFE Instability

Up to now, the more credible reason for the different limits found at different fields is searched in a relation (still under study) with the different maximum value of the safety

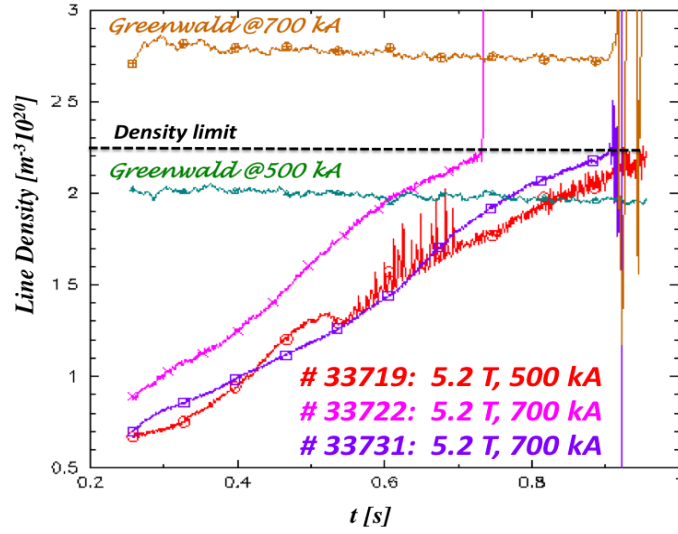


Figure 4.12: Density limits found for three discharges, with the same 5.2 T field but 500 kA plasma current (shot #33719, red) and 700 kA (shot #33722, light purple, and shot #33731, violet). Despite the *Greenwald* limit is higher at 700 kA (brown line) than at 500 kA (green line), the disruption occurs at identical densities for the two currents.

factor q at the edge. During 2010 it was demonstrated, in a more detailed way with respect to the past, that higher densities are only obtained for higher values of q . In particular, the *Greenwald* limit has been overcome only for $q \gtrsim 5$, like shown in Figure 4.15. It could be calculated that the use of lithium extended the working density range in FTU beyond the standard operational limits, but only for safety factors higher than approximately 5. The only difference between shots with different currents, that seems to be evident from the interferometric signals (see for instance Figure 4.12) concerns the presence of the MARFE instability, at least the very strong activity phase, when it is also detected by the interferometer⁹. The oscillations present in the central density signal of shot #33719, performed at 500 kA plasma current, are not present in the other two shots, at 700 kA. In fact, it is demonstrated that this kind of instability, which is more easily obtained with the use of lithium in the camera and which depends only on the average value of the density, always appears above a critical density. Such a critical threshold seems to be higher for

⁹The MARFE instability is not always easily detectable. In general, the oscillations in the interferometric density signals, like the ones visible in the traces of Figure 4.11, at 0.6 s, clearly give evidence of the presence of MARFE. Nevertheless, a non-oscillating character of the traces does not imply the absence of MARFE, with certainty.

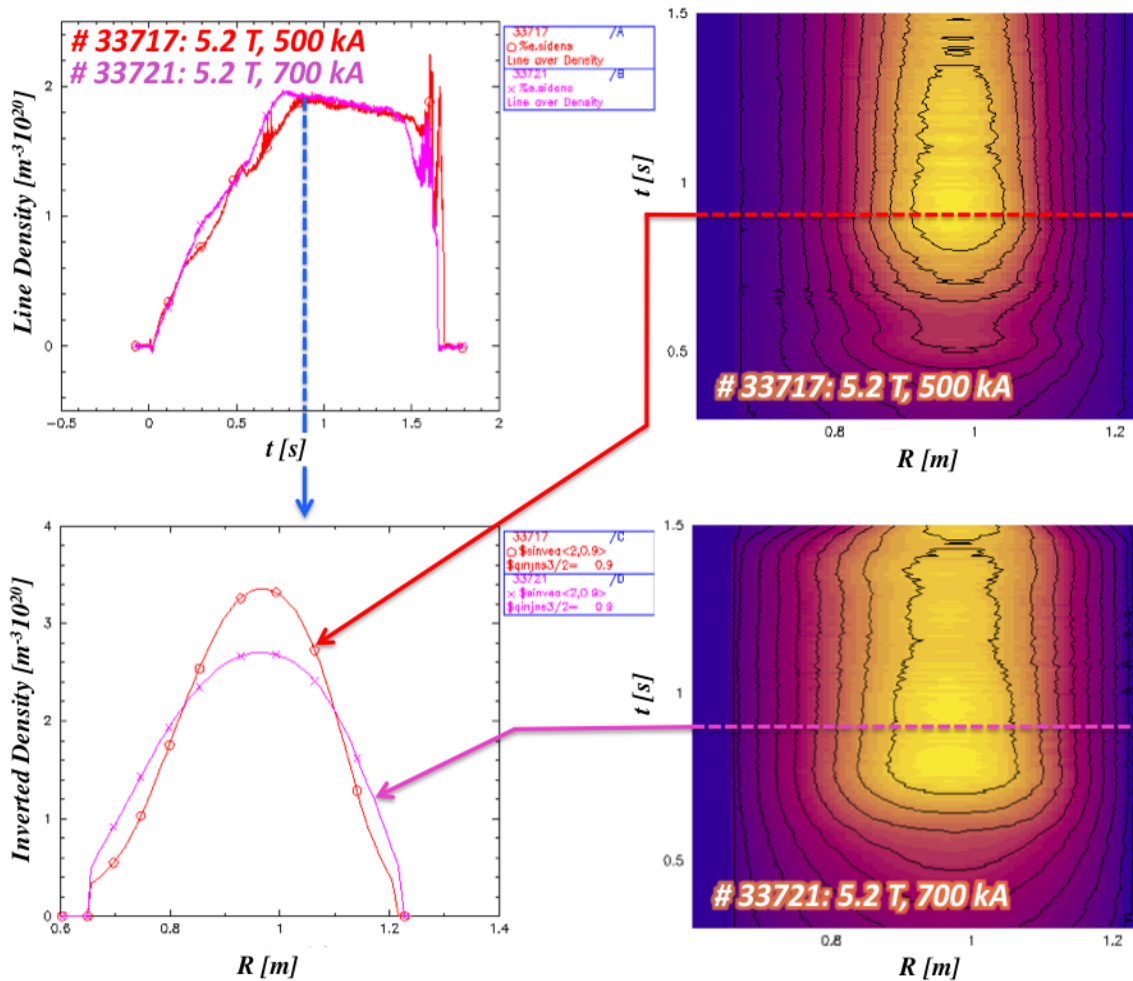


Figure 4.13: Two representative discharges, performed at the same field 5.2 T, but at different currents 500 kA and 700 kA. Both shots have a sustained line density plateau, at the same density value (top left). At 0.9 s, when the two signals indicate exactly the same integrated density (blue dotted arrow), the inverted density profiles have been calculated (bottom left). It is evident how the density peaking of shot #33717, performed at 500 kA, is higher than in shot #33721, at 700 kA. This is a typical difference found between 500 kA and higher fields lithized discharges. On top and bottom right, the local density of the two shots, versus major radius (abscissa) and time (ordinate), and calculated on the magnetic equilibrium, are shown. The density peaking factor is higher for shot #33717 than in #33721, that means steeper slope of the density profiles, more suitable for O-X power transmission. In the two plots the colors are normalized to different peak density values: $3.42 \cdot 10^{20} \text{ m}^{-3}$ for shot #33717 and $2.77 \cdot 10^{20} \text{ m}^{-3}$ for shot #33721. The red and purple arrows indicate the time at which the profiles in the bottom left have been calculated.

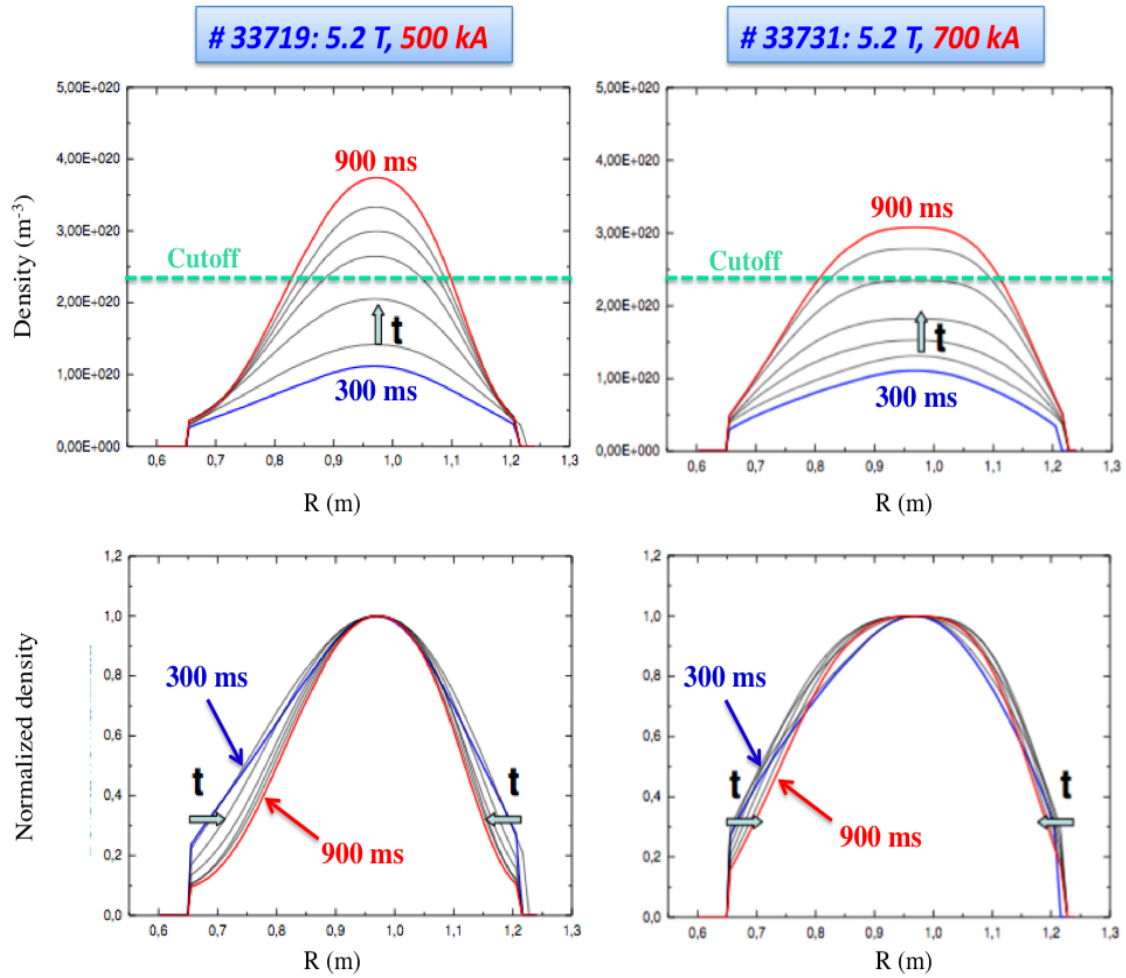


Figure 4.14: Local density (top) and normalized density profiles (bottom), at different time between 300 ms and 900 ms, of shots #33719, at 5.2 T, 500 kA (on the left) and #33731, at 5.2 T, 700 kA (on the right). It is clear that the stronger density peaking given by the lower 500 kA plasma current than 700 kA, at any time. In particular, from the normalized profiles, it can be seen how the peaking factor rises with the time during the shot. The light blue arrows indicate the profile change with the time. The cutoff density is also shown with the green dotted lines.

higher plasma currents. For this reason, in the two shots of Figure 4.12, performed at 700 kA, the typical oscillations given by the presence of MARFE are not yet present, at the performed densities.

As already emphasized, an important aspect to be considered in view of an optimal plasma target for mode conversion is the local density gradient at the cutoff surface, hence the slope of the inverted density profiles. From the *Mjølhus formula* [86] it is evident that a steeper profile is of course preferable, since it gives rise to less constraints on the precision of the optimal injection. The analysis of the high density discharges performed at different currents and in presence of MARFE led to identify a different behavior of the particles radial distribution, i.e. the shape of the density profile. While the density peaking¹⁰ of

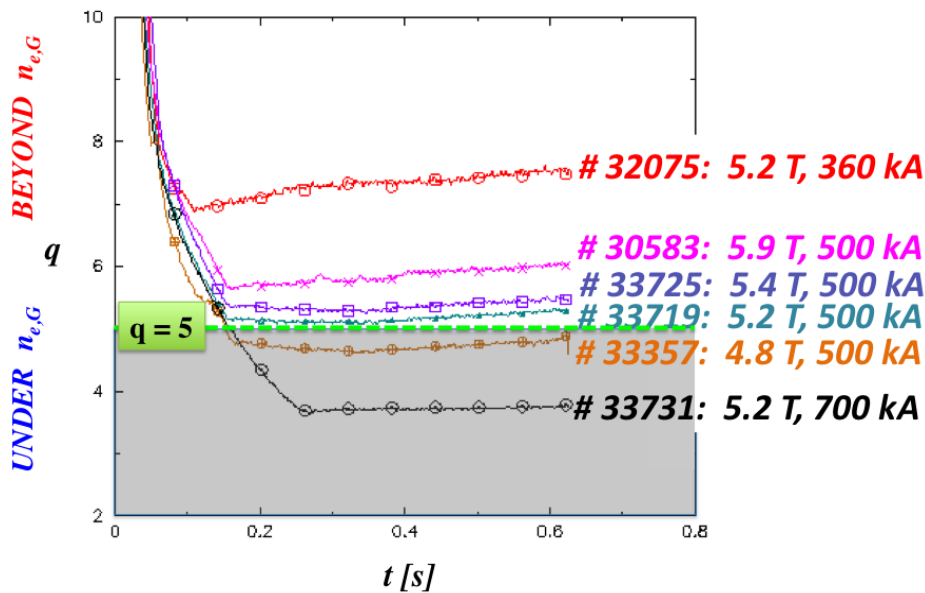


Figure 4.15: Some discharges with different combinations of field and currents, having typical values of the safety factor at the edge, are considered. The value $q \approx 5$ seem to be confirmed in the experiments as the threshold between discharge which density limit is under the respective *Greenwald* limit (for lower q indicated with the grey area) and the ones that overcome it (for higher q , white area). discharges with 5.2 T and 500 kA are near this threshold.

the profiles in absence of MARFE instability seems to be independent from current and field, both density and temperature distributions turn out to be considerably modified by

¹⁰Already defined above, as the ratio between the peak density of the profile and the mean density: $n_{e,0} / \langle n_e \rangle$.

them, when MARFE is present. Concerning the temperature, a marked shrinking of the profiles is always evident, during MARFE, with an edge temperature usually dropping below 20-30 eV for several centimeters in the peripheral regions of the plasma. From the point of view of the density, the peaking is clearly influenced by the plasma current, when MARFE is present. Higher currents tend to lower the density peaking factor, leading to a lower central peak of the profiles and lower local density gradients on the slope of the profiles at cutoff, like showed in the examples of Figures 4.13 and 4.14. This lower density gradient would imply a strong reduction in the conversion efficiency, according to *Mjølhus* equation. Since MARFE instability is easier, in general, to be found with lithized walls, and turns out to be practically always present at the high densities of interest for our experiments¹¹, the increase of the density peaking found at a lower current can be considered of general validity, for our aims. Such a result brought to conclude that lower plasma currents should be preferable in view of EBWH experiments.

Concerning the definition of the best candidate magnetic field for the plasma target, in Section 4.3.1 we have shown that several discharges with different fields relevant for ECRH between 4.8 T and 5.5 T, have been performed during last campaigns. We demonstrated that lower values, like 4.8 T, had to be discarded, since it does not allow to achieve the overdense regime for the 140 GHz frequency. On the other side, a higher field, like 5.5 T, turn out not to be convenient, since no effective increasing of the density limit could be obtained in this case, while an higher value of the optimal wave $N_{||}$ at cutoff is requested for such a field, in order to convert, and a higher field imply also a 'shift' of the EC resonance towards more external regions of the plasma, leading to further difficulties in the achievement of the proper overdense region around the resonance.

These results led to the choice of the intermediate value of 5.2 T as the best field for the target.

4.3.2 Analysis of 360kA, 5.2 T Discharges from the FTU Database

Since lower currents have been demonstrated to be more suitable for our aims, after the last FTU campaign of 2010, discharges performed at high electron densities, lower current and 5.2 T magnetic field were selected among the FTU database, to be analyzed. Despite these discharges were dedicated to different kind of experimental programs, some high density shots performed at 5.2 T and 360 kA could be found (see Figure 4.16). The same

¹¹Also when such MARFE activity can not be detected with oscillations in the line density signal.

procedures of analysis¹² were applied to these shots.

Since for experimental reasons, from the end of the density ramp-up, ECRH was used

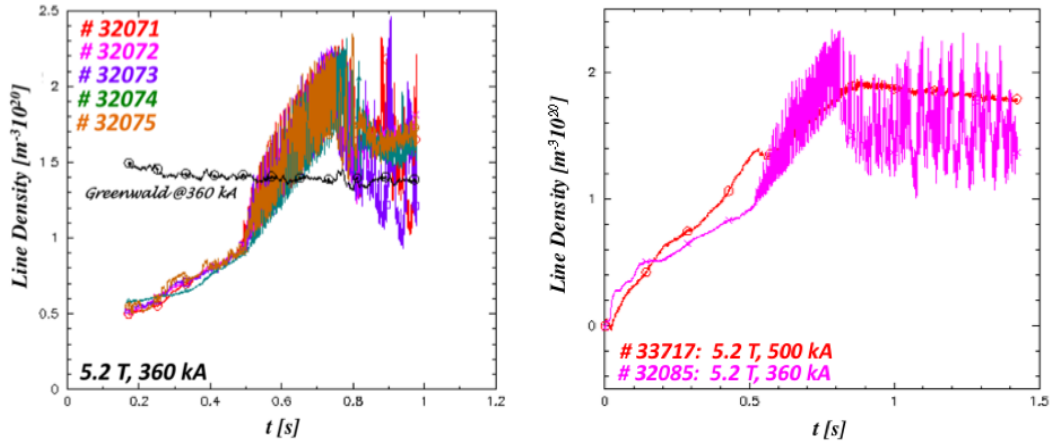


Figure 4.16: Line density profiles of several discharges, performed for different experimental programs at 5.2 T, 360 kA, then taken into consideration for the analysis aimed to find the plasma target for O-X-B experiments (left). The lower *Greenwald* limit, calculated for the 360 kA current, is showed (black trace). From the oscillations of the measurements it is evident that a strong MARFE instability establishes at this low current and noisily affects the control of a stable plateau. On the right, the comparison between a typical 360 kA and 500 kA is shown. The plateau obtained at 500 kA is more stable and the high density results maintained during the shot.

in such shots, the peaking of the profiles could be compared with the previous ohmic discharges only in the density ramp-up phase, when EC heating was not present. This was done in order to prevent the risk that the EC power could affect the density profiles we were going to study. In accordance with the results obtained previously, the density peaking factor found at a current of 360 kA tends to be higher than at 500 kA (during a similar density ramp-up phase), like shown in Figure 4.17. This is true for local density profiles

¹²The discharges at 360 kA here considered were performed in a non-litized vessel condition; thus, in principle, they were performed in a different regime with respect to the other shots considered in this Thesis, all performed with LLL. Nevertheless, the standard procedure of covering the internal walls of the FTU camera with boron, that periodically is carried out to eliminate 'heavier' impurities like oxygen, had been carried out just few days before these discharges. From the past experimental evidences, it is demonstrated that the influence of two 'light' impurities like boron and lithium on the plasma regime are approximately the same, from the point of view of confinement at different currents and of induction of MARFE instability at the edge. In this sense, such discharges can be compared, at least at a first step, with the other ones analyzed above.

calculated at the same line integrated density and for the same plasma dimensions. In addition to this feature, beneficial for O-SX coupling, a very strong activity of the MARFE instability is detected by the interferometer diagnostic, which completely affects the quality of the measurement. The control on the density becomes very difficult, especially after

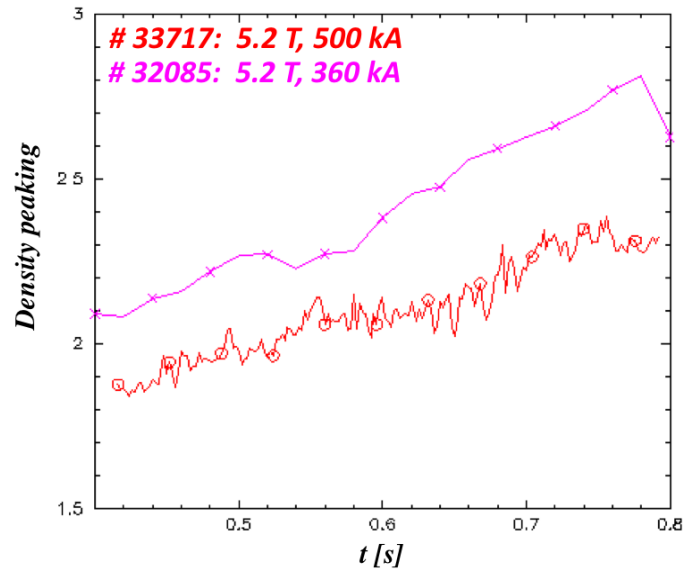


Figure 4.17: Density peaking factor, calculated in real time with the real parameters of two different typical shots, at 360 kA and 500 kA, both with 5.2 T of the magnetic field. The trend of the peaking factor is showed just for the initial ramp-up phase of the density, when the EC power was not injected in the plasma of shot #32085 yet, in order to compare two identical ohmic conditions.

the density ramp-up, and the reliability of the density measurements drops. Moreover, the density level of the plateau tends to decrease, after the ramp-up phase. The density turns out not to be sustained by such a low plasma current, at least, in absence of lithium in the camera. The result of this is the partial (and sometimes total) compensation of the beneficial effect given by a steep slope of the density profiles at 360 kA. When this tendency to decrease is particularly marked during the plateau phase, the unstable regulation of the density sometimes even leads to a non-overdense regime for the 140 GHz frequency, in some time intervals during the shot. These preliminary results, obtained without the use of LLL, should in principle prevent the use of such a low current for future experiments on O-X-B conversion. However, the repetition of such a low current, high density regime at 5.2 T and in lithized conditions, will be of great interest, of course, for the next campaigns.

4.3.3 The Optimal Plasma Target for EBWH Experiments

In addition to the experiments described so far, where the high density regime has been obtained through the regulation of the sole gas puffing in the camera, by using apposite injection valves in both manual and feedback control modes, also a pellet injection system was used, to increase the plasma density. This technique has been only preliminarily tested in order to reproduce the optimal plasma target for testing the O-X-B scheme; the first results obtained so far have been reported in Appendix B.

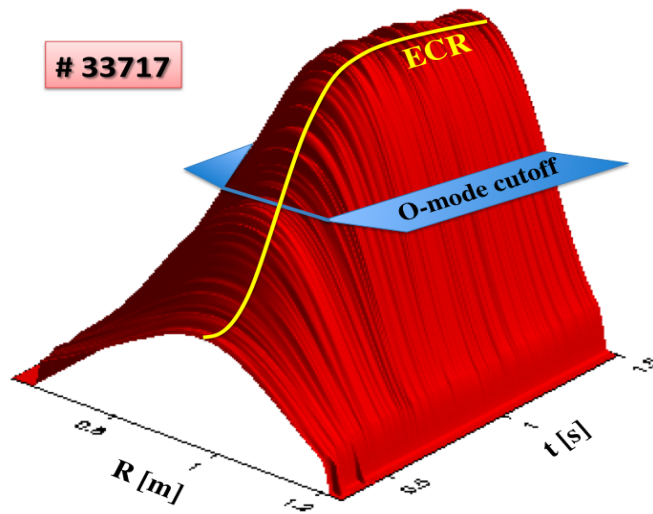


Figure 4.18: 3D reconstruction of the real density profile of a typical 5.2 T, 500 kA discharge (shot #33717), selected as one of the best target obtained for O-X-B experiments. The calculation of the density distribution is based on the real magnetic equilibrium of the discharge. The slope of the profile is steep and a considerable overdense plasma region for the 140 GHz frequency (region above the cutoff density level indicated by the blue plane) is centered near the O1-mode resonance (yellow line), which corresponds at 5 T of the magnetic field.

In conclusion, a central ECR scenario at 5.2 T, 500 kA, like the one shown in Figure 4.18, turns out to be the most promising, up to now, for our aims, giving rise to a quite consistent overdense region, centered around the 1st harmonic resonance of the EC waves, where the EBWs will be expected to be absorbed. High density discharges performed at 5.2 T and 500 kA, have been already routinely produced, with high repeatability and control of most parameters, and the optimization may continue in this sense. This conclusion is based just on the results that could be obtained so far: the study of the high density regimes of FTU,

at 5.2 T and intermediate plasma currents between 360 kA and 500 kA, is of great interest now, of course. A number of discharges will be dedicated in the next campaigns, in order to find out an even better compromise between stability of the plasma and density peaking or, on the contrary, to confirm 5.2 T and 500 kA as the best parameters for the optimal target for future EBWH experiments.

The work described in the present Chapter also opened several other interesting issues concerning the confinement of the high density fusion plasmas. In FTU, such a subject can be studied in detail, thanks to the wide ranges of densities and fields available. Such investigations have a more general importance, well beyond the purpose of the work carried out for this Thesis and are presently under study in FTU.

Chapter 5

Evaluations of O-SX Mode Conversion in FTU

5.1 Introduction

In order to study mode conversion in FTU from a predictive point of view, the *ECWGB* 3D beam tracing code for electron cyclotron wave propagation/absorption, based on a complex eikonal equation for the evolution of Gaussian beams in an inhomogeneous and anisotropic toroidal plasma [132], developed at IFP/CNR-Milano, has been modified, in order to calculate the quantities of interest for mode coupling while providing a very high spatial resolution (0.16 mm step), and then used to perform ray tracing calculations. Several simulations have been carried out, in which the data obtained from the plasma during the experiments described in Chapter 4 were considered, in order to evaluate the injection angles required to obtain optimal O-SX conversion with the typical FTU parameters.

In the present Chapter the preliminary evaluations on mode conversion obtained performing geometrical calculations in FTU are presented in Section 5.2. The results of the simulations carried out with the ray tracing code, using real plasma parameters, are reported in Sections 5.3, while the description and the results of the application to the FTU case of a 1D model of O-SX mode conversion developed for this Thesis and based on a Gaussian beam-mode analysis, are showed in the following Section 5.3.3.

At the end of the Chapter, in Section 5.4, a 2D model of O-SX coupling available since recent years in literature and the effects expected with this more realistic description of the plasma, with respect to a 1D slab description, are briefly reported. The application

of such a model to FTU is presented, by using real high density plasma parameters.

5.2 Geometrical Calculations

The preliminary phase was carried out with geometrical calculations, in order to have a first approach to the phenomena under study, before the detailed analysis with the ray tracing code. In this phase, purely equatorial propagation of the rays in the middle plane of the machine were assumed. For the sake of simplicity, in some cases the plasma density profiles have been described with analytical functions, with density peak centered on the axis of the FTU camera¹. Such a preliminary phase gave a first idea of the precision required to study mode coupling in the subsequent work. Then, it was possible to perform the proper modifications to the *ECWGB* ray tracing code and to consider the data from the FTU database with the correct precision.

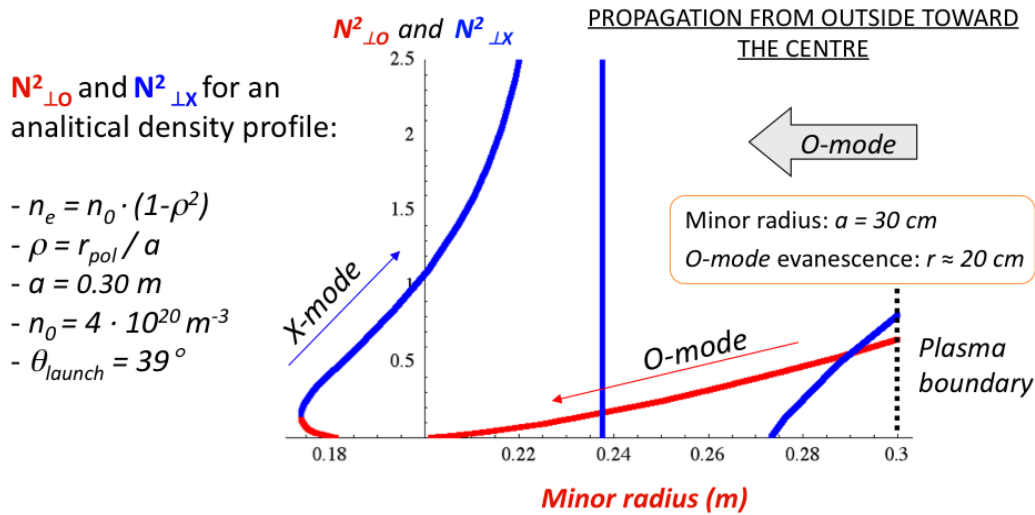


Figure 5.1: Dispersion relation branches of O- and X-mode, calculated with typical parameters of FTU. For the sake of simplicity, the considered density profile has been written using an analytical form. It is shown how a $\approx 39^\circ$ launch is needed to make the O- and X-branches coalesce, thus obtaining O-X mode conversion. The blue branch on the right is the one of the FX-polarized wave, which plays no role in the conversion scheme.

The Appleton-Hartree dispersion relation 3.22 for electron cyclotron waves in a cold plasma

¹As already said, this condition does not hold true, since generally the internal magnetic surfaces of the plasma are not concentric and are centered on more external axes.

model, reported in Chapter 3, can be used to calculate the branches of the O- and X-mode, for a given set of plasma and launch parameters, in the FTU case. For a given central magnetic field, assumed pure toroidal and scaling radially as $1/R$ (with R being the major radius coordinate of FTU), the cold dispersion relation for a 140 GHz wave propagating in the equatorial plane, is determined just by the local density (given by the plasma frequency) and by the angle between the wave vector and the antenna axis (injection angle), which is the complementary angle with respect to the one appearing in the Appleton-Hartree equation. If, for the sake of simplicity, an analytical fit of the real density profile is assumed, the dispersion branches for the FTU case can be plotted as a function of the angle between the propagation vector and the toroidal direction. By varying this angle, different branches result from the dispersion relation, for O-, FX- and SX-modes. If the angle between \mathbf{k} and \mathbf{B} at the launch is optimal, the two branches of mode and X-mode at cutoff coalesce, giving rise to perfect power transmission at the O-mode cutoff, like the ones shown in Figure 5.1. By changing the density profiles, then, different optimal angles are required for conversion. The $1/R$ scaling of a toroidal magnetic

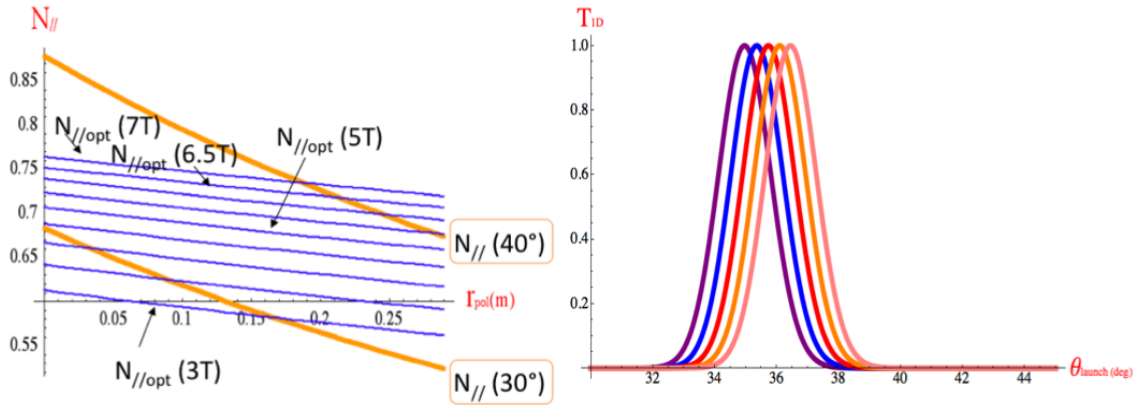


Figure 5.2: Left: variation of the optimal $N_{\parallel, \text{opt}}$ for different values of the central magnetic field (from 3 T to 7 T) and of the actual N_{\parallel} of the ray for a 30° and 40° injection into the vessel, calculated with geometrical calculations on a straight path in vacuum ($N = 1$). A purely toroidal magnetic field, varying spatially as $1/R$, has been supposed. Right: preliminary calculations of the O-X power transmission efficiency, calculated at the equatorial plane of the machine, for an analytical density profile of FTU and for some different central fields, from 5.0 T (dark purple curve) to 5.8 T (pink curve).

field in a tokamak-like geometry, can be used to plot the critical quantity $Y/(Y + 1)$ to be

reached as N_{\parallel}^2 for optimal conversion. Such a function is monotonic and increasing from LFS towards the HFS, if calculated as function of the radial coordinate and for a given central field. A higher field implies higher $Y/(Y + 1)$, locally. The straight propagation (in vacuum) of a ray on the equatorial plane in a toroidal magnetic configuration, is such that the local N_{\parallel} of the ray is not a constant, but is an increasing function of the radial coordinate as well, for propagation from the LFS to the center. This is a consequence of the $1/R$ scaling of the field. The scaling of the local N_{\parallel} with the radial position has been geometrically calculated and led to the following expression:

$$N_{\parallel} = \sin(\vartheta_l + \Theta_0), \quad (5.1)$$

with:

$$\Theta_0 = \arcsin \left(\frac{\frac{R_l}{(R_0+r) \tan \vartheta_l} - \sqrt{\frac{R_l^2}{(R_0+r)^2 \tan^2 \vartheta_l} - \frac{1}{\sin^2 \vartheta_l} \left(\frac{R_l^2}{(R_0+r)^2} - 1 \right)}}{\frac{1}{\sin^2 \vartheta_l}} \right),$$

where R_0 is the major radius of the torus (0.935 m in the case of FTU), R_l is the radial position of the launching point, ϑ_l is the toroidal launching angle on the equatorial plane and r is minor radius coordinate. The calculated expression 5.1 was useful to plot N_{\parallel} , for different injection angles, together with the local critical value $Y/(Y + 1)$, for different central magnetic field. The result is shown on the left side of Figure 5.2. The intersections (i.e. coupling) between N_{\parallel} and the critical value are found at launching angles between 35° and 40° , for central fields between 5 T and 5.5 T, if the cutoff radius is assumed in the range 10-15 cm, as usually holds true in FTU. The range of variation on the intersection depends on the density profile, which thus must be well approximated, if one wants to perform predictions with precision. By applying the *Mjølhus formula* 3.26 for the power transmission to SX-mode, the same simplified model was used to calculate, for different values of the central field, the power transmission efficiency for different cases, which is a Gaussian-shaped function, peaked at the optimal injection angle of the ray, in the slab plasma (Figure 5.2, on the right).

5.3 Simulations with Real FTU Parameters

The first simulations with the ray tracing code have been performed in order to understand with precision the behavior of EC waves in the configurations such that both O- and X-mode were in cutoff from the LFS. In Figure 5.3 an example of a ray tracing calculation

performed for the injection of an O-wave in an overdense plasma is shown. Such a situation is quite unusual in calculations with propagation codes, since, in general, predictions are performed in order to estimate the power absorption of the ECRH waves, in conditions where the resonances are accessible to the propagating mode. For this reason, the existing ray tracing code *ECWGB* was modified increasing the spatial resolution to the level (0.16 mm step) necessary to simulate the propagation path with the required precision.

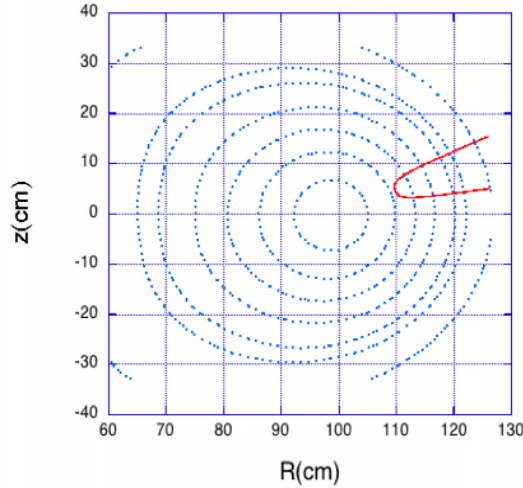


Figure 5.3: Poloidal view of a typical ray path (in red) in an over-dense plasma. The O-polarized wave propagates inside the plasma until the $X = 1$ cutoff is reached. At that point, the wave is back-reflected, since the center of the plasma is prevented (overdense) for a general injection angle. In the picture, also the magnetic flux surfaces of the FTU shot (taken from the magnetic equilibrium of the plasma) are represented with the dotted circular blue lines. In this case, the z -coordinate is the perpendicular one and R in the major radius of the device.

The first simulations performed with real FTU parameters clearly showed that the refraction influences the trajectories such that a small angular change at the wave injection into such a dense medium has strong repercussions on the actual path and on the maximum depth that can be reached by the ray in the plasma (some examples in Figure 5.4). This is true for both poloidal and toroidal angles. Thus, the constraints in the injection precision are very stringent, in an overdense plasma, when the O-mode cutoff has to be approached by the wave in order to convert to SX-mode.

Assuming the FTU plasma as a slab, with both density and magnetic field gradients on the radial coordinate, the launching condition for a perfect coupling between O- and SX-mode is represented with the green ray of Figure 5.5, which represents in 2D the real 3D case.

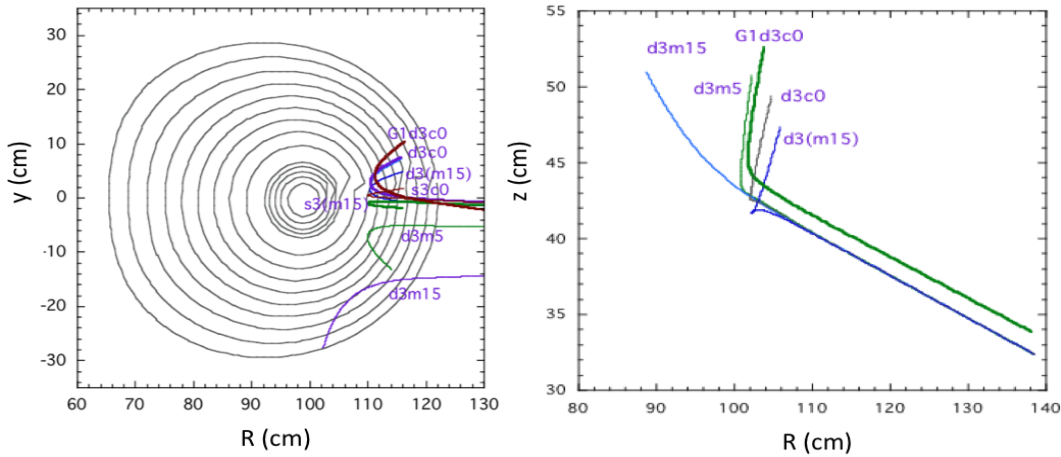


Figure 5.4: First results obtained with preliminary ray tracing calculations performed from the launching point of the EC launcher presently installed in FTU. These calculations were performed to obtain a first evaluation of the wave paths at different poloidal and fixed toroidal $\pm 30^\circ$ steering angles, using real high density plasma parameters. The poloidal view of the simulations is on the left, with y being the vertical component; the toroidal one is on the right of the picture, with z being the toroidal coordinate. Thanks to this first simulations, it was demonstrated that no poloidal component could be used in the wave injection to increase the N_{\parallel} of the wave, since only the rays aiming the center of the plasma can reach the O-mode cutoff.

When a wave (here represented only with a singular ray, assumed to be the beam axis) reaches the $X = 1$ layer (blue dotted line in Figure 5.5) with a value of the $|N_{\parallel}|$ which is lower than the optimal one for conversion $\sqrt{Y/(Y+1)}$, it is back-reflected (red rays). If the optimal value is reached exactly in correspondence of the cutoff layer, the O-mode is converted to SX-mode beyond the $X = 1$ region (green ray). Finally, if the condition $N_{\parallel}^2 = Y/(Y+1)$ is satisfied 'before' reaching the density O-mode cutoff (blue dotted line), the back-reflection occurs in correspondence of lower densities regions, namely towards the LFS (yellow rays). In this case the local density corresponding to the cutoff is the one indicated in Section 3.5.2. The higher is the local N_{\parallel} of the wave in the plasma, the lower is the local density corresponding to the back-reflection point.

Calculations for different toroidal and poloidal launching angles done with *ECWGB* code allow to draw maps which represent the real 3D description of what has been sketched in the simpler two-dimensional case above. The result, obtained for a real shot, can be represented in Figure 5.6. For the shot considered in this case typical cutoff minor radius is found at 10-15 cm, namely in the proximity of half the minor radius of the plasma,

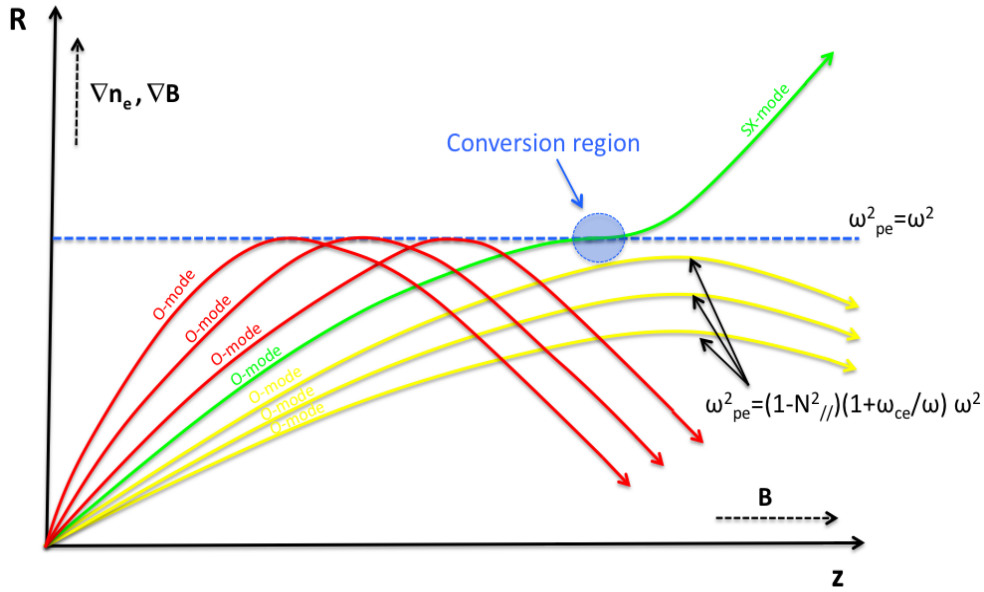


Figure 5.5: The optimal launch for O-SX mode conversion (green) is represented in this simplified representation of a slab geometry plasma, together with several other non-converting launched O-waves (red and yellow arrows). If the $N_{||}$ becomes too high along the ray path (yellow arrows), the wave does not even reach the $X = 1$ layer and the corresponding cutoff becomes the one reported in Section 3.5.2, re-written again here in the picture, on the right. The only wave which reaches $X = 1$ with the optimal value of the parallel refractive index $N_{||}^2 = Y/(Y + 1)$ is the green one, which couples SX-mode in the conversion region (blue area).

which is around 30 cm.

In Section 3.5.2, it was shown that the only way to obtain a complete coupling between the O-mode and the SX-mode, in a slab geometry, consists in satisfying $\vartheta = 0$ and $X = 1$ together, in the Appleton-Hartree cold dispersion relation 3.22. This can occur only when the phase velocity \mathbf{v}_{ph} of the wave is completely parallel to the magnetic field ($\vartheta = 0 \Rightarrow N_x = N_y = 0$) at the O-mode cut off layer $P = 0$, namely when $X = 1$ ($\Rightarrow \omega_{pe} = \omega$). The higher is the toroidal injection angle, the narrower is the range of poloidal angles which enable the ray to reach the $X = 1$ region. In a magnetically confined plasma, the condition of $\mathbf{v}_{ph} \parallel \mathbf{B}$ at $X = 1$ can be obtained just for a couple of toroidal-poloidal injection angles. Only such an injection let the ray reach the cutoff with optimal value of the refractive index 3.24, here again reported:

$$N_{||,c}^2 = \frac{Y}{Y + 1} = \frac{\omega_{ce}}{\omega_{ce} + \omega}. \quad (5.2)$$

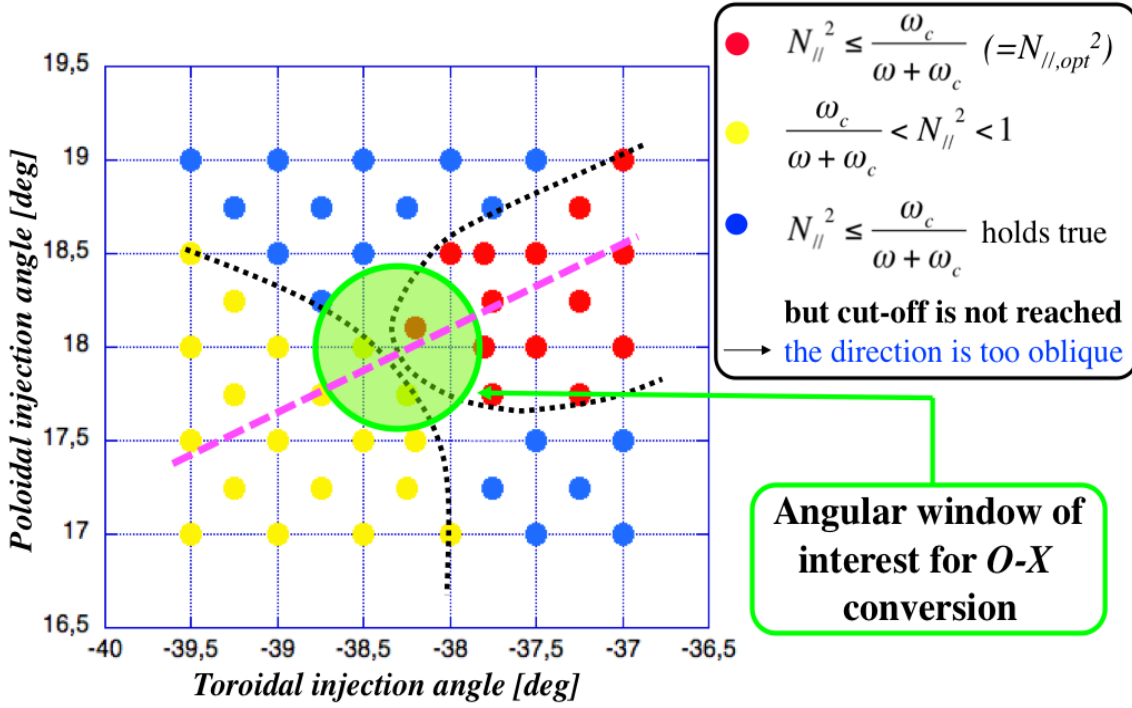


Figure 5.6: The three different regions, resulting from the ray tracing calculation performed with real FTU parameters and explained in detail in the text, are shown in the toroidal-poloidal injection angle map. The region of interest for O-SX coupling is indicated here with the green area. The purple oblique dashed line indicates a sort of 'section' of this graphics, which representation is Figure 5.5, where a correspondence between the colors have been kept for clearness.

being the maximum allowed for N_{\parallel} of the wave at cutoff. For higher values the cutoff shifts toward the LFS. A set of ray tracing evaluations has been performed with launch from a single position and poloidal/toroidal angles variable in a region around the expected optimal angle. Looking at the ray tracing propagation and evaluating the N_{\parallel} and N_{\perp} along the trajectory, each run can be classified into three sets, which define three regions in the poloidal/toroidal injection angles map shown in Figure 5.6.

A first region of launching angles, shown with red dots, is defined by the couples of toroidal-poloidal launching angles such that the O-wave reaches the density cutoff, where it is back-reflected. In this region the condition $N_{\parallel}^2 \leq Y/(Y+1)$ holds true. The red dots in the present figure are the generalization in 3D of the red rays in Figure 5.5.

A second area (blue dots) is given by injections such that the above condition still holds true, in principle, along the entire path of the injected ray, but the $X=1$ region can not

be reached, since the injection is too oblique in some direction and the refraction, implied by the high density, does not allow the ray to penetrate enough into the plasma. The case here represented with blue dots has no correspondence in Figure 5.5, since such injections lie in the additional dimension not considered in the 2D representation of Figure 5.5.

The last region (yellow dots), corresponding to the yellow paths in Figure 5.5, collects all the cases for which $Y/(Y+1) < N_{\parallel}^2 < 1$ at a certain point of the ray propagation. In these cases, the reflection layer for the O-mode does not correspond to $\omega_{pe} = \omega$ any more, since it is shifted to outer regions, with respect to the plasma core. The position of cutoff is shown in Figure 5.8, as calculated for another discharge of FTU, in a plot where the radial position of the cutoff layer is shown as function of the N_{\parallel} of the incident wave. Thus, the

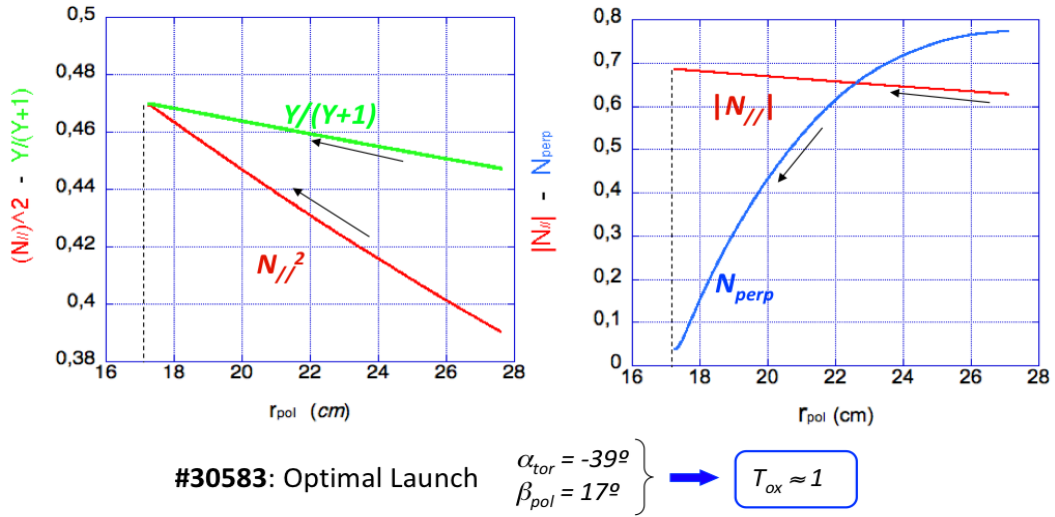


Figure 5.7: Left: values of N_{\parallel}^2 and $Y/Y + 1$ versus minor radius. Right: N_{\parallel} , and N_{\perp} versus minor radius. The computations are performed with the *ECWGB* code, at optimal launch for O-X conversion and plasma parameters of shot #30583, where a central field scaled down from the 5.9 T of the shot to 5.3 T has been used for the simulation. Since the injection performed with the ray tracing is close to the optimal one, at the 140 GHz cutoff radius $N_{\parallel}^2 = Y/Y + 1$ (left) and $N_{\perp} \approx 0$.

optimal propagation for perfect O-X coupling at $X = 1$ layer is defined by the boundary region between the red and the yellow areas of the map. For these injection angles the wave approaches the $\omega_{pe} = \omega$ layer, with a monotonically increasing parallel refractive index and reaches the maximum allowed parallel refractive index $N_{\parallel}^2 = Y/(Y+1)$, with a totally parallel propagation (phase velocity) at cutoff, giving rise to optimal (or partial) conversion. The situation described above is shown in Figure 5.7, calculated for a real

shot of FTU with the use of the *ECWGB* ray tracing code. It can be seen that the N_{\perp} of the wave vanishes at the cutoff layer. The local power transmission efficiency to SX-mode,

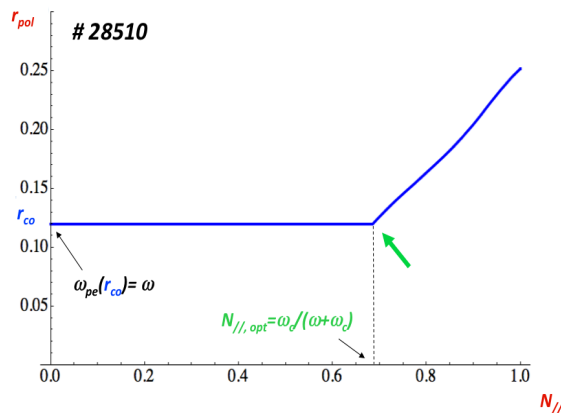


Figure 5.8: O-mode cutoff position in the plasma versus parallel refractive index, calculated with the parameters shot #28510. The optimal N_{\parallel} for conversion (green) corresponds to the 'knee' of the curve (green arrow).

in the proximity of the conversion region, using the formula 3.26 was calculated using the N_{\parallel} and N_{\perp} on the trajectory. Hence, it was possible to compute the power transmission efficiency of several rays launched with injection angles very close to each other, centered around the direction allowing the maximum values of the ray N_{\parallel} at the O1-mode cutoff. The simulations with the real plasma parameters of a couple of overdense discharges led to estimate of the power conversion window² shown in Figure 5.9. As expected, the conversion window turns out to be very narrow, for a 140 GHz injection (that means high k_0), despite the steep density gradient of the plasma. A 50% drop of the conversion efficiency is expected for angular deviations $\lesssim 1^\circ$, in both poloidal and toroidal directions, as shown in Figure 5.9.

5.3.1 Effects of Density Fluctuations

In the general description of the theory of the O-SX coupling in Section 3.5.3, it has been anticipated that the density fluctuations given by plasma turbulence can degrade the perfect coupling, at least when a plane wave propagation is considered. This is the consequence of a 'rough' cutoff surface caused by plasma turbulences, giving rise to a change

²Already defined as the angular window (at the launching point) such that 50% of the launched power is transmitted beyond the cutoff.

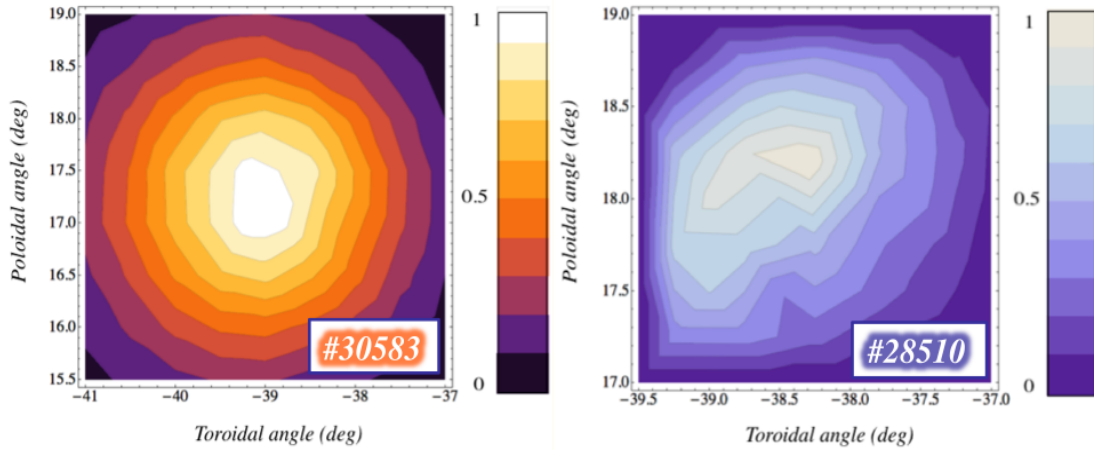


Figure 5.9: Angular transmission window, centered on the optimal launching angles, in the case of two different high density plasma discharges of FTU, calculated with a single ray tracing simulations, starting from the launching point of the new ECRH launcher. Each level corresponds to 10% of transmission efficiency. The angular window diameter, defining 50% of power transmission, is around 2° in both poloidal and toroidal directions.

in the local density, which affects the effective value of N_{\parallel} at the conversion region. Since such local changes are unpredictable, only a statistical approach, like the one introduced in [64] and reported in Section 3.5.3, can be considered, in order to estimate the effects of density fluctuations. The probability density function in the case of FTU could be obtained with precision only by knowing the parameters which have a role in this expression, like $\sigma_x = L_n \Delta n_e / n_e$, which represents the standard deviation of the fluctuation amplitude, and λ_y the poloidal correlation length of the fluctuations. Both the relative fluctuation amplitude $\Delta n_e / n_e$ and λ_y should be obtained by reflectometry measurements performed at the region of the cutoff layer, namely with a 140 GHz diagnostic, which is not available nowadays in FTU. Thus, typical values for these parameters found in other machines have been considered in order to estimate the degradation due to fluctuations presented in Figures 5.10 and 5.11.

5.3.2 Effects of Wave Polarization

Another important issue to be considered in the real case, in order to correctly predict the amount of coupled power, concerns the purity of the launched polarization. As described in detail in Chapter 2, the polarization of pure O- and X-modes in a magnetized plasma,

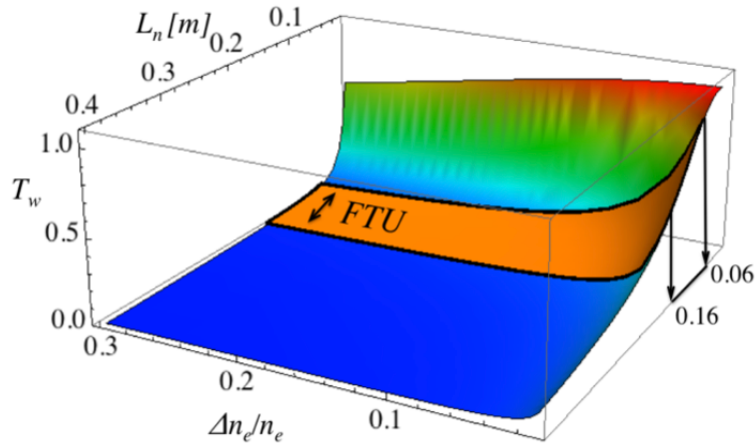


Figure 5.10: Conversion efficiency versus relative density fluctuation amplitudes and density scale length L_n , calculated with the statistical model introduced in Section 3.5.3. The region defined by the FTU parameters, obtained so far with experiments, is shown (orange area).

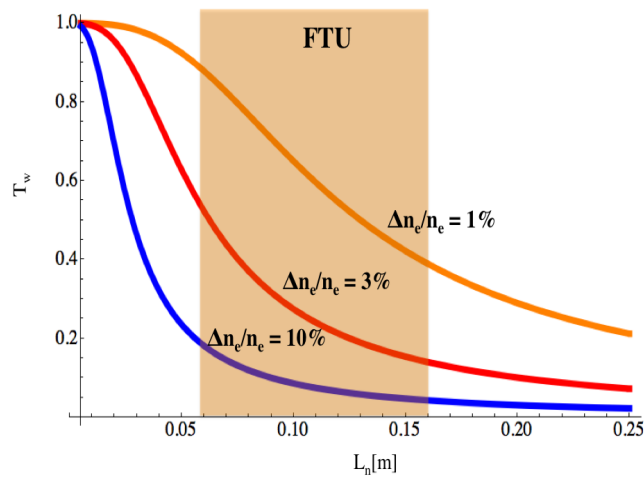


Figure 5.11: Power transmission efficiency at cutoff, in a slab geometry, weighted with a statistical description of the turbulences at the conversion region, versus the density scale length L_n , calculated for a single ray propagation. A poloidal correlation length of 3 cm has been assumed. The three curves corresponds to different relative fluctuation amplitudes $\Delta n_e/n_e$. The typical range of L_n for FTU is indicated with the orange region.

gradually changes, from linear, for propagation at 90° across the field, to perfectly circular (co- or counter-clockwise), when the propagation is directed along the field lines, with $\mathbf{N} \equiv N_{\parallel}$. This means that when an O-polarized wave is launched at oblique angle, the existing deviations of the polarization from the one with the correct ellipticity for given propagation angle and local magnetic field, must be known, in order to estimate the amount of power lost because launched in X-mode. Every polarization mismatch at the launch, from the perfect pure mode coupling in the plasma, implies a weighting coefficient < 1 to be considered in the overall efficiency of the O-SX conversion. The amount of radiation which couples (F)X-mode at the plasma edge is totally reflected at its $\omega = \omega_R$ cutoff, in the LFS of the plasma, and increases the stray radiation level in the vessel. Part of such a stray components may mode convert from O- to X-mode, because of the reflections at the vessel walls and may participate partially to the overall plasma heating, mainly reaching the non-overdense regions. The estimation of all these processes is beyond the scopes of this work, requiring dedicated statistical and geometrical models developed explicitly for the FTU case.

Presently, not all the ECRH lines of FTU have the possibility to launch elliptical wave

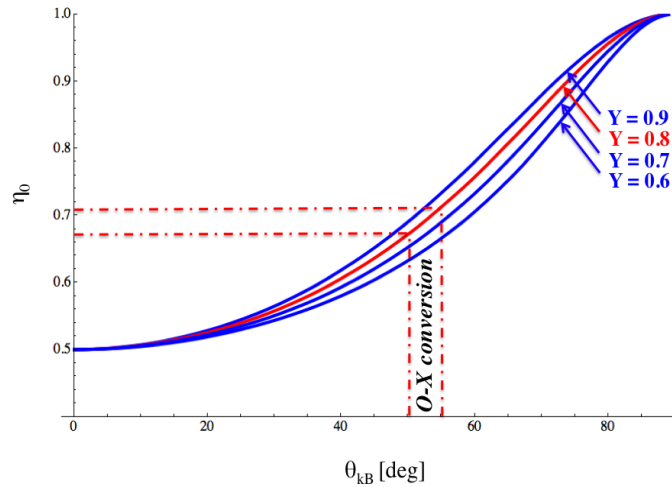


Figure 5.12: Normalized power content in the O-mode versus the angle ϑ_{kB} between the wavenumber and the magnetic field, for a linearly polarized wave. The different curves corresponds to different values of the normalized electron cyclotron wave Y . In the case of FTU, the red curve ($Y = 0.8$ at the plasma-vacuum threshold) is the one aiming at the cutoff with the angle between \mathbf{k} and \mathbf{B} $50^\circ \leq \vartheta_{kB} \leq 55^\circ$, corresponding to the launch angle $35^\circ \leq \vartheta_l \leq 40^\circ$.

polarizations; but some can only launch linearly polarized beams into the plasma also in the case of oblique injection. In these cases pure O- and X-modes can be injected only for 90° injections with respect to the magnetic field. When the launch of a linearly polarized wave is performed at angles different from 90° in the field, the efficiency of mode coupling are less than one, depending from the injection angle and the local magnetic field at the plasma edge. The ratio of the power content in the O-mode to the total power content in the incident linearly polarized wave has been calculated (see Figure 5.12), accordingly to equation 3.33. Typical local value of the parameter Y at the plasma-vacuum threshold, for instance at 5.2 T of the central magnetic field, is around 0.8. In Figure 5.12 it is shown that for a linearly polarized wave injected with these conditions at the oblique angles needed for O-SX coupling in FTU, the power losses to the unwanted mode are around 30-35%; this power can be considered as stray radiation.

The more appropriate angle for the polarization launched by the optics of the launching system, was also verified experimentally on the plasma with dedicated plasma discharges with 6 T central magnetic field. Since the resonant layer at 5 T is still in the plasma, while

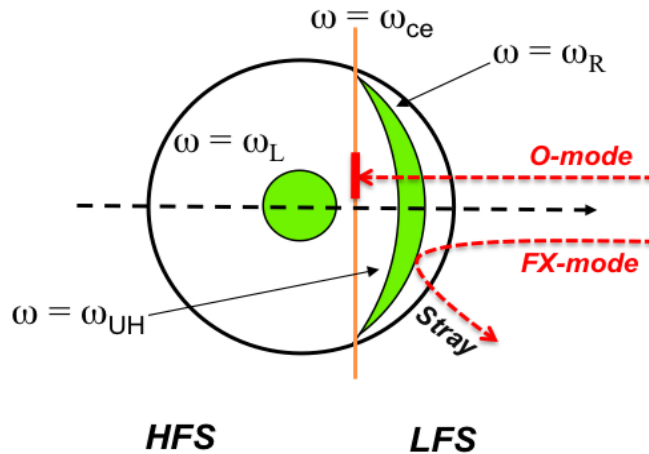


Figure 5.13: Poloidal view of the wave accessibilities of the X-mode, where the green regions are the prevented ones. The O-mode had no problem with accessibility during the performed tests on the plasma, since the density was well below the one of cutoff. Thus, it was completely absorbed at the resonance. The FX-mode, instead, was completely reflected at its low density cutoff (green region on the right) and became stray radiation in the vessel.

the X-mode cutoff being in front of the port end of the launcher, all the power coupled to

O-mode can directly reach the resonance and be absorbed, while the component coupled to (F)X-mode is back reflected at its $\omega = \omega_R$ cutoff layer and becomes stray radiation. The launch configuration used for these tests is represented in Figure 5.13. The signals of

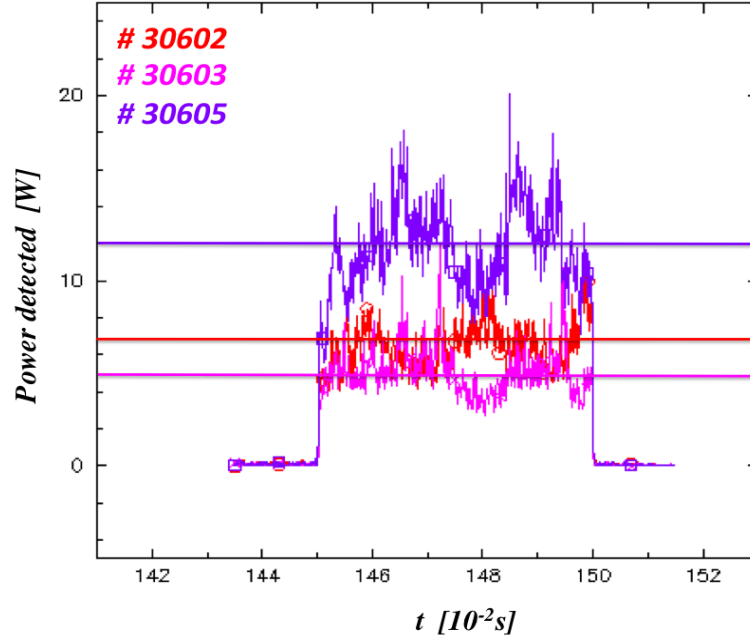


Figure 5.14: Signal detected by the sniffer probe #1 (located at the port #12 of the FTU camera), proportional to the stray radiation amount in the vessel. It is evident that the signal is lower in shot #30603 than in the other two shots, during which the encoder controllers of the polarizing optics were slightly changed, in two opposite directions, with respect to the nominal encoder, that has been used for the wave polarization control in shot #30603. The mean values of the noisy signals are marked with the three horizontal lines, with a color correspondence with the stray signal traces.

the stray radiation power detected by sniffer probes located at different toroidal positions into the FTU vessel, are shown in Figure 5.14 for three different discharges performed with a 90° injection of an O-wave. In shots #30602 and #30605 the rotation of the polarization direction has been slightly changed³, with respect to the one used in shot #30603, where the minimum stray radiation was detected, providing the minimum of FX-mode coupling (corresponding to the stray radiation) occurring in this case. The check of the stray radiation signal can similarly give an information on the effective coupling during O-X-B

³Since the optic is corrugated, its rotation gives rise to a rotation of the wave polarization.

experiments.

5.3.3 O-SX Mode Conversion in a Slab Geometry based on a Gaussian Beam-Mode Analysis

The predictions of O-X conversion, carried out up to now in a slab geometry, considered only the propagation of a plane wave. Since predictive models of conversion of a Gaussian beam in a slab model were not found in literature (apart from for the one that will be introduced in the next Section, developed using a 2D description for the coupling rather than a slab geometry), we developed in the frame of this Thesis a way to evaluate the expected coupling in case of paraxial propagation of a beam in the Gaussian beam-mode decomposition. Theoretical background for this issue could be found in [133].

A general solution to the wave-equation can be mathematically written as the superposition of infinite plane waves, propagating in infinite possible directions. This means that such a general solution is the integral over an angular spectrum of plane waves, which amplitude on each direction plays the role of a sort of weighting function for the considered component of the spectrum. A paraxial beam can be represented as a superposition of independent beam-modes, which can be demonstrated to follow from the angular spectrum of plane waves. This enables to 'construct' a real beam structure, starting from a 'basis' of beam-modes, properly weighted. The evaluation of O-SX mode conversion of a generic real field distribution (in the specific case of FTU it is the simple case of a generic Gaussian beam) is made by summing infinite plane waves propagating on infinite directions, and applying the well known formula of mode conversion in a slab description to the real FTU plasma and of the beams launched by the ECRH antenna. The conversion is being estimated and opportunely 'weighted' for each component of the angular spectrum, first, and consequently integrated over the infinite components of the angular spectrum, in order to obtain the overall conversion efficiency.

Let us assume the direction of propagation of the beam on the z -axis and the two orthogonal directions on x - and y -axes. The integral over an angular spectrum of plane waves, defining the general solution of the wave equation, can be written as:

$$\psi(x, y, z) = \int_{-\infty}^{+\infty} \int_{-\infty}^{+\infty} A(k_x, k_y) \exp -i(k_x x + k_y y + k_z z) dk_x dk_y. \quad (5.3)$$

The quantity $A(k_x, k_y)$ defines completely the field for all the $z > 0$ regions. The mathematical form of the field on the $z = 0$ plane, written as:

$$\psi(x, y, 0) = \int_{-\infty}^{+\infty} \int_{-\infty}^{+\infty} A(k_x, k_y) \exp -i(k_x x + k_y y) dk_x dk_y, \quad (5.4)$$

leads to define $A(k_x, k_y)$ as the inverse 2D Fourier Transform of $\psi(x, y, 0)$, i.e. its spatial-frequency spectrum:

$$A(k_x, k_y) = \frac{1}{4\pi^2} \int_{-\infty}^{+\infty} \int_{-\infty}^{+\infty} \psi(x_0, y_0, 0) \exp i(k_x x_0 + k_y y_0) dx_0 dy_0, \quad (5.5)$$

where x_0 and y_0 are the x and y coordinates at the $z = 0$ plane.

Making the paraxial assumption for propagation, which consists in the assumption that $k_x \ll k$ and $k_y \ll k$, the field $\psi(x, y, z) \equiv u(x, y, z) \exp -ikz$ can be re-written in the approximated form:

$$\psi(x, y, z) = \exp -ikz \int_{-\infty}^{+\infty} \int_{-\infty}^{+\infty} A(k_x, k_y) \exp[i(k_x^2 + k_y^2)z/2k] \exp -i(k_x x + k_y y) dk_x dk_y,$$

from which:

$$u(x, y, z) = \int_{-\infty}^{+\infty} \int_{-\infty}^{+\infty} A(k_x, k_y) \exp[i(k_x^2 + k_y^2)z/2k] \exp -i(k_x x + k_y y) dk_x dk_y,$$

turns out to be the Fourier Transform of:

$$A(k_x, k_y) \exp[i(k_x^2 + k_y^2)z/2k]. \quad (5.6)$$

In order to describe a beam-like field distribution, the *Gauss-Hermite functions*:

$$\psi_{\mathcal{H}_n}(x) = \exp\left(-\frac{x^2}{2}\right) \mathcal{H}_n(x)$$

are very useful, where $\mathcal{H}_n(x)$ are the *Hermite polynomial* of grade n .

Since the spectrum of plane waves $A(k_x, k_y)$ is the inverse 2D Fourier Transform of $\psi(x_0, y_0)$, which can be de-composed into the *Gauss-Hermite functions*, using the properties of the Fourier Transform, it can be demonstrated that:

$$A(k_x, k_y) = \sum_{n,m} \mathbb{C}_{nm} \frac{(i)^{n+m}}{2\pi} \cdot \psi_{\mathcal{H}_n}\left(\frac{\sqrt{2}k_x}{w_{k_x}}\right) \cdot \psi_{\mathcal{H}_m}\left(\frac{\sqrt{2}k_y}{w_{k_y}}\right), \quad (5.7)$$

where the beam width factors in k -space w_{k_x} and w_{k_y} are equal to $2/w_{0,x}$ and $2/w_{0,y}$, and:

$$\mathbb{C}_{nm} = \int_{-\infty}^{+\infty} \int_{-\infty}^{+\infty} u(x_0, y_0) \cdot \psi_{\mathcal{H}_m}\left(\frac{\sqrt{2}x_0}{w_{0,x}}\right) \cdot \psi_{\mathcal{H}_n}\left(\frac{\sqrt{2}y_0}{w_{0,y}}\right) dx_0 dy_0.$$

Coming back to the FTU case, the electric field distribution in the launched beam is assumed to be in the following Gaussian form:

$$u(x_0, y_0) = \sqrt{\frac{2}{\pi(w_{0,x}w_{0,y})}} \exp - \left(\frac{x_0^2}{w_{0,x}^2} + \frac{y_0^2}{w_{0,y}^2} \right), \quad (5.8)$$

such that $\int_{-\infty}^{+\infty} \int_{-\infty}^{+\infty} |u(x, y) dx dy| = 1$. Assuming the typical waist of the circular (i.e. non-astigmatic) beams launched in the ECRH system of FTU, $w_{0,x} \equiv w_{0,y} = 12$ mm, the spatial frequency spectrum 5.7 of the wave can be calculated for this specific case in the simplest way, since only the first order beam-mode plays a role in the description.

Assuming pure ordinary polarization of the considered Gaussian beam, the *Mjølhus formula* 3.26 for the transmission to SX-mode can be applied to every singular component of the spectrum:

$$\mathbb{T}_k(k_x, k_y) = \exp \left\{ -\pi k_0 L_n \sqrt{\frac{Y}{2}} \left[2(1+Y) \left(N_{\parallel, opt} - \sqrt{N^2 - \frac{c^2(k_x^2 + k_y^2)}{\omega^2}} \right)^2 + \frac{c^2(k_x^2 + k_y^2)}{\omega^2} \right] \right\}.$$

where the quantities L_n and Y (and hence $N_{\parallel, opt}$) are the ones of the experimental density and magnetic configurations of the FTU overdense plasma. The refractive index N here introduced in the formula, coincides with $N_{\parallel, opt}$, for the component with null components k_x and k_y , orthogonal with respect to the propagation axis, i.e. the central axis of the beam. This mean that such beam axis is considered on the optimal direction for the single ray conversion, and all the other components of the k vector on the x - and y -axes represent a deviation from the optimal propagation, since are both orthogonal. In this way the conversion of the real beam is calculated assuming the optimal aiming of the wave to the conversion region⁴. Thus, finally, to make an estimation of the overall conversion $\mathbb{T}_{O-SX,G}$ of the real Gaussian beam structure (5.8) in a slab description of the plasma, all the conversion efficiencies, relative to the single spectral components, have been properly 'weighted' and normalized with the spectrum, and then integrated:

$$\mathbb{T}_{O-SX,G} = \int_{-\infty}^{+\infty} \int_{-\infty}^{+\infty} \mathbb{T}_k(k'_x, k'_y) \frac{A(k'_x, k'_y)}{\int_{-\infty}^{+\infty} \int_{-\infty}^{+\infty} A(k''_x, k''_y) dk''_x dk''_y} dk'_x dk'_y. \quad (5.9)$$

The quantity (5.9) has been calculated using the real beam shape and waist. The perfect injection, in this case, is the one such that the beam axis turns out to be on the direction

⁴The model here presented holds true under the approximation of propagation in vacuum, since no refraction, given by the presence of the plasma, is taken into account for the components of the k -spectrum of the Gaussian beam approaching the cutoff layer.

of optimal aiming at the conversion region, found previously with the single ray tracing simulations. The optimal injection of such a Gaussian beam in the FTU plasma gives:

$$\mathbb{T}_{O-SX,G} \approx 0.43 \quad (5.10)$$

as the resulting conversion efficiency. According to this model, the result 5.10 has to be considered as a maximum limit for the overall power transmission efficiency to be expected in FTU, with such a beam waist and with the plasma parameters (density gradient at cutoff) obtained so far with the experiments, thus when a more realistic field distribution is considered.

When a beam reaches the conversion region, another factor that is expected to have an influence on the coupling is the curvature of the beam phase front with respect to the curvature of the plasma cutoff layer. The optimal beam should have a (negative) phase front curvature such that a perfect matching with the (positive) curvature of the cutoff layer might occur. According to the Gaussian description of wave propagation, such a situation occurs only in the case that the beam minimum waist is inside the overdense plasma region. This is not the case of FTU, since the optics of the launching system are such that the minimum waist of the propagating Gaussian beam is out of the plasma, close to the antennas. Hence, the curvature of the beam phase front at the conversion region is positive and a geometrical mismatching between the front and the plasma surface is expected, affecting partially a description of the field based on plane waves. No quantitative predictive model could be developed in this sense, but it will be interesting to verify experimentally the influence of different phase fronts⁵ on conversion. It should be stressed that the spatial frequency spectrum 5.7 of the Gaussian beam depends uniquely by the beam waist $u(x_0, y_0)$, and not by the local geometrical dimension $u(x, y)$ of the beam. Thus, the influence of the angular spectrum of the beam (fixed by the geometry of the minimum waist w_0 of Gaussian) can be described with the model above, while the implications of curvature mismatches of phase front and cutoff layer (given by local beam and plasma parameters) may introduce a further influence on conversion. This is because the two effects have a different nature, despite they are not completely independent issues, since a narrower waist w_0 implies a higher divergence of the field, which implies a larger surface of the phase front playing a role in the curvature mismatches.

⁵The change of the local phase front at cutoff can be obtained by changing the position of the beam waist back and forth along the path, accordingly to a Gaussian description of beam propagation. See reference [105] for details.

5.4 Prediction of O-SX Conversion in FTU with a 2D Model

In Section 3.6, recent bi-dimensional models of O-X conversion available in literature, whose development started during the last years, were presented. Such models, based on a more realistic description of the density and magnetic gradients of the plasma, have been applied to the case of FTU. In order to check the results presented in the previous Sections, based on a slab description of the plasma, or, in case, to predict the difference arising from a two-dimensional description, in the FTU case. The modified *ECWGB* ray tracing code

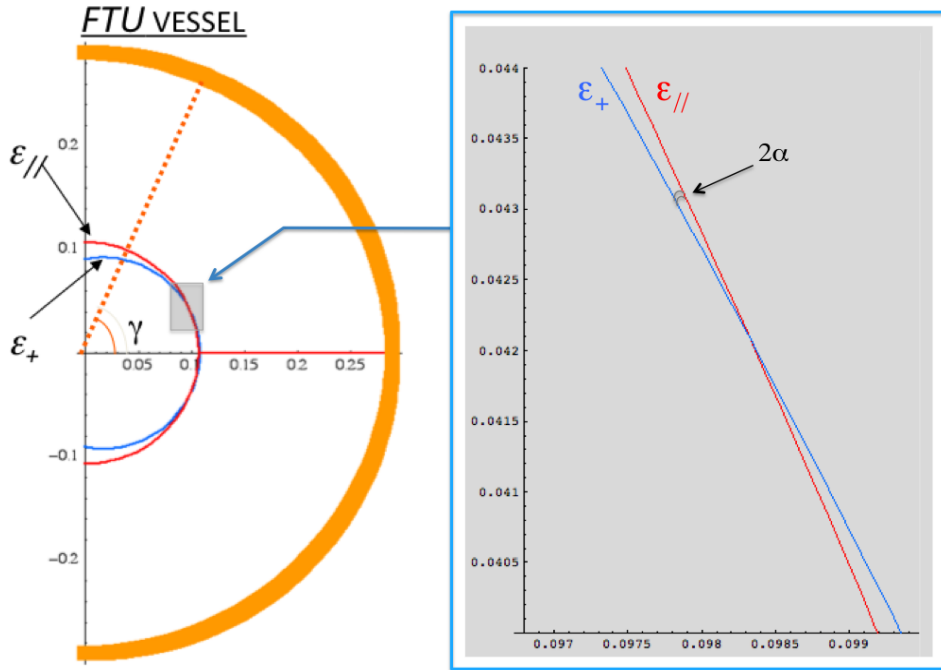


Figure 5.15: On the left: reconstruction of the O- and X-mode cutoff surfaces, respectively $\epsilon_{//} = 0$ (red) and $\epsilon_{+} = N_{//}^2$ (blue), at the conversion region, performed with the real parameter of a typical FTU discharge. The camera of the machine is the thick orange circle. The grey rectangular region around the intersection of the two layer is zoomed in the picture on the right. The angle 2α between the two cutoffs is indicated in the picture on the right.

was used in this case, to simulate the propagation of the rays in the overdense plasma target and calculate the needed parameters at the conversion region. As a first step, the real directions of the magnetic and density gradients in FTU have been considered and a more realistic plasma geometry has been constructed. The main parameters at the basis of the model, like L_{∇} (3.41) and the α angle, defined by equation 3.42, have been

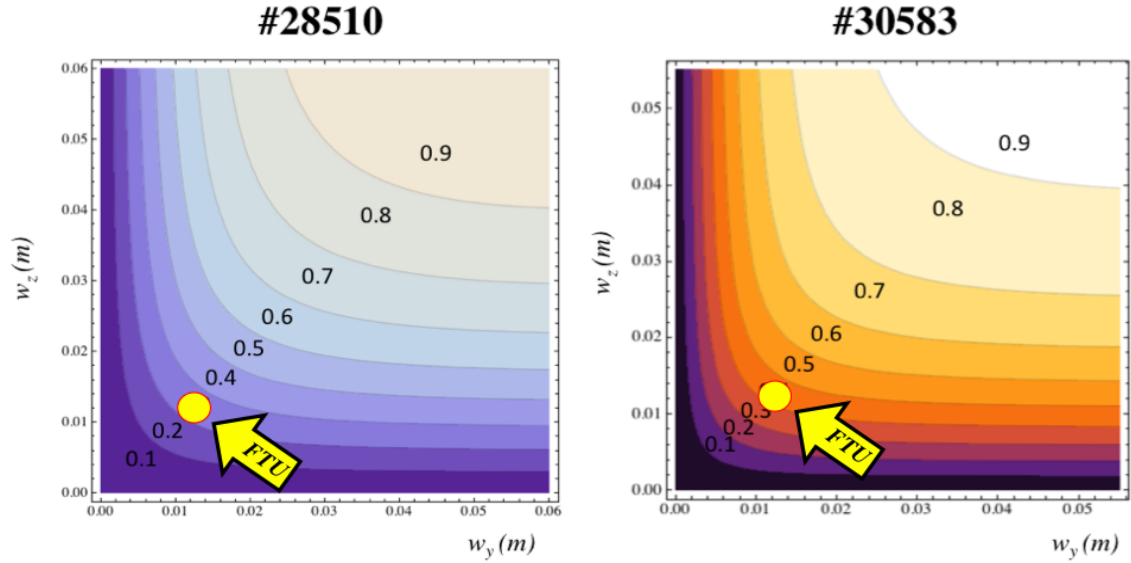


Figure 5.16: Contour plot of power transmission efficiency versus the vertical (y) and toroidal (z) beam waist, calculated for two discharges of FTU, using the 2D model of O-SX conversion presented in this Chapter. Optimal aiming of the beam to the conversion region has been considered for the plots. Each level corresponds to 10% of power transmission efficiency.

calculated for the FTU plasma. The 2α angle between the $\varepsilon_{\parallel} = 0$ and $\varepsilon_{+} = N_{\parallel}^2$ cutoff surfaces, defined in Figure 3.7, turned out to be very small, as a consequence of the high field needed to operate at 140 GHz (see Figure 5.17). Typical values of the α angle in FTU are around 0.5° - 1° . It can be demonstrated [99] that the 2D model predicts results close to the more approximated 1D description⁶ if:

$$|\alpha| \ll \min \left[1, \frac{L_{\nabla}}{L_y} \right] = \min \left[1, \frac{L_n}{L_y} \frac{1}{\sqrt{k_0 L_n}} \sqrt[4]{\frac{\omega_{ce}}{2\omega}} \right] \quad (5.11)$$

holds true (where angles are measured in radians), where $L_n = n_e / (\partial n_e / \partial r)$ is the usual radial density scale length and L_y is a characteristic width of the beam in the y -direction, which, in our case, can be considered to be approximately the one of the local w_y of the beam. In FTU, the relation 5.11 turns out to be satisfied. Thus, in principle, the non-parallel nature of the O- and X-mode cutoffs is not expected to have much influence on conversion, as well as the asymmetric effects implied by a 2D geometry (presented in Section 3.6) should not be too strong. Nevertheless, the application to FTU of the 2D model turned out to be interesting in any case, not only to evaluate the entity of the

⁶Namely, the non-parallel nature of the two cutoff surfaces can be neglected.

expected two-dimensional effects in FTU, but, in particular, in order to make a comparison between the results obtained using this model with the ones of the mono-dimensional model developed in this Thesis and presented in the previous Section, since they are both able to consider, with different approximations, a real spatial distribution and a angular spectrum of the beam⁷, even if they are derived in different ways.

Calculations in the frame of the 2D model of O-SX coupling, with the FTU parameters

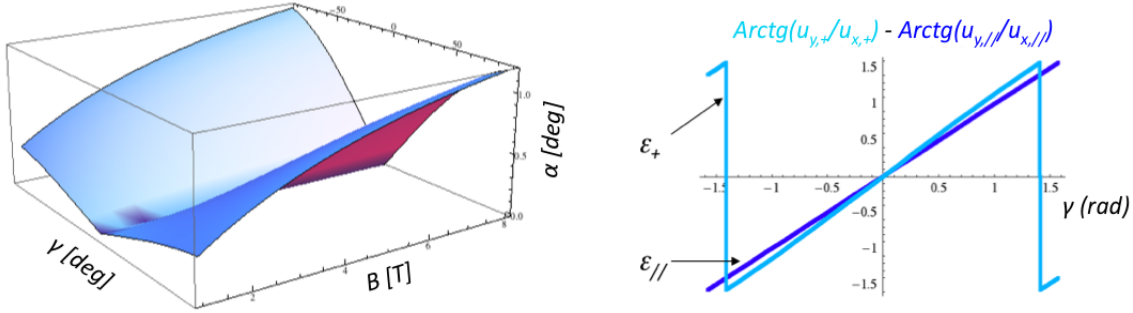


Figure 5.17: Scaling of the α angle with the magnetic field, at different poloidal positions, defined by the central γ angle of Figure 5.15 (left). On the right: circularity of the two cutoff surfaces $\epsilon_{//} = 0$ and $\epsilon_+ = N_{//}^2$, calculated with real FTU parameters, at different γ angles, defined by the ratios between the x and y components of the radial unitary vectors perpendicular to the surfaces. It is shown that the two real cutoff surfaces are not perfectly concentric and hence intersect at a certain point, depending on $N_{//}$.

have been performed assuming both optimal (see Figure 5.16) and non-optimal aiming of the beam to the conversion region, in order to estimate the entity of the asymmetries predicted by such a model and not expected in a mono-dimensional description. It must be noted that, according to the results of the 2D model presented in Section 3.6, the change of either the beam propagation, or the toroidal field sign or the poloidal injection/detection point symmetrically with respect to the equatorial plane, implies a change of the sign of the α angle, between the two cutoff surfaces. Therefore, since all of them are equivalent from the point of view of the resulting power conversion efficiency, an odd number of these changes with respect to the optimal configuration of signs imply a non-optimal conversion (see equation 3.45). The two-dimensional model reduces to a mono-dimensional one, in the limit of α going to zero (i.e. when the O- and X-mode cutoff surfaces become parallel, like in a slab description). Such a reduced mono-dimensional approach has been then

⁷Despite not the curvature of the phase front

applied using the typical parameters of the overdense plasma of FTU. As expected, the

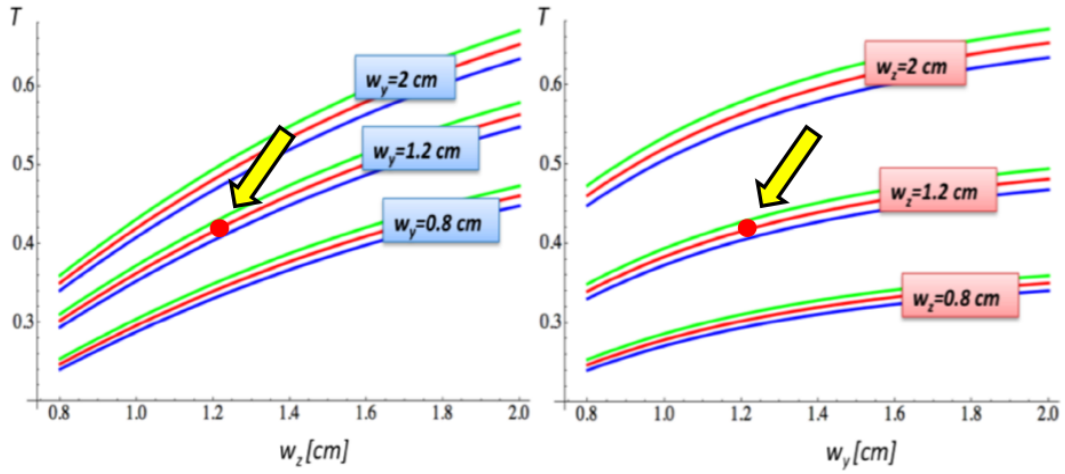


Figure 5.18: O-X conversion evaluations based on the 2D model versus different values of waist sizes w_z (toroidal direction) and w_y (vertical direction), for an incident Gaussian electric field distribution $E \propto \exp(-z^2/w_z^2 - y^2/w_y^2)$. Green and blue lines represent the cases of optimal and non-optimal directions of the beam respect to the magnetic field, i.e. different signs of N_{\parallel} or, equivalently, symmetric poloidal launching points with respect to the equatorial plane of the machine. Red lines show the results of the 2D model reduced to 1D ($\alpha \rightarrow 0$), where the influence of the beam spectrum on the conversion is considered. The case of FTU ($w_y \equiv w_z = 1.2$ cm) is represented by the red dots and yellow arrows, showing an agreement with the results of the previous Section.

resulting asymmetries of the 2D description applied to FTU, using typical real values of the α angle, turn out to be very small, while the results of the reduced 1D case (in the limit of null α) are in the middle of the two-dimensional asymmetries predicted for the power conversion efficiencies [134]. The results of these computations are shown in Figure 5.18, where green and blue lines represent the asymmetric conversions predicted by the 2D model applied with a typical finite α angle of FTU plasma, while the red lines show the results for the case $\alpha \rightarrow 0$.

According to what are the expectations typical of a 2D approach [99], the scaling of the coupling efficiency as function of the w_z of the beam waist, at a fixed w_y (left side of Figure 5.18), is slightly different from the scaling predicted by varying w_y , at a fixed w_z (right side of Figure 5.18). The dimensions w_y and w_z here reported are intended as the dimensions of the minimum waist of the incident beam on the two orthogonal y -

and z -directions; hence, the dimensional parameters originating the k -spectrum of the Gaussian beam. The expected differences in the power conversion efficiency, for optimal and non-optimal launching configurations, are just some percent (below 5%) around the conversion region of the circular waist of the typical beam launched in the ECRH system of FTU ($w_y \equiv w_z = 1.2$ cm). For this reason, from an experimental point of view, the effects of a 2D treatment are not easily detectable in EBWH experiments, which involve the application of the direct O-X-B mode conversion scheme. Nevertheless, the detection at the proper view angle, of the EBE radiation originating from a reverse B-X-O scheme, performed at two poloidally symmetric positions with respect to the plane of the machine, will be of great interest. In fact, the more stable configuration of a purely ohmic overdense plasma target (namely, when no active heating occurs), together with the possibility to detect two different signals, by performing a contemporaneous measure during the same shot interval, are expected to give chances of measuring such small asymmetries.

The 2D average conversion efficiency (red lines in Figure 5.18) for an O-polarized Gaussian beam with circular waist $w_0 = 1.2$ cm to SX-mode is predicted around 42%. Such result is in agreement with the value $\mathbb{T}_{O-SX,G} \approx 0.43$ found in Section 5.3.3, by using the 1D model with the beam-mode analysis developed in the same Section.

Chapter 6

The New Front-Steering EC H&CD Launcher

6.1 Introduction

The results of the evaluations of O-X mode conversion performed with the FTU plasma parameters presented in Chapter 5 show that with the ECRH antenna now available the wave can not be launched with the conditions required to perform O-X-B mode conversion experiments in FTU.

The first predictive evaluations of this Thesis have been carried out in coincidence with the beginning phase of the design of a new front-steering EC H&CD launching/receiving antenna, to be installed in FTU, as an additional launcher (a description of the present EC system and its limitations for EBWH experiments will be given in Sections 6.2 and 6.2.1 of this Chapter).

This fact allowed to perform the design taking into account the needs of the foreseen experiments on O-X-B heating, presented in Chapter 5. The contribution given to the design and construction of this new EC millimeter-waves launcher for FTU, presented in Section 6.4, has been part of the experimental work of this Thesis. Such a contribution has been focused to the realization of the project, with an interest which has been beyond the focus on the O-X-B experiments. Some effort has been spent on technical issues, like the ones presented in Sections 6.4.3, 6.4.5 and 6.4.6, which are not directly related to the aims of the Thesis but concern the functionality of the system. However, the work carried out for the new launcher will allow to perform the O-X-B coupling and the overdense plasma

heating experiments.

6.2 The Present ECRH Launcher of FTU

The present ECRH system of FTU tokamak ($R_0 = 0.935$ m, $a = 0.30$ m, $B_0 \leq 8$ T, $I_p \leq 1.6$ MA, pulse length $t_{pulse} \approx 1.5$ s, in Figure 6.1) is composed by four 0.5 MW gyrotron sources, each one generating Gaussian shaped microwave beams at the output [135]. Four matching optic units, formed by a focusing mirror and two corrugated polarizing optics, acting on the beams emitted by the four gyrotrons, provide for spurious modes filtering full polarization control and alignment for proper injection into the transmission lines. The waveguides sections are circular, with a 88.9 mm diameters and the input shaping optics produce a beam with a 28.6 mm waist at the entrance of the line, for maximum coupling of the HE_{11} mode in the waveguide¹, with around 98% efficiency. The lines, connecting the sources to the tokamak hall, are 40 m long each and are truncated at the end, to let the beam reach the matching mirrors of the optics of the launcher.

The electron cyclotron launching/receiving system, is constituted by four launching mirrors (one for each line) and their mountings, put under vacuum but on the external side of the vessel. The four mirrors are shaped in such a way to provide a Gaussian beam with

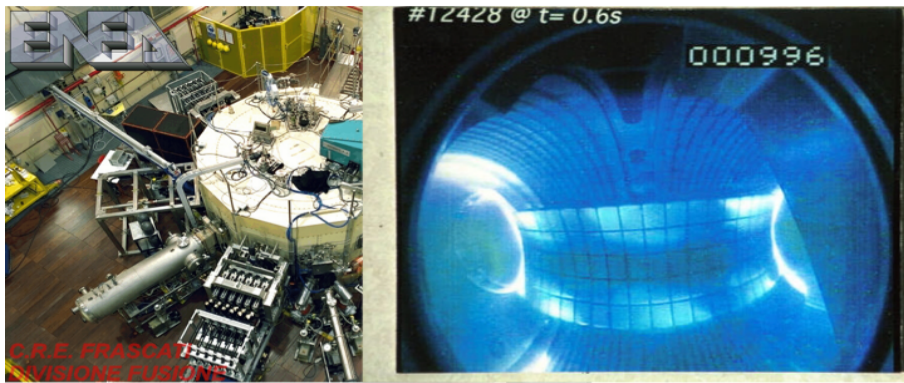


Figure 6.1: View of FTU tokamak in the torus hall (left) and visible light detection from a plasma discharge, from inside the vessel (right).

waist in the plasma region in the range of 20-21 mm. The peak power density on the beam axis at the plasma edge is $\simeq 60kW/cm^2$ for each line, giving the possibility to reach an

¹The HE_{11} mode features the more Gaussian-like electric field distribution among the propagation modes.

average heating power densities up to $100W/cm^3$, with all the beams depositing power in the same plasma volume [136].

Since at the time of the installation of the system no real-time control on the movements of the steering mirrors was needed for experiments, the system was designed such that the launching mirrors can be moved only shot by shot, with no real-time control system able to regulate automatically the injection angles on the basis of plasma parameters, and with a rotational speed of the mirror not sufficient to move them during the ECRH pulse length (0.5 s). This fact, together with the narrow port dimensions of 80 mm in width and 428 mm in height and the need to launch the four beams from a single port, led to the use of large launching mirrors located outside the port, thus far from the plasma, able to launch the beams with the smallest size in the plasma. This launcher is mounted at equatorial position, in correspondence of the 12th port of the machine vessel, which is composed by 12 identical sectors. The beams, coming out from the truncated waveguides, reach the matching mirrors, which are positioned into two vacuum vessels (upper and lower), each one provided with RF windows. The beams coming from two lines are coupled to the optics located in the upper box, while the other two lines are matched to the second (lower) box. The whole antenna is rigidly fixed to the camera of the machine, preserving the capability to follow either radially or vertically the contractions (typically of 5 mm) caused by the temperature variation due to the liquid nitrogen cooling during the operations of the machine.

The beam steering is performed by four mirrors, with 250 mm diameter ellipsoidal shaped surfaces, tilted independently one from the others, in both toroidal and poloidal directions. The different poloidal scanning capabilities for two of the four mirrors at the vessel center are showed in Figure 6.2.

While the poloidal scan can be continuous, due to the port narrowness in the horizontal direction, a continuous toroidal beam steering in a reasonable angular range is not achievable. For this reason the toroidal scan is performed by exploiting the reflections of the beam at the internal port walls. This has been made possible by inserting two reflecting plates (3 mm thick) on the lateral sides of the port, covered with 1 μ m thick gold plates, in order to enhance their reflectivity while reducing power losses (and hence thermal stresses during the pulse). In such a system, different toroidal tilts on the launching mirrors imply a different number of reflections at the inner port walls experienced by the beam, which hence penetrates the plasma with a corresponding toroidal injection angle, at the end of

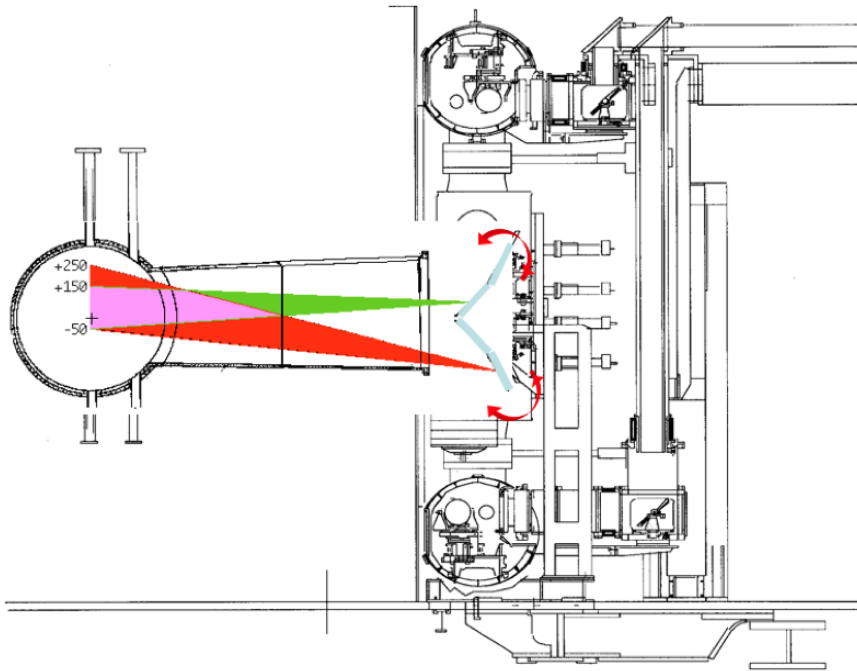


Figure 6.2: Poloidal view of the ECRH launching system, presently installed on FTU. The angular ranges of one of the central (green) and external (red) steering mirrors are shown.

the port. For a discrete number of reflections, ranging from 0 to 3, each line can correspondingly inject EC beams into the plasma with respectively 0° , $\pm 10^\circ$, $\pm 20^\circ$ and $\pm 30^\circ$ toroidal angles², in such a way that the poloidal injections is still possible independently from the toroidal one.

For the sake of simplicity in the calculations, when simulations are performed using a ray tracing code (i.e. when the divergence of the Gaussian beam is neglected), the ray path in vacuum with reflections inside the port can be replaced with a linear propagation, starting from the actual launching point at the mirror center and with a remote injection angle corresponding to the real one of the ray at the plasma edge. These angles have been calculated for the four mirrors and for the possible launching angles of the launcher, and are shown in table 6.1. The correct tilt³, which is performed using calibrated encoders, is firstly transmitted to the actuators and subsequently to the mirrors, through the vacuum

²We will show that the discrete toroidal steering capability of the present EC launcher of FTU, together with its limited possibility given by a maximum injection angle of $\pm 30^\circ$, represent a crucial limitation in view to perform experiments on O-X-B conversion.

³Which takes into account also a $7^\circ 35'$ angle between the two reflective walls inserted in the port.

Corresponding Injection Angles			
★	$\pm 10^\circ$	$\pm 20^\circ$	$\pm 30^\circ$
$M_1 - M_4$	$\mp 4.54^\circ$	$\pm 8.95^\circ$	$\mp 13.2^\circ$
$M_2 - M_3$	$\mp 4.73^\circ$	$\pm 9.35^\circ$	$\mp 13.8^\circ$

Table 6.1: Steering angles for the linear propagation from the remote position of the four mirrors to the plasma, corresponding to the injection angles from the end of the port, after the ray bouncings at the port walls. These values have been used for performing calculations with the ray tracing code for propagation in the present launcher of FTU.

flange, with the use of bars and bellows which convert rotation to a linear movement at the mirrors (and vice-versa). For all the steering angles, the tilts are such that the beam comes out at the center of the port, in order to minimize its interactions with the port edges.

6.2.1 Limitations of the Present Launcher for Experiments on O-X-B Mode Coupling

The present ECRH launcher of FTU was installed on a single equatorial port of the machine and was designed to inject four independent (140 GHz) beams, steerable continuously in poloidal direction but just in a set of fixed toroidal angles. The limitation to $\pm 30^\circ$ in the maximum toroidal steering and the discrete capability of the system in the launch, are not compatible with the fine regulations needed to perform O-X-B experiments and demonstrate EBWH in FTU. As shown in Chapter 5, the required toroidal angles predicted for the typical plasma parameters of FTU turn out to be in the range $38^\circ - 40^\circ$. Such steering angles can not be reached with the present launching system, which is then capable to provide a parallel component of the wave refractive index which is too low for the O-SX coupling. Geometrical computations were performed, in the beginning, in order to evaluate the increase of N_{\parallel} along its path towards the plasma center (see Figure 6.3). Also the possibility to launch the beams not exactly from the center of the port exit (slightly changing the toroidal angle of the launching mirror) was considered, to enhance the N_{\parallel} of the launched wave. A simplified model was developed to evaluate these launching conditions (see Figure 6.4), using *Mathematica*[®] software. Several alternative launching configurations could be studied, where the beam passes from a non-central point of the

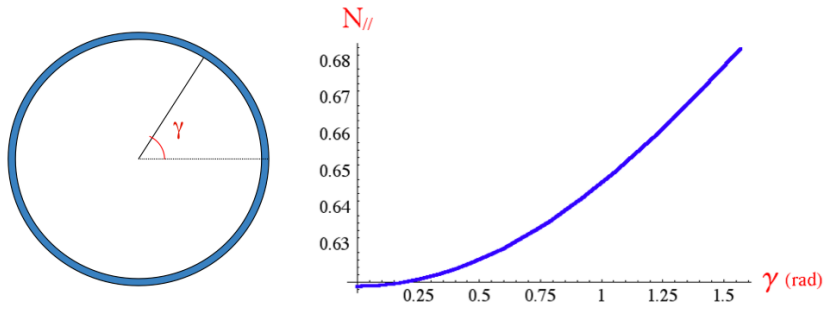


Figure 6.3: Increasing of the N_{\parallel} that, in principle, can be obtained at given circular surface (represented with the blue circle on the left) by using a poloidal component in the ray injection, versus the central angle γ . The computations are performed assuming a fixed toroidal component of the refractive index, a straight path of the ray and a purely toroidal magnetic field scaling as $1/R$.

port exit. Nevertheless, since the maximum toroidal injection angle that can be reached with this technique is not higher than $\approx 31.5^\circ$, while a more risky launch is performed, from the point of view of the interaction of the beam with the side-walls at the port exit, also this option had to be rejected.

In addition to the limitation in the maximum injection angle, also the discrete capability of the system does not enable to provide the correct direction of the beam for conversion at cutoff. The O-X (X-O) conversion window to be reached with the ray launch has been demonstrated to be very narrow ($\sim 2^\circ \times 2^\circ$) and centered around couples of very precise (toroidal and poloidal) angles. Such a discrete launching capability, with a 10° step, can not satisfy the needed injection fine tuning, at all. For these reasons, an O-SX mode coupling (and consequently EBWH at the plasma center) can not be performed in FTU tokamak, using the present ECRH system.

6.3 Motivations for a New ECRH Launcher

In addition to the limitations of this launcher in view of EBWH experiments, recently its features were not suitable for other applications conceived for modern tokamak, like ITER, despite the present system has been used with success for a large number of experiments, up to now. The limitations in the toroidal injection of the beam, together with a launch control performed not in real-time during the shot and the remote-steering configuration of the optics, prevent experiments aimed to validate schemes, techniques, and algorithms

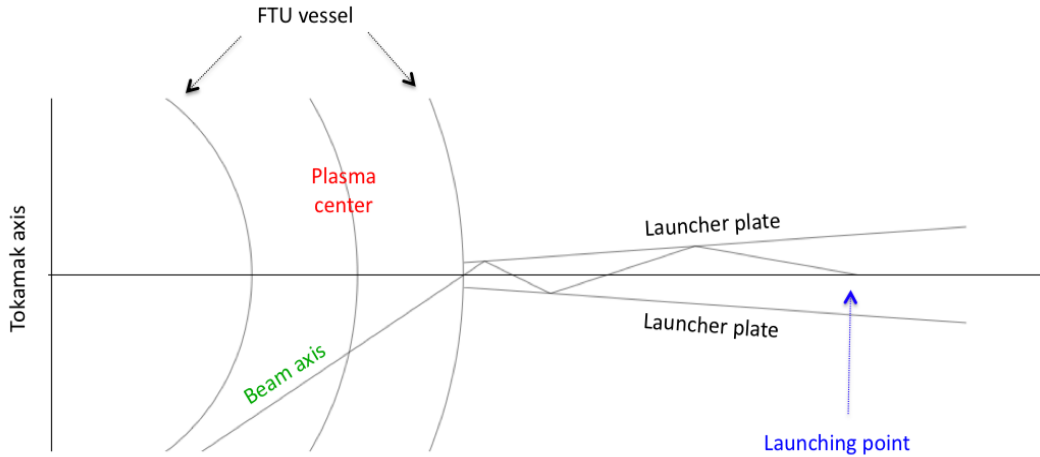


Figure 6.4: Real scale model of the present FTU launcher, made using *Mathematica*[®] software. The two oblique side walls of the launcher, used for beam bouncing, and the FTU camera are represented. In the picture, an example of wave injection at -30° is shown, exploiting three bounces of the beam at the internal gold-covered walls of the launcher. In the example, the beam axis passes from the center of the port aperture. Such condition is usually chosen in FTU, to minimize the interactions of the beam sides with the port walls. This geometrical model have been used to evaluate other possible launching configurations, able to increase the N_{\parallel} of the beam in the plasma, in view of O-X-B experiments.

to control MHD instabilities with EC H&CD so important for ITER. These experiments require fast-steerable mirrors in the launcher of course, in addition to an increased toroidal capabilities needed for the O-X-B experiments. The NTM stabilization requires algorithms developed to detect and stabilize magnetohydrodynamic instabilities [47], [48], [137]. The possibility to change the location of the power deposition following the magnetic island in real-time is necessary, in order to test such an ITER-relevant NTM control system in present devices, like FTU. This requires, for instance, that the poloidal steering mirror drive is controlled automatically by a feedback control loop.

Finally, other important experiments, already carried out in FTU during the past campaigns, could not be implemented without a time-dependent current profile shaping, obtainable performing local ECCD whose location is controlled in real-time during the evolution of the plasma. Indications of crucial importance for ITER may derive also from repetition of such experiments with a feedback controlled current drive.

Therefore, the interest in demonstrating EBWH at 140 GHz in the FTU plasma, via O-X-

B mode conversion, together with the other scientific motivations described above, with particular attention to the test and validation of several strategies proposed for ITER, aimed to control MHD instabilities, brought to the design and construction of a new EC H&CD front-steering launcher, at IFP/CNR Milano. This new system is characterized by an extended versatility in term of either beam injection or dimension control, with respect to the present one. Its installation on FTU tokamak is scheduled for the beginning of 2011. The active participation to the work carried out for the design and construction of this new launcher represents the main technical aspect of the effort put into this PhD Thesis.

6.4 Design of the New EC H&CD Launching System

Two ECRH transmission lines, now feeding the present ECRH launcher, could be switched to a different equatorial position in order to feed the new launcher being installed in FTU [138], [139] (see Figure 6.5). The system is designed with two identical antennas

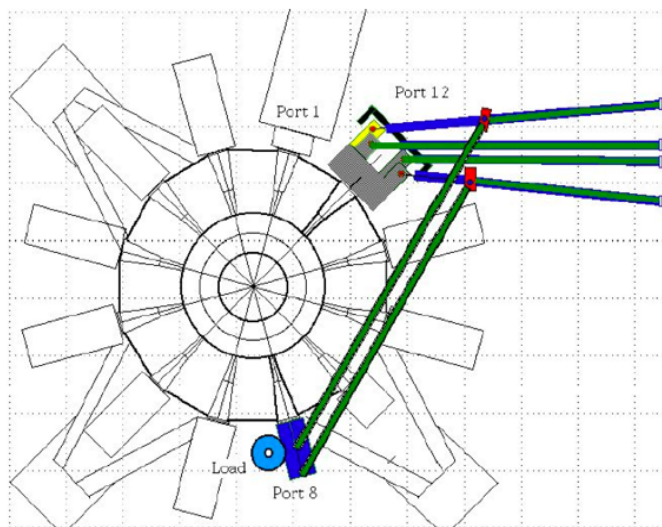


Figure 6.5: Top view of FTU. Two (lines #1 and #4) of the four transmission lines of the present launcher (top-right) are switched from port #12 to port #8, to feed the new system (bottom).

in a front-steering configuration. A picture of the system and a couple of schematic representations of it are shown in Figure 6.6 and 6.7. The system presently installed on the machine will be left unchanged. The installation of the new launcher is foreseen in correspondence of a different equatorial port of FTU (port #8), in such a way that an

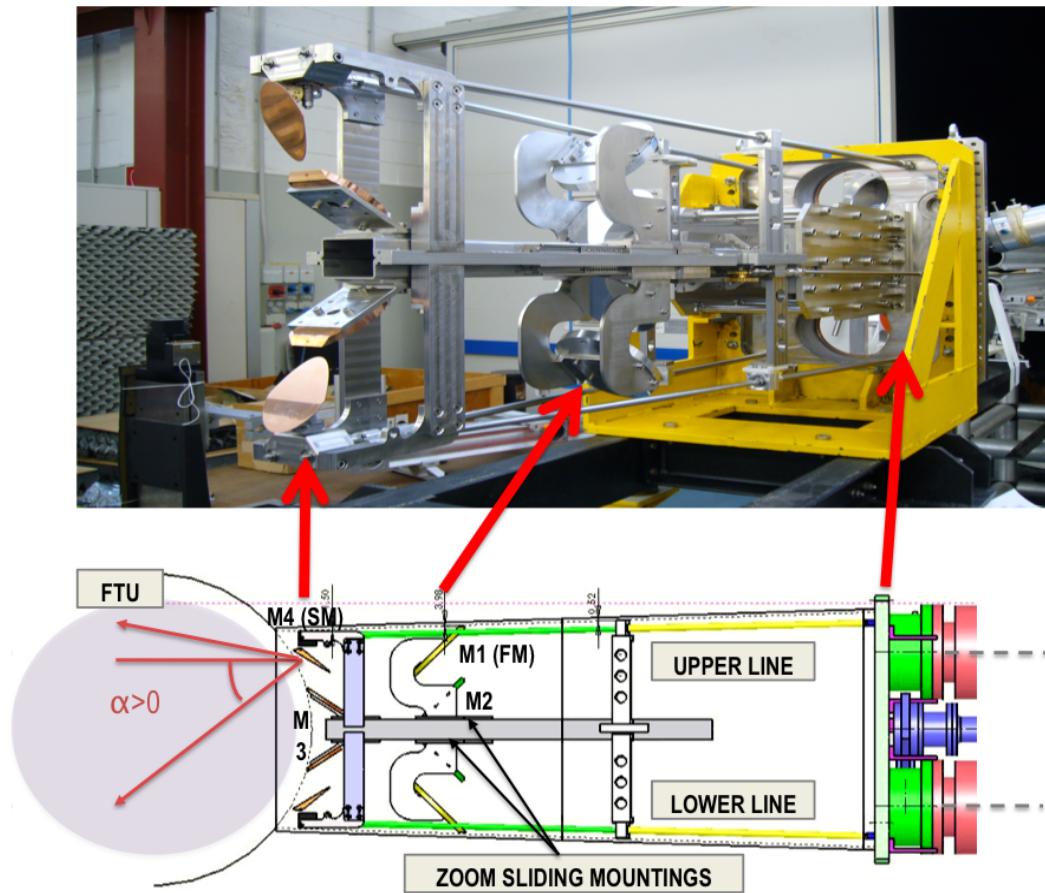


Figure 6.6: Picture of the final version of the launcher, in the laboratories at IFP-CNR Milano (up) and a schematic representation of the system (down), where the positions of the steering mirrors, the zooming optics and the vacuum flange are shown (red arrows).

easy plugging in (and out) of the system on (from) FTU can be carried out easily. In this way, in case of necessity, it could be fully extractable for maintenance or refurbishment of components, with a low impact on the plant. Port #8 is located at a toroidal angular position of 120° with respect to the port dedicated to the present ECRH launcher (port #12). Four ECRH lines of the six that will be available on the present and the new launcher, will be matched to the four gyrotron sources and will become useful to launch EC waves, while the two spare lines can be used for millimeter-wave diagnostics, since the new antennas will also be switchable to receiving lines. In the future, a seventh line could be available, since place has been reserved in the design of the new launcher for the future insertion of a square waveguide, to be used as a remote-steering antenna. Despite

each gyrotron of FTU is capable to deliver 500 kW and 500 ms as maximum power and pulse length, the lines of the new launcher are designed such that a doubled power can be handled, in a way that the radiation coming from all the four gyrotrons might be combined in future experiments, making use of combiner devices being developed also at IFP-CNR Milano [140], in collaboration with other associations [141] [142] [143]. When not directed into the plasma, the total power delivered to the end of the transmission will be absorbed and measured with calorimetric matched spherical loads, [19] [144], realized at IFP-CNR Milano.

The new system is capable to launch two beams into the plasma, by using small movable mirrors put in the plasma proximity, in a front-steering configuration. The two beams can be steered independently and, unlike the present system, the launching angles will be changed during the ECRH pulse length, in real-time, in both toroidal and poloidal directions, using a control system operating on a closed feedback loop algorithm, based on precise reference plasma parameters. The feasibility of an independent beam injection, in real-time, is of crucial importance in view to perform experiments with an ITER-relevant approach. As already said, one of the main scientific purposes for the design and

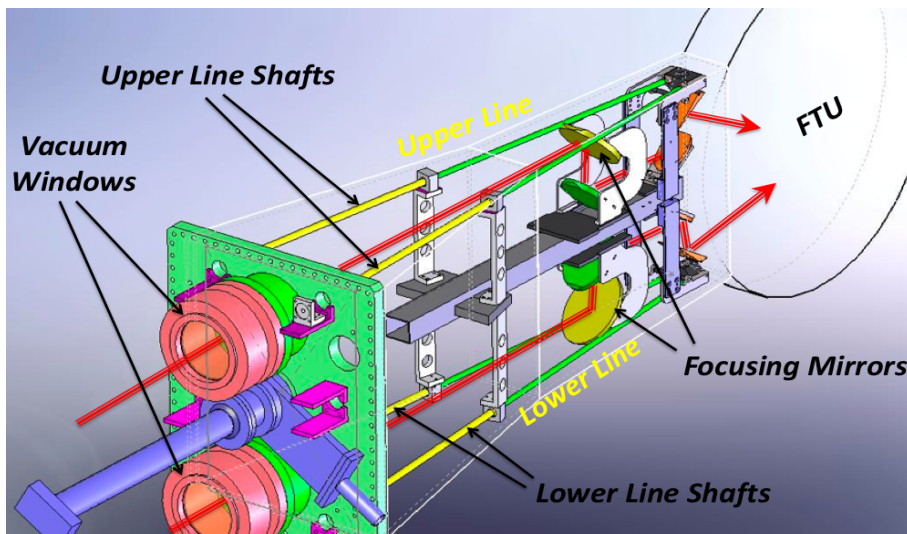


Figure 6.7: 3D drawing of the overall new system. The two symmetric lines are shown (upper and lower), with the respective components: vacuum windows, zooming systems, shafts for the transmission of the toroidal-poloidal movements and internal optics. The ray path in the lines of the launcher are indicated with the two thick red arrows.

construction of a new ECRH launcher for FTU is the demonstration of EBWH in the

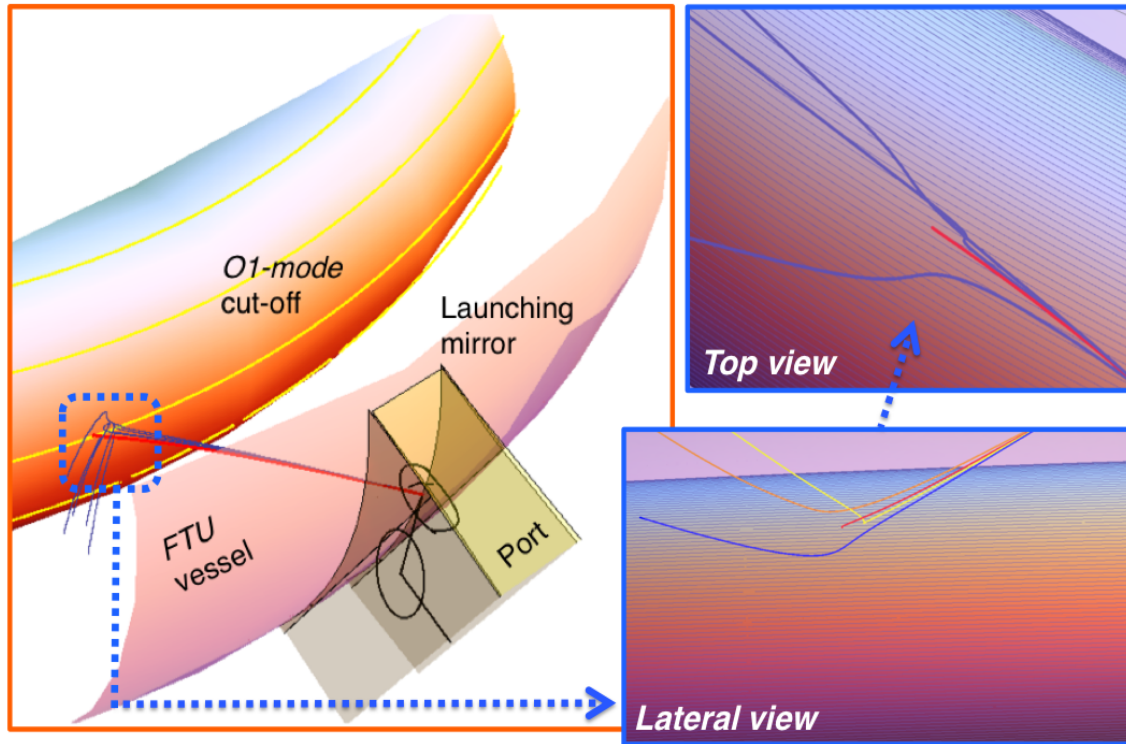


Figure 6.8: Left: view of the upper line of the new launcher, in a simulation relevant for O-X-B mode conversion experiments. Ray tracing computations of some rays (blue) steered towards the 1st harmonic ordinary mode (O1-mode) cutoff layer with slightly different injection angles, centered around the optimal ones for O-SX coupling (red ray), are shown. The cutoff surface, nested by the magnetic sheared field lines (yellow curves), is calculated from the real plasma parameters of a typical high density discharge of FTU. Right-down: zoomed view in the proximity of the cutoff region where the blue rays (non-optimal) are back-reflected and the red ray (optimal) is converted to SX-mode beyond the cutoff layer (such a SX-polarized ray is not visible in the picture). Right-up: the region of conversion further zoomed, in a top view. The ray tracing calculations show how the phase velocity of the red ray, which is the only one with optimal aiming, is parallel to the magnetic field lines (thin blue lines) at cutoff.

tokamak-like plasma of FTU, at the 140 GHz frequency. The stimulus in doing that was born from the high density regimes reachable in this device with the use of Liquid Lithium Limiter, as shown in Chapter 4. The new launching system, which is capable to satisfy the toroidal requests in the launch, in order to enable optimal coupling between O- and X-mode. Such features are a toroidal injection up to $\pm 40^\circ$ and a fine continuous scanning capability, in both the directions. The angular range of the poloidal steering at the plasma center ranges approximately from -25.5° to $+25.5^\circ$, ensuring the scan of more than 75% of the plasma volume.

6.4.1 Real-Time Control of the Steering Mirrors

For the precise definition of the dynamic of the system, the typical plasma target for MHD stabilization experiments was considered. In particular, the dynamic of the poloidal feedback control has to follow the magnetic island movement during the shot, in absence of any feedback on plasma position. The position of the island will be tracked with the beam in real-time, controlling the injection angle at the mirrors, with the dynamics required in the FTU plasma, so that the power can be deposited in the island even when it moves following the Shafranov shift. This will open the possibility to improve MHD stabilization techniques, already tested in FTU during past campaigns [47] [145], in which fixed launching angles have been used.

The requirements on acceleration, speed, and position precision on the wave injection, given by the experimental needs, are very stringent, since the required scanning dynamic for tracking the rational surfaces in the plasma is estimated, from experimental observations, to be 1 cm in 10 ms in poloidal direction [47]. In fact, the evidences (shot #27714) showed a poloidal displacement of the magnetic island of 4 cm in 40 ms. The maximum instantaneous error of the deposition must remain limited to 0.5 cm, which provides a minimum limit in the required angular steering accuracy, that must be $< 0.5^\circ$. The dynamic requested in the FTU case are faster than the one expected for ITER, because of the faster time of MHD instability growth rate⁴. Given the geometry of the system, such a dynamic means a poloidal angular velocity of approximately $1^\circ / 10$ ms.

Despite the fact that the precise speed request for the design of the launcher was chosen considering the MHD stabilization experiments, a fast dynamic, together with a real-time control of the system in feedback on the plasma parameters, turns out to be useful for

⁴The time between the appearance of the island and its maximum development is ≈ 20 ms.

experiments on EBWH, if an automatic control of the wave injection angle could be performed. In principle, in this case, the faster is the dynamic of the steering, the higher is the efficiency of the tracking, since, as already said, some phenomena, like density fluctuations and the stability of a tokamak-like plasma configuration, may affect the fine angular tuning of the injection. Such phenomena can not be predicted completely a-priori and may change the plasma parameters very quickly, on the time scale of a typical launching dynamic. For this reason, the minimum target level for the velocity of the system considered in the design was defined on the basis of the typical development dynamics of the tearing modes in FTU; and actually, such a minimum request turns out to be already challenging, as well.

The main parameter to be considered for the feedback control, in case of EBWH, is the amount of stray radiation detected in the vessel by the sniffer probes, during the operations. In fact the level of stray radiation is complementary to the launched power which is absorbed by the plasma. In the O-X-B scheme, such a power is the one coupled to EBWs and then absorbed at the cyclotron harmonics. Thus, the correct algorithm to be inserted in the feedback control loop should allow to inject the wave while keeping the minimum level of the stray radiation signal. Such a control, may allow to perform first an identification and then a tracking in real-time of the angular conversion window at the launch, in order to inject the wave with the direction that allow the maximum power conversion efficiency at cutoff. Despite not included in the first step design, also a toroidal feedback control is being considered in the final design for this aim, in addition to the poloidal one. Only acting on both directions, in fact, a fine tuning of the optimal launch can be performed.

Concerning the algorithm for tracking the conversion window, different preliminary solutions are now under discussion. The differences between the approaches under study concern mainly the different exploitation of the launcher dynamics, when different typologies of spatial scans are performed with the launched beam around the (presumed) initial optimal direction, while measuring in real-time the signal of the sniffer probes, proportional to the stray radiation in the camera. Such techniques will be implemented and tested with preliminary simulations in the next future.

Other important objectives of the newly proposed system, in addition to the overdense plasma heating via O-X-B scheme and the TM stabilization, are, for instance, the automatic control of the driven current profile and the Electron Cyclotron-assisted plasma

start-up. The system will in principle enable a real-time control of all the plasma parameters affected by local EC power deposition, like the transport barriers formation and temperature profile shaping, including control of sawteeth crashes frequency. Finally, the antenna can be alternatively used for diagnostics. For instance, to detect the perpendicular and oblique ECE signal, to perform reflectometry measurements and Collective Thomson Scattering diagnostics.

6.4.2 The Steering Mirror and the Driving Mechanism

The fast dynamics required for the experiments, led to the choice of movable parts with the minimum possible momentum of inertia, in particular for the last steering mirrors. This request adds to the geometrical limits imposed by optical needs and thermal loads on the surface of the mirror, which increase with the inverse square of the spot size.

Additionally, strong physical limitations are given by the reduced dimensions of the port (90 mm in width and 428 mm in height, to be shared by both the mirrors of the two lines) in the plasma proximity.

Additional constraints for an efficient O-X conversion are very stringent on the choice of the launching mirror size. They consist in a toroidal launching angle up to around $\pm 40^\circ$ with respect to the beam axis⁵, together with a toroidally symmetric injection.

The final dimension and shape of the mirrors is the result of a trade-off between the requirements and the geometrical constraints. The final shape that was chosen, consists in a 81.4 mm height, 52.1 mm width surface, elliptically shaped on the plasma edge and with a parabolic profile elsewhere (see Figure 6.10).

The material selected for constructing the fast steering mirrors is the *Glidcop*[®] DS copper, chosen after an accurate analysis of the thermal stresses during the operational conditions [138] [139], in order to lower its inertia, the backside of the steering mirror is constructed with a decreasing thickness, ranging from 5 mm, at the central region, where the thermal stresses are higher, to 1 mm at the edges, since lower power density is expected in this region. This structure will be sufficient to prevent possible damages to the mirror, given by power accumulation. Additionally, to enhance radiative cooling of the copper body from shot to shot, its backside has been covered with a thin plasma sprayed Cr_2O_3 thin layer, used as a ceramic cover with high emissivity.

The mirror is connected to the driving mechanism on the backside, shown in Figure 6.11.

⁵Corresponding to a range $\pm 60^\circ$ for the actual rotation of the mirror around its own axis.

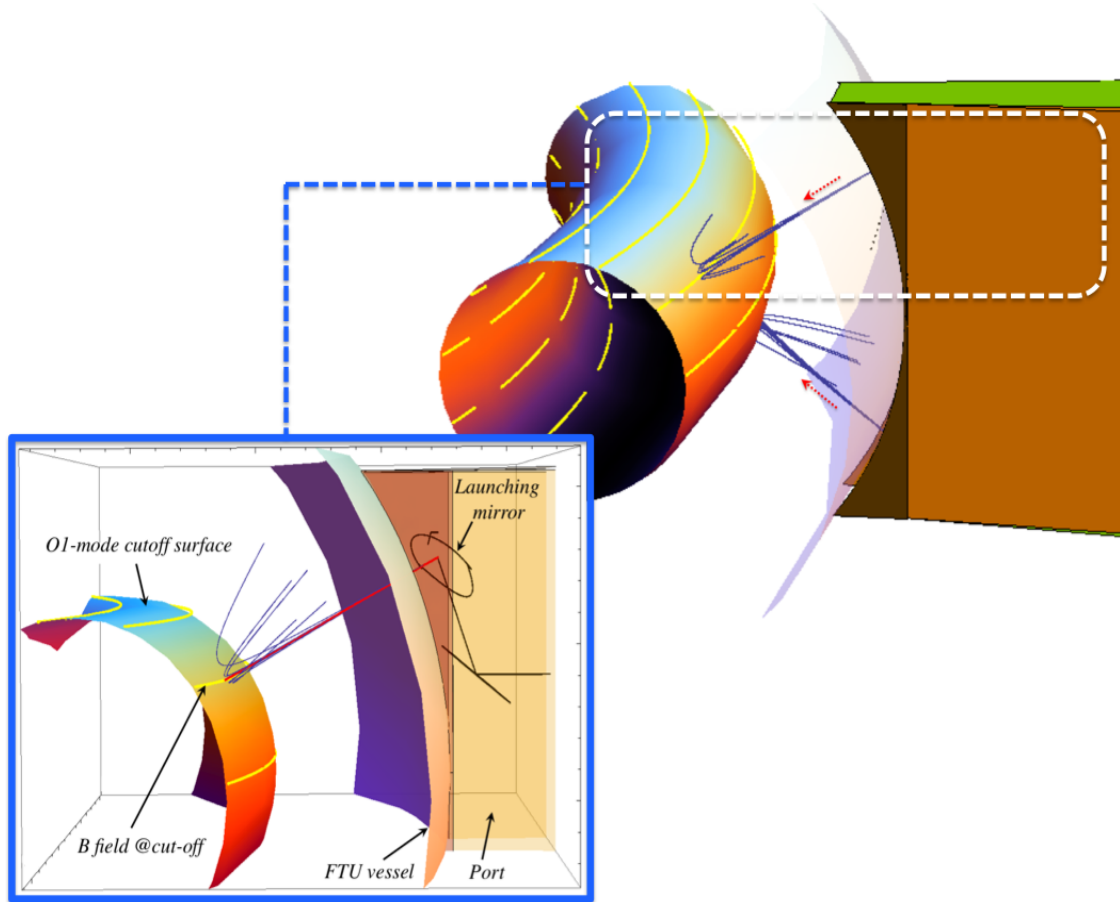


Figure 6.9: Tridimensional view of the front part of the new EC launching system of FTU, in a simulation performed with *Mathematica*[®] software, in a relevant operation for O-X-B mode conversion. The upper and lower lines are shown, while launching several rays with opposite sign of the N_{\parallel} ad from opposite poloidal points, as will be possible to do with the new system (top right). The O1-mode cutoff surface and the magnetic field lines on it (yellow lines), are calculated with the real plasma parameters of FTU. In the figure on top, the side of port #8 closest to the plasma is represented. The picture on the bottom left is a more detailed view of the upper line (zoom of the white dotted region). Despite all the rays are injected approximately with the same toroidal and poloidal angles, only the red ray represents the beam axis for optimal O-X conversion. All the others (represented by blue rays) are reflected partially or totally at cutoff, since they propagate with non-optimal aiming to the conversion region. In the picture on the bottom left, the last two mirrors of the line and the path of the ray internal to the launcher are shown.

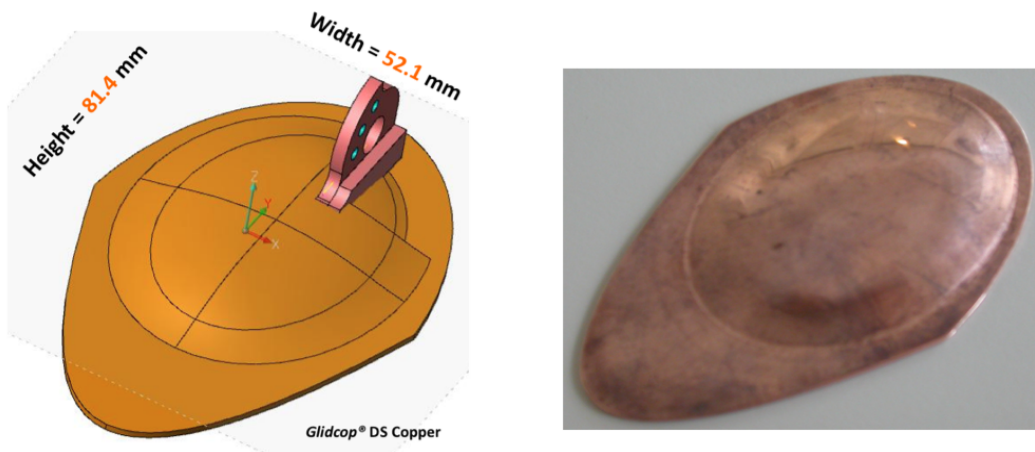


Figure 6.10: Drawing (on the left) and picture (on the right) of the back side of the steering mirror, before the deposition of the plasma sprayed Cr_2O_3 layer, used to enhance the thermal emissivity. The particular shaping of the back side is shown, together with the dimensions of the mirror, indicated in the drawing on the left.

This choice derives from the need to minimize weights and moments of inertia of the overall system. Both poloidal and toroidal motions are transferred to the mirror through the same axis and coaxially in the mechanism. The motions is transferred to the outside with shafts connected to worm-wheels with low reduction ratio and backlash minimization, mounted in the driving mechanism on one side and to the motors located outside of the vacuum flange thanks to the use of rotary vacuum feedthroughs.

The coupling of toroidal and poloidal movement has to be considered during operations with the launcher and it must be accordingly corrected, when toroidal dynamics are involved, since no toroidal coupling exists when the mirror is moved only poloidally (at a fixed toroidal angle).

6.4.3 Motors and their Control

The fast dynamics required to perform MHD stabilization and O-X-B mode conversion experiments, exploiting a tracking in real-time of the tearing modes and of the O-SX conversion window, respectively, has been taken into account for the choice of all the main components, in particular the motors to be used to move the steering mirrors. The overall mechanical inertia of the system has been modeled estimating in a simplified way [146] the torque due to the eddy currents induced in the complex structure of the steering mirrors

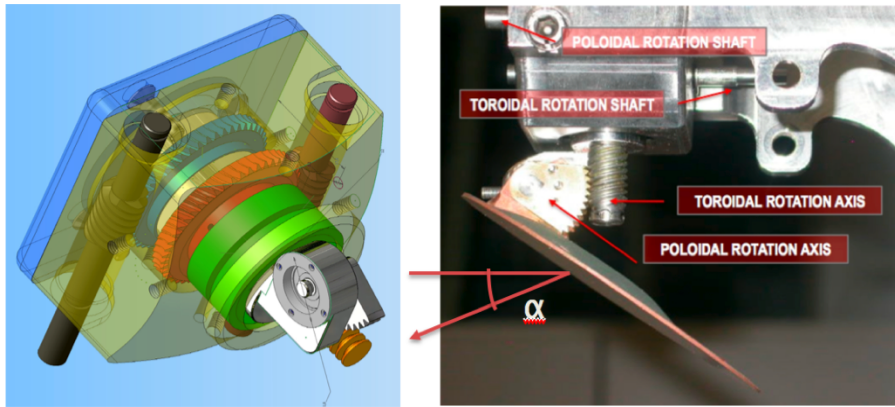


Figure 6.11: The inner structure of the moving mechanism of the last mirrors is shown in the picture, on the left; the real mechanism, with the mirror attached, is shown on the right.

put in the region of high tokamak field.

Motors with maximum rotational speed capability of 10000 rpm and the peak torque ($\pm 10\%$) of 1.44 Nm were selected. Predictive evaluations on dynamics have been performed also in order to insert the proper motor drives, to control the motion of the motors. Digital drive inverter model [147] provided with a PI speed controller [148] were selected.

To move the steering mirrors of the launcher in real-time during operations without crossing the safe boundary of the permitted angular workspace⁶, an antenna position controller and a predictive software protection system [149], based on a real-time algorithm, have been implemented, in collaboration with the University *Politecnico di Milano*. Such a protection system is important in particular in view of operations performed in the proximity of the extreme angular regions of the launcher, like the ones expected for O-X-B experiments. In fact, the highest values of the toroidal injection angles, up to the maxima allowed values of $\pm 40^\circ$, are foreseen during these kind of experiments, while performing a real-time control of the steering mirrors position in feedback with the plasma parameters. This position is then compared with the region of available angles that will have been fixed in the control system before the operations on the plasma. In case of intervention of the protection system, the speed reference is set immediately to zero and a motor brake, fed by the drive with a 24 V DC power supply, intervenes on the shafts.

⁶In particular, this may happen in case of a fault in the controller.

The control system to be used in FTU is implemented on a PXI PC-based platform⁷, in which two Digital Signal Processor and five I/O Field Programmable Gate Array (FPGA) boards useful for parallel processing are mounted on the communication buses. FPGA boards collect the fast analog channels coming from the FTU plasma⁸ and implement the plasma shape and the ray tracing code, while the last one implements two Bayesian filters, used to match plasma shape and ray tracing [132] predictions, with the observed quantities. The tests performed so far, led to an optimization of the proportional, integral and derivative gains of the PID controller, to the best compromise between rising time, overshoot and settling time in the motor response, demonstrating that the system is capable to reach the dynamics of $\simeq 1^\circ$ poloidally at the mirror in 10 ms, required in the design phase.

6.4.4 The Influence of Different Beam Size on O-X-B Mode Coupling

In order to have a control on the deposited power density, also the possibility to change the beam radius in the plasma is included in the design of the launcher. Such a zooming system, shown in Figure 6.12 is obtained with a couple of mirrors in a dog-leg configuration, installed under vacuum. The position of the mirrors, one of which has a focal length $f = 510$ mm, can shift ± 100 mm with respect to a zero reference position, providing a beam waist of 12 mm in different positions around the steering mirror region (see Figure 6.13), for different positions of the zooming optics, thus providing a range of different local spot sizes at the plasma center, in the range 17 - 27 mm. Measurements carried out at IFP/CNR Milano [151], using one of the two lines of the system, confirmed the design goals.

Despite the plane wave spectrum of the launched beam depends only by the waist at the reference plane w_0 (and hence, in our case, it is fixed by the value $w_0 = 12$ mm), also the curvature of the phase front at the cutoff layer is expected to have an influence on the mode coupling. Such an influence, when not negligible, might affect the optimal value of power transmission efficiency. In fact, since in the FTU case the reference plane of the launched Gaussian beams are always external to the overdense plasma region for all

⁷During the test phase the PXI was generally substituted by a NI Compact-RIO [150] as a control and data acquisition system.

⁸The signal detected by the sniffer probes, in the case of the real-time control that will be performed for EBWH experiments.

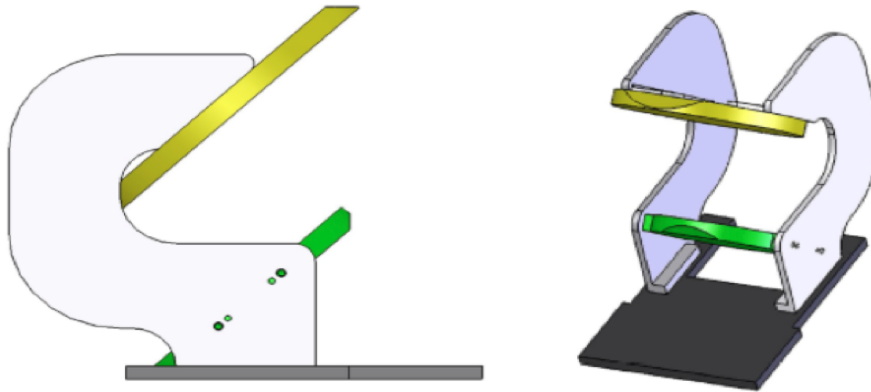


Figure 6.12: One of the sliding optics mounted in the two lines, used as zooming systems. One of the mirror (green) is flat, the other one (yellow) is focusing.

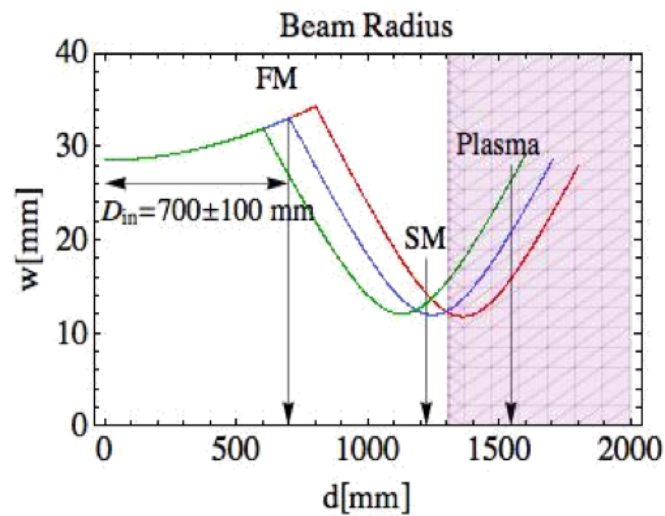


Figure 6.13: Beam radius, at different distances from the last waveguide aperture and for central and extremes positions of the sliding mounting of the zooming optics. The positions of the focusing mirror (FM) and of the steering mirror (SM) are shown (picture taken from [151]).

the position of the sliding mounting⁹ the curvatures of the beam phase front and of the O-mode cutoff surface, are always one the opposite with respect to the other. This implies a sort of curvature mismatching that was not considered in the frame of the models of mode conversion described in the previous Chapter. Thus, the zooming system available in the new launcher will offer the possibility to test the actual influence of different spot dimensions (i.e. of different phase front curvature radii) at the conversion region.

6.4.5 Low Power Tests with the Launcher at Angles Relevant for O-X-B Mode Conversion

The low power tests at 140 Ghz have been performed at IFP/CNR Milano [152] [151], in order to define the optical performances launcher. An input beam waist $w_0 = 28.6$ mm was reproduced in correspondence of the waveguide aperture.

Several beam patterns have been acquired with the VNA, at different output (injection) angles and for different shifts of the inner zooming optics (a couple of pattern measurements are shown in Figure 6.14). In some tests, also a metallic side-walls mock-up of the real FTU port was used, to reproduce realistic conditions from the point of view of either reflections and interactions of the beam with the walls or diffraction and beam truncation effects at the exit of the launcher. Estimates of the beam dimensions at the distance of the vessel center where performed in order to evaluate the beam shape and astigmatism. Further measurements were performed then, at fixed injection positions and at the reference or extreme positions of the zooming optics. Patterns have been measured also for the case of toroidal injection angle $\beta = 39.5^\circ$ and a poloidal angle $\alpha \approx 26^\circ$, relevant for O-X-B experiments.

Beam pattern were taken with the mock-up of the FTU port surrounding the launcher, in order to measure the effects of the tight closeness between the mirror and the port, in particular for high values of the toroidal angle. The observed pattern corresponds to a well shaped Gaussian beam, which shape is acceptable either from the point of view of the symmetry or for the presence of side lobes, despite some diffraction effects are visible, due to the expected partial interception of the beam edge by part of the port mock-up.

⁹The design of the launcher is such that the waist w_0 of the beam corresponds approximately to the region near the exit of the port, in order to have the narrower beam spot size on the last steering mirror.

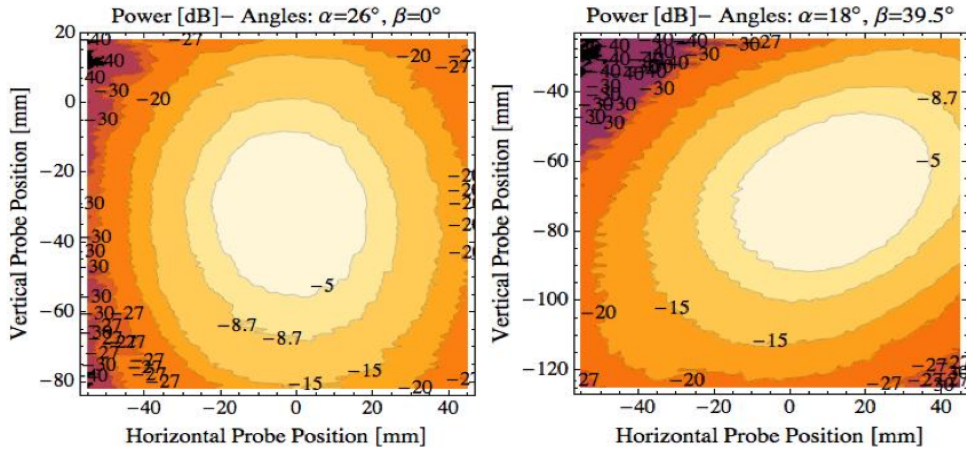


Figure 6.14: On the left, the beam pattern at the output of one of the lines is shown, measured at plasma center, with null toroidal angle ($\alpha = 26^\circ$, $\beta = 0^\circ$). In the example, the zooming mounting was put at the minimum distance 600 mm from the waveguide end (i.e. configuration for the largest spot in the plasma). On the right, a beam pattern acquired at plasma center, with a typical angular position of the steering mirror foreseen for O-X-B experiments. The poloidal and toroidal angles are $\alpha = 18^\circ$ and $\beta = 39.5^\circ$ with respect to the mirror axis. The distance of the zooming system from the waveguide exit is the nominal one (700 mm) in this case. The elongation of the spot is a geometrical implication of the measure, performed with a scan of the receiver on a plane perpendicular to the port axis, while the beam is incident on this plane with an angle $\neq 90^\circ$.

6.4.6 Dynamical Tests on a Real Scale Mock-up of the New System

The preliminary tests on the dynamics of the fast EC launcher for FTU have been performed on a real-scale mock-up, reproducing one of the two lines of the system. Two of the motors have been mounted on the launcher mock-up and a prototype control system, selected in collaboration with *Politecnico di Milano*, was assembled, including brakes, encoders and controlling hardware. The response of the system (i.e. antenna, gears, shafts, motors and drive inverters) has been obtained for different reference steps. In particular, the dynamics foreseen in the real-time controlled operations of the future O-X-B experiments, could be tested in a preliminary phase. The main aim was the optimization of the proportional, integral and derivative gains (PID) of the motors controller, taking into account the constraints of the rising time, overshoot and settling time required by the experiment. The resulting proper PIDs, for both toroidal and poloidal movements of the antenna have been selected, to be included in the control algorithm.

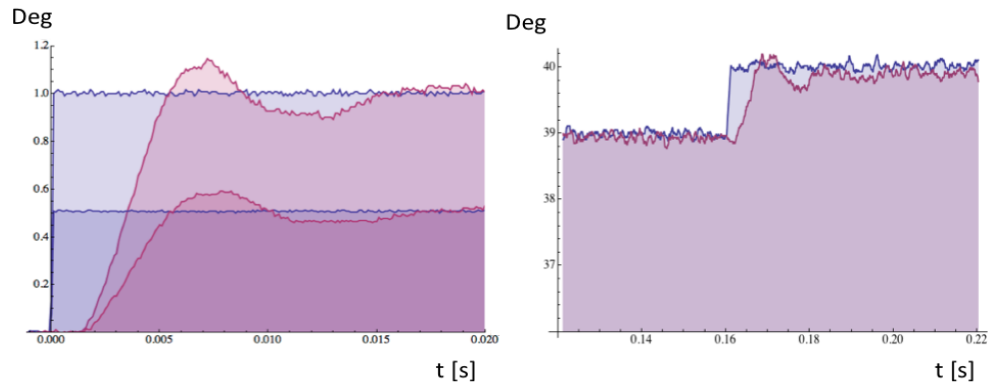


Figure 6.15: On the left, the toroidal response of the positioning system (purple lines) of the launcher mock-up to 0.5° and 1° steps (blue lines), with the launching mirror connected to the shaft. These kinds of request on the movement are the typical ones requested during an automatic tracking in real-time of the conversion window. In this example, the PID parameters of the controller were regulated in such a way to have a fast response (rise time near 5 ms) and a higher overshoot and settling times. On the right, a similar 1° step request is showed, but this time starting from a 39° toroidal angle to 40° , in the typical angular range for O-X-B experiments.

In the tests results obtained on the mock-up, also the steering speed required on the launching mirror for MHD stabilization experiments, corresponding to a scan speed of 1 cm to be scanned at plasma center in 10 ms, on the vertical axis (corresponding to an angular velocity of $1^\circ/10$ ms in the poloidal direction), turns out to be satisfied. Actually, the system is capable to reach even faster dynamics, but this is obtained to the detriment of the precision in reaching the proper position, due to the larger overshoot for faster movements. For instance, the results reported in Figure 6.15 show how both a 0.5° and 1° angular movements can be performed in $t \approx 5$ ms, namely shorter than the design specifications, but with a consequent overshoot, such that the final positioning is reached steadily only after $t \approx 20$ ms. Hence, the proper balance in the choice of the best PID parameters for the controller, to be used for O-X-B experiments, is linked to the choice of the optimal algorithm to be used for the experiments. More precisely, the requests and the allowed tolerances on the rising time, on the overshoot and on the settling time of the system response will be closely related to the technique considered for the control of the wave injection angle. Since such an algorithm is still under study now, the final optimization for O-X-B experiments will have to be carried out once the kind of control to be used for the tracking of the conversion window will have been conclusively defined.

The dynamics of the brushless motors was tested also in presence of an external magnetic

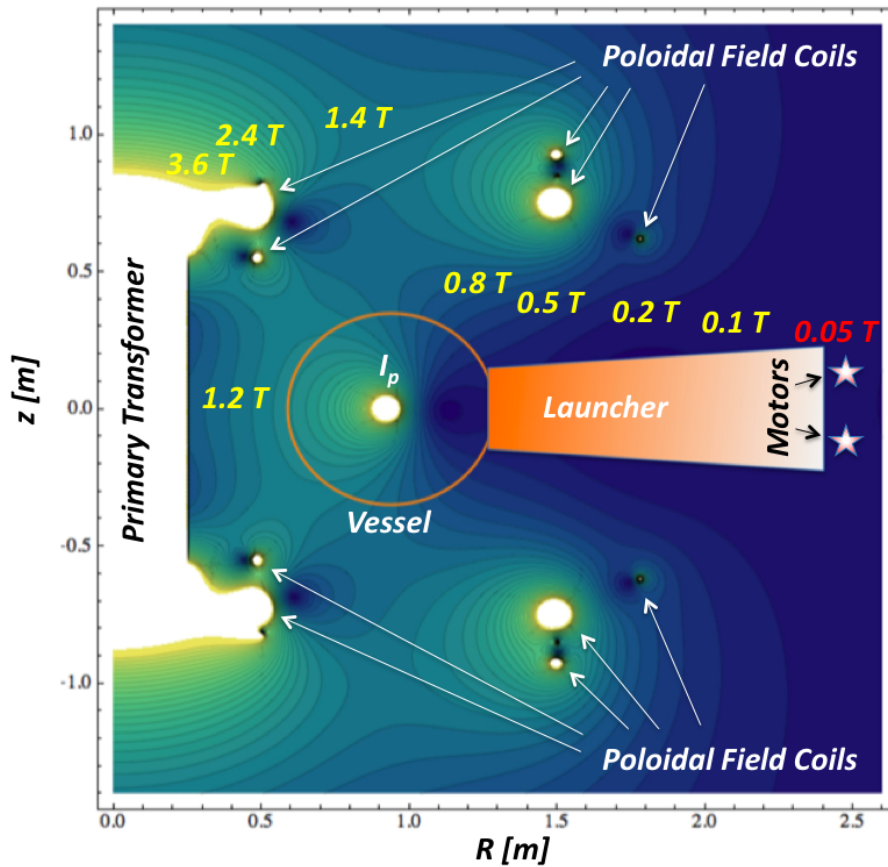


Figure 6.16: Example of a poloidal map of the absolute value of the stray magnetic field, calculated with real FTU parameters, at the shot time of maximum value (≈ 0.05 T, in red) at the position of the motors in the torus hall (indicated with the two stars). The regions of maxima values of the field (in white) correspond to the poloidal field coils of FTU, including the plasma current (1.1 MA in the example considered in the figure). The FTU camera and the launcher are drawn in orange, together with some local absolute values of the stray field (yellow), in correspondence of several points of the hall.

field ($B_{max}=0.1$ T) expected in the FTU hall during the operations. In particular, the main aim was the inspection of possible delays or reduction of precision in the operations of the positioning system, in presence of the external field interacting with the internal fields of the brushless motors or of the position resolving system. Such an influence should be considered when choosing of the proper algorithm for O-X-B operations in the real-time controller. To have an idea of the level of external magnetic field to be applied

to the motors during the tests, thus, the expected value of the stray magnetic field in the FTU hall was estimated, first, at the location foreseen for the motors in the hall. This calculation was performed by assuming the real conditions of typical plasma operations in FTU.

A 3-D model was developed, by using the formalism of the 1st and 2nd order complete elliptic integrals [153], able to provide maps of the local value and sign of the stray field surrounding FTU during the shot, while considering the real spatial distributions of all the poloidal field coils (including the plasma current), together with the typical values of the currents in the coils during the shot time, taken from the data of real FTU discharges. A map of the field in the tokamak hall computed with this model is shown in Figure 6.16. Such a model gave a maximum limit of ≈ 0.058 T for the stray magnetic field expected during typical plasma discharges, at the point where the motors are being installed in the FTU hall. This value has been considered for tests on the motors. A permanent magnetic field source, able to produce 0.1 T as a maximum field at its poles was used. Since the field provided by this magnet in the air gap, is ≈ 0.05 T, such a source could be used to immerse the motors of the launcher in approximately the same field intensity expected in the FTU hall during the operations. The results of these tests confirmed that the external stray magnetic field does not affect the correct operations of either the brushless motors or the resolver, confirming the validity of the results obtained in the dynamical measurements performed with no external field.

Chapter 7

Conclusions

The results of the predictive work presented in Chapter 5 confirm that the required precision in the injection of the wave into the FTU plasma is very high in order to obtain the optimal O-X coupling.

The simulations on conversion efficiency performed using a first model in which an incident plane wave is assumed, show that angular deviations of $\pm 1^\circ$ with respect to the optimal injection, in either vertical or horizontal direction, imply a 50% drop in the power transmission efficiency.

A second model which accounts for a more realistic shape of the incident beam has been developed using the Gaussian beam-mode decomposition, valid in case of paraxial propagation. The model was used to evaluate the expected coupling of a real beam in the FTU plasma in the frame of a mono-dimensional slab description at the conversion region, and showed that the maximum reachable efficiency under optimal wave injection does not exceed 45% and that a larger angular O-X conversion window is expected at the cutoff surface. This derives from the fact that the drop in the conversion efficiency of a spectral component of the incident field distribution should be partially compensated by a higher conversion efficiency of other components. For the same reason, also the degradation of the coupling efficiency caused by the plasma density fluctuations predicted assuming an incident real beam distribution is lower than the one expected assuming an incident plane wave.

Also a 2D model of mode conversion, available in literature since recent years and taking into account a more realistic description of the plasma, has been applied to evaluate the O-SX coupling efficiency in the FTU plasma. The effects in the power conversion efficiency

implied by a two-dimensional description of the plasma turn out to be small ($< 5\%$) for the considered EC-wave frequency of 140 GHz. The results of the application of this model to the FTU case, predicting a power conversion efficiency around 42%, are in agreement with the ones found using the model based on the paraxial propagation of a real beam.

A dedicated experimental activity, aimed to the search of an optimal target for the experiments on O-X-B mode conversion, has been performed during the last campaigns of FTU and has been presented in Chapter 4. Proper procedures have been developed, in order to obtain with reliability the optimal plasma parameters for the conversion of the O-wave at cutoff. A detailed study of the density profiles and gradients, which characterize the overdense plasma regimes, has been carried out. The best reproducible plasma has been experimentally defined in FTU during the last experimental campaigns, with 5.2 T of central magnetic field and 500 kA of plasma current.

The technical limitations of the present EC antenna for the O-X-B experiments, due to the discrete toroidal steering capability (with a step of 10°) limited by a maximum angle ($\pm 30^\circ$) which is below the one request for O-X coupling in the FTU case (ranging between 38° and 40°), led to the realization of a new ECRH launcher, designed and constructed during last years and now ready to be installed in the FTU tokamak.

The present work led to the choice to include as design goals the steering capability required for O-X-B experiments, which means a controlled injection in real-time in both directions with a continuous scan capability and with a maximum toroidal launching angle of 40° .

The characteristics and the first tests on the operation of both the new launching system and its steering control have been presented in Chapter 6, showing a good agreement with the design specifications, in particular with the ones needed to perform experiments on mode conversion in FTU.

Future Prospects:

- The fine definition of the optimal plasma target for the O-X-B experiments will continue during the next campaigns. Discharges with 5.2 T of magnetic field and 360 kA of plasma current will be repeated with lithium-coated vessel walls, in order to study the density peaking factor of the profiles in plasma regimes given by the presence of Lithium and with low current, in the same operational conditions used to test the configurations of currents and magnetic fields presented in Chapter 4. For the same reasons also plasma currents in the range $360 \text{ kA} < I_p < 500 \text{ kA}$ will be tested in overdense regimes, to investigate the possibility to find an even better compromise between the presence of an overdense central plasma region and a high density gradient at the cutoff surface in the plasma density profiles. Other shots will be dedicated to the pellet injection (see Appendix B), in order to verify if this technique turns out to be useful in the optimization of the plasma parameters of interest, since the results obtained so far are not sufficient to evaluate the usefulness of this technique in the reproduction of the optimal plasma target for the aims of this Thesis.
- A proposal for a first step phase of experiments on mode conversion will be the detection of the Electron Bernstein Emission (EBE) radiation at the optimal angles expected for the wave injection for the overdense plasma heating experiments. This would allow to obtain a first experimental verification of the optimal launching conditions predicted in this Thesis for the O-X-B mode conversion, being this a reversible scheme, at least at a first step. Moreover, the measurement of the EBE radiation from the overdense plasma performed from the two poloidally symmetric detection points available in the new launcher of FTU, is expected to enable to reach the measure precision required to test the small effects predicted by the 2D models of O-X conversion in the FTU case, more likely than heating the plasma through a direct O-X-B scheme.
- Since the maximum reachable O-X power transmission with optimal wave injection is expected to be lower than 45%, the development of a control system operating in real-time and in feedback on the plasma parameters turns out to be important,

in order to perform an overdense plasma heating with acceptable efficiency. For this reason, a dedicated algorithm for O-X-B experiments is under study, to be implemented in the automatic control system of the new launcher and operating in feedback on the stray radiation signal detected by the sniffer probes of FTU. Such an algorithm will enable to track the conversion window in real-time during the shot and might ensure the maximum heating efficiency during the experiments, by adapting the optimal injection to the changes of the plasma parameters during the shot.

Appendix A

EBWs Absorption

Electron Bernstein Waves are strongly damped (absorbed) near the cyclotron harmonic resonance. The absorption mechanism can be differently described in the two different cases [27], of quasi-perpendicular propagation, defined when $N_{\parallel} < \beta = v_{th}/c$, and the more general case $N_{\parallel} > \beta$. In the first case the absorption is dominated by the relativistic electron cyclotron interaction, and relativistic effects, like mass increase, make the deposition become broadened. In the other case, instead, a non-relativistic Doppler-broadened absorption can be assumed to be valid. As an example, the absorption coefficient for obliquely propagating EBWs first harmonic [115] [62] and X-wave second harmonic [27], which can both reach plasma regions where the local parameters are the same, can be calculated and compared, starting from the radiative transfer equation [154]:

$$\alpha_{\omega,r}^{B_1} = 2\sqrt{\pi} \frac{s}{s_{\perp}} \frac{N}{N_{\parallel}} k_0 \frac{\tilde{I}X}{\beta^3} e^{-\zeta_{-1}^2}, \quad (\text{A.1})$$

$$\alpha_{\omega}^{X_2} = \frac{\sqrt{2\pi}}{8} \frac{G}{N} k_0 \frac{X\beta}{Y} e^{-\zeta_{-2}^2}, \quad (\text{A.2})$$

where the symbols are referred to the quantities already introduced in Chapter 3, while s is the coordinate along the ray¹ and G is the following geometrical factor:

$$G = \frac{\sin^2 \vartheta}{|\cos \vartheta|} \left(1 + \cos^2 \vartheta + \frac{\sin^4 \vartheta + 8 \cos^2 \vartheta}{\sqrt{\sin^4 \vartheta + 16 \cos^2 \vartheta}} \right),$$

being ϑ the angle between \mathbf{B} and \mathbf{N} . Considering that the refractive index N is usually large, because of the shortness of the EBWs wavelength, while $N_{\parallel} \simeq 1$ and $\beta < 1$, it can be

¹The multiplicative factor s/s_{\perp} is introduced to re-define in radial units (radial direction of the torus) the absorption coefficient α (from which the subscript r) which is generally defined as a decay rate, per unit length, in the propagation direction s .

noticed that the Bernstein Waves power absorption takes place in a much smaller region than the one of the electromagnetic waves.

Appendix B

Preliminary Tests with the Pellet Injection System

Among the procedures put into action for the 'construction' of the optimal plasma target for O-SX conversion in FTU, also the pellet injection system was considered. The pellet injection features the possibility to reach the highest densities in a very fast way, since the plasma density obtained in this case is the effect of ablation of a pellet directly injected in the central region of the plasma, differently from what happens using the gas puffing with injection valves located outside. Hence, the pellet injection technique is such that the density peak is not influenced by the wall conditioning of the machine or by the recycling at the edge and no diffusive times scale of the particles have to be taken into account in the density control process. In this sense the increase of the density can be considered instantaneous with respect to the other typical time scales of the plasma. The first idea to use pellets was born from the interest in testing the overcoming of the *Greenwald* limit (for instance $\approx 2.0 \cdot 10^{20} \text{ m}^{-3}$, for 500 kA of the plasma current), in lithized discharges, in the swiftest possible way and then to test the possibility to sustain the higher density plateau reached with pellet, by a strong gas puffing with valves. For example, in shot #33727, which integrated line density is shown in the left side of Figure B.1, a single pellet injection was performed at 0.6 s. The gas puffing had been regulated in such a way to start from a medium-level density plateau before the injection of the pellet (to avoid possible disruptions at its injection) and a subsequent sustained puffing from 0.6 s on, but the plateau could not be sustained after the injection of the pellet, despite the critical threshold of the *Greenwald* limit could be overcome without any problem. After having

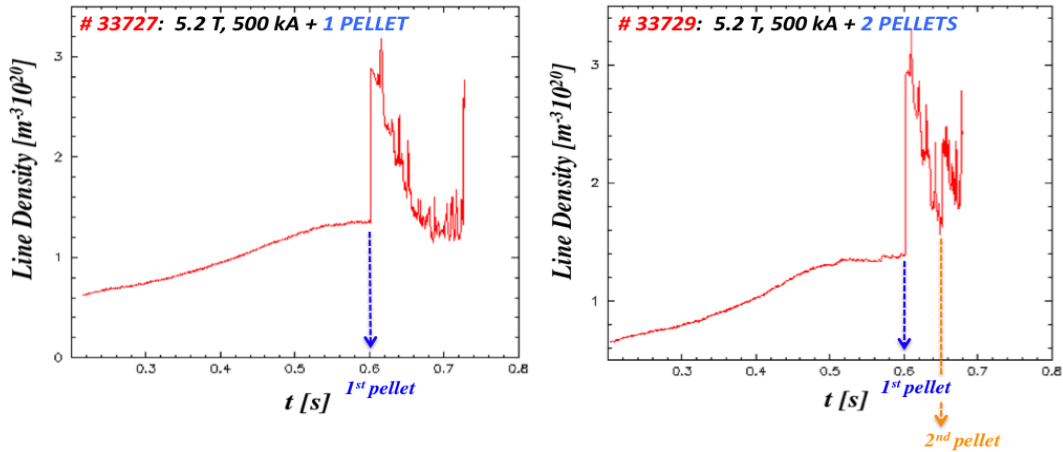


Figure B.1: Line density of two shots, at 5.2 T and 500 kA, in which one (left) and two (right) deuterium pellet injections were performed at 0.6 s. The pellet is injected when the regulation of the density plateau is not too high ($\approx 1.2 \cdot 10^{20} \text{ m}^{-3}$) not to induce a disruption of the plasma at the arrival of the pellet. The critical *Greenwald* threshold is overcome ($\approx 2.0 \cdot 10^{20} \text{ m}^{-3}$) but the density plateau could not be sustained, neither with the sole use of gas puffing nor with the use of multiple injections. Both plasmas disrupt around 0.7 s.

reached a very high level, the line density decreases and the plasma disrupts, like in Figure B.2. Only a second attempt could be made, in shot #33729, using a similar regulation of valves for the gas puffing before and after the pellet injection, but making use of repeated injections of pellet, from 0.6 s, every 0.05 s. Also in this case very high densities could be reached, at first, but the density plateau could not be sustained, even with the synergy between pellet and gas puffing. Unlike the expectations, at the second pellet injection the density did not increase more than after the first injection, and does not even reach the same density value. The second peak was lower and the density was still decreasing, like in shot #33727, until the disruption of the plasma occurs, about 80 ms after the second pellet was injected.

The regulation of a stable density plateau is an important key point, in order to consider a certain technique to create a suitable plasma target for mode conversion. Without a stability of the overdense plasma region, it is difficult to envisage a satisfactory demonstration of the O-X-B scheme. However, since the slope of the density profile just after the pellet injection is very steep, such a high density peaking obtainable for a few tens of milliseconds after pellet, may be used for some preliminary experiments aimed to verify

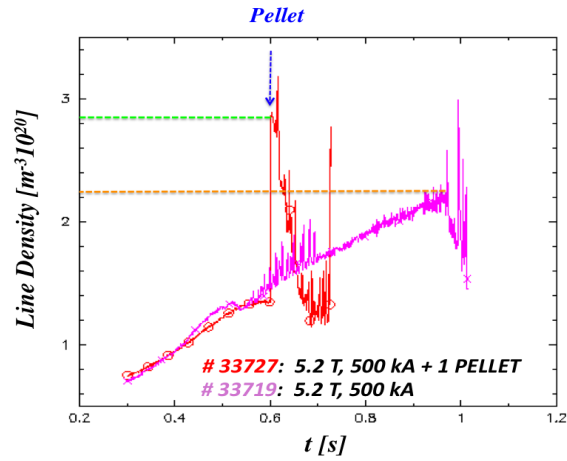


Figure B.2: Comparison between the line densities of shot #33727, where a single pellet injection has been performed at 0.6 s, and the gradual ramp-up from zero to the disruption for density limit, performed in shot #33719. It is evident how the regime given by the pellet is completely different from the one obtained with a more standard ramp-up of the density, being field and current the same. The regime with pellet allows to reach higher densities (green dotted line) than in a standard ramp (orange dotted line). Nevertheless, the density is not sustained with the gas puffing alone after its initial peaking.

the real conversion window by receiving EBE radiation, at the correct oblique view angle, in correspondence of the proper ramp-down of the density, after the pellet injection. The results obtained so far with this technique are still very preliminary and the use of pellet will be broadened in the next campaigns of FTU.

List of Figures

1.1	Cross-section of several fusion reactions between light elements vs the energy of $D + p$. It can be noticed that the D-T reaction has the maximum cross-section.	4
1.2	Results of several fusion devices. The red dots correspond to experiments performed in JET (in Europe) and TFTR (in the US) devices with D-T. . .	6
1.3	Section of the International Thermonuclear Experimental Reactor (ITER). The dimensional scale of the machine can be deduced by comparing the device with the representation of a man, put in the bottom right of the picture.	9
2.1	The fundamental O-mode (on the right) and X-mode (on the left) accessibility, represented in a poloidal section of a tokamak-like device, which axes are on the left of the two sections. The green regions are prevented to the respective EC-waves.	17
2.2	A representation of the O- and X-mode accessibility in a cold plasma, called Clemmow-Mullaly-Allis CMA diagram. Resonances and cutoffs form regions which are unaccessible by the waves launched from LFS, represented with the arrows. Picture taken from [17].	19
2.3	In this figure, taken by [17], the resonance curves in the velocity space are represented by the colored curved lines, the boundary of the particle trapped in the field (see further on for a description of the trapping process) by colored straight lines and black curves are the contours of constant velocity.	22

2.4	The <i>Fisch-Boozer</i> (on the left) and the <i>Ohkawa</i> (on the right) processes responsible for ECCD in plasmas, are illustrated schematically in velocity space, where the trapped particles boundary are indicated on the right with straight oblique lines.	24
3.1	In this figure, modified from [62], the Electron Bernstein Waves are schematically represented. The collective rotation in phase of the electrons around their guiding centers sustain the longitudinal EBW. The red and blue regions have been added to visualize the periodic charge accumulation and lack.	33
3.2	EBW dispersion relation, where the frequency is normalized with the cyclotron frequency and the wave vector with the thermal electron gyroradius, taken from [62].	34
3.3	Behavior of the radial component of the refractive index, perpendicular to the magnetic field, versus the normalized plasma frequency, calculated with the parameters of the stellarator device W7-AS, for an O-X-B mode conversion (see further on in this Chapter for the description of this scheme). It can be noticed how the X-branch in the dispersion relation is the natural extension of the B-branch, in a hot plasma description. Picture taken from reference [64].	36
3.4	Schematic poloidal view of the (direct) coupling between a SX-wave launched from the HFS and the B-mode, at the UHL. The green regions are the ones prevented to X-mode.	39
3.5	Schematic poloidal view of the FX-SX-B scheme. The FX-wave couples the SX-wave by tunneling the evanescent region (green) between the low density cutoff of the X-mode and the UHL. The SX-mode, then, converts to B-mode.	40

3.6	Schematic poloidal view of the O-(S)X-B mode conversion scheme. The O-wave is launched from the LFS and excites the SX-wave at the O-mode density cutoff layer. The X-wave, then, mode converts to EBWs, which can reach the central overdense plasma regions. The O-mode encounters no evanescent regions while approaching its cutoff layer. This is the reason why a white area has been drawn at its passage through the green region on the right of the picture, which is evanescent only for the X-mode.	42
3.7	O-X transformation region in a 1D slab geometry (on the left), where the plasma density and magnetic field strength both vary along the radial direction of the machine (x -axis). A more realistic 2D geometry (on the right), where the plasma density and magnetic field strength vary in the xy -plane and cross in a certain point. The evanescent regions $\varepsilon_{\parallel}(\varepsilon_{+} - N_{\parallel}^2) < 0$ are dashed. The figure has been taken and modified from [102].	54
3.8	Normalized stray radiation power measured in TCV in a poloidal scan with the gyrotron (left), at fixed toroidal angle, and in a toroidal scan (right), at fixed poloidal angle. The dashed lines indicates the 50% of the maximum stray level. A minimum in the stray radiation level is found in both cases. .	59
3.9	In this figure, the dots, representing the experimental measure of the stray radiation in the TCV camera during the EC scans are compared with the results on the conversion efficiency obtained using simulations.	60
4.1	On the left, picture of the three units of the lithium limiter installed on their supporting structure. On the right, the following components of the LLL are showed: 1) ceramic break, 2) stainless steel case, 3)lithium filled-capillary structure, 4) heater, 5) Li evaporating surface 6) Mo heat accumulator, 7) thermocouples (figure taken from [121]).	62
4.2	Picture of the internal side of the FTU vessel, taken from [126]. The red arrow indicates the position of the toroidal limiter, the green one show where the Liquid Lithium Limiter is inserted in the camera (only when used).	63
4.3	Sketch of the scanning interferometer of FTU. It can be seen that the two scanning interferometers are capable to cover 2/3 of the plasma diameter. .	65

4.4	3D reconstruction of a typical inverted high density profile of FTU (shot #28510). The radius where the O-mode cutoff density is overcome is shown. When the plasma density is high, such radius is typically in the range 10-15 cm from plasma center.	67
4.5	Inverted density profile of shot #32240 at three different times. The inversion of the profile (plasma axis and magnetic surfaces) is calculated on the magnetic equilibrium of the discharge. The density value corresponding to the O1-mode cutoff is indicated with the red line.	69
4.6	Central density values of some discharges performed using the LLL, with $B_0 = 5.9$ T and $I_p = 500$ kA, versus time. The density value typically corresponding to the appearing of the O-mode cutoff in the inverted density profiles (considering the typical plasma radius of FTU) is marked. It is evident that this value is overcome by the peak density of the considered discharges.	70
4.7	Normalized integrated line density profiles of three discharges performed at 5.9 T, 500 kA, measured by the central chord of the <i>SIRIO</i> interferometer [25], installed in FTU. Since in the three discharges the plasma currents and the magnetic equilibria are approximately the same, the <i>Greenwald</i> limit of one discharge (#30583), in green, is representative also for the others. It is evident that the <i>Greenwald</i> limit is extensively overcome at 5.9 T of the magnetic field.	71
4.8	Density limit (green dashed line) found with a programmed density ramp-up (in red), until the disruption of the plasma occurs. In both the discharges taken as example, performed at 4.8 T, 500 kA, the density limit is found around $2.2 \cdot 10^{20} \text{ m}^{-3}$ line integrated density, normalized to the mean minor plasma radius (0.3 m). The oscillations in the density measurement that start around 0.5 s in both shots, indicate the presence of the MARFE instability. The light purple lines indicate the <i>Greenwald</i> limit versus time, calculated with the real-time measurements of plasma current and (major and minor) plasma radius.	73

4.9	The inversion of the density profile performed on the magnetic equilibrium when the discharge is stable (at 0.5 s, in the example), put on the right, shows that the O-mode cutoff is reached just by the central peak density, but no overdense regions creates, in particular around the layer of the 1 st harmonic EC resonance. Thus, staying at the results that could be obtained so far, the configurations with 4.8 T of the magnetic field can not be considered for the experiments on overdense plasma heating.	74
4.10	Density limits found in shot #33719 (light purple), performed in 2010 campaign, and in shot #32400 (red), performed in 2009, both at 5.2 T, 500 kA. The two limits seem to be slightly different. The reason for that probably lies in the different conditioning of the machine, which implies non-identical plasma conditions. As better shown in the zoomed area of the picture (on the right), the difference between the two limits is $\approx 1.0 \cdot 10^{19} \text{ m}^{-3}$ in the line density signal. The <i>Greenwald</i> limit for the two 500 kA currents, calculated in real-time, is also shown (dark purple line).	75
4.11	The line density of shot #33725, reaching the density limit at 5.5 T, 500 kA, superimposed to the one of shot #33719, used to find the limit at 5.2 T, 500 kA. The two limits turn out to be similar, both around $2.3 \cdot 10^{20} \text{ m}^{-3}$ despite the higher field of shot #33725 would lead to expect a higher threshold. The accurate procedure carried out during recent experiments, in the regulation of the reference density using the gas puffing, is evident in this picture. Identical increase of the two density ramps, despite the different magnetic equilibria of the two shots, could be performed. Also the MARFE instability, that can be recognized from the strong oscillations on the interferometer signal and which typically 'start' at a certain time during the discharge, has the same starting point in the two traces, showing a behavior independent on the magnetic field.	76
4.12	Density limits found for three discharges, with the same 5.2 T field but 500 kA plasma current (shot #33719, red) and 700 kA (shot #33722, light purple, and shot #33731, violet). Despite the <i>Greenwald</i> limit is higher at 700 kA (brown line) than at 500 kA (green line), the disruption occurs at identical densities for the two currents.	77

- 4.13 Two representative discharges, performed at the same field 5.2 T, but at different currents 500 kA and 700 kA. Both shots have a sustained line density plateau, at the same density value (top left). At 0.9 s, when the two signals indicate exactly the same integrated density (blue dotted arrow), the inverted density profiles have been calculated (bottom left). It is evident how the density peaking of shot #33717, performed at 500 kA, is higher than in shot #33721, at 700 kA. This is a typical difference found between 500 kA and higher fields lithized discharges. On top and bottom right, the local density of the two shots, versus major radius (abscissa) and time (ordinate), and calculated on the magnetic equilibrium, are shown. The density peaking factor is higher for shot #33717 than in #33721, that means steeper slope of the density profiles, more suitable for O-X power transmission. In the two plots the colors are normalized to different peak density values: $3.42 \cdot 10^{20} \text{ m}^{-3}$ for shot #33717 and $2.77 \cdot 10^{20} \text{ m}^{-3}$ for shot #33721. The red and purple arrows indicate the time at which the profiles in the bottom left have been calculated. 78
- 4.14 Local density (top) and normalized density profiles (bottom), at different time between 300 ms and 900 ms, of shots #33719, at 5.2 T, 500 kA (on the left) and #33731, at 5.2 T, 700 kA (on the right). It is clear that the stronger density peaking given by the lower 500 kA plasma current than 700 kA, at any time. In particular, from the normalized profiles, it can be seen how the peaking factor rises with the time during the shot. The light blue arrows indicate the profile change with the time. The cutoff density is also shown with the green dotted lines. 79
- 4.15 Some discharges with different combinations of field and currents, having typical values of the safety factor at the edge, are considered. The value $q \approx 5$ seem to be confirmed in the experiments as the threshold between discharge which density limit is under the respective *Greenwald* limit (for lower q indicated with the grey area) and the ones that overcome it (for higher q , white area). discharges with 5.2 T and 500 kA are near this threshold. 80

4.16	Line density profiles of several discharges, performed for different experimental programs at 5.2 T, 360 kA, then taken into consideration for the analysis aimed to find the plasma target for O-X-B experiments (left). The lower <i>Greenwald</i> limit, calculated for the 360 kA current, is showed (black trace). From the oscillations of the measurements it is evident that a strong MARFE instability establishes at this low current and noisily affects the control of a stable plateau. On the right, the comparison between a typical 360 kA and 500 kA is shown. The plateau obtained at 500 kA is more stable and the high density results maintained during the shot.	82
4.17	Density peaking factor, calculated in real time with the real parameters of two different typical shots, at 360 kA and 500 kA, both with 5.2 T of the magnetic field. The trend of the peaking factor is showed just for the initial ramp-up phase of the density, when the EC power was not injected in the plasma of shot #32085 yet, in order to compare two identical ohmic conditions.	83
4.18	3D reconstruction of the real density profile of a typical 5.2 T, 500 kA discharge (shot #33717), selected as one of the best target obtained for O-X-B experiments. The calculation of the density distribution is based on the real magnetic equilibrium of the discharge. The slope of the profile is steep and a considerable overdense plasma region for the 140 GHz frequency (region above the cutoff density level indicated by the blue plane) is centered near the O1-mode resonance (yellow line), which corresponds at 5 T of the magnetic field.	84
5.1	Dispersion relation branches of O- and X-mode, calculated with typical parameters of FTU. For the sake of simplicity, the considered density profile has been written using an analytical form. It is shown how a $\approx 39^\circ$ launch is needed to make the O- and X-branches coalesce, thus obtaining O-X mode conversion. The blue branch on the right is the one of the FX-polarized wave, which plays no role in the conversion scheme.	88

5.2	Left: variation of the optimal $N_{\parallel, opt}$ for different values of the central magnetic field (from 3 T to 7 T) and of the actual N_{\parallel} of the ray for a 30° and 40° injection into the vessel, calculated with geometrical calculations on a straight path in vacuum ($N = 1$). A purely toroidal magnetic field, varying spatially as $1/R$, has been supposed. Right: preliminary calculations of the O-X power transmission efficiency, calculated at the equatorial plane of the machine, for an analytical density profile of FTU and for some different central fields, from 5.0 T (dark purple curve) to 5.8 T (pink curve).	89
5.3	Poloidal view of a typical ray path (in red) in an over-dense plasma. The O-polarized wave propagates inside the plasma until the $X = 1$ cutoff is reached. At that point, the wave is back-reflected, since the center of the plasma is prevented (overdense) for a general injection angle. In the picture, also the magnetic flux surfaces of the FTU shot (taken from the magnetic equilibrium of the plasma) are represented with the dotted circular blue lines. In this case, the z -coordinate is the perpendicular one and R in the major radius of the device.	91
5.4	First results obtained with preliminary ray tracing calculations performed from the launching point of the EC launcher presently installed in FTU. These calculations were performed to obtain a first evaluation of the wave paths at different poloidal and fixed toroidal $\pm 30^\circ$ steering angles, using real high density plasma parameters. The poloidal view of the simulations is on the left, with y being the vertical component; the toroidal one is on the right of the picture, with z being the toroidal coordinate. Thanks to this first simulations, it was demonstrated that no poloidal component could be used in the wave injection to increase the N_{\parallel} of the wave, since only the rays aiming the center of the plasma can reach the O-mode cutoff.	92

5.5	The optimal launch for O-SX mode conversion (green) is represented in this simplified representation of a slab geometry plasma, together with several other non-converting launched O-waves (red and yellow arrows). If the N_{\parallel} becomes too high along the ray path (yellow arrows), the wave does not even reach the $X = 1$ layer and the corresponding cutoff becomes the one reported in Section 3.5.2, re-written again here in the picture, on the right. The only wave which reaches $X = 1$ with the optimal value of the parallel refractive index $N_{\parallel}^2 = Y/(Y + 1)$ is the green one, which couples SX-mode in the conversion region (blue area).	93
5.6	The three different regions, resulting from the ray tracing calculation performed with real FTU parameters and explained in detail in the text, are shown in the toroidal-poloidal injection angle map. The region of interest for O-SX coupling is indicated here with the green area. The purple oblique dashed line indicates a sort of 'section' of this graphics, which representation is Figure 5.5, where a correspondence between the colors have been kept for clearness.	94
5.7	Left: values of N_{\parallel}^2 and $Y/Y + 1$ versus minor radius. Right: N_{\parallel} , and N_{\perp} versus minor radius. The computations are performed with the <i>ECWGB</i> code, at optimal launch for O-X conversion and plasma parameters of shot #30583, where a central field scaled down from the 5.9 T of the shot to 5.3 T has been used for the simulation. Since the injection performed with the ray tracing is close to the optimal one, at the 140 GHz cutoff radius $N_{\parallel}^2 = Y/Y + 1$ (left) and $N_{\perp} \approx 0$	95
5.8	O-mode cutoff position in the plasma versus parallel refractive index, calculated with the parameters shot #28510. The optimal N_{\parallel} for conversion (green) corresponds to the 'knee' of the curve (green arrow).	96
5.9	Angular transmission window, centered on the optimal launching angles, in the case of two different high density plasma discharges of FTU, calculated with a single ray tracing simulations, starting from the launching point of the new ECRH launcher. Each level corresponds to 10% of transmission efficiency. The angular window diameter, defining 50% of power transmission, is around 2° in both poloidal and toroidal directions.	97

5.10	Conversion efficiency versus relative density fluctuation amplitudes and density scale length L_n , calculated with the statistical model introduced in Section 3.5.3. The region defined by the FTU parameters, obtained so far with experiments, is shown (orange area).	98
5.11	Power transmission efficiency at cutoff, in a slab geometry, weighted with a statistical description of the turbulences at the conversion region, versus the density scale length L_n , calculated for a single ray propagation. A poloidal correlation length of 3 cm has been assumed. The three curves corresponds to different relative fluctuation amplitudes $\Delta n_e/n_e$. The typical range of L_n for FTU is indicated with the orange region.	98
5.12	Normalized power content in the O-mode versus the angle ϑ_{kB} between the wavenumber and the magnetic field, for a linearly polarized wave. The different curves corresponds to different values of the normalized electron cyclotron wave Y . In the case of FTU, the red curve ($Y = 0.8$ at the plasma-vacuum threshold) is the one aiming at the cutoff with the angle between \mathbf{k} and \mathbf{B} $50^\circ \leq \vartheta_{kB} \leq 55^\circ$, corresponding to the launch angle $35^\circ \leq \vartheta_l \leq 40^\circ$	99
5.13	Poloidal view of the wave accessibilities of the X-mode, where the green regions are the prevented ones. The O-mode had no problem with accessibility during the performed tests on the plasma, since the density was well below the one of cutoff. Thus, it was completely absorbed at the resonance. The FX-mode, instead, was completely reflected at its low density cutoff (green region on the right) and became stray radiation in the vessel.	100
5.14	Signal detected by the sniffer probe #1 (located at the port #12 of the FTU camera), proportional to the stray radiation amount in the vessel. It is evident that the signal is lower in shot #30603 than in the other two shots, during which the encoder controllers of the polarizing optics where slightly changed, in two opposite directions, with respect to the nominal encoder, that has been used for the wave polarization control in shot #30603. The mean values of the noisy signals are marked with the three horizontal lines, with a color correspondence with the stray signal traces.	101

5.15	On the left: reconstruction of the O- and X-mode cutoff surfaces, respectively $\varepsilon_{\parallel} = 0$ (red) and $\varepsilon_{+} = N_{\parallel}^2$ (blue), at the conversion region, performed with the real parameter of a typical FTU discharge. The camera of the machine is the thick orange circle. The grey rectangular region around the intersection of the two layer is zoomed in the picture on the right. The angle 2α between the two cutoffs is indicated in the picture on the right.	106
5.16	Contour plot of power transmission efficiency versus the vertical (y) and toroidal (z) beam waist, calculated for two discharges of FTU, using the 2D model of O-SX conversion presented in this Chapter. Optimal aiming of the beam to the conversion region has been considered for the plots. Each level corresponds to 10% of power transmission efficiency.	107
5.17	Scaling of the α angle with the magnetic field, at different poloidal positions, defined by the central γ angle of Figure 5.15 (left). On the right: circularity of the two cutoff surfaces $\varepsilon_{\parallel} = 0$ and $\varepsilon_{+} = N_{\parallel}^2$, calculated with real FTU parameters, at different γ angles, defined by the ratios between the x and y components of the radial unitary vectors perpendicular to the surfaces. It is shown that the two real cutoff surfaces are not perfectly concentric and hence intersect at a certain point, depending on N_{\parallel}	108
5.18	O-X conversion evaluations based on the 2D model versus different values of waist sizes w_z (toroidal direction) and w_y (vertical direction), for an incident Gaussian electric field distribution $E \propto \exp(-z^2/w_z^2 - y^2/w_y^2)$. Green and blue lines represent the cases of optimal and non-optimal directions of the beam respect to the magnetic field, i.e. different signs of N_{\parallel} or, equivalently, symmetric poloidal launching points with respect to the equatorial plane of the machine. Red lines show the results of the 2D model reduced to 1D ($\alpha \rightarrow 0$), where the influence of the beam spectrum on the conversion is considered. The case of FTU ($w_y \equiv w_z = 1.2$ cm) is represented by the red dots and yellow arrows, showing an agreement with the results of the previous Section.	109
6.1	View of FTU tokamak in the torus hall (left) and visible light detection from a plasma discharge, from inside the vessel (right).	112

6.2	Poloidal view of the ECRH launching system, presently installed on FTU. The angular ranges of one of the central (green) and external (red) steering mirrors are shown.	114
6.3	Increasing of the N_{\parallel} that, in principle, can be obtained at given circular surface (represented with the blue circle on the left) by using a poloidal component in the ray injection, versus the central angle γ . The computations are performed assuming a fixed toroidal component of the refractive index, a straight path of the ray and a purely toroidal magnetic field scaling as $1/R$	116
6.4	Real scale model of the present FTU launcher, made using <i>Mathematica</i> [®] software. The two oblique side walls of the launcher, used for beam bouncing, and the FTU camera are represented. In the picture, an example of wave injection at -30° is shown, exploiting three bounces of the beam at the internal gold-covered walls of the launcher. In the example, the beam axis passes from the center of the port aperture. Such condition is usually chosen in FTU, to minimize the interactions of the beam sides with the port walls. This geometrical model have been used to evaluate other possible launching configurations, able to increase the N_{\parallel} of the beam in the plasma, in view of O-X-B experiments.	117
6.5	Top view of FTU. Two (lines #1 and #4) of the four transmission lines of the present launcher (top-right) are switched from port #12 to port #8, to feed the new system (bottom).	118
6.6	Picture of the final version of the launcher, in the laboratories at IFP-CNR Milano (up) and a schematic representation of the system (down), where the positions of the steering mirrors, the zooming optics and the vacuum flange are shown (red arrows).	119
6.7	3D drawing of the overall new system. The two symmetric lines are shown (upper and lower), with the respective components: vacuum windows, zooming systems, shafts for the transmission of the toroidal-poloidal movements and internal optics. The ray path in the lines of the launcher are indicated with the two thick red arrows.	120

- 6.8 Left: view of the upper line of the new launcher, in a simulation relevant for O-X-B mode conversion experiments. Ray tracing computations of some rays (blue) steered towards the 1st harmonic ordinary mode (O1-mode) cutoff layer with slightly different injection angles, centered around the optimal ones for O-SX coupling (red ray), are shown. The cutoff surface, nested by the magnetic sheared field lines (yellow curves), is calculated from the real plasma parameters of a typical high density discharge of FTU. Right-down: zoomed view in the proximity of the cutoff region where the blue rays (non-optimal) are back-reflected and the red ray (optimal) is converted to SX-mode beyond the cutoff layer (such a SX-polarized ray is not visible in the picture). Right-up: the region of conversion further zoomed, in a top view. The ray tracing calculations show how the phase velocity of the red ray, which is the only one with optimal aiming, is parallel to the magnetic field lines (thin blue lines) at cutoff. 121
- 6.9 Tridimensional view of the front part of the new EC launching system of FTU, in a simulation performed with *Mathematica*[®] software, in a relevant operation for O-X-B mode conversion. The upper and lower lines are shown, while launching several rays with opposite sign of the N_{\parallel} ad from opposite poloidal points, as will be possible to do with the new system (top right). The O1-mode cutoff surface and the magnetic field lines on it (yellow lines), are calculated with the real plasma parameters of FTU. In the figure on top, the side of port #8 closest to the plasma is represented. The picture on the bottom left is a more detailed view of the upper line (zoom of the white dotted region). Despite all the rays are injected approximately with the same toroidal and poloidal angles, only the red ray represents the beam axis for optimal O-X conversion. All the others (represented by blue rays) are reflected partially or totally at cutoff, since they propagate with non-optimal aiming to the conversion region. In the picture on the bottom left, the last two mirrors of the line and the path of the ray internal to the launcher are shown. 125

6.10 Drawing (on the left) and picture (on the right) of the back side of the steering mirror, before the deposition of the plasma sprayed Cr_2O_3 layer, used to enhance the thermal emissivity. The particular shaping of the back side is shown, together with the dimensions of the mirror, indicated in the drawing on the left. 126

6.11 The inner structure of the moving mechanism of the last mirrors is shown in the picture, on the left; the real mechanism, with the mirror attached, is shown on the right. 127

6.12 One of the sliding optics mounted in the two lines, used as zooming systems. One of the mirror (green) is flat, the other one (yellow) is focusing. 129

6.13 Beam radius, at different distances from the last waveguide aperture and for central and extremes positions of the sliding mounting of the zooming optics. The positions of the focusing mirror (FM) and of the steering mirror (SM) are shown (picture taken from [151]). 129

6.14 On the left, the beam pattern at the output of one of the lines is shown, measured at plasma center, with null toroidal angle ($\alpha = 26^\circ$, $\beta = 0^\circ$). In the example, the zooming mounting was put at the minimum distance 600 mm from the waveguide end (i.e. configuration for the largest spot in the plasma). On the right, a beam pattern acquired at plasma center, with a typical angular position of the steering mirror foreseen for O-X-B experiments. The poloidal and toroidal angles are $\alpha = 18^\circ$ and $\beta = 39.5^\circ$ with respect to the mirror axis. The distance of the zooming system from the waveguide exit is the nominal one (700 mm) in this case. The elongation of the spot is a geometrical implication of the measure, performed with a scan of the receiver on a plane perpendicular to the port axis, while the beam is incident on this plane with an angle $\neq 90^\circ$ 131

6.15	On the left, the toroidal response of the positioning system (purple lines) of the launcher mock-up to 0.5° and 1° steps (blue lines), with the launching mirror connected to the shaft. These kinds of request on the movement are the typical ones requested during an automatic tracking in real-time of the conversion window. In this example, the PID parameters of the controller where regulated in such a way to have a fast response (rise time near 5 ms) and a higher overshoot and settling times. On the right, a similar 1° step request is showed, but this time starting from a 39° toroidal angle to 40° , in the typical angular range for O-X-B experiments.	132
6.16	Example of a poloidal map of the absolute value of the stray magnetic field, calculated with real FTU parameters, at the shot time of maximum value (≈ 0.05 T, in red) at the position of the motors in the torus hall (indicated with the two stars). The regions of maxima values of the field (in white) correspond to the poloidal field coils of FTU, including the plasma current (1.1 MA in the example considered in the figure). The FTU camera and the launcher are drawn in orange, together with some local absolute values of the stray field (yellow), in correspondence of several points of the hall. . .	133
B.1	Line density of two shots, at 5.2 T and 500 kA, in which one (left) and two (right) deuterium pellet injections where performed at 0.6 s. The pellet is injected when the regulation of the density plateau is not too high ($\approx 1.2 \cdot 10^{20} \text{ m}^{-3}$) not to induce a disruption of the plasma at the arrival of the pellet. The critical <i>Greenwald</i> threshold is overcome ($\approx 2.0 \cdot 10^{20} \text{ m}^{-3}$) but the density plateau could not be sustained, neither with the sole use of gas puffing nor with the use of multiple injections. Both plasmas disrupt around 0.7 s.	VI

B.2 Comparison between the line densities of shot #33727, where a single pellet injection has been performed at 0.6 s, and the gradual ramp-up from zero to the disruption for density limit, performed in shot #33719. It is evident how the regime given by the pellet is completely different from the one obtained with a more standard ramp-up of the density, being field and current the same. The regime with pellet allows to reach higher densities (green dotted line) than in a standard ramp (orange dotted line). Nevertheless, the density is not sustained with the gas puffing alone after its initial peaking. VII

List of Tables

1.1	Years of use of the different fuels available nowadays, calculated using the current rate of consumption. Table taken from reference [1].	2
1.2	Contributions of the different most important primary energy sources to the overall energy production in the World, updated to 2006. Table taken from [1].	3
1.3	Typical parameters of a fusion reactor. Table taken from [8].	7
1.4	Main ITER parameters. Table taken from [11].	8
1.5	Heating and current drive actuators of ITER, with the power respectively delivered to the plasma by each system.	10
6.1	Steering angles for the linear propagation from the remote position of the four mirrors to the plasma, corresponding to the injection angles from the end of the port, after the ray bouncings at the port walls. These values have been used for performing calculations with the ray tracing code for propagation in the present launcher of FTU.	115

Acknowledgments - Ringraziamenti

I miei primi ringraziamenti vanno alle persone che mi hanno dato la possibilità di svolgere questo lavoro di Tesi presso l'*Istituto di Fisica del Plasma* di Milano e presso il Centro di Ricerca ENEA di Frascati. Ringrazio prima di tutto il mio relatore, nonché collega, Alex Bruschi, per avermi supportato durante lo svolgimento di questo lavoro di Dottorato e per tutti gli spunti che mi ha dato nel corso di questi anni di lavoro presso IFP.

Ringrazio moltissimo Sante Cirant e Gustavo Granucci, che sono state, oltre ad Alex, le altre persone per me fondamentali, dalle quali ho imparato giorno per giorno che cosa vuole dire portare avanti il fantastico lavoro del ricercatore.

Ringrazio Franco Gandini e Valerio Muzzini, che ormai da tempo lavorano altrove, ma che negli anni mi hanno costantemente offerto la possibilità di avere preziosi e sempre costruttivi scambi di idee.

Un grazie a Silvana Nowak per l'infinita disponibilità che solo lei riesce sempre ad offrire e a Gabriella Ramponi ed Enzo Lazzaro, per essere stati rispettivamente un'ottima Responsabile di Commessa e il Direttore che per primo ha fatto in modo che nuove forze 'giovani' potessero entrare a far parte di IFP.

Un ringraziamento a Giovanni Grosso, per il suo inesauribile impegno nei confronti di IFP e del precariato, ad Alessandro Simonetto, per la sua sempre pronta disponibilità e a Daniela Farina, per il supporto scientifico sempre di ottimo livello.

Grazie a Mario Zannoni, Massimo Gervasi e Giorgio Sironi dell'Università di Milano-Bicocca per la pazienza che hanno avuto nell'organizzare i miei seminari nel corso degli anni di Dottorato.

Un grazie a tutte le persone che lavorano presso l'ENEA di Frascati, in particolare Afra Romano, Onofrio Tudisco, Giuseppe Mazzitelli, Basilio Esposito, Angelo Tuccillo, Giuseppe Calabrò, Antonio Botrugno, Cristina Mazzotta, Daniele Marocco, Gianluca Pucella, Enzo Di Ferdinando, Mario Mezzacappa, i tecnici di macchina e le persone del *CODAS* and thanks a lot to the colleagues from Politecnico di Milano for the precious scientific collaboration carried out during the last years, in particular Gabriele D'Antona, Mhosen Davoudi and Roberto Ferrero.

Un ringraziamento particolare ad Alba, per essere l'amica che è e per essere stata sempre una persona davvero speciale e grazie a Daria, Giò, Ale, ODA, Lorenzo, Eros, Edo in quanto grandi amici prima ancora che colleghi. Grazie a Betty, Carolina ed Angela perchè

sono le più forti amministrative che IFP potesse sperare di avere.

Un grande ringraziamento a tutti gli "Amici della Piazza", in particolare il Desio, il Pelato, la Pi, Sfera, Pido, Gabri, Igor, Marinella, Vape, i Polli, i Colli ecc...e grazie a quei disadattati dei Mauna Kea, per tutte le esperienze fatte insieme nel corso degli anni...alcune delle quali direi indimenticabili!

Infine vorrei fare un ultimo sentitissimo ringraziamento speciale a papà Valter e mamma Gina...per essere come sono.

Grazie a tutti...

Bibliography

- [1] J. Ongena and A. M. Messiaen. HEATING, CONFINEMENT AND EXTRAPOLATION TO REACTORS. *FUSION SCIENCE AND TECHNOLOGY*, 57(2T):457–473, FEB 2010.
- [2] J.F. McManus, G.C. Bond, W.S. Broecker, S. Johnsen, L. Labeyrie, and S. Higgins. High-resolution climate records from the north atlantic during the last interglacial. *Nature*, 317:326–329, 1994.
- [3] *U.S. Department of the Interior, U.S. Geological Survey, Mineral Commodity Summaries 2000.*
- [4] M. Van Schoor and R. R. Weynants. FUSION MACHINES. *FUSION SCIENCE AND TECHNOLOGY*, 57(2T):39–45, FEB 2010.
- [5] D. A. Hartmann. STELLARATORS. *FUSION SCIENCE AND TECHNOLOGY*, 57(2T):46–57, FEB 2010.
- [6] J. Wesson. *Tokamaks*. Oxford Engineering Science Series, Second Edition, 1997.
- [7] D. Van Eester. MODELING PARTICLE HEATING AND CURRENT DRIVE IN FUSION MACHINES: BRIEF OVERVIEW OF ADOPTED TECHNIQUES. *FUSION SCIENCE AND TECHNOLOGY*, 57(2T):106–113, FEB 2010.
- [8] F.R. Casci M.Q. Tran. Iter, the major step towards fusion energy for the world. In *Proc. 19th World Energy Congress, Sidney, 2004.*
- [9] J. Wesson. *The Science of JET*. downloadable from <http://www.jet.efda.org>.
- [10] www.jet.efda.org.

- [11] D. V. Bartlett. THE EUROPEAN FUSION PROGRAMME. *FUSION SCIENCE AND TECHNOLOGY*, 57(2T):27–36, FEB 2010.
- [12] <http://www.iter.org/>.
- [13] *4th ITER International Summer School, Austin, TX USA*, 2010.
- [14] V.E. Golant. Electron cyclotron heating of a tokamak plasma. *Physica Scripta*, T2/2:428–434, 1982.
- [15] S. Cirant. Overview of electron cyclotron heating and electron cyclotron current drive launcher development in magnetic fusion devices. *FUSION SCIENCE AND TECHNOLOGY*, 53(1):12–38, JAN 2008.
- [16] H. Zohm. Recent experimental progress in electron cyclotron resonance heating and electron cyclotron current drive in magnetically confined fusion plasmas. *FUSION SCIENCE AND TECHNOLOGY*, 52(2):134–144, AUG 2007.
- [17] R Prater. Heating and current drive by electron cyclotron waves. *PHYSICS OF PLASMAS*, 11(5):2349–2376, MAY 2004.
- [18] J. P. Hogge, T. P. Goodman, S. Alberti, F. Albajar, K. A. Avramides, P. Benin, S. Bethuys, W. Bin, T. Bonicelli, A. Bruschi, S. Cirant, E. Droz, O. Dumbrajs, D. Fasel, F. Gandini, G. Gantenbein, S. Illy, S. Jawla, J. Jin, S. Kern, P. Lavanchy, C. Lievin, B. Marletaz, P. Marmillod, A. Perez, B. Piosczyk, I. Pagonakis, L. Porte, T. Rzesnicki, U. Siravo, M. Thumm, and M. Q. Tran. FIRST EXPERIMENTAL RESULTS FROM THE EUROPEAN UNION 2-MW COAXIAL CAVITY ITER GYROTRON PROTOTYPE. *FUSION SCIENCE AND TECHNOLOGY*, 55(2):204–212, FEB 2009.
- [19] W. Bin, A. Bruschi, S. Cirant, V. Erckmann, F. Gandini, G. Granucci, F. Hollmann, H. P. Laqua, V. Mollera, V. Muzzini, A. Nardone, F. Noke, B. Piosczyk, F. Purps, T. Rzesnicki, M. Schmid, C. Sozzi, W. Spies, N. Spinicchia, and M. Stoner. Advances in high power calorimetric matched loads for short pulses and CW gyrotrons. *FUSION ENGINEERING AND DESIGN*, 82(5-14):775–784, OCT 2007.
- [20] Yu.A.Arsenyev, V.M.Glagolev, G.A.Eliseev, and N.S.Cheverev. In *Digest of Reports at the International Conference on Plasma Physics and Controlled Fusion (C-10/218)*, Zaltsburg, 1961.

- [21] V.M.Glagolev, I.N.Khromkov, and N.S.Cheverev. *At. Energ.*, 20:401, 1966.
- [22] V.V.Alikaev et al. In *Proceedings of the Conference on Plasma Physics and Controlled Nuclear Fusion Research*, volume 2, page 877, 1965.
- [23] R. J. Goldston and P. H. Rutherford. *Introduction to Plasma Physics*. IOP PUBLISHING LTD, 1995.
- [24] A. A. Tuccillo, A. Alekseyev, B. Angelini, S. V. Annibaldi, M. L. Apicella, G. Apruzzese, J. Berrino, E. Barbato, A. Bertocchi, A. Biancalani, W. Bin, A. Botrugno, G. Bracco, S. Briguglio, A. Bruschi, P. Buratti, G. Calabro, A. Cardinali, C. Castaldo, C. Centioli, R. Cesario, L. Chen, S. Cirant, V. Cocilovo, F. Crisanti, R. De Angelis, U. de Angelis, L. Di Matteo, C. Di Troia, B. Esposito, G. Fogaccia, D. Frigione, L. Gabellieri, F. Gandini, E. Giovannozzi, G. Granucci, F. Gravanti, G. Grossetti, G. Grosso, F. Iannone, H. Kroegler, V. Lazarev, E. Lazaro, I. E. Lyublinski, G. Maddaluno, M. Marinucci, D. Marocco, J. R. Martin-Solis, G. Mazzitelli, C. Mazzotta, V. Mella, F. Mirizzi, S. Mirnov, G. Monari, A. Moro, V. Muzzini, S. Nowak, F. P. Orsitto, L. Panaccione, D. Pacella, M. Panella, F. Pegoraro, V. Pericoli-Ridolfini, S. Podda, S. Ratynskaia, G. Ravera, A. Romano, A. Ruffoloni, A. Simonetto, P. Smeulders, C. Sozzi, E. Sternini, B. Tilia, O. Tudisco, A. Vertkov, V. Vitale, G. Vlad, R. Zagorski, M. Zerbini, and F. Zonca. Overview of the FTU results. *NUCLEAR FUSION*, 49(10), OCT 2009.
- [25] O. Tudisco, G.M. Apruzzese, P. Buratti, L. Cantarini, A. Canton, V. Cocilovo, R. De Angelis, M. De Benedetti, B. Esposito, L. Gabellieri, E. Giovannozzi, G. Granucci, L.A. Grosso, G. Grosso, P. Innocente, H. Kroegler, M. Leigheb, G. Monari, D. Pacella, L. Panaccione, V. Pericoli-Ridolfini, G. Pizzicaroli, S. Podda, M.E. Puiatti, G. Rocchi, A. Sibio, A. Simonetto, P. Smeulders, U. Tartari, N. Tartoni, B. Tilia, M. Valisa, V. Zanza, and M. Zerbini. The diagnostic systems in the FTU. *Fusion Science and Technology*, 45(3):402–421, MAY 2004.
- [26] R Dumont and G Giruzzi. Hot plasma effects on the polarization of electron cyclotron waves. *PHYSICS OF PLASMAS*, 6(3):660–665, MAR 1999.
- [27] M. Bornatici, R. Cano, and O. De Barbieri. Electron cyclotron emission and absorption in fusion plasmas. *Nuclear Fusion*, 23(9):1153–1257, 1983.

- [28] F. F. Chen. *Introduction to Plasma Physics*. Plenum Press, 1974.
- [29] V. D. Shafranov. Electromagnetic waves in a plasma. In M. A. Leontovich, editor, *Reviews of Plasma Physics*, volume 3, pages 1–157. Consultants Bureau, New York, 1967.
- [30] RW HARVEY, MG MCCOY, and GD KERBEL. POWER DEPENDENCE OF ELECTRON-CYCLOTRON CURRENT DRIVE FOR LOW-FIELD AND HIGH-FIELD ABSORPTION IN TOKAMAKS. *PHYSICAL REVIEW LETTERS*, 62(4):426–429, JAN 23 1989.
- [31] N.J. Fisch. Theory of Current Drive in Plasmas. *Reviews of Modern Physics*, 59(1):175–234, JAN 1987.
- [32] D. W. Faulconer. Current drive. *FUSION SCIENCE AND TECHNOLOGY*, 53(2T):210–219, FEB 2008.
- [33] J.A. Hoekzema. Plasma heating and current drive: Electron cyclotron waves. In *6th Carolus Magnus Summer School proceedings, Trilateral Euregio Cluster, Institut für Plasmaphysik, Forschungszentrum Jülich GmbH*, 2003.
- [34] D. Farina and R. Pozzoli. Absorption and Current Drive by Electron-Cyclotron Waves at Upshifted and Downshifted Resonances in the Lower Hybrid Current Drive Regime. *Physics of Fluids B-Plasma Physics*, 1(5):1042–1048, MAY 1989.
- [35] G. Granucci, M. Aquilini, W. Bin, A. Bruschi, P. Buratti, G. Calabrò, S. DiGiovane, D. Farina, F. Gandini, C. Gormezano, G. Grossetti, C. Mazzotta, V. Mellera, F. Mirizzi, A. Moro, V. Muzzini, S. Nowak, L. Panaccione, V. Pericoli-Ridolfini, P. Petrolini, S. Podda, C. Sozzi, A. Tuccillo, O. Tudisco, ECRH, and FTU team. Quantification of suprathreshold current drive on ftu. In *Proc. 32nd EPS Conference on Plasma Phys., ECA, 29C, P-1.098*, 2005.
- [36] C. Sozzi, G. Granucci, S. Nowak, A. Bruschi, D. Farina, F. Gandini, L. Panaccione, V. Pericoli-Ridolfini, B. Angelini, S.V. Annibaldi, M.L. Apicella, G. Apruzzese, E. Barbato, P. Buratti, G. Calabrò, C. Castaldo, S. Cirant, M. De Benedetti, J. Berrino, A. Bertocchi, A. Cardinali, L. Carraro, C. Centioli, R. Cesario, V. Cocilovo, F. Crisanti, R. DeAngelis, F. De Marco, B. Esposito, D. Frigione, L. Gabellieri, E. Giovannozzi, F. Iannone, H. Kroegler, E. Lazzaro, M. Leigheb,

- M. Marinucci, D. Marocco, G. Mazzitelli, C. Mazzotta, F. Mirizzi, G. Monari, F. Orsitto, D. Pacella, M. Panella, L. Pieroni, S. Podda, M. E. Puiatti, G. Ravera, G. Regnoli, G. B. Righetti, F. Romanelli, M. Romanelli, A. Simonetto, P. Smeulders, E. Sternini, B. Tilia, O. Tudisco, A. A. Tuccillo, V. Vitale, G. Vlad, and F. Zonca. *J. Phys. Conf. Ser.*, 25:198, 2005.
- [37] N.J. Fisch and A.H. Boozer. Creating an Asymmetric Plasma Resistivity With Waves. *Physical Review Letters*, 45(9):720–722, 1980.
- [38] T. Ohkawa. Steady state operation of tokamaks by rf heating. National Technical Information Service Document PB2000-108008. Copies may be ordered from NTIS, Springfield, Virginia 22161, General Atomics Report GA-A13847, 1976.
- [39] E. Westerhof. Electron cyclotron waves. *Fusion Science and Technology*, 53(2T):202–209, FEB 2008.
- [40] H. J. de Blank. MHD instabilities in tokamaks. *FUSION SCIENCE AND TECHNOLOGY*, 53(2T):122–134, FEB 2008.
- [41] R. J. La Haye, A. Isayama, and M. Maraschek. Prospects for stabilization of neo-classical tearing modes by electron cyclotron current drive in ITER. *NUCLEAR FUSION*, 49(4), APR 2009.
- [42] R.J. La Haye, D.P. Brennan, R.J. Buttery, and S.P. Gerhardt. Islands in the stream: The effect of plasma flow on tearing stability. *Physics of Plasmas*, 17:056110, 2010.
- [43] O. Sauter and H. Zohm. Quantification of suprathreshold current drive on ftu. In ECA, editor, *Proc. 32th EPS Conference on Plasma Phys.*, volume 29C, P-2.059, 2005.
- [44] S. von Goeler, W. Stodiek, and N. Sauthoff. Studies of internal disruptions and $m = 1$ oscillations in tokamak discharges with soft—x-ray techniques. *Phys. Rev. Lett.*, 33(20):1201–1203, Nov 1974.
- [45] S. Nowak, G. Granucci, C. Sozzi, A. Bruschi, B. Esposito, F. Gandini, L. Panaccione, O. Tudisco, P. Buratti, S. Cirant, D. Farina, E. Giovannozzi, C. Mazzotta, G. Ramponi, P. Smeulders, and ECRH-FTU team. Electron cyclotron current drive experiments in the ftu tokamak. *Proc. 32nd EPS Conference on Plasma Phys., ECA Vol.29C, P-1.095*, 2005.

- [46] S. Cirant, A. Airoidi, L. Bertalot, G. Bracco, A. Bruschi, P. Buratti, A. Cenacchi, B. Esposito, G. Gervasini, G. Granucci, E. Lazzaro, S. Nowak, G. Ramponi, A. Simonetto, C. Sozzi, O. Tudisco, M. Zerbini, F. Alladio, L. Acitelli, B. Angelini, M.L. Apicella, G. Apruzzese, E. Barbato, A. Bertocchi, G. Buceti, A. Cardinali, C. Centioli, R. Cesario, C. Cianfarani, S. Ciattaglia, V. Cocilovo, F. Crisanti, R. De Angelis, F. De Marco, D. Frigione, L. Gabellieri, G. Gatti, C. Goullan, M. Grolli, A. Imparato, H. Kroegler, M. Leigheb, E. Giovannozzi, G. Maddaluno, G. Maffia, M. Marinucci, G. Mazzitelli, F. Mirizzi, F.P. Orsitto, D. Pacella, L. Panaccione, M. Panella, V. Pericoli Ridolfini, L. Pieroni and S. Podda, G.B. Righetti, F. Romanelli, F. Santini, M. Sassi, S.E. Segre, S. Sternini, A.A. Tuccillo, V. Vitale, G. Vlad, V. Zanza, and F. Zonca. Sawteeth stabilization and ion temperature enhancement by localized ecrh in ftu plasmas. In ECA, editor, *Proc. 1998 ICCPP and 25th European Conference on Controlled Fusion and Plasma Physics*, volume 22C, page 1174, 1998.
- [47] S. Cirant, J. Berrino, P. Buratti, G. D'Antona, F. Gandini, G. Granucci, E. Iannone, E. Lazzaro, V. Mellerer, V. Muzzini, P. Smeulders, and O. Tudisco. ECH/ECCD applications for MHD studies and automatic control in FTU tokamak. *FUSION SCIENCE AND TECHNOLOGY*, 53(1):174–183, JAN 2008.
- [48] G. D'Antona, S. Cirant, D. Farina, F. Gandini, E. Lazzaro, W. Treuterer, and A. Manini. Algorithms for the control of ntm by localized ecrh. principles and requirements of the real time diagnostic and control system. *Proc. International Conference on Burning Plasma Diagnostics, Varenna.*, 2007.
- [49] R. J. La Haye. Neoclassical tearing modes and their control. *Physics of Plasmas*, 13:055501, 2006.
- [50] G. Granucci, G. Ramponi, G. Calabrò, F. Crisanti, G. Ramogida, W. Bin, A. Botrugno, P. Buratti, O. D'Arcangelo, D. Frigione, G. Pucella, A. Romano, FTU, and ECRH team. Ecrh assisted start-up studies and experiments on ftu. In ECA, editor, *Proc. 36th EPS Conference on Plasma Phys.*, volume 33E, P-1.139, 2009.
- [51] G. Calabrò, F. Crisanti, G. Ramogida, R. Albanese, A. Cardinali, A. Cucchiaro, G. Granucci, G. Maddaluno, M. Marinucci, S. Nowak, A. Pizzuto, V. Pericoli Ridolfini, A. Pironti, A.A. Tuccillo, and F. Zonca. FAST plasma scenarios and equilibrium configurations. *Nuclear Fusion*, 49(5), MAY 2009.

- [52] G. Ramogida, G. Calabro, V. Cocilovo, F. Crisanti, A. Cucchiaro, M. Marinucci, A. Pizzuto, C. Rita, F. Zonca, R. Albanese, G. Artaserse, F. Maviglia, and M. Mattei. Plasma scenarios, equilibrium configurations and control in the design of FAST. *Fusion Engineering and Design*, 84(7-11):1562–1569, JUN 2009.
- [53] B. Esposito, G. Granucci, P. Smeulders, S. Nowak, J.R. Martn-Solis, L. Gabellieri, FTU, and ECRH teams. Disruption avoidance in the frascati tokamak upgrade by means of magnetohydrodynamic mode stabilization using electron-cyclotron-resonance heating. *Physical Review Letters*, 100:045006, 2008.
- [54] B. Esposito, G. Granucci, S. Nowak, J.R. Martin-Solis, L. Gabellieri, E. Lazzaro, P. Smeulders, M. Maraschek, G. Pautasso, J. Stober, W. Treutterer, L. Urso, F. Volpe, H. Zohm, FTU, ECRH, and ASDEX Upgrade Teams. Disruption control on ftu and asdex upgrade with ecrh. *Nucl. Fusion*, 49:065014 (10pp), 2009.
- [55] G. Granucci, B. Esposito, M. Maraschek, S. Nowak, J.R. Martin-Solis, W. Bin, A. Botrugno, L. Gabellieri, E. Lazzaro, G. Pautasso, A. Romano, P. Smeulders, J. Stober, W. Treutterer, O. Tudisco, L. Urso, F. Volpe, H. Zohm, FTU, and ASDEX Upgrade teams. Ecrh: A tool to control disruptions in tokamaks. In *Proc. 18th Topical Conference on Radio Frequency Power in Plasmas (RF 2009)*, 2009.
- [56] S. Cirant, E. Lazzaro, and A. Bruschi. In *Proceedings of the 19th IAEA Fusion Energy Conference, Lyon, France - International Atomic Energy Agency, Vienna 2000, Paper EX/C4-2Rb*, 2002.
- [57] B. Angelini, M.L. Apicella, and G. Apruzzese et al. In *Proceedings of the 19th IAEA Fusion Energy Conference, Lyon, France - International Atomic Energy Agency, Vienna 2000, Paper OV/4-5*, 2002.
- [58] V. Pericoli-Ridolfini, E. Barbato, and P. Buratti et al. In *Proceedings of the 19th IAEA Fusion Energy Conference, Lyon, France - International Atomic Energy Agency, Vienna 2000, Paper EX/C3-6*, 2002.
- [59] C.P. Moeller. In *Proc. 23rd Int. Conf. on Infrared and Millimeter Waves (Colchester, 1998)*, pp. 116-118. ed T.J. Parker and S.R.P. Smith, 1998.
- [60] H Idei, K Hanada, H Zushi, K Ohkubo, M Hasegawa, S Kubo, S Nishi, A Fukuyama, KN Sato, K Nakamura, M Sakamoto, A Yomasa, S Kawasaki, H Nakashima, A Hi-

- gashijima, T Notake, T Shimosuma, S Ito, H Hoshika, N Maezono, K Nakashima, M Ogawa, and TRIAM Expt Grp. Electron cyclotron current drive experiments in LHCD plasmas using a remote steering antenna on the TRIAM-1M tokamak. *NUCLEAR FUSION*, 46(5):489–499, MAY 2006.
- [61] T. H. Stix. *Waves in Plasmas*. AIP Press, 1992.
- [62] Heinrich Peter Laqua. Electron Bernstein wave heating and diagnostic. *PLASMA PHYSICS AND CONTROLLED FUSION*, 49(4):R1–R42, APR 2007.
- [63] I.B. Bernstein. *Phys.Rev.*, 109:10, 1958.
- [64] H.P. Laqua, V. Erckmann, H.J. Hartfuss, and H. Laqua. Resonant and nonresonant electron cyclotron heating at densities above the plasma cutoff by O-X-B mode conversion at the W7-As stellarator. *PHYSICAL REVIEW LETTERS*, 78(18):3467–3470, MAY 5 1997.
- [65] Puri S., Leuterer F., and Tutter M. *J . Plasma Phys.*, 9:89, 1973.
- [66] F.W. Crawford et. al. *Physical Review Letters*, 13(229), 1964.
- [67] G. Landauer. In *IPP-Report 2/53 Max-Planck-Institut fur Plasmaphysik*, 1996.
- [68] F. Leuterer. *Plasma Phys.*, 14:499–521, 1972.
- [69] T. Maekawa et al. *Physical Review Letters*, 86:3783, 2001.
- [70] V. Shevchenko et al. *Phys. Rev. Lett.*, 89:265005, 2003.
- [71] R Wilhelm, V Erckmann, G Janzen, W Kasperek, G Muller, E Rauchle, PG Schuller, K Schworer, and M Thumm. Electron-Cyclotron Resonance Heating and Confinement in the W VII-A Stellarator. *Plasma Physics and Controlled Fusion*, 26(12):1433–1444, 1984.
- [72] F.S. McDermott et al. *Phys. Fluids*, 25:1488, 1982.
- [73] S. Shiraiwa et al. *Phys. Rev. Lett.*, 96:185003, 2006.
- [74] K.G. Budden. *The Propagation of Radio Waves*, volume 596 – 602. Cambridge Univ Press, 1985.

- [75] AK Ram and SD Schultz. Excitation, propagation, and damping of electron Bernstein waves in tokamaks. *PHYSICS OF PLASMAS*, 7(10):4084–4094, OCT 2000.
- [76] V. Fuchs, A.K. Ram, S.D. Schultz, A. Bers, and C.N. Lashmore-Davies. *Phys. Plasmas*, 2:1637, 1995.
- [77] A.K. Ram, A.Bers, S.D. Schultz, and V. Fuchs. *Phys. Plasmas*, 3:1976, 1996.
- [78] J.Preinhaelter and V.Kopecky. *J.Plasma Phys.*, 10:1, 1973.
- [79] B. Rossi. *Ottica*. Masson Italia Editori, 1981.
- [80] K.G. Budden. *Radio Waves in the Ionosphere*. Cambridge Univ Press, 1961.
- [81] F. De Luca and C. Maroli. Ray-tracing in the electron cyclotron frequency region. *Rapporti FP 78*, 2, 1978.
- [82] F.R. Hansen, J.P. Lynov, and P. Michelsen. The O-X-B Mode Conversion Scheme for ECRH Of a High-Density Tokamak Plasma. *Plasma Physics and Controlled Fusion*, 27(10):1077–1100, 1985.
- [83] J. Preinhaelter. Penetration of an Ordinary Wave into a Weakly Inhomogeneous Magnetoplasma at Oblique-Incidence. *CZECHOSLOVAK JOURNAL OF PHYSICS*, 25(1):39–50, 1975.
- [84] R. Weitzner and D.B. Batchelor. *Phys. Fluids*, 22:1355, 1979.
- [85] A.A. Zharov. *Sov. J. Plasma Phys.*, 10:642, 1984.
- [86] E. Mjølhus. Coupling to Z-Mode Near Critical Angle. *Journal of Plasma Physics*, 31(FEB):7–28, 1984.
- [87] B. Brañas, M. Hirsch, J. Sánchez, and V. Zhuravlev. *Rev. Sci. Instrum.*, 70:1025–9, 1999.
- [88] V Erckmann, HP Laqua, H Massberg, NB Marushchenko, W Kasperek, and GA Muller. 20 years of ECRH at W7-A and W7-AS. *NUCLEAR FUSION*, 43(11):1313–1323, NOV 2003.
- [89] R Brakel and W7-AS Team. Electron energy transport in the presence of rational surfaces in the Wendelstein 7-AS stellarator. *NUCLEAR FUSION*, 42(7):903–912, JUL 2002.

- [90] A. Bers and A.K. Ram. Symmetries in dissipation-free linear mode conversion. In Proc. 29th EPS Conference on Plasma Phys., editor, *ECA*, volume 26B, O-4.06, 2002.
- [91] Josef Preinhaelter, Heinrich P. Laqua, Jakub Urban, Linda Vahala, and George Vahala. EBW power deposition and current drive in WEGA-comparison of simulation with experiment. *PLASMA PHYSICS AND CONTROLLED FUSION*, 51(12), DEC 2009.
- [92] H.P. Laqua, S. Marsen, M. Otte, J. Preinhealter, T. Stange, J. Urban, and D. Zhang. Electron bernstein wave experiments at the wega stellarator. In Proc. 36th EPS Conference on Plasma Phys., editor, *ECA*, volume 33E, 2009.
- [93] S. J. Diem, G. Taylor, J. B. Caughman, P. Efthimion, H. Kugel, B. P. LeBlanc, J. Preinhaelter, S. A. Sabbagh, J. Urban, and J. Wilgen. Electron Bernstein wave emission based diagnostic on National Spherical Torus Experiment (invited). *REVIEW OF SCIENTIFIC INSTRUMENTS*, 79(10), OCT 2008.
- [94] HP Laqua, W7-AS Team, and ECRH Grp. Electron Bernstein wave heating and emission via the OXB process at W7-AS. *PLASMA PHYSICS AND CONTROLLED FUSION*, 41(Suppl. 3A):A273–A284, MAR 1999.
- [95] HP Laqua, HJ Hartfuss, and W7-AS Team. Electron Bernstein wave emission from an overdense plasma at the W7-AS stellarator. *PHYSICAL REVIEW LETTERS*, 81(10):2060–2063, SEP 7 1998.
- [96] M. Shimada et al. *NUCLEAR FUSION*, 47(S1-S17), 2007.
- [97] RA Cairns and CN Lashmore-Davies. The prospects for electron Bernstein wave heating of spherical tokamaks. *PHYSICS OF PLASMAS*, 7(10):4126–4134, OCT 2000.
- [98] H Weitzner. O-X mode conversion in an axisymmetric plasma at electron cyclotron frequencies. *PHYSICS OF PLASMAS*, 11(3):866–877, MAR 2004.
- [99] E. D. Gospodchikov, A. G. Shalashov, and E. V. Suvorov. On the influence of 2D inhomogeneity on electromagnetic mode conversion near the cut-off surfaces in magnetized plasmas. *PLASMA PHYSICS AND CONTROLLED FUSION*, 48(6):869–883, JUN 2006.

- [100] A. Popov and A. Piliya. *Plasma Phys. Rep.*, 109, 2007.
- [101] A. G. Shalashov and E. D. Gospodchikov. On perfect O-X mode conversion near the cut-off surfaces in magnetized plasmas. *PLASMA PHYSICS AND CONTROLLED FUSION*, 50(4), APR 2008.
- [102] E. D. Gospodchikov, A. G. Shalashov, and E. V. Suvorov. Effects of two-dimensional inhomogeneity in O-X mode conversion in tokamak plasmas. *FUSION SCIENCE AND TECHNOLOGY*, 53(1):261–278, JAN 2008.
- [103] A. Yu Popov. On O-X mode conversion in 2D inhomogeneous plasma with a sheared magnetic field. *PLASMA PHYSICS AND CONTROLLED FUSION*, 52(3), MAR 2010.
- [104] T. H. Stix. *The Theory of Plasma Waves*. McGraw-Hill, 1962.
- [105] P. F. Goldsmith. *Quasioptical Systems: Gaussian Beam Quasioptical Propagation and Applications*. IEEE Press, 1997.
- [106] M. Greenwald. Density limits in toroidal plasmas. *Plasma Phys. Control. Fusion*, 44:R27–R53, 2002.
- [107] M. Greenwald et al. *Nucl. Fusion*, 28:2199, 1988.
- [108] A. Pochelon, A. Mueck, L. Curchod, Y. Camenen, S. Coda, B. P. Duval, T. P. Goodman, I. Klimanov, H. P. Laqua, Y. Martin, J. M. Moret, L. Porte, A. Sushkov, V. S. Udintsev, F. Volpe, and TCV Team. Electron Bernstein wave heating of overdense H-mode plasmas in the TCV tokamak via O-X-B double mode conversion. *NUCLEAR FUSION*, 47(11):1552–1558, NOV 2007.
- [109] L. Porte, S. Coda, and S. Alberti. *Nuclear Fusion*, 47:952, 2007.
- [110] F WAGNER, G BECKER, K BEHRINGER, D CAMPBELL, A EBERHAGEN, W ENGELHARDT, G FUSSMANN, O GEHRE, J GERNHARDT, G VONGIERKE, G HAAS, M HUANG, F KARGER, M KEILHACKER, O KLUBER, M KORNHERR, K LACKNER, G LISITANO, GG LISTER, HM MAYER, D MEISEL, ER MULLER, H MURMANN, H NIEDERMEYER, W POSCHENRIEDER, H RAPP, H ROHR, F SCHNEIDER, G SILLER, E SPETH, A STABLER, KH STEUER, G VENUS, O VOLLMER, and Z YU. REGIME OF IM-

PROVED CONFINEMENT AND HIGH-BETA IN NEUTRAL-BEAM-HEATED DIVERTOR DISCHARGES OF THE ASDEX TOKAMAK. *PHYSICAL REVIEW LETTERS*, 49(19):1408–1412, 1982.

- [111] R. Bilato, F. Volpe, A. Koehn, R. Paccagnella, D. Farina, E. Poli, and M. Brambilla. Feasibility of electron Bernstein wave coupling via O-X-B mode conversion in the RFX-mod reversed field pinch device. *NUCLEAR FUSION*, 49(7), JUL 2009.
- [112] H.P.Laqua et al. *Phys. Rev. Lett.*, 90:075003, 2003.
- [113] A.K. Ram et al. *J. Plasma Phys.*, 71:675, 2005.
- [114] A. Fasoli and TCV Team. Overview of TCV results. *NUCLEAR FUSION*, 48(3), MAR 2008.
- [115] F Volpe, HP Laqua, and W7-AS Team. BXO mode-converted electron Bernstein emission diagnostic (invited). *REVIEW OF SCIENTIFIC INSTRUMENTS*, 74(3, Part 2 Sp. Iss. SI):1409–1413, MAR 2003.
- [116] F. Volpe. Ipp report 13/1. Technical report, Max-Planck Institut für Plasmaphysik, IPP Garching and Greifswald, 2003.
- [117] A. Mueck, H.P. Laqua, S. Coda, B.P. Duval, T.P. Goodman, I. Klimanov, Y. Martin, A. Pochelon, and L. Porte. O-x-b mode conversion in the tcv tokamak. In ECA, editor, *Proc. 32th EPS Conference on Plasma Phys.*, volume 29C, P-4.110, 2005.
- [118] A. Mueck, L. Curchod, Y. Camenen, S. Coda, T. P. Goodman, H. P. Laqua, A. Pochelon, L. Porte, and F. Volpe. Demonstration of electron-Bernstein-wave heating in a tokamak via O-X-B double-mode conversion. *PHYSICAL REVIEW LETTERS*, 98(17), APR 27 2007.
- [119] A. Mueck, Y. Camenen, S. Coda, L. Curchod, T. P. Goodman, H. P. Laqua, A. Pochelon, L. Porte, V. S. Udintseva, F. Volpe, and TCV Team. Electron Bernstein wave heating and emission in the TCV tokamak. *FUSION SCIENCE AND TECHNOLOGY*, 52(2):221–229, AUG 2007.
- [120] M. L. Apicella, G. Mazzitelli, V. Pericoll Ridolfini, V. Lazarev, A. Alekseyev, A. Vertkov, R. Zagorski, and FTU Team. First experiments with lithium limiter on FTU. *JOURNAL OF NUCLEAR MATERIALS*, 363:1346–1351, JUN 15 2007.

- [121] G. Mazzitelli, M.L. Apicella, G. Apruzzese, R. De Angelis, D. Frigione, E. Giovannozzi, L. Gabellieri, G. Granucci, C. Mazzotta, M. Marinucci, A. Romano, and FTU Team O. Tudisco, and ECRH Team. Review of ftu results with the liquid lithium limiter. *Proc. 2nd NIFS-CRC Symposium on Plasma Surface Interactions*, January 18th-20th 2010.
- [122] M. L. Apicella, V. Lazarev, I. Lyublinski, G. Mazzitelli, S. Mirnov, and A. Vertkov. Lithium capillary porous system behavior as PFM in FTU tokamak experiments. *JOURNAL OF NUCLEAR MATERIALS*, 386:821–823, APR 30 2009.
- [123] M.L. Apicella, G. Mazzitelli, V. Pericoli, V. Lazarev, A. Alekseyev, A. Vertkov, and R. Zagorski. *J. Nucl. Mater.*, pages 363–365, 2007.
- [124] G. Mazzitelli, M.L. Apicella, A. Botrugno, R. De Angelis, D. Frigione, G. Granucci, M. Marinucci, C. Mazzotta, M. Romanelli, O. Tudisco, A. G. Alekseyev, and FTU Team. FtU results with the liquid lithium limiter. *Proc. 23rd IAEA Fusion Energy Conference. Daejon, Korea Rep.*, October 11th-16th 2010.
- [125] G. Mazzitelli, M.L. Apicella, G. Apruzzese, R. De Angelis, L. Gabellieri, E. Giovannozzi, M. Marinucci, C. Mazzotta, A. Romano, O. Tudisco, and FTU team. Recent ftu experimental results with liquid lithium limiter in cps configuration. *Proc. 19th International Conference on Plasma Surface Interactions*, May 24th-28th 2010.
- [126] O. Tudisco, C. Mazzotta, A. Botrugno, G. Mazzitelli, M.L. Apicella, G. Apruzzese, D. Frigione, L. Gabellieri, A. Romano, and FTU team. Peaked density profiles and mhd activity on ftu in lithium dominated discharges. *Presentation of 2nd NIFS-CRC Symposium on Plasma Surface Interactions*, January 18th-20th 2010.
- [127] F ALLADIO, R BARTIROMO, B CASALI, P BURATTI, F DEMARCO, M DE-PRETIS, R GIANNELLA, M GROLLI, L PIERONI, A TANGA, A TUCCILLO, and O TUDISCO. THE REGIME OF ENHANCED PARTICLE RECYCLING IN HIGH-DENSITY TOKAMAK DISCHARGES IN THE FRASCATI TORUS. *PHYSICS LETTERS A*, 90(8):405–409, 1982.
- [128] B LIPSCHULTZ, B LABOMBARD, ES MARMAR, MM PICKRELL, JL TERRY, R WATTERSON, and SM WOLFE. MARFE - AN EDGE PLASMA PHENOMENON. *NUCLEAR FUSION*, 24(8):977–988, 1984.

- [129] C. Mazzotta, O. Tudisco, A. Canton, P. Innocente, M. DeBenedetti, E. Giovannozzi, D. Marocco, P. Micozzi, G. Monari, and G. Rocchi. Measurement of density profiles using the new infrared scanning interferometer for FTU. *PHYSICA SCRIPTA*, T123:79–83, 2006.
- [130] F ALLADIO and P MICOZZI. EXPERIMENTAL PLASMA EQUILIBRIUM RECONSTRUCTION FROM KINETIC AND MAGNETIC MEASUREMENTS IN THE FTU TOKAMAK. *NUCLEAR FUSION*, 35(3):305–328, MAR 1995.
- [131] et al. M. Murakami. *Nucl. Fusion*, 16:347, 1976.
- [132] S NOWAK and A OREFICE. 3-DIMENSIONAL PROPAGATION AND ABSORPTION OF HIGH-FREQUENCY GAUSSIAN BEAMS IN MAGNETOACTIVE PLASMAS. *PHYSICS OF PLASMAS*, 1(5, Part 1):1242–1250, MAY 1994.
- [133] Martin D.H. Gaussian beam-mode analysis of paraxial propagation. From "Queen Mary College Lectures".
- [134] W. Bin, A. Bruschi, S. Cirant, G. Granucci, A. Moro, and S. Nowak. O-x mode conversion evaluations in ftu tokamak for the design of a new launching system. *Proc. 36th EPS Conference on Plasma Phys., ECA Vol.33E, P-1.138*, 2009.
- [135] A Bruschi, R Bozzi, S Cirant, F Gandini, G Granucci, S Mantovani, V Mollera, V Muzzini, A Nardone, S Nowak, A Simonetto, C Sozzi, and N Spinicchia. ECRH antenna at 140 GHz on FTU Tokamak. *FUSION ENGINEERING AND DESIGN*, 53:431–441, JAN 2001.
- [136] S Cirant, A Airoidi, L Bertalot, A Bruschi, G Bracco, P Buratti, G Cenacchi, B Esposito, G Granucci, H Kroegler, E Lazzaro, S Nowak, G Ramponi, C Sozzi, O Tudisco, M Zerbini, IFP Grp, and FTU Team. ECRH at high heating power density in FTU tokamak. *FUSION ENGINEERING AND DESIGN*, 53:301–308, JAN 2001.
- [137] E Lazzaro, RJ Buttery, TC Hender, P Zanca, R Fitzpatrick, M Bigi, T Bolzonella, R Coelho, M DeBenedetti, S Nowak, O Sauter, M Stamp, and EFDA-JET work programme. Error field locked modes thresholds in rotating plasmas, anomalous braking and spin-up. *PHYSICS OF PLASMAS*, 9(9):3906–3918, SEP 2002.

- [138] W. Bin, A. Bruschi, S. Cirant, G. Granucci, S. Mantovani, A. Moro, and S. Nowak. Design of a new ECRH launcher for FTU tokamak. *FUSION ENGINEERING AND DESIGN*, 84(2-6):451–456, JUN 2009.
- [139] A. Bruschi, W. Bin, S. Cirant, G. Granucci, S. Mantovani, A. Moro, and S. Nowak. A New Launcher For Real-Time ECRH Experiments On FTU. *FUSION SCIENCE AND TECHNOLOGY*, 55(1):94–107, JAN 2009.
- [140] A. Bruschi, V. Erckmann, W. Kasperek, M.I. Petelin, M. Thumm, Fellow, IEEE, W. Bin, S. Cirant, O. D’Arcangelo, F. Hollmann, L. Lubyako, F. Noke, B. Plaum, F. Purps, H. Zohm, and ECRH Team at IPP Greifswald. Diplexers for power combination and switching in high power ecrh systems. *IEEE TRANSACTIONS ON PLASMA SCIENCE*, 38(6), 2010.
- [141] W. Kasperek, M. Petelin, V. Erckmann, A. Bruschi, F. Noke, F. Purps, F. Hollmann, Y. Koshurinov, L. Lubyako, B. Plaum, and W. Wubie. High-power microwave diplexers for advanced ECRH systems. *FUSION ENGINEERING AND DESIGN*, 84(2-6):1002–1005, JUN 2009.
- [142] M. Petelin, V. Erckmann, J. Hirshfield, W. Kasperek, D. Shchegolkov, and A. Tolkahev. New Concepts for Quasi-Optical Structures for Use With Gyrotron Systems. *IEEE TRANSACTIONS ON ELECTRON DEVICES*, 56(5, Sp. Iss. SI):835–838, MAY 2009.
- [143] V. Erckmann, W. Kasperek, Y. Koshurinov, L. Lubyako, M. I. Petelin, D. Yu. Shchegolkov, F. Hollmann, G. Michel, F. Noke, F. Purps, Ecrh Grp IPP Greifswald, IPF Stuttgart, IAP Nizhny Novgorod, FZK Karlsruhe, and IFP Milano. POWER COMBINATION OF TWO 140-GHz GYROTRONS AND FAST SWITCHING OF THE COMBINED BEAM. *FUSION SCIENCE AND TECHNOLOGY*, 55(1):23–30, JAN 2009.
- [144] A. Bruschi, W. Bin, S. Cirant, F. Gandini, V. Mellera, and V. Muzzini. High-power millimeter-wave calorimetric beam absorbers. *FUSION SCIENCE AND TECHNOLOGY*, 53(1):62–68, JAN 2008.
- [145] J. Berrino, C. Centioli, S. Cirant, B. Esposito, F. Gandini, G. Granucci, F. Iannone, M. Panella, and V. Vitale. Real-time control of magnetic islands in FTU. *FUSION ENGINEERING AND DESIGN*, 81(15-17, Sp. Iss. SI):1917–1921, JUL 2006.

- [146] R. Ferrero, W. Bin, A. Bruschi, S. Cirant, G. D'Antona, M. Davoudi, G. Granucci, and A. Moro. Dynamic tests on the new front-steering ecrh launcher for ftu. *Submitted to FUSION ENGINEERING AND DESIGN*.
- [147] *Infranor - Servo Drives and Motion Control, CD1-a Digital Drive Manual*, 2008.
- [148] *Linear Feedback Control*. D. Xue, and Y.Q. Chen, and D.P. Atherton, 2007.
- [149] G. D'Antona, M. Davoudi, R. Ferrero, and H. Giberti. A model predictive protection system for actuators placed in hostile environments. *Proc. IEEE Instrumentation and Measurement Conference (I2MTC), USA*, 2010.
- [150] <http://www.ni.com/compactrio>.
- [151] A. Moro, W. Bin, A. Bruschi, S. Cirant, G. D'Antona, O. D'Arcangelo, M. Davoudi, R. Ferrero, S. Garavaglia, G. Granucci, S. Mantovani, V. Mellerà, V. Muzzini, and A. Simonetto. The new front steering ecrh antenna for ftu tokamak: Design and low power tests. In *Workshop on RF Heating Technology of Fusion Plasmas*, 2010.
- [152] A. Moro, W. Bin, A. Bruschi, G. D'Antona, O. D'Arcangelo, M. Davoudi, R. Ferrero, S. Garavaglia, G. Granucci, S. Mantovani, V. Mellerà, V. Muzzini, and A. Simonetto. Low power tests on the new front steering ecrh launcher for ftu. *Submitted to FUSION ENGINEERING AND DESIGN*.
- [153] H. E Knoepfel. *Magnetic Fields*. Wiley-Interscience, 2000.
- [154] G. Bekefi. *Radiation Processes in Plasmas*. Wiley N.Y., 1966.